JARA|FIT

Annual Report 2011

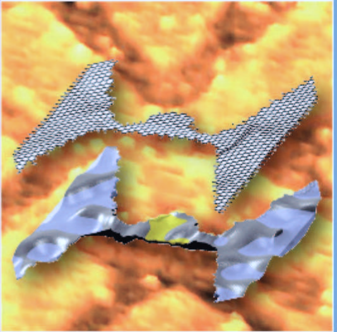

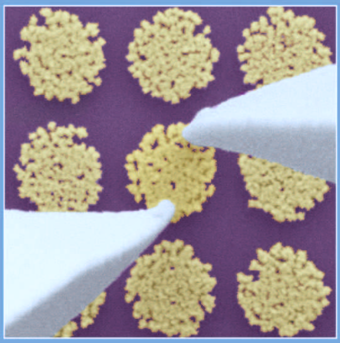

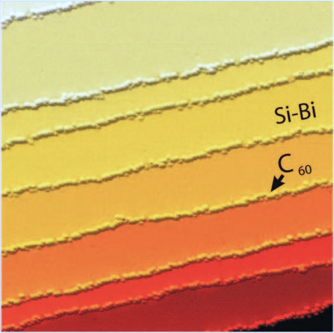

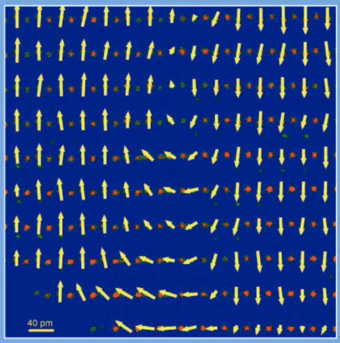

AN INITIATIVE OF

RWTH AACHEN UNIVERSITY

JÜLICH FORSCHUNGSZENTRUM

Publication Details

JARA-FIT
Jülich Aachen Research Alliance
for Fundamentals of Future Information Technologies
Annual Report 2011

Published by:
Forschungszentrum Jülich GmbH, 52425 Jülich
RWTH Aachen University, 52062 Aachen

Editors:
Prof. Dr. Detlev Grützmacher
Scientific Director JARA-FIT
Peter Grünberg Institute – Semiconductor Nanoelectronics
Forschungszentrum Jülich GmbH
52425 Jülich
Germany
Phone: ++49-2461-612340/1

Dr. Wolfgang Speier
Managing Director JARA-FIT
Forschungszentrum Jülich GmbH
52425 Jülich
Germany
Phone: ++49-2461-613107

Prof. Dr. Matthias Wuttig
Scientific Director JARA-FIT
I. Institute of Physics A
RWTH Aachen University
52074 Aachen
Germany
Phone: ++49-241-8027155

Contact:
Dr. Wolfgang Speier
w.speier@fz-juelich.de

Layout:
Silke Schilling
Janine Lenzen

Year of publication: 2012

2012

JARA-FIT

Jülich Aachen Research Alliance for Fundamentals of Future Information Technology

Annual Report 2011

Forschungszentrum Jülich

RWTH Aachen

Dear Reader,

the rapid developments in micro- and nanoelectronics have a pronounced impact on our lives. Smart phones, digital cameras, notebooks are most visible examples, but, even more importantly, nanoelectronics has become one of the key enabling technologies driving progress in industries related to mobility, health care, environment and energy. These and many other advances in technology would not have been possible without the ongoing miniaturization of semiconductor devices. However, it is also becoming increasingly clear that this size reduction is reaching physical limits. This necessitates the development of novel approaches to continue improving device performance at simultaneously reduced power consumptions. JARA-FIT meets this and related challenges with a number of dedicated activities. As already emphasized last year, RWTH Aachen University and Forschungszentrum Jülich have established a successful center for quantum information centered around Humboldt Professor David di Vincenzo and Alfried-Krupp award winner Hendrik Bluhm.

Last year was also successful for a second line of research within JARA-FIT, i.e. the research activities focusing on resistive nanoswitches to develop novel devices and architectures. In conventional semiconductor devices, structural defects are often detrimental for performance. Researchers in Aachen and Jülich, on the contrary, explore a paradigm change, exploring the idea that defects could become the building blocks of advanced nanoswitches. Their research activities are supported by the German Science Foundation which approved installing SFB 917, a collaborative research center devoted to the study of resistive nanoswitches to realize novel devices and architectures. To meet the challenges of this demanding research topic, scientists from RWTH Aachen University and Forschungszentrum Jülich are closely working together in interdisciplinary teams lead by program speaker Matthias Wuttig and vice-speaker Rainer Waser. The infrastructure developed within JARA-FIT to get up with the close corporations established over the last years was crucial for the success of the research proposal for the German Science Foundation. Among these, just to mention the most recent developments, are the new state-of-the-art ultra-low vibration laboratory for precision scannning tunnelling microscopy established last year in Jülich and the most advanced ultrahigh-resolution transmission electron microscope inaugurated this February. This microscope, known as PICO, is hosted by the Ernst Ruska-Centre, which is operated jointly by RWTH Aachen University and the Forschungszentrum Jülich. It reaches an unprecedented resolution allowing precision measurements of atomic distances and atomic displacement; thus opening fascinating scientific routes in our effort to explore the nanoworld.

This summer could bring further highlights important to the advance of JARA-FIT. On June 15th, the German Council of Science and Humanities together with the German Research Foundation will decide which universities will obtain funding to become a German University of Excellence. In the last five years, RWTH Aachen has benefitted substantially from the funding obtained through the Excellence Initiative, which has helped to promote a culture of support and competition of novel ideas and has provided the research infrastructure to compete globally. If successful in June, RWTH Aachen University and Forschungszentrum Jülich would further strengthen their joint research platform JARA. Within JARA-FIT, the most important new measure that could be implemented with a successful third funding line would be the creation of joint research institutes focusing on Quantum Information and Green-IT. This would establish a new level of cooperation with significantly increased possibilities and mutual obligations. Moreover, a second research proposal has the potential to advance research, training and education within JARA-FIT. A graduate school has been proposed by JARA-FIT (speaker: Joachim Mayer) which would offer novel training programs for talented Ph.D. students. Hence, the scientists active within JARA are eager to learn about the decision of the German Council of Science and Humanities and the German Research Foundation.

Just a few days later, Aachen is hosting the first Nature Conference in Germany organized by members of JARA-FIT lead by Rainer Waser. From June 17th to June 20th more than 500 scientists will discuss Frontiers in Electronic Materials with a focus on correlation effects and memristive phenomena. Hence we are looking forward to an exciting month ahead and hope that you share our enthusiasm about the developments in nanoelectronics described in this report.

Matthias Wuttig	Detlev Grützmacher
Scientific Director JARA-FIT	Scientific Director JARA-FIT

Contents

JARA-FIT in Headlines

Ultra-Low Vibration STM Laboratory completed

After three years of construction, our state-of-the-art ultra-low vibration laboratory for precision scannning tunnelling microscopy (STM) has been completed in 2011 – a reason to celebrate! The opening ceremony was held on 29. March 2011, in the presence of Dr. Ulrich Krafft and Prof. Dr. Sebastian M. Schmidt from the Board of Directors of Forschungszentrum Jülich and the architects of pbr.

The laboratory consists of two rooms which are shielded against sound, vibrations and electromagnetic radiation. Scanning tunnelling microscopes can not only be used to image surfaces with atomic resolution, but also to record spectra from single atoms. With an STM, it is even possible to move individual atoms and molecules at will.

It is clear that STM experiments require ultimate mechanical stability of the microscope. The smallest vibration of the tip against the surface will disturb the experiment. Although scanning tunnelling microscopes are constructed in a way to mimimize their susceptibility to mechanical vibrations, for the most demanding applications it is still necessary to shield the microscope from the detrimental influence of sound and floor vibrations. For this purpose we have designed two specially shielded rooms in our Ultra-Low Vibration STM Laboratory.

The Ultra-Low Vibration STM Laboratory is based on a room-in-room concept. Two sound-proof and electromagnetically shielded rooms that house one STM each are located in a hall from where the microscopes are operated. Each room is built on a 100-ton concrete foundation that floats on passive air dampers and is therefore decoupled from the surrounding building. The large mass of the foundations ensures a low mechanical resonance frequency (below 1 Hz), thereby offering optimum vibration-insulation of the microscopes in the rooms.

PICO – Unique Electron Microscope launched at the ER-C

A unique next generation transmission electron microscope referred to as the PICO (Advanced Picometre Resolution Project) was delivered in spring 2011 and officially inaugurated at the Ernst Ruska-Centre on 29 February 2012. With the commissioning of the PICO, the scientists at the Ernst Ruska-Centre and external users can now advance further into the nanoworld to the physical limits of optics. PICO is the first transmission electron microscope at ER-C with a resolution of up to fifty picometres. The instrument allows researchers to study atomic structures with the highest precision and to achieve progress in areas as energy research and information technology. With the commissioning of PICO, the operators of the centre, the Forschungszentrum Jülich and RWTH Aachen University, continue to strengthen their position at the forefront of ultrahigh-resolution electron microscopy. Funding of about 7.5 million Euros for the microscope was provided by the German Research Foundation (DFG), the Provinces of North Rhine and Westphalia, the Federal Ministry for Education and Research (BMBF), the Forschungszentrum Jülich and RWTH Aachen University.

PICO is one of currently two devices worldwide capable of correcting a lens error known as chromatic aberration, which could not be avoided in electron optics before now. In addition to improving the resolution, this also increases the precision in measuring atomic distances and atomic displacement, from five picometres to merely one. PICO is based on aberration-corrected electron optics, which was developed in the 1990s by scientists of the European Molecular Biology Laboratory (EMBL) in Heidelberg, Technische Universität Darmstadt and the Forschungszentrum Jülich. The scientists at ER-C are also developing sophisticated computer methods that will make it possible to fully exploit the capacity of modern electron microscopes.

PICO 2012 – Symposium on Frontiers of Aberration Corrected Electron Microscopy

PICO 2012 – a symposium on frontiers of aberration corrected electron microscopy also comprising the opening of the ER-C annexe and the start-up of PICO user services with a colloquium honouring former ER-C director Knut Urban – a was held in Jülich from 29. February to 2. March 2012. First in a series of conferences to be held biennially in the future, PICO 2012 focused on the most recent advances and future directions in methods and applications of aberration corrected electron microscopy for the study of structural and electronic properties of the solid state. The symposium attracted more than 250 participants from 21 countries. Topical issues of aberration corrected microscopy were highlighted in 25 keynote presentations given by leading invited speakers. A follow-up conference is scheduled to take place in October 2013.

New Ernst Ruska-Centre Laboratory Building commissioned

An opening ceremony was held on 29 September 2011 solemnising the commissioning of a 1020 square metre (402 sq. m. b.ar.) laboratory annexe to the Ernst Ruska-Centre. During the past four years a constructionally advanced, likewise architecturally exceptional building was put up with a total sum of about five million Euros having been invested by the Federal Ministry for Education and Research (BMBF) and the Forschungszentrum Jülich. Standing to benefit from virtually vibration and stray field free site conditions, the improved infrastructure enables the ER-C to maintain its position as a frontrunner in ultrahigh-resolution microscopy worldwide allowing for the operation of two ultra high resolution transmission electron microscopes as well as the installation of three standard electron microscopes plus additional laboratory equipment.

The above extension of the ER-C suprastructure complements an additional twelve million Euros investment by the German Research Foundation, the Federal Ministry for Education and Research, the Ministry of Innovation, Science, Research and Technology (MIWFT) of the Provinces of North Rhine and Westphalia, the Helmholtz Association, the Forschungszentrum Jülich and RWTH Aachen University during the past five years for purchase of state-of-the art electron optical instruments now being operated inside the ER-C annexe.

JARA Senior Professorship granted to Knut Urban

Former ER-C Director Prof. Knut Urban has been appointed as the first JARA Senior Professor by the Jülich Aachen Research Alliance. A certificate was presented to Knut Urban by the Chairman of the Board of Directors of Forschungszentrum Jülich, Professor Achim Bachem, and the Rector of RWTH Aachen University, Professor Ernst Schmachtenberg, on 27. January 2012. The appointment will allow Prof Urban to continue his research at the ER-C in the field of basic and applied electron microscopy following his formal retirement in 2011.

with permission of Martin Lux/RWTH Aachen

SFB 917 "Nanoswitches" successfully started

In May 2011, the German Research Foundation approved the application for a Collaborative Research Centre (Sonderforschungsbereich, SFB) by JARA-FIT: „Resistively switching Chalcogenides for Future Electronics – Structure, Kinetics, and Device Scalability" (SFB 917). The Collaborative Research Centre was established on July 1st, 2011 at the RWTH Aachen University. It comprises of the coordinated work of 13 institutes of the RWTH Aachen University and the Forschungszentrum Jülich. Speaker of SFB 917 is Matthias Wuttig. The Steering Committee is made up of Rainer Waser (deputy speaker), Regina Dittmann (PGI-7), Joachim Mayer (GfE & ER-C), Martin Salinga (I. Physikalisches Institut), and Ulrich Simon (Institut für Anorganische Chemie). The SFB 917 addresses non-volatile changes of the resistance of nanocells made out of two electron conducting contacts and a resistive material, typically a metal oxide or higher chalcogenides. These resistance changes are electrically induced phase transformation or redox processes in the bulk of the chalcogenides or at one of electrode interfaces. In all these processes, lattice defects are involved, and it is one of main tasks of the SFB 917 to reveal the microscopic mechanisms of the switching processes and unfold the role of defects. In the long term, a tailoring of the relevant defects on a nanometer scale will enable novel approaches in electronics and may result in a paradigm shift towards a chalcogenides-based electronics technology. On the social side, the start of the SFB 917 was celebrated with a joint event of the members of all participating institutes at Gut Melaten in Aachen in mid July.

Christoph Stampfer member of *Das Junge Kolleg* of the North Rhine-Westphalian Academy of Sciences and Humanities

Prof. Dr. Christoph Stampfer, JARA-FIT junior professor, was named as a member of *Das Junge Kolleg* by the selection committee of the North Rhine-Westphalian Academy of Sciences and Humanities. He was selected along with six other early-career scientists from over 100 applicants from all over North Rhine-Westphalia. Members of *Das Junge Kolleg* are given an opportunity to discuss their projects in interdisciplinary working groups under the auspices of the academy and to exchange ideas with the established scientific elite. Members receive a research scholarship and travel expenses of € 10,000 per annum.

Award for young scientist of JARA-FIT

Lars Knoll, PhD student at the Peter Grünberg Institute in Jülich, received the Sinano Best Paper Award for the best scientific contribution for the ULIS2011 conference. The prize was handed out within the frame of the ULIS2012 conference in Grenoble on March 6th, 2012. His paper was entitled "20 nm gate length Schottky MOSFET with ultra thin NiSi/epitaxial NiSi2 source/drain". Presently, Lars Knoll investigates Tunnel-FETs, so called "green transistors" which are expected to be much more energy efficient than standard MOS transistors.

JARA-FIT Science Days 2011

The JARA-FIT Science Days serve the purpose of providing a biannual forum for intense scientific exchange among JARA-FIT scientists and initiation of new interdisciplinary projects. Participants are PhD students, PostDocs and scientists from RWTH Aachen University and Forschungszentrum Jülich. The Science Days in 2011 brought 110 scientists together for two days, on 28. and 29. October 2011, in a retreat in Schleiden, a small town in the Eifel mountains close to Aachen and Jülich. During the Science Days the participants elected two projects awarding poster prizes to: PhD student Christian Volk, a physicist, for his work on "Quantum dots in in single-layer and bilayer graphene" (1. Prize amounting to 1000€) and PhD Student Manuel Wesche, a medical student, for his work “Towards controlling activity in designed neuronal networks” (2. Prize amounting to 500€).

JARA-FIT Lab Course Nanoelectronics

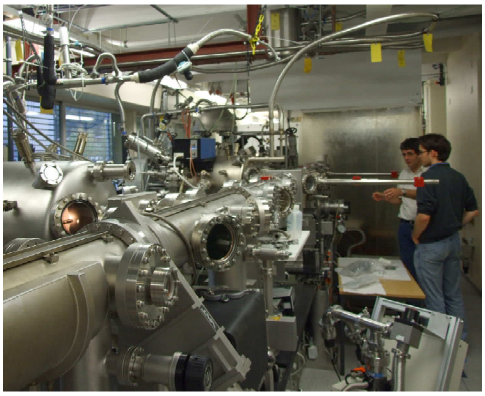

Last year, 85 Students participated in our week-long 6th JARA-FIT Lab Course Nanoelectronics. Addressees were students of physics, electrical engineering, chemistry and the material sciences after Bachelor degree. The Lab Course introduced the students to current research topics of nanoelectronics and gave them the opportunity to use the top-level laboratory research equipment of JARA-FIT. They received introductory lectures, performed one experiment per day in small groups and were able discuss job perspectives in the automotive industry in a special evening session with a scientist from the Robert Bosch Company. The students came from Aachen as part of their Master courses, additionally 15 students came from all over Germany.

JARA-Conference with Polish Scientists

On 13. and 14. October 2011, scientists from JARA visited the AGH University of Science and Technology (AGH-UST) in Krakow for the „Conference on Energy and Future Information Technology“. The conference consolidated an existing cooperation established last year in the context of the Poland North Rhine-Westphalia Year 2011/2012 organized by the government of the federal state. The focus of the conference was on electron microscopy and future information technology. One of the highlights of the conference was the official opening of the International Centre of Electron Microscopy for Materials Science, a facility planned last year by partners from Poland and JARA.

Computational Neuroscience implemented in Jülich

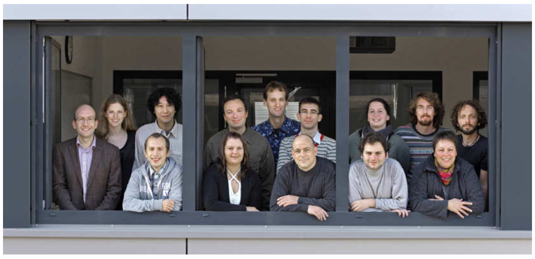

Computational Neuroscience integrates the experimental data on the structure and the dynamics of the brain into mathematical models. Today simulations are a major research tool to confront model results with data from living tissue and advanced statistical techniques are employed to extract the relevant information from massively parallel data. As in other fields of science, insight is gained from models at the appropriate level of abstraction not at the most detailed level. The self-organized and plastic nature of brain circuits makes it unlikely that a pure bottom-up approach will succeed. Therefore research needs to incorporate top-down approaches starting from the function of the system. The field has long underestimated its dependence on efficient and reliable software. Consequently intense research is now required to overcome bottlenecks in simulation technology and workflows. In March 2011 the Institute of Neuroscience and Medicine (INM-6), Computational and Systems Neuroscience started operation at the Forschungszentrum Jülich with the groups "Statistical Neuroscience" (Grün) and "Computational Neurophysics" (Diesmann). The institute is closely linked with the Faculty of Medicine and the Faculty of Mathematics, Computer Science and Natural Sciences of the RWTH Aachen University. The institute also builds a bridge to the Jülich Supercomputing Center. The main aim of the institute is to develop technologies advancing neuroscience. However, the research also contributes to the design of novel massively parallel computing devices optimized for brain-like computing.

43. IFF Spring School: Scattering Methods for Condensed Matter Research

The "IFF Spring School" was held for the 43st time lasting from 5.-16. March 2012. The motto of the Spring School run by the former Institute for Solid State Research was "Scattering Methods for Condensed Matter Research - Towards Novel Applications at Future Sources". Scattering investigations on condensed matter and life-science systems are an extremely rapidly developing field at modern synchrotron radiation sources, free electron lasers, dedicated neutron research reactors and neutron spallation sources. Scattering methods are ideally suited to provide essential and unique contributions to the grand challenges facing modern industrial society including information technology. Within the framework of this course, JARA-scientists from Jülich and Aachen together with other institutions gave 230 students and young scientists from all over the world a comprehensive overview. This year's IFF spring school was the first to welcome nine Palestinians which came from the universities of Al-Quds, Birzeit, and An-Najah.

15th Laboratory Course on Neutron Scattering

The laboratory course on neutron scattering organized by Jülich Center for Neutron Science (JCNS) at the Jülich branch lab in Garching near Munich took place form 5. –16. September 2011. During the two-week course, 54 science students from 16 countries first familiarized themselves with the theoretical principles of neutron scattering at Jülich. The practical part of the course with exercises at the neutron scattering experiments took place at the research neutron source FRM-II. Before being admitted to the course, those interested had to take part in a selection procedure since 155 students had applied.

General Information

JARA-FIT Members

Prof. Dr. S. Andergassen, Institut für Theorie der Statistischen Physik, RWTH Aachen (till january 2012)

Prof. Dr. St. Appelt, Lehrstuhl für Makromolekulare Chemie,
Lehr- und Forschungsgebiet Niederfeld-NMR(Methoden der NMR), RWTH Aachen
Zentralinstitut für Elektronik, Forschungszentrum Jülich

Prof. Dr. H. Bluhm, II. Physikalisches Institut C, RWTH Aachen

Prof. Dr. S. Blügel, Peter Grünberg Institut – Quanten-Theorie der Materialien, Forschungszentrum Jülich
Institute for Advanced Simulation, Forschungszentrum Jülich

Prof. Dr. T. Brückel, Peter Grünberg Institut – Streumethoden, Forschungszentrum Jülich
Jülich Centre for Neutron Science

Prof. Dr. A. Böker, Makromolekulare Materialien und Oberflächen, DWI an der RWTH Aachen

Prof. Dr. D. P. DiVincenzo, Institut für Quanteninformation, RWTH Aachen
Peter Grünberg Institut – Theoretische Nanoelektronik, Forschungszentrum Jülich
Institute for Advanced Simulation, Forschungszentrum Jülich

Prof. Dr. R. Dronskowski, Lehrstuhl für Festkörper- und Quantenchemie und Institut für Anorganische Chemie, RWTH Aachen

Prof. Dr. R. Dunin-Borkowski, Peter Grünberg Institut – Microstrukturforschung, Forschungszentrum Jülich
Ernst Ruska-Centrum für Mikroskopie und Spektroskopie mit Elektronen

Prof. Dr. D. Grützmacher, Peter Grünberg Institut – Halbleiter-Nanoelektronik, Forschungszentrum Jülich

Prof. Dr. S. Grün, Institut für Neurowissenschaften und Medizin, Computational and Systems Neuroscience
Forschungszentrum Jülich

Prof. Dr. C. Honerkamp, Institut für Theoretische Festkörperphysik, RWTH Aachen

Prof. Dr. P. Kögerler, Institut für Anorganische Chemie (Molekularer Magnetismus), RWTH Aachen
Peter Grünberg Institut – Elektronische Eigenschaften, Forschungszentrum Jülich

Prof. Dr. U. Klemradt, II. Physikalisches Institut B, RWTH Aachen

Prof. Dr. J. Knoch, Institut für Halbleitertechnik, RWTH Aachen

Prof. Dr. P. Loosen, Lehrstuhl für Technologie Optischer Systeme, RWTH Aachen
Fraunhofer-Institut für Lasertechnik, Aachen

Prof. Dr. S. Mantl, Peter Grünberg Institut – Halbleiter-Nanoelektronik, Forschungszentrum Jülich

Prof. Dr. M. Martin, Institut für Physikalische Chemie, RWTH Aachen

Prof. Dr. J. Mayer, Gemeinschaftslabor für Elektronenmikroskopie, RWTH Aachen
Ernst Ruska-Centrum für Mikroskopie und Spektroskopie mit Elektronen

Prof. Dr. R. Mazzarello, Institut für Theoretische Festkörperphysik, RWTH Aachen

Prof. Dr. V. Meden, Institut für Theorie der Statistischen Physik, RWTH Aachen

Prof. Dr. Chr. Melcher, Lehrstuhl I für Mathematik, RWTH Aachen

Prof. Dr. W. Mokwa, Institut für Werkstoffe der Elektrotechnik 1 – Mikrostrukturintegration, RWTH Aachen

Prof. Dr. M. Morgenstern, II. Physikalisches Institut B, RWTH Aachen

Prof. Dr. T. Noll, Lehrstuhl für Allgemeine Elektrotechnik und Datenverarbeitungssysteme, RWTH Aachen

Prof. Dr. A. Offenhäusser, Peter Grünberg Institut – Bioelektronik, Forschungszentrum Jülich
Institute of Complex Systems, Forschungszentrum Jülich

Prof. Dr. E. Pavarini, Peter Grünberg Institut & Institut for Advanced Simulation, Forschungszentrum Jülich

Prof. Dr. R. Poprawe, Fraunhofer-Institut für Lasertechnik, Aachen

Prof. Dr. G. Roth, Institut für Kristallographie, RWTH Aachen

Prof. Dr. Th. Schäpers, II. Physikalisches Institut A, RWTH Aachen (interim)
Peter Grünberg Institut – Halbleiter-Nanoelektronik, Forschungszentrum Jülich

Prof. Dr. H. Schoeller, Institut für Theorie der Statistischen Physik, RWTH Aachen

Prof. Dr. U. Simon,	Institut für Anorganische Chemie, RWTH Aachen
Prof. Dr. J. Splettstößer,	Institut für Theorie der Statistischen Physik, RWTH Aachen
Prof. Dr. C. Stampfer,	II. Physikalisches Institut B, RWTH Aachen Peter Grünberg Institut – Halbleiter-Nanoelektronik, Forschungszentrum Jülich
Prof. Dr. C. M. Schneider,	Peter Grünberg Institut – Elektronische Eigenschaften, Forschungszentrum Jülich
Prof. Dr. T. Taubner,	I. Physikalisches Institut A, RWTH Aachen
Prof. Dr. S. Tautz,	Peter Grünberg Institut – Funktionale Nanostrukturen an Oberflächen, Forschungszentrum Jülich
Prof. Dr. B.M. Terhal,	Institut für Quanteninformation, RWTH Aachen
Prof. Dr. A. Vescan,	Lehr- und Forschungsgebiet GaN-Bauelementtechnologie, RWTH Aachen
Prof. Dr. R. Waser,	Institut für Werkstoffe der Elektrotechnik 2, RWTH Aachen Peter Grünberg Institut – Elektronische Materialien, Forschungszentrum Jülich
Prof. Dr. M. Wegewijs,	Peter Grünberg Institut – Theoretische Nanoelektronik, Forschungszentrum Jülich
Prof. Dr. J. Witzens,	Lehr- und Forschungsgebiet Integrierte Photonik, RWTH Aachen
Prof. Dr. M. Wuttig,	I. Physikalisches Institut A, RWTH Aachen

JARA-FIT Institutes

Peter Grünberg Institut / Institut for Advanced Simulation – Quanten-Theorie der Materialien, Forschungszentrum Jülich

S. Blügel

The analysis and computation of electronic properties of solid-state systems relevant for basic science and practical applications in collaboration with experimentalists is the hallmark of our research. An important asset of our institute is the competence in developing conceptual and computational methods (density functional theory and beyond, wave-packet propagation, diagrammatic techniques). Emphasis is on the investigation of complex magnetism, magnetism in reduced dimensions, oxide interfaces and heterostructures, topological insulators, graphene, organic molecules in contact with metallic an insulating substrates, spin- and spin-orbit-dependent electronic transport phenomena, collective excitations and quasi-particles. A second research theme is nano-scale tribology, friction, adhesion, plastic deformation. Computational materials science research is established by combining first-principles results with macroscopic methods (molecular dynamics, Monte Carlo).

II. Physikalisches Institut (IIC), RWTH Aachen

H. Bluhm

The research group is aiming to realize highly coherent two-level quantum systems in semiconductor quantum dots for quantum information processing. The group studies the physics governing these devices and pushes forward their technological development. Crucial techniques for high-speed control and measurement will be further improved, and multi-qubit systems will be designed, fabricated, and tested. In addition, the group is pursuing scanning SQUID microscopy at ultra-low temperatures for magnetic imaging and ultra-sensitive magnetic measurements on mesoscopic structures.

Lehrstuhl für Makromolekulare Materialien und Oberflächen, DWI an der RWTH Aachen

A. Böker

The chair of Macromolecular Materials and Surfaces is part of the DWI an der RWTH Aachen. The DWI is an independent research institute affiliated to RWTH Aachen University focused on polymer / soft matter materials development with the mission of novel and active properties. Under the heading “Science for Innovation” we aim at a tailor-made surface functionality of soft materials, especially fibers, films, membranes, textiles, and biomaterials. Beyond knowledge-oriented, basic approaches, work at DWI is dedicated to the translation and implementation of this knowledge into application-oriented concepts for functional films and surfaces, antimicrobial polymers and surfaces, encapsulation and release, functional membranes, and biomedical devices. The major research topics at the chair of Macromolecular Materials and Surfaces include bioconjugate polymer materials, nanoparticle composites and guided self-assembly.

Peter Grünberg Institut - Streumethoden, Forschungszentrum Jülich

Th. Brückel

At the Institute of Scattering Methods, we focus on the investigation of structural and magnetic order, fluctuations and excitations in complex or nanostructured magnetic systems and highly correlated electron systems. Our research is directed at obtaining a microscopic atomic understanding based on fundamental interaction mechanisms. The aim is to relate this microscopic information to macroscopic physical properties. To achieve this ambitious goal, we employ the most advanced synchrotron X-ray and neutron scattering methods and place great emphasis on the complementary use of these two probes. Some of our efforts are devoted to dedicated sample preparation and characterization from thin films and multilayers via nano-patterned structures to single crystals for a wide range of materials from metals to oxides.

Peter Grünberg Institut/ Institut for Advanced Simulation – Theoretische Nanoelektronik, Forschungszentrum Jülich

D. DiVincenzo, group leaders E. Pavarini, M. Wegewijs

The behavior of interacting electrons in nano-scale structures is a primarly focus. The Kondo effect, involving the interaction of an isolated spin impurity with conduction electrons, or the formation and transport of high-spin complexes forming spin quadripoles, are particular areas of expertise. Novel computational techniques permit accurate calculations with thousands of atoms, and in complex multi-functional perovskites.

Correlated electrons also form the basis of the physical creation of qubits, and the coherence and dynamics of such qubits, and mutiqubit systems, is being investigated.

Institute for Quantum Information, RWTH Aachen

D. P. DiVincenzo, group leaders B. M. Terhal, F. Hassler, and N. Schuch

The institute has a broad agenda of topics in the theory of quantum information. New principles for the implementation of quantum computation in noisy systems, particularly Fermionic many-body systems. This includes particularly the investigation of Majorana qubits realized in semiconductor nanowires. Protocols for fault tolerance in quantum computation are investigated. New applications of the theory of quantum entanglement for efficient classical simulations are developed. Detailed modeling of hardware for superconducting qubits and circuit-quantum electrodynamic structures is underway, in close collaboration with experiment.

Lehrstuhl für Festkörper- und Quantenchemie und Institut für Anorganische Chemie, RWTH Aachen

R. Dronskowski

The institute is specialized in the fields of synthetic and quantum-theoretical solid-state chemistry, bordering with materials science, solid-state and theoretical physics, crystallography, as well as quantum and computational chemistry. In detail, we synthesize novel, sometimes extremely sensitive, compounds and elucidate their compositions and crystal structures by means of X-ray and neutron diffractional techniques. The characterization of their physical properties, that is electronic transport and magnetism, also plays a very important role.

We regularly perform solid-state quantum-chemical calculations from first principles to yield the electronic (band) structures and, in particular, to extract the important chemical bonding information needed to thoroughly understand the interplay between chemistry and physics. Syntheses are theory-driven and experiments challenge theories.

Peter Grünberg Institut – Mikrostrukturforschung, Forschungszentrum Jülich & Ernst Ruska-Centrum für Mikroskopie und Spektroskopie mit Elektronen

R. Dunin-Borkowski

The institute works on topical fields in solid-state physics. Strategically two directions are followed. Firstly, to make key contributions to the development and application of ultra-high resolution transmission electron microscopy, in particular to aberration-corrected electron optics for subangstrom structural and spectroscopic resolution. Secondly, to produce a number of selected material systems and to study their physical properties. Examples are high-temperature superconductors and the novel complex metallic alloys. The former provide the basis of our work on SQUID sensors and on ac-Josephson effect based Hilbert spectroscopy for the THz range. The head of the institute is co-director of the Ernst Ruska Centre for Microscopy and Spectroscopy with Electrons.

Institute of Neuroscience and Medicine (INM-6), Computational and Systems Neuroscience, Forschungszentrum Jülich

S. Grün, M. Diesmann

Progress in the understanding of complex systems like the brain can only be achieved by integrating data and models on many different scales. The new INM-6 develops multi-scale models of the brain, combining data-driven development of brain theory with the bottom-up approach of directly simulated structured networks, and the top down approach, mapping functional models of higher brain function to neuronal dynamics. Considerable resources are devoted to the development of technology to simulate brain circuits on modern supercomputers. The technology advances neuroscience but also provides architectural constraints with respect to memory layout and communication patterns for the partners of INM-6 concerned with neuromorphic hardware.

Peter Grünberg Institut – Halbleiter-Nanoelektronik, Forschungszentrum Jülich

D. Grützmacher

The institute's research activities are based on its competence in semiconductor heterostructure and nanostructure research, both in fundamental and device physics as well as in material and process development. They address three major fields. (1) Si-CMOS technology: novel materials and new device concepts are used to drive CMOS to its limits. (2) III-V and III-nitride semiconductors: high frequency devices are developed up to and into the terahertz range. (3) Nanostructures for quantum electronics: devices based on the tunneling effect and ferromagnetic/semiconductor hybrid structures are investigated, the latter particularly in view of spintronic applications.

Institut für Theoretische Festkörperphysik, RWTH Aachen

C. Honerkamp, R. Mazzarello, M. Schmidt, S. Wessel

The research groups in this institute study many-particle interactions in solids, ranging from quantum effects in magnetic systems over electron correlation effects leading to unconventional superconductivity and magnetism to the dynamics of structural phase transitions. Recent work has focused on interaction effects in graphene systems, topological insulators, pnictide high-temperature superconductors and chalcogenide phase-change materials. The powerful theoretical methods employed and developed here comprise quantum Monte Carlo techniques, the functional renormalization group, density-functional theory and molecular dynamics.

II. Physikalisches Institut (IIB) – Röntgenstreuung und Phasenumwandlungen, RWTH Aachen

U. Klemradt

Our research is centered at the investigation of nanoscale structures and fluctuations, with focus on nanoparticles, polymer-based nanocomposites and ferroic materials. Of particular interest are phase transitions in smart materials like shape memory alloys. The main experimental tools are X-ray scattering and acoustic emission spectroscopy. We use both laboratory tubes and synchrotron facilities for X-ray experiments and operate a 6-circle diffractometer at HASYLAB (DESY, Hamburg), which is especially suited to the analysis of thin films. Core techniques are small angle X-ray scattering (SAXS), grazing incidence scattering (GISAXS and reflectometry), and photon correlation spectroscopy using coherent X-rays (XPCS).

Institut für Halbleitertechnik, RWTH Aachen

J. Knoch

The institute carries out research on semiconductor technology and device with a special focus on low power and energy harvesting technologies with the long-term vision of energy autonomous systems. To be specific, we work on nanoelectronics transistor devices based on Si- and III-V nanowires as well as on carbon nanotubes and graphene particularly aiming at a realization of so-called steep slope switches that enable a significant reduction of the power consumption of highly integrated circuits. In addition, the institute has broad experience in the science and engineering of Si wafer-based solar cells and also performs research on Si-based third generation photovoltaic cells. A combination of our know-how in micro- and nanotechnology with the solar cell technology is used to investigate and realize novel concepts for energy harvesting and storage based e.g. on efficient direct solar water splitting.

Institut für Anorganische Chemie – Molekularer Magnetismus, RWTH Aachen & Peter Grünberg Institut – Elektronische Eigenschaften (Molekularer Magnetismus), Forschungszentrum Jülich

P. Kögerler

The Molecular Magnetism Group focuses on the chemistry and fundamental physics of discrete and networked magnetically functionalized inorganic molecules. Based on its experience with the control and understanding of magnetic characteristics of purely molecular origin, the group synthesizes magnetic materials based on transition metal clusters that exhibit a complex interplay of charge transport and static/dynamic magnetic properties such as phase transitions, hysteresis, or quantum tunneling. To functionally combine magnetic state switching and charge transport in systems for FIT spintronic devices, the molecule-surface interface is addressed, in particular employing surface structure-directed coupling reactions to molecular aggregates, single-stranded molecular conductors, or 2D networks.

Lehrstuhl für Technologie Optischer Systeme, RWTH Aachen (RWTH-TOS) & Fraunhofer-Institut für Lasertechnik, Aachen

P. Loosen

Extreme ultraviolet radiation (XUV, 1-50 nm, or EUV at 13.5 nm) enables new optical, analytical and manufacturing technologies because of its characteristic interaction with matter, its short wavelength and recent progress on light sources and optical components (e.g. EUV lithography). XUV tools are already deployed by the semiconductor industry, which significantly pushes the further development of XUV technology. Future applications which will support scientific progress in a variety of fields such as nanoelectronics or biotechnology are also within the scope of our research. Activities include structuring on a nanometer scale using interference lithography, XUV microscopy for imaging of dynamic processes or at-wavelength inspection of multilayer mask-blanks for hidden defects, and characterization of thin film coated surfaces using grazing-incidence reflectometry.

Institut für Physikalische Chemie (IPC), RWTH Aachen

M. Martin

The institute's research activities are based on its competence in the physical chemistry of solids with a special emphasis on defects and diffusion in inorganic solids, in particular oxides. Within JARA-FIT two major fields are addressed. (1) Ionic transport: transport of oxygen ions in the bulk, across and along grain boundaries and in space charge zones is investigated by means of secondary ion mass spectrometry (SIMS). (2) Electronic transport: amorphous and highly non-stoichiometric oxides are investigated concerning correlations between structure, electrical conductivity, and electronic structure. Insulator–metal transitions are studied with a view to applications in data storage.

GFE – Gemeinschaftslabor für Elektronenmikroskopie & Ernst Ruska-Centrum für Mikroskopie und Spektroskopie mit Elektronen

J. Mayer

GFE is a central facility of RWTH Aachen University and has state-of-the-art equipment in the fields of transmission electron microscopy, scanning electron microscopy, electron microprobe analysis, focused ion beam instruments and atomic force microscopy. GFE provides services for a large number of institutes from RWTH Aachen University and a broad range of industrial companies. In the field of information technology, GFE participates in research projects on nonvolatile memories and on nanoscale CMOS devices. The head of the GFE is co-director of the Ernst Ruska Centre for Microscopy and Spectroscopy with Electrons and coordinates the RWTH user activities and contribution to the Centre.

Institut für Theorie der Statistischen Physik, RWTH Aachen

S. Andergassen (till january 2012), V. Meden, H. Schoeller, J. Splettstösser, M. Wegewijs

The members of the institute are investigating the spectral and transport properties of low-dimensional quantum systems in contact with heat and particle reservoirs. The research focuses on the development of many-body methods for strongly correlated mesoscopic systems in nonequilibrium (quantum field theory and renormalization group in nonequilibrium) as well as on the application to experimentally realizable physical systems like semiconductor quantum dots, quantum wires (e.g. carbon nanotubes), and molecular systems.

Lehrstuhl I für Mathematik, RWTH Aachen

Ch. Melcher

The research at the Chair of Mathematics I has a focus on nonlinear partial differential equations from mathematical physics and materials science. We are particularly interested in the emergence and dynamics of patterns and topological defects in models from micromagnetics and Ginzburg-Landau theory. Using tools from functional and multiscale analysis, our aim is to capture the qualitative behavior of solutions to such complex theories and, if possible, to identify simpler models, whose behavior is easier to understand or simulate.

Institut für Werkstoffe der Elektrotechnik 1 – Mikrostrukturintegration, RWTH Aachen

W. Mokwa

The institute's research activities are focused on the development of micro systems for medical and life-science applications. In particular different transponder-based systems for measuring intraocular and intravascular pressure were tested successfully. The EPIRET-implant for stimulation the retina of blind patients shows excellent results. For life science applications the focus is on micro fluidic applications for fluidic management and biological cell handling, development of sensors for fermentation processes in micro titer plates, micro electrodes for neuron cell stimulation, and on micro coils for mobile compact nuclear magnetic resonance devices. In 500 m^2 clean room thin-film-, assembly-, and testing processes can be carried out under DIN-ISO-9001:2000 requirements.

II. Physikalisches Institut (IIB) – Rastersondenmethoden, RWTH Aachen

M. Morgenstern

The research group develops scanning probe methods working in particular at low temperatures down to 0.3 K and in high magnetic fields up to 14 T in order to investigate the electronic structure of interacting electron systems and systems relevant for nanoelectronic applications. Thereby, we exploit the advantage of mapping the electronic structure down to the atomic scale at an energy resolution down to 0.1 meV, but also use the scanning probes for the excitement of the systems under study. Current topics of interest are graphene flakes and monolayers, quantum Hall physics in III-V-materials, confined wave functions in quantum dots, artificial spin chains, nanomagnetic systems, and phase change materials.

Chair of Electrical Engineering and Computer Sciences, RWTH Aachen

T. Noll

The research group is working on developing semiconductor-based architectural strategies for high-throughput digital signal processing, circuit concepts, and design methodologies, with a focus on energy-efficient circuits. The group wants to contribute to the development of highly-integrated, massively-parallel architectures based on nano-electronic device concepts. Emphasis is placed on the issue of reliability and fault-tolerant design.

Peter Grünberg Institut / Institute of Complex Systems – Bioelektronik, Forschungszentrum Jülich

A. Offenhäusser

Our research aims for the application of micro- and nanoelectronics to brain and life sciences. Research activities focus on two main topics: electromagnetic sensing and bioelectronic hybrid systems. This requires a better understanding of the interactions between biological systems and electronic substrates and the development of new technologies, resulting in new concepts of the interconnection of biological matter to electronic probes, and novel approaches to study cellular functions at the micro- and nanoscale. Here, we aim at a better understanding of the physiological behavior and mechanisms of neuronal information processing and new tools for diagnostics and imaging.

Institute of Crystallography, RWTH Aachen

G. Roth

The institute's research profile covers the topics synthesis, structure and properties of novel materials. The synthetic activities include the preparation of new or crystal-chemically modified compounds with interesting properties in bulk poly- or single-crystalline form. Crystal and magnetic structures are studied by powder and single crystal X-ray as well as neutron diffraction methods (outstation at FRM-II/Garching) with special emphasis on complex, defect dominated systems such as partially disordered, incommensurately modulated structures and composite crystals. Among the materials recently studied are superconductors (modulated CaAlSi), fullerenes (C70 high pressure polymer), spin-chain-compounds (vanadates and cuprates) and pyroxene-type multiferroics.

II. Physikalisches Institut (IIA), RWTH Aachen

Th. Schäpers *(interim)*

Our research activities are focused on i) semiconductor-based spinelectronics, ii) "spin-momentum transfer torque" for magnetization switching in magnetic nanostructures, and on iii) nanomagnetism of magnetic heterointerfaces. These areas are based on our dedicated expertise in i) ultrafast pump-probe experiments of the all-optical or all-electrical type for investigating the electron spin dynamics in semiconductors, ii) patterning of magnetic nanostructures and high-frequency measurements of magnetization dynamics and its excitations and iii) nanomagnetic investigations of exchange-biased ferro-/antiferromagnetic interfaces for magnetization pinning in magnetic multilayers. - While all-optical schemes are applied to III-V semiconductors, the all-electrical methods open the path toward Si- or C-based spintronic devices. Both techniques allow us to inject and detect phase-triggered coherent spin packets, subject to manipulation by electric or magnetic fields, representing a basis for future quantum information processing.

Peter Grünberg Institut – Elektronische Eigenschaften, Forschungszentrum Jülich

C. M. Schneider

The institute is engaged in the study of electronic and magnetic phenomena in novel materials and is one of the birthplaces of magnetoelectronics. Present research concentrates on the fundamental aspects, properties, and control of spin-transfer processes. The activities cover several facets, e.g., the development of new magnetic materials or the engineering of interfaces to improve the spin injection efficiency. Further important research fields comprise nanomagnetism and nanospintronics, which may form a bridge to quantum information processing. To this end new techniques and procedures are being established. Spintronics is also firmly linked to the condensed matter program, providing access to and knowledge about new material classes for use in the spintronics activities of the present program.

Institut für Anorganische Chemie (IAC), RWTH Aachen

U. Simon

Our research is devoted to the preparation, characterization and assembly of electrically functional molecules as well as ligand stabilized metal- and semiconductor nanoparticles. We focus on fundamental questions related to the size and ligand-dependent properties of the prepared nanoparticles with respect to the uptake mechanism into cells, the impact on relevant biological systems and their use in nanoelectronics. Investigations related to the assembly in one, two and three dimensions and the electrical characterization of the formed nanostructures by means of local probe measuring techniques are performed in this context. Dip-pen nanolithography and chemical e-beam lithography are applied to fabricate electrically conducting nanostructures. A further topic is the formation of anisotropic nanostructures, like nanopillars, of controlled size and shape utilizing nanosphere lithography (NSL) in combination with reactive ion etching.

II. Physikalisches Institut (IIB) – Kohlenstoff-Nanoelektronik, RWTH Aachen & Peter Grünberg Institut – Halbleiter-Nanoelektronik, Forschungszentrum Jülich

C. Stampfer

The research group focus on studying electronic and mechanical properties of carbon-based systems that have critical dimensions on the nanometer scale. Such structures approach the atomic scale and the ultimate limit of solid state miniaturization. In particular we investigate systems based on nanostructured graphene (a monoatomic sheet of graphite) and carbon nanotubes. Current interests include (i) developing advanced processing technologies for fabricating novel nanodevices, (ii) understanding new and interesting transport phenomena that arise in these devices, and (iii) learning how to control and detect the charge, spin and mechanical degrees of freedom in these systems. Potential applications include ultra-fast electronics, new spin-based nanoelectronic device concepts and applied quantum technology.

Peter Grünberg Institut – Funktionale Nanostrukturen an Oberflächen, Forschungszentrum Jülich

S. Tautz

Our research tackles fundamental issues in the quest towards functional nanostructures at surfaces, with a particular emphasis on nanoelectronics. Since our focus is placed on molecular materials, an important aspect of our work covers the structural investigations and spectroscopy of complex molecular adsorbates on metal, semiconductor and insulator surfaces. Based on these interface studies, the growth of thin films and nanostructures is investigated. Here, our work is directed towards hybrid materials, comprising both organic and inorganic components. Charge transport being the most important function in the context of nanoelectronics, transport experiments on single molecules and nanostructures round off our activities. It is a specific asset of our institute that we combine well-established surface techniques with the development of new experimental methods.

Lehr- und Forschungsgebiet GaN-Bauelementtechnologie, RWTH Aachen

A. Vescan

The research activities of the GaN Device group are focused on the area of group-III nitride device and technology development. The activities include investigation and development of practical technological building blocks for electronic devices, but also address fundamental device issues and limitations. Currently, particular interest is given to high-frequency and high-power device applications, where scaling issues as well as robustness aspects are being investigated. Novel gate dielectric materials are being pursued and their interface properties to GaN are being investigated. Also, alternative heterostructure device concepts are being developed, aimed at enhanced linearity in high-frequency devices as well improved switching behavior in the high-power regime.

Institut für Werkstoffe der Elektrotechnik 2, RWTH Aachen & Peter Grünberg Institut - Elektronische Materialien, Forschungszentrum Jülich

R. Waser

We focus on the physics and chemistry of electronic oxides and organic molecules, which are promising for potential memory, logic, and sensor functions. Our research aims at a fundamental understanding of nanoelectronic functions based on ferroelectricity, piezoelectricity, space charge effects, and electrochemical redox processes and at the elucidation of their potential for future device application. For this purpose, our institute provides a broad spectrum of facilities ranging from dedicated material synthesis, atomically controlled film deposition methods, molecular self-assembly routes, and integration technologies, to the characterization of processes, structures, and electronic properties with atomic resolution.

Integrated Photonics Laboratory, RWTH Aachen

J. Witzens

The realization of photonic components and systems in Silicon allows to realizing complex integrated optical systems at the chip scale. The integrated photonics laboratory is working on the development of Silicon Photonics devices and systems with activities ranging from core device development, system integration, as well as integration with analog circuitry.

I. Physikalisches Institut (IA), RWTH Aachen

M. Wuttig

The institute’s research activities are focused on the development of novel materials for advanced optoelectronic applications. In particular, materials for optical and electronic data storage have been developed in the last few years. For this class of materials we developed design rules and an atomistic understanding of essential material properties. This work has enabled novel functionalities of phase change materials in applications as non-volatile memories. Organic materials are a second focus, where we work on routes to tailor material properties for optoelectronic applications ranging from displays, to solar cells and electronic devices.

Selected Research Reports

Strained Silicon Nanowire Array and Si/SiGe Heterostructure Tunneling Field-Effect Transistors

S. Richter[1], M. Schmidt[1], L. Knoll[1], S. Lenk[1], J.-M. Hartmann[2], A. Schäfer[1], R. Luptak[1], K. K. Bourdelle[3], Q. T. Zhao[1], S. Mantl[1]

[1]Peter Grünberg Institute 9 (PGI 9-IT), Forschungszentrum Jülich, 52425 Jülich
[2]CEA-LETI, MINATEC, 17 rue des Martyrs, 38054 Grenoble, France
[3]SOITEC, Parc Technologique des Fontaines, 38190 Bernin, France

TFETs with strained Si nanowire channels and HfO_2/TiN gate stacks were fabricated and analyzed. Inverse subthreshold slopes down to 76 mV/dec were observed. Temperature dependence of the subthreshold slope was investigated and compared to MOSFET devices. In addition, heterostructure TFETs with SiGe source and Si channel/drain were fabricated with a stepped gate structure. These devices exhibit S = 65 mV/dec with an applied back gate voltage and decreased ambipolar behavior.

Tunneling field-effect transistors (TFETs) are promising devices to overcome the switching slope limitation of conventional MOSFETs of 60mV/dec. Devices with a steep switching slope are necessary in order to lower supply voltage in integrated circuits and thus lower the power consumption. In TFET devices excellent electrostatic control is crucial in order to increase the band-to-band tunneling current. As illustrated in the SEM image in Fig. 1 (a), the fabricated TFET devices feature an array of trigated nanowires with a HfO_2 high-κ gate dielectric in combination with a TiN metal gate, as shown in the cross-section TEM image of Fig. 1 (b). The devices were fabricated on strained silicon on insulator (SSOI) substrates using a gate first process [1]. Self aligned ion implantation was used in order to form the n-doped source and the p-doped drain region. Fig. 2 shows the transfer characteristics of a p-channel TFET with 100 nm gate length. The p-channel transfer-characteristics are measured with a negative voltage applied to the p-doped drain region and a negative voltage applied to the gate, while the n-doped region is grounded as source. The transfer characteristics exhibit point slopes down to 76 mV/dec and an average slope of 97 mV/dec over four orders of magnitude of I_D at V_{DS} = -0.3 V. The inset in Fig. 2 shows the gate leakage current I_G which is at least two orders of magnitude lower than I_D, showing that the best obtained slopes are not caused by gate leakage effects. Fig. 3 illustrates the temperature dependence of the transfer characteristics between 100 K and 350 K. The inset

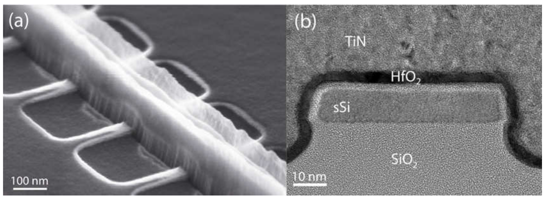

FIG. 1: (a) Scanning electron micrograph of nanowire array with a 100 nm gate length TiN metal gate. (b) Cross-sectional transmission electron micrograph of a single nanowire with HfO_2/TiN gate stack.

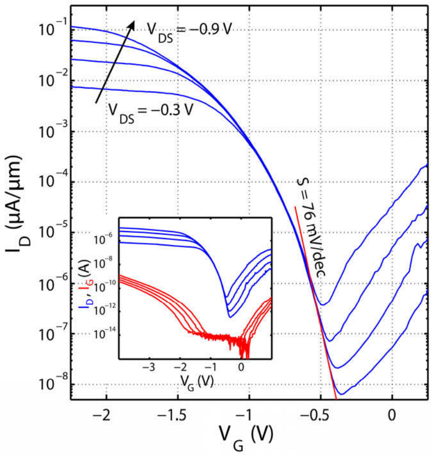

FIG. 2: Transfer characteristic of a strained Si nanowire array TFET with 100 nm gate length. The inset shows both, drain current I_D and gate leakage current I_G vs. gate voltage V_G.

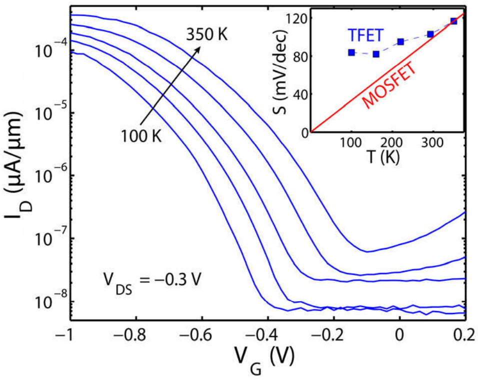

FIG. 3: Transfer characteristic of nanowire array TFET measured between 100 K and 350 K. The inset shows the measured temperature dependence of S for the TFET and the linear S(T) for a MOSFET.

depicts the inverse subthreshold slope in dependence of the temperature. In comparison with the theoretically expected linear dependence of S(T) for a MOSFET the change of S with temperature is much smaller for a TFET.

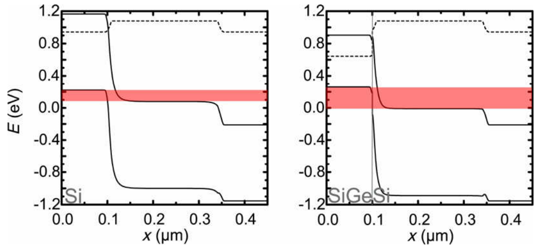

FIG. 4: Comparison of the simulated band structure of an all Si TFET (left) and $Si_{0.5}Ge_{0.5}$/Si heterostructure TFET (right). The energy regions where BTBT may occur is colored.

The band structure of TFET devices can be optimized for band-to-band tunneling (BTBT) by employing heterostructures [2].

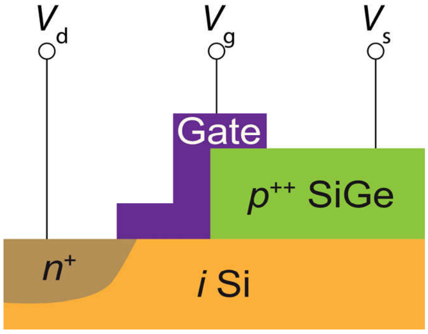

FIG. 5: Scheme of a step-like SiGe/Si heterostructure TFET.

Fig. 4 shows the simulated p-i-n band structure of an all-Si TFET (left) and a TFET with $Si_{0.5}Ge_{0.5}$ source and Si channel/drain (right) with an applied gate voltage $V_{gs} = 0.5$ V and drain voltage $V_{ds} = 0.1$ V. The energy range where band-to-band tunneling is enabled is larger for the SiGe/Si heterostructure and the tunneling distance is decreased. These simulations indicate that the BTBT current should be higher in a TFET with $Si_{1-x}Ge_x$ source, due to decreased bandgap E_g and smaller effective mass m^* of $Si_{1-x}Ge_x$, with increasing Ge concentration *x. A* schematic layout of such a heterostructure device with p-SiGe source, an intrinsic Si channel and an n-implanted Si drain is shown in Fig. 5. We fabricated TFETs on fully strained 12 nm $Si_{0.5}Ge_{0.5}$ layers, which were grown on thinned-down SOI substrates (20 nm Si/145 nm buried oxide) at 550 °C by reduced pressure chemical vapor deposition (RP-CVD). The $Si_{0.5}Ge_{0.5}$ layer was in-situ doped during growth with B which resulted in a homogeneous impurity concentration of about $N_A = 2\times10^{20}$ cm^{-3} of this layer. It was subsequently capped with 10 nm of Si to prevent large-area oxidation of the SiGe. After thinning down the Si cap mesa structures were etched, followed by the removal of SiGe on the drain side by highly selective wet etching. The structure was cleaned by subsequent H_2SO_4 and HCl, immediately followed by conformal 2.6 nm HfO_2 atomic layer deposition (ALD) and ~80 nm TiN atomic vapor deposition (AVD). The gate was patterned by standard optical lithography and reactive ion etching (RIE). The gate length amounts to 25 µm. The drain side was implanted with 3 keV As^+ ions at a dose of 1×10^{15} cm^{-2}. The activation was carried out at a low temperature of 650 °C for 1 min, to avoid B and Ge interdiffusion into the SOI layer, which would have degraded the junction significantly. After passivation of the structure by plasma-enhanced chemical vapor deposition (PE-CVD) of SiO_2, the devices were metalized with Cr/Al. For further improvement of the gate oxide quality, a forming gas anneal (FGA) was carried out at 450 °C for 10 min under N_2:H_2 atmosphere, to saturate the interfacial $Si/SiO_x/HfO_2$ dangling bonds.

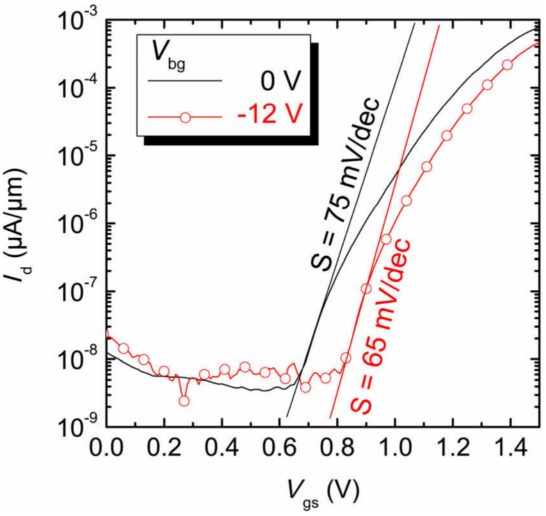

FIG. 6: Transfer characteristics of a SiGe source/Si channel/Si drain heterostructure TFET for applied Vds = 0.5 V and Vbg = -12 V.

For electrical characterization, the gate voltage was swept from $V_{gs} = 0$ to 1.5 V. The devices showed a sub-threshold point slope of $S = 75$ mV/dec, which could be improved to 65 mV/dec by applying a backgate voltage of $V_{bg} = -12$ V. From C-V measurements an EOT of ~1 nm was extracted. The key to understand the improvement of S and I_{on}/I_{off} lies in the understanding of the impact of the device parameters on these characteristics. A steeper tunneling junction, provided by the in-situ doped source, combined with a good electrostatic control, achieved by use of a high-*k* gate stack, positively impacts the device performance. However, the high resistance on the drain side limits the on-current. In future, the S/D resistance will be reduced by silicidation.

This work was financially supported by the FP7 EU STREP project STEEPER.

---

[1] S. Richter, M. Schmidt, S. Trellenkamp, R. Luptak, K. K. Bourdelle, Q. T. Zhao, S. Mantl, EDL-2012-02-0248, unpublished (2012).

[2] M. Schmidt, L. Knoll, S. Richter, A. Schäfer, J.-M. Hartmann, Q. T. Zhao, S. Mantl; Proceedings of the 13th International Conference on Ultimate Integration on Silicon 2012, p.237-240 (2012).

Ultrathin Epitaxial Ni-Silicide Contacts on SiGe: Structural and Electrical Investigations

Qing-Tai Zhao[1], Lars Knoll[1], Bo Zhang[1,2], Dan Buca[1], Jean-Michel Hartmann[3], Siegfried Mantl[1]

[1] Peter Grünberg Institut-9, Forschungszentrum Jülich, 52425 Jülich
[2] Shanghai Institute of Microsystem and Information Technology, CAS, Shanghai, China
[3] CEA-LETI, MINATEC, 17 rue des Martyrs F-38054 Grenoble, France

Epitaxial NiSiGe layers on (100) SiGe were achieved by employing an Al interlayer for the thermal reaction of Ni with SiGe. Interestingly, the Al interlayer mediates the epitaxial growth, hard to obtain otherwise. The incorporation of some Al into the NiSiGe layer increases the transition temperature from the Ni-rich germano-silicide phase to the mono-germano-silicide phase. The formed epitaxial NiSi$_{0.7}$Ge$_{0.3}$ shows an orthorhombic structure with a (101) base plane rotated by 45° with respect to the (100) Si$_{0.7}$Ge$_{0.3}$ substrate with an atomically sharp interface

As the scaling of device dimensions continues, new materials like SiGe for high hole mobility channels and thin silicides for low contact resistivity source/drain (S/D) regions are required. According to the International Technology Roadmap for Semiconductors (ITRS) for the 18nm technology node, the silicide layer thickness should not exceed 12 nm and its specific contact resistivity on highly doped S/D should be smaller than $8\times10^{-8}\,\Omega\text{cm}^2$. Reducing the contact resistance is the challenge for achieving small S/D resistance. The silicide contact resistance contributes to more than 80 % at the total S/D series resistance at 18 nm node, according to MASTAR simulations. High quality epi-NiSi$_2$ layers fulfill ITRS requirements and can easily be formed on pure Si with a Ni thickness in the range of 1 to 3 nm [1, 2]. In the ternary (Ni,Si,Ge) systems, the phase reactions and morphological transformations are more complex as compared to the binary reactions of Ni and pure Si. Island structures and Ge segregation have been observed after high-temperature treatments [3, 4]. The difference of enthalpy of formation of NiSi (-45 kJmol^{-1}) and NiGe (-32 kJmol^{-1}) hinders the formation of uniform NiSi$_{1-x}$Ge$_x$ layers [5]. Ge is incorporated in the NiSi$_{1-x}$Ge$_x$ phase when formed at lower temperatures, while at higher temperatures diffuses out driven by a minimization of the Gibbs free energy via the formation of thermodynamically more stable phases, like NiSi [6]. The epitaxial growth of ternary silicides adds the difficulty of “adjusting” different crystal structures: the orthorhombic one of NiSi$_{1-x}$Ge$_x$ with the cubic lattice of the strain relaxed Si$_{1-x}$Ge$_x$ crystal.

In this Letter, we present the formation of ultra-thin NiSiGe on SiGe. Special emphasis is placed on epitaxial NiSiGe layers. Their structural and electrical properties will be presented. Here, we show a method to grow single crystalline NiSiGe layers on SiGe(100) with 30at% Ge.

Intrinsic single crystalline strain-relaxed Si$_{0.7}$Ge$_{0.3}$ layers with a thickness of about 800 nm were used for the NiSiGe growth. Prior to the deposition of the Ni films, the samples were cleaned by a standard Si process, followed by a 30 s dip in 1% HF solution to remove the native oxide. A 3 nm thin Al layer and subsequently 11 nm Ni were deposited on Si$_{0.7}$Ge$_{0.3}$. For comparison, the Ni layer was also deposited directly on Si$_{0.7}$Ge$_{0.3}$ substrates without Al. The solid-phase reactions between Ni or Ni/Al and Si$_{0.7}$Ge$_{0.3}$ during RTP in N$_2$ ambient for 30 sec were studied at temperatures ranging from 300°C to 750°C. The unreacted Ni was selectively etched before layer characterization.

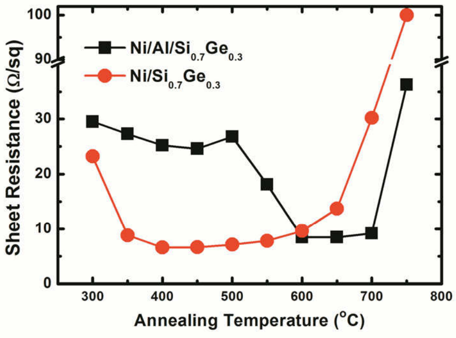

FIG. 1: Thermal stability of Ni germanosilicides formed on SiGe with pure Ni and with 3nm Al interlayer.

Fig.1 shows the sheet resistance, an indicator of the thermal stability of Ni germano-silicide layers formed on Si$_{0.7}$Ge$_{0.3}$ substrates. For the Ni/SiGe system, the layer resistance exhibits a rapid decrease at 400°C, attributed to the mono-germano-silicide (NiSi$_{0.7}$Ge$_{0.3}$) phase formation. The NiSiGe phases were determined by RBS measurements (spectra not shown in this short Letter). The layer suffers pronounced degradation when the temperature increases above 600°C. The morphology of a NiSiGe layer formed at 400°C, with agglomeration of polycrystalline $NiSi_{0.7}Ge_{0.3}$ grains is presented in Fig.2 (a).

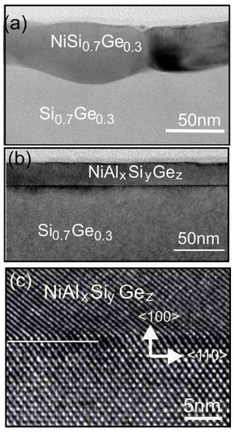

Fig.2 XTEM image of (a) NiSiGe formed at 400°C; (b) Ni(Al)SiGe formed at 700°C; (c) high-resolution TEM image of sample (b) indicating an epitaxial Ni(Al)SiGe layer with an atomically flat interface to SiGe.

For the Ni/Al/SiGe system, the sheet resistance remains at a higher value in a temperature window from 300°C to 500°C due to the formation of a Ni rich germano-silicide phase ($Ni_2Al_xSi_yGe_z$). The sheet resistance decreases abruptly to the value of the Ni/SiGe system for annealing at 600°C and remains constant up to 700°C. At this temperature a very uniform single crystalline germano-silicide layer with a thickness of 24 nm is formed (Fig.2 (b)). The high resolution TEM image in Fig.2 (c) proves an atomically flat crystalline $Ni_2Al_xSi_yGe_z$/ $Si_{0.7}Ge_{0.3}$ interface. RBS data demonstrated that the layer composition corresponds to $NiSi_{0.7}Ge_{0.3}$, indicating fully Ge incorporation into the ternary silicide. Considering the sheet resistance and the thickness of the Ni germanosilicide layer, a specific resistivity of ~22 μΩ-cm was obtained, which is similar to the resistivity of polycrystalline Ni-germano-silicide.

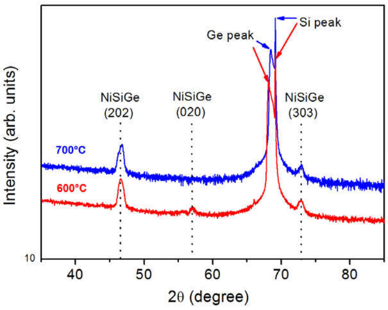

Fig.3 XRD results for NiSiGe layers formed with Ni/Al at 600°C and 700°C. The NiSiGe layer has a (101) based plane.

The XRD results for Ni(Al)SiGe layers formed at 600°C and 700°C, respectively, are shown in Fig.4. For the 600°C anneal the XRD spectrum shows, in addition to the peaks corresponding to the SiGe substrate, two sharp peaks at 46.6° and 72.9°, and one low intensity peak at 57.1°. The peaks at 46.6° and 72.9° correspond to NiSiGe (202) and (303) planes, respectively, while the low intensity peak at 57.1° is attributed to the NiSiGe (020) reflection. This indicates the existence of a low density of {100} oriented grains. For the Ni germano-silicide layer formed at 700°C the small peak at 57.1° vanishes and only the sharp (202) and (303) peaks are visible. This confirms a highly oriented single-crystalline germano-silicide film as shown in the TEM images of Fig.2. The combined information from TEM and XRD affirms that the germano-silicide layer has a predominant (101) base plane. The measurements of the chemical composition of the Ni(Al)SiGe systems using energy dispersive X-ray spectroscopy (EDX) implemented in scan-TEM (STEM) indicate that Al diffused through the Ni layer to the surface, while Ni diffused simultaneously through the Al and germano-silicide towards the SiGe substrate (Fig.4). Only a very small amount of Al atoms is distributed uniformly in the germano-silicide layer. The uniform Ni and Ge atom distributionsalso confirms, that only one phase was formed. It is very difficult to grow NiSiGe layers epitaxially on SiGe substrates using only a Ni layer. Obviously, the Al interlayer plays a decisive role for the epitaxial growth. We assume that the Al interlayer causes the following effects during germanosilicidation: (i) reduction of the Ni diffusion, (ii) altering the reactions of Ni with SiGe and (iii) changing the lattice structure and the thermal expansion of NiSiGe [7]. All these effects change the dynamic reactions of Ni with SiGe, leading to the reordering of the atoms to a single crystalline NiSiGe structure by lowering the Gibbs free energy. However, the mechanism of the epitaxial growth of NiSiGe with an Al interlayer is still not completely understood. Further investigations are needed to further analyze the lattice alignment of NiSiGe to SiGe layers with various Ge contents and the impact of lattice strain.

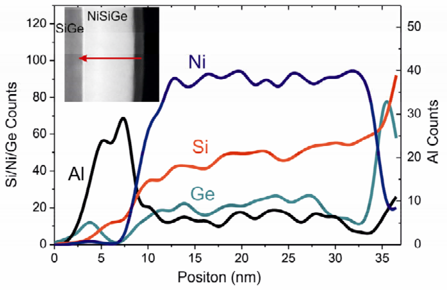

Fig.4 EDX profiles measured with STM for Ni(Al)Si0.7Ge0.3 formed with Ni/Al at 700°C

---

[1] R.T. Tung, J. M. Gibson, J. M. Poate, Phys. Rev. Lett. Vol.50, pp.429, 1983

[2] L. Knoll, Q. T. Zhao, S. Habicht, C. Urban, S. Mantl, IEEE Electron. Dev. Lett., Vol. 2010

[3] J. Segera, S. L. Zhang, D. Mangelinck, and H. H. Radamson, Appl. Phys. Lett. 81, 1978 (2002).

[4] Q. T. Zhao, D. Buca, S. Lenk, R. Loo, M. Caymax, and S. Mantl, Microelectron. Eng. 76, 285 (2004).

[5] J. Li, Q. Z. Hong, J. W. Mayer, and L. Rathbun, J. Appl. Phys. 67, 2506 (1990).

[6] F. R. Deboer, R. Boon, W. C. Mattens, A. R. Miedema, and A. K. Niessen, in Cohesion in Metals: Transition Metal Alloys, North-Holland, Amsterdam 1988.

[7] A. Schubert, Dipl. thesis, Tech. Univ. Chemnitz, 2005.

Epitaxy and Structural Characterization of 270 nm thick Quaternary AlInGaN films grown on GaN by MOVPE

B. Reuters[1], B. Holländer[2], A. Wille[1], M. Heuken[1,3], H. Kalisch[1], A. Vescan[1]

[1]RWTH Aachen University, GaN Device Technology, Sommerfeldstrasse 24, 52074 Aachen
[2]Peter Grünberg Institut-9 (PGI9-IT), Forschungszentrum Jülich, 52425 Jülich
[3]Aixtron SE, Kaiserstr. 98, 52134 Herzogenrath

Quaternary AlInGaN recently broke into the focus of GaN-based electronic device research as an alternative to ternary AlGaN and AlInN barrier layers. In contrast to ternary compounds, the quaternary approach establish a further degree of freedom in device design. In detail, it is possible to separately adjust several parameter, such as the bandgap and the lattice constant [1, 2]. This offers a wide application range, i.e. lattice-matched or bandgap-matched growth with varying internal total polarization in the AlInGaN layer [3, 4]. By reducing the polarization difference of AlInGaN and the underlying GaN buffer layer, enhancement-mode HFET operation can be realized with competitive performance to depletion-mode HFET [5, 6].

The heterosctructure was deposited on a 2-inch c-plane sapphire substrate in an AIXTRON metal organic vapour phase epitaxy (MOVPE) reactor with standard precursors trimethylaluminum (TMAl), trimethylindium (TMIn) and trimethylgallium (TMGa). Here we investigate a thick (270 nm) AlInGaN film in a layer stack, shown in Figure 1. AlInGaN was grown on a buffer structure consisting of a 0.3 µm thick AlN layer and a 2.0 µm thick GaN layer. Before buffer growth, AlN nucleation with a thickness of about 7 nm is applied, due to its insulating characteristics and due to enhanced reproducibility in our process. All layers can be grown under H_2, except AlInGaN, because In is etched by H_2. Hence we use N_2 for AlInGaN growth. For precursor supply of nitrogen, we use NH_3.

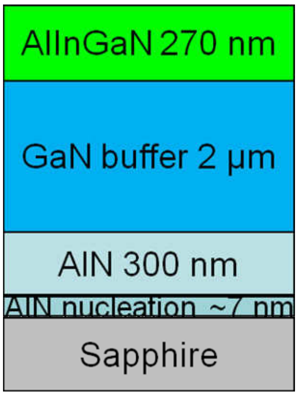

FIG. 1: Epitaxial-grown layer stack of the investigated sample.

Compositional characterization of ternary layers can be performed by the measurement of the lattice constant by high-resolution x-ray diffraction (HRXRD). For AlInGaN, several compositions exhibit equal lattice constants, thus an additional measurement has to be performed to determine the composition accurately. Here, Rutherford backscattering spectrometry (RBS) is an excellent method to acquire a depth-resolved composition profile of AlInGaN. This helps not only to determine an accurate average composition, but also reveals any changing composition with thickness. With that, a detailed analysis of the growth process and compositional pulling can be investigated.

Figure 2 shows the RBS spectrum using 1.4 MeV He+ ions at a scattering angle of 170 degrees (blue cyrcles) and the channeling spectrum (green squares), which was measured after alignment of the [0001] sample normal with respect to the incoming ion beam. Details about the experimental setup can be found in [7]. The RBS spectrum was fitted (red line) with a multi-layer AlInGaN structure illustrated in the inset of Figure 2. The 270 nm thick layer was separated in 5 layers, each 54 nm thick, with increasing In content from 6% near the AlInGaN/GaN interface to 9% at the surface (decreasing Ga content from 37% to 34%). The Al content is assumed to be constant at 57%, as AlN exhibits the strongest bond in nitride films.

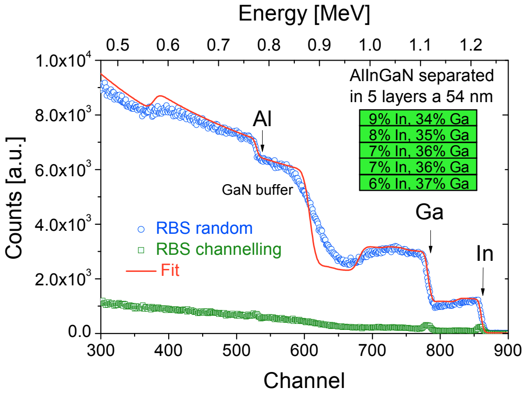

FIG. 2: RBS spectra of a 270 nm thick AlInGaN layer. The blue cyrcles represent the random measurement, the green squares represent the channeling signal and the red curve is a simulation with a multi-layer stack, consisting of 5 layers, each 54 nm thick with changing In and Ga contents. The inset illustrates the multi-layered AlInGaN.

The low channeling minimum yield value of about 5% indicates the good crystalline quality of the AlInGaN layers.

The 2Θ-ω (0002) HRXRD scan for this sample is shown in Figure 3. One can observe the GaN peak with the highest intensity located at the smallest angle of 34.55°, the AlN peak located at a higher angle of about 36.07° and several quaternary peaks between these two buffer layer peaks. The position of peaks is reciprocally proportional to the lattice constant c and reveals that AlInGaN lattice constant c is located between GaN and AlN. It cannot be concluded from this symmetrical scan that lattice constant a, which is the in-plane lattice constant, lies also between those of GaN and AlN, but from reciprocal lattice mapping analysis, we determined the AlInGaN layer to be tensile strained on the GaN buffer. This means that the lattice constant a is smaller than the GaN lattice constant (but larger than that of AlN).

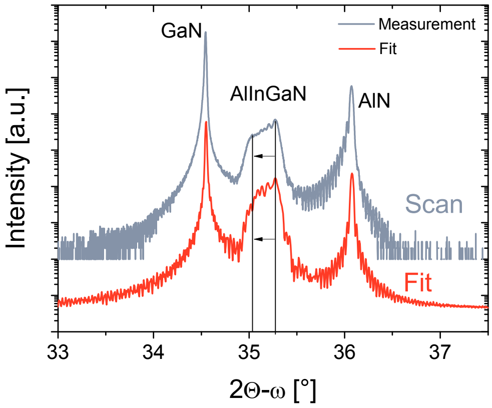

FIG. 3: HRXRD 2θ–ω scan and the fit of the measurement with an increasing In content from interface to surface.

The AlInGaN layer shows several peaks, which overlap. A simulation taking the multi-layer model into account with increasing In content from the AlInGaN/GaN interface to the surface, as determined by RBS, is very consistent with the HRXRD scan (Figure 3, lower red curve). The highest intensity is shown by the near-interface region with a low In content of 6%. With thicker growth, the In content increases to 9%, which shifts the AlInGaN peak to smaller angles due to the increase of the nominal lattice constant c and a smaller elastic deformation (c-direction) due to lowered in-plane strain. The latter mentioned effect arises due to the decreased lattice mismatch of AlInGaN and GaN, because the a lattice constant becomes more similar to the one of GaN and hence the in-plane tensile strain decreases.

In Figure 4, the calculated bandgap is plotted over the lattice constant a. The red dots indicate the composition of the investigated AlInGaN layer. One can observe that the near-interface region is located at the left of the lattice-matched line to GaN, which corresponds to tensile strain. The material at the surface approaches the lattice-matched line, by incorporating more In, which increases the lattice constant a. This shows that AlInGaN reduces tensile stress by changing its composition during growth. The incorporation of In is hence controlled by stress in this layer.

We have discussed structural properties of a 270 nm thick AlInGaN layer with changing compostion. RBS and HRXRD results are very consistent and represent a strong depth-resolved characterization method, if the results are combined. Especially for quaternary AlInGaN layers, it is necessary to perform an additional direct measurement of the composition beside HRXRD to fully describe structural properties.

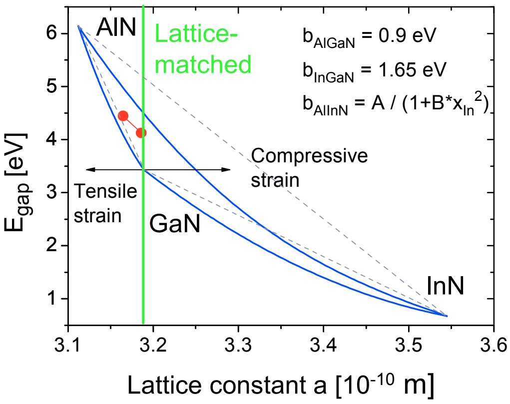

FIG. 4: Bandgap E_{gap} vs. lattice constant a diagram for group III nitrides. The blue curves illustrate the bandgap bowing of ternary alloys. Escpecially for AlInN, the bowing parameter $b_{AlInGaN}$ might be In-dependent. The green line indicates the lattice-matched growth, the black arrows the same bandgap as GaN, which is typically used as buffer layer. A smaller (larger) lattice constant induces in-plane tensile (compressive) strain. The red dots indicate the determined composition at the bottom and the surface of AlInGaN.

The results show that to control stress is a very important issue in an AlInGaN film. Compositional pulling is likely to be suppressed by adjusting the composition near the lattice-matched region.

This work was supported by Deutsche Forschungsgesellschaft (DFG) and JARA-FIT.

---

[1] Y. Liu, “Growth and characterization of high-quality quaternary AlInGaN epilayers on sapphire”, J. Cryst. Growth 259, 245 (2003).

[2] Y. Kobayashi, “Structural and Optical Properties of AlGaInN/GaN Grown by MOVPE”, Jpn. J. Appl. Phys. 42, 2300 (2003).

[3] N. Ketteniss, “Study on quaternary AlInGaN/GaN HFETs grown on sapphire substrates”, Semicond. Sci. Technol. 25, 075013 (2010).

[4] O. Ambacher, “Pyroelectric properties of Al(In)GaN/GaN hetero- and quantum well structures”, J. Phys.: Condens. Matter 14, 3399 (2002).

[5] N. Ketteniss, “Polarization-reduced quaternary InAlGaN/GaN HFET and MISHFET devices”, Semicond. Sci. Technol. 27 (2012) 055012.

[6] H. Hahn, “First polarisation-engineered compressively strained AlInGaN barrier enhancement-mode MISHFET”, Semicond. Sci. Technol. 27 (2012) 055004.

[7] B. Holländer, Nucl. Instrum. Methods Phys. Res., Sect. B 161-163 (2000) 227-230

Advances towards future III-nitride based THz OEICs in the UV range

M. Mikulics[1], H. Hardtdegen[1], A. Winden[1], R. Adam[1], D. Gregušová[2], P. Kordoš[2], M. Marso[3], R. Sobolewski[4], H. Lüth[1], D. Grützmacher[1]

[1] Peter Grünberg Institute 9, Forschungszentrum Jülich, 52425 Jülich
[2] Slovak Academy of Science, 84101 Bratislava, Slovakia
[3] Université du Luxembourg, 1359 Luxembourg
[4] University of Rochester, Rochester NY14627-0231, USA

A group III-nitride based MSM photodetector integrated with a MESFET in an OEIC circuit is presented exhibiting an exceptionally high 3 dB-bandwidth of 410 GHz. Advances towards circuit improvement by the future implementation of a gate recessed AlGaN/GaN HEMT device are reported. μ-PL is used directly on the processed device to optimize processing with respect to processing related strain and damage effects. It is demonstrated that μ-PL allows insight into device and material optimization which are the strategic key to improved future III-nitride based UV-optoelectronic integrated circuits (OEIC) operated up to the THz range.

THz sources are of utmost importance for spectroscopy since they can be employed for material production control, the detection of safety relevant chemicals as well as in the analysis of food and the environment. In the past it has been demonstrated that semiconductor materials and especially group III group V alloys are very well suited for the generation of THz radiation especially due to their tunability in the low THz range. The sources can be integrated into sophisticated circuits which allow the amplification of the signals. Further improvements with respect to the signal to noise ratio would increase the efficiency of the sources and are in the focus of this report. The starting point for our investigations were our recent achievements in the field of UV-sensitive and visible-light-blind metal-semiconductor-metal photodetectors (MSM PDs) and their integration with MESFET structures [1].

Figure 1 presents both devices which form an optoelectronic integrated circuit (OEIC). The PD is excited by a train of 100-fs-wide and 360-nm-wavelength laser pulses. Its photoresponse transient is amplified by the MESFET device. The frequency response of our MSM PD yields a 3 dB-bandwidth of 410 GHz that is the highest bandwidth ever reported for a GaN-based PD (Figure 1). It should be also noted that the MSM signal amplified by the MESFET exhibits a higher amplitude than the actual input MSM PD signal of up to 150 GHz. These results show that our device is a very promising candidate for future THz operated UV optoelectronic integrated circuits.

Further improvements of the amplifier performance could be obtained by substituting the GaN MESFET layer by an optimized AlGaN/GaN or InAlN/GaN [2] high electron mobility transistor (HEMT), which is known reduce the noise and is also faster leading to a decrease of the amplified signal`s FWHM. The usability of the circuit in this material system at high powers and its thermal and radiative robustness makes it attractive for future satellite and wireless communication at high data transfer rates. To this end the performance of the AlGaN/GaN HEMT calls for improvement with respect to the threshold voltage towards a normally off device

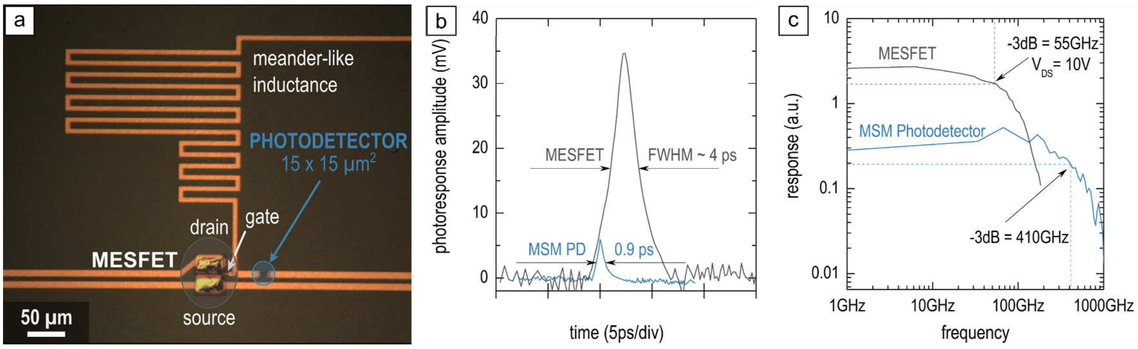

FIG. 1: (a) OEIC circuit containing an MSM PD integrated with MESFET in a CPS line layout fabricated on GaN/AlN/SiC The meander structure that biases the gate acts as an inductor to block the high-frequency signal from the PD. (b) Time-resolved photoresponse transients of just the MSM PD and the amplified signal at the drain side of the MESFET. (c) Optoelectronic frequency response of the MSM PD (bottom trace) and of our entire OEIC (top trace). (Fast Fourier transform of the time domain measurements of (b)).

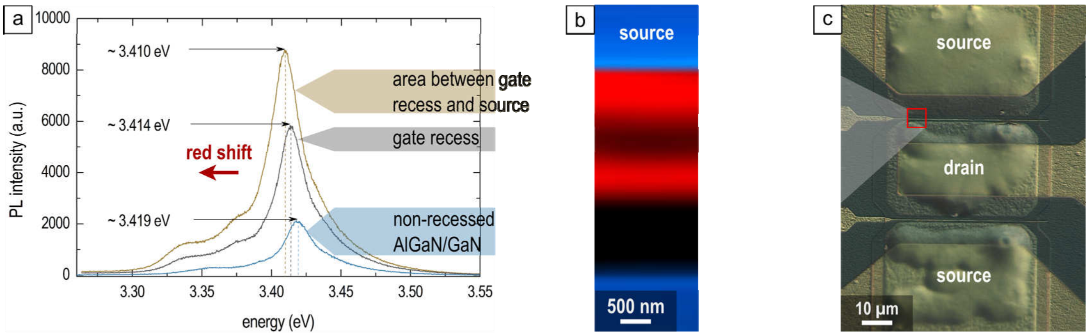

FIG. 2: (a) Photoluminescence spectra of three regions of a 6 nm recessed AlGaN/GaN heterostructure. (b) PL intensity mapping across the recessed gate at an emission wavelength of 363 nm. (c) Micrograph of a transistor. It becomes clear that strain and defects are non-uniformly distributed.

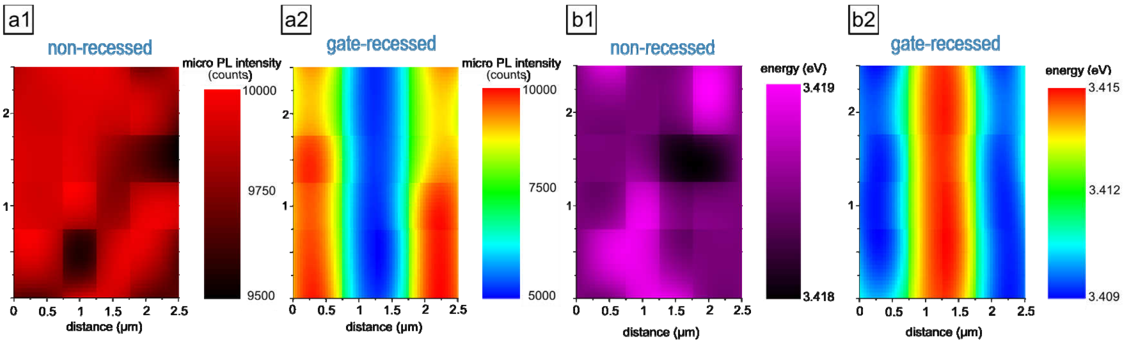

FIG. 3: Mapping of (a) micro PL intensity and (b) band edge PL energy for (1) a non-recessed and (2) its 6nm gate-recessed HFET counterpart.

and to the aspect ratio for improved DC and high frequency performance. Gate recessing was developed to address both topics [3] necessitating the employment of dry etching technology. This technology calls for careful etching parameter optimization to minimize surface roughening / damage and to reduce detrimental in-depth defects due to channelling. Additionally, the influence of recessing on strain in the device needs to be carefully monitored since strain distribution/relaxation will eventually affect the channel properties and therefore the device characteristics. Micro photoluminescence (µ-PL) studies are particularly suited as a powerful and non-destructive technique for the study of induced strain and damage after gate recess etching. The high lateral resolution of µ-PL studies allowed the observation of a non-uniform band edge luminescence energy – related to strain – and of the PL-intensity – related to differences in non-radiative recombination centers (defects) – in the device region [4].

The AlGaN/GaN layer system deposited on 6H-SiC substrates was comparatively investigated for a recessed and a non-recessed device. Typical micro PL spectra of the non-recessed and ~ 6 nm recessed HFET structures are shown in Figure 2. The peak emission energy for non-recessed structures is recorded at a wavelength of ~ 362.7 nm (3.419 eV) which is in good agreement with the energy reported recently for GaN on 6H-SiC substrates [5]. A closer look at the spectra recorded of the recessed device reveals (see the inset of Fig. 2) a slight red-shift of the band edge emission (3.414 eV). It is well known that GaN layers are not fully relaxed and exhibit residual strain. The strain depends on many device process factors and especially on the layer thickness.

The energy shift ΔE = 5 meV observed after 6 nm recessing corresponds to a slight decrease of the in-plane stress from about −0.9GPa to −0.68 GPa [5]. This indicates that the thickness change of the AlGaN barrier layer leads to a partial strain relaxation in the underlying GaN buffer layer. Due to the reduction of strain, the polarization charge should be lower in recessed structures compared to non-recessed ones. Additionally, the lateral intensity distribution of the luminescence over the device structure for the recessed device is not uniform as presented in detail also in Figure 3.

All these factors need to be taken into account to further fine tune the device performance. In Future these optimized HEMTs will be integrated into the optoelectronic integrated circuit (OEIC) reported above allowing a high power operation at harsh environment conditions in the THz range.

---

[1] M. Mikulics et al., IEEE Photonics Technology Lett., vol. 23, no. 17, 1189 (2011).

[2] M. Mikulics et al., Appl. Phys. Lett. 97, 173505 (2010).

[3] Y. Pei et al., IEEE Electron Device Lett. 29, 300 (2008).

[4] M. Mikulics et al., Phys. Status Solidi C 9, no. 3–4, 911 (2012).

[5] D. G. Zhao et al., Appl. Phys. Lett. 83, 677 (2003)

Molecular-Beam Epitaxy of Topological Insulator Bi_2Te_3 Thin Films

G. Mussler[1], J. Kampmeier[1], J. Krumrain[1], S. Borisova[1], L. Plucinski[2], M. Luysberg[3], D. Grützmacher[1]

[1]Peter Grünberg Institut-9, Forschungszentrum Jülich, 52425 Jülich
[2]Peter Grünberg Institut-6, Forschungszentrum Jülich, 52425 Jülich
[3]Peter Grünberg Institut-5, Forschungszentrum Jülich, 52425 Jülich

We report on molecular-beam epitaxy (MBE) of Bi2Te3 thin films on Si(111) substrates. At carefully optimized MBE growth parameters, atomically smooth, single-crystal Bi_2Te_3 films with large areas of single quintuple layers (QLs) on top are obtained. Angular-resolved photoelectron spectroscopy reveals a linear energy dispersion of charge carriers at the surface, evidencing topologically insulating properties of the Bi_2Te_3 epilayers. Further analyses show that in the very beginning of the growth, two different domains, in-plane rotated by 60°, are formed. After the growth of a few QLs an overlapping occurs, causing one domain to prevail.

Recently a new state of matter called the topological insulator (TI) has been theoretically predicted and experimentally observed in a number of materials, such as $Bi_{1-x}Sb_x$, Bi_2Se_3, Sb_2Te_3, and Bi_2Te_3. The main feature of TIs lies in its band structure, which is depicted in figure 1a. The bulk of TIs is an insulator with conduction and valence band, separated by a band gap. The surface, however, hosts gapless states with a linear energy dispersion, in a similar way as graphene. Hence, carriers at the surface of TIs are expected to have unparalleled properties, such as extremely high mobilities and a spin-locked transport behavior. Consequently, these features may lead to new applications in the field of spintronics, or quantum computing [1].

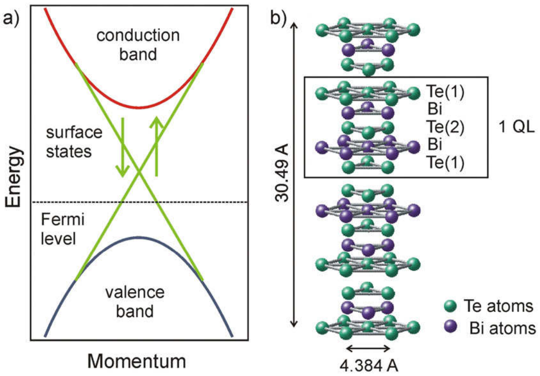

FIG. 1: a) The TI energy dispersions of bulk and surface states. b) The unit cell of Bi_2Te_3.

The TI behavior in Bi_2Te_3 is based on the crystalline structure (Fig. 1b), which includes a sequence of five atomic layers Te(1)-Bi-Te(2)-Bi-Te(1), so called quintuple layer (QL). A unit cell consists of three QLs, and there are only weak van der Waals bonds between the QLs.

Concerning the MBE growth of Bi_2Te_3, very important parameters are the Bi and Te effusion cell temperatures. We have found that a Te overpressure condition is mandatory for the growth of single-crystal Bi_2Te_3 epilayers. In order to investigate the influence of the Bi and Te effusion cell temperatures on the growth rates, x-ray reflectivity (XRR) scans were performed. Figure 2a shows XRR curves of three Bi_2Te_3 layers, grown with different Te effusion cell temperatures. Same layer thickness of 31 nm is obtained for all three samples, evidencing that for Te overpressure and the used substrate temperature of 400°C, the growth rate of Bi_2Te_3 does not depend on the Te partial pressure. In contrast, fig 2b shows XRR curves of three Bi_2Te_3 epilayers grown with different Bi effusion cell temperatures. We can see that there is an increase in thickness from 15 to 55 nm for higher Bi fluxes. Hence, the growth rate is solely determined by the Bi flux. The Te overpressure condition has a consequence on the growth of Bi_2Te_3, whereas the surface is always Te-terminated, in a similar fashion as the MBE growth of GaAs [2].

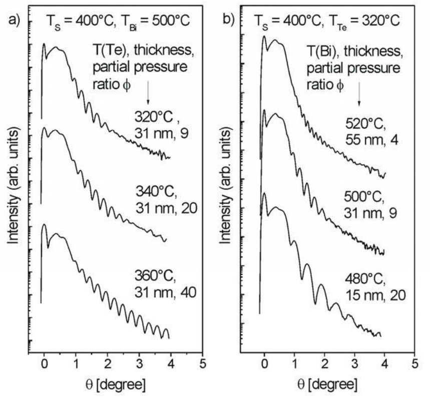

FIG. 2:XRR curves for series of Bi_2Te_3 samples grown with different Te (a) and Bi (b) effusion cell temperatures.

In order to prove the stoichiometry of the grown Bi_2Te_3 films, scanning tunneling electron microscopy (STEM) measurements were carried out. Figure 3a shows a cross-sectional image of the epilayer. The bright and dark spots show the Bi and Te atoms, respectively. The image reveals the correct order sequence of the QL (cf. figure 1b). Moreover, the data reveal that the Bi_2Te_3 epilayer is of single-crystal nature and the out-of-plane direction is the c-axis, which was also confirmed by x-ray diffraction. Figure 3b shows a color-coded atomic force microscopy (AFM) image of the Bi_2Te_3 surface, showing three different atomically smooth plateaus, whereas one QL covers more than 75% of the surface. Figure 3c illustrates the step height analysis along the dashed line in figure 3b. The step heights are always an integer of 1 nm, which represents the height of 1 QL, evidencing the QL by QL growth mode. Figure 2d shows an ARPES scan. The Dirac cone is clearly seen, proving the linear energy dispersion at the surface of the Bi_2Te_3 layer. From the slope, a Fermi velocity $v_F = 4.28 \cdot 10^5$ m/s is determined [3], which is in agreement with theoretical calculations. Besides, the hexagonal-shaped rim is seen, which is typical of Bi_2Te_3 due to an interaction of the surface states with the bulk bands in reciprocal space.

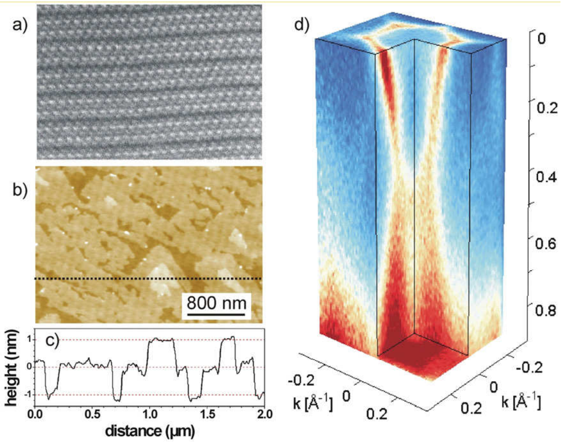

FIG. 3: a) Cross-sectional STEM image of the Bi_2Te_3 layer. The bright and dark spots are Bi and Te atoms, respectively. b) AFM image of the Bi_2Te_3 surface. c): Height profile along the dashed line in b). d) ARPES scan showing the Dirac cone.

The choice of substrate is of high importance for realizing single-crystal Bi_2Te_3 epilayers. We have used Si(111) substrates because of their hexagonal arrangement of the surface atoms, which match the hexagonal crystal structure of Bi_2Te_3. It was found that the large lattice mismatch (~14%) is not crucial for the growth of the Bi_2Te_3 epilayers, as the epilayers are only weakly bonded to the substrates via van der Waals forces. However, the substrate determines the in-plane crystal orientation of the Bi_2Te_3 epilayers. Figure 4a shows a pole figure measurement around the (105) reflection of the Bi_2Te_3 epilayer and around the (311) and (221) reflections of the Si substrate. Evidently, the peaks of the Bi_2Te_3 epilayer have same angular orientation of the Si substrate peaks, indicating the same in-plane orientation of substrate and epilayer. Despite the three-fold symmetry of this reflection, six peaks of the (105) reflection are seen. This can be explained by the formation of domains, in-plane rotated by 60°, in the early stage of growth. In fact, the Bi_2Te_3 crystal may nucleate on the Si(111) substrate in two different orientations, as depicted in figure 4b. Here crystal 1 and 2 cannot be transformed into each other by a translation, but a 60° rotation is necessary. Consequently, when these crystalline domains coalesce, grain boundary defects are formed. An example of such domain boundary is given in the STEM image of Fig. 4c, where a Fourier-filtered image shows the contributions of two reflections belonging to two different domains. Domain II (green), which extends over about 60 nm, is encapsulated by domain I (red). It has to be noticed that the presence of two domains is found by STEM only within the first 5-6 monolayers. At a later stage, when the growth mode is QL by QL, only one domain dominates. Fig. 4d displays the domain wall at right side of domain II in a higher resolution image. The vertical wall reveals small facets.

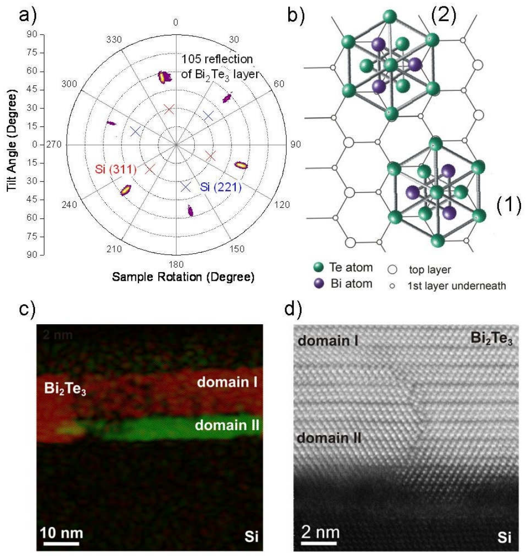

FIG. 4: a) Pole figure scans of the Bi_2Te_3 epilayer and the Si substrate. b) Sketch of the two different Bi_2Te_3 crystals that can nucleate on the Si(111) surface. c) Fourier-filtered STEM image shows the contributions of two reflections, which belong to two different domains. d) Magnification of the domain boundary.

Future works will be devoted on transport measurements. Preliminary results show a large contribution of the bulk electrons, hiding the surface electronic transport. The possible origin of the high bulk electron concentration might be attributed to the observed domain boundary defects. Hence special emphasis will be put on reducing the amount of bulk electrons, for example by doping the TI epilayers. The goal is to minimize the impact of bulk carriers, and obtain a dominant transport of the surface carriers with the expected high mobilities and spin-resolved transport features. We can however conclude that the MBE-grown TI materials of high crystalline quality may be harnessed for device applications, as well as for very interesting fundamental researches.

[1] J. E. Moore, Nature 464, 194 (2010).

[2] J. Krumrain, G. Mussler, S. Borisova, T. Stoica, L. Plucinski, C. M. Schneider, D. Grützmacher, J. Crystal Growth 324, 115 (2011).

[3] L. Plucinski, G. Mussler, J. Krumrain, A. Herdt, S. Suga, D. Grützmacher, C.M. Schneider, Appl. Phys. Lett. 98, 222503 (2011).

Probing two topological surface bands of Sb_2Te_3 by spin-polarized photoemission spectroscopy

C. Pauly[1], G. Bihlmayer[2], M. Liebmann[1], M. Grob[1], A. Georgi[1], D. Subramaniam[1], M. Scholz[3], J. Sanchez-Barriga[3], A. Varykhalov[3], S. Blügel[2], O. Rader[3], M. Morgenstern[1]

[1]II. Physikalisches Institut B, RWTH Aachen University
[2]Peter Grünberg Institut (PGI-1) and Institute for Advanced Simulation (IAS-1), Forschungszentrum Jülich
[3]Helmholtz-Zentrum Berlin für Materialien und Energie, Elektronenspeicherring BESSY II

Using high resolution spin- and angle-resolved photoemission spectroscopy, we map the electronic structure and spin texture of the surface states of the topological insulator Sb_2Te_3. In combination with density functional calculations, we directly show that Sb_2Te_3 exhibits Z_2 topological properties with a partially occupied, single spin-Dirac cone around the Fermi energy, E_F. Furthermore, we observe a strongly spin-orbit split surface band at lower energy. This state starts at the Γ-point with $E\text{-}E_F \approx -0.8$ eV, disperses upwards, and disappears at about $E\text{-}E_F = -0.4$ eV into two different bulk bands. Along the Γ-K direction, the band is located within a spin-orbit gap. According to an argument given by Pendry and Gurman, such a surface state must be present within each spin-orbit gap located away from the high symmetry points of the Brillouin zone. Thus, similar to the topological Dirac cone, this novel state is protected by symmetry.

Topological insulators (TIs) are a new phase of quantum matter giving rise to, e.g., a quantum spin Hall phase without external magnetic field. Large spin orbit (SO) interaction and inversion symmetry lead to nontrivial edge or surface states which reside in a bulk energy gap and are protected by time reversal symmetry. In three dimensions, the surface states form an odd number of massless Dirac cones exhibiting a chiral relationship between spin and momentum of the electrons. Calculations showed that the thermoelectric materials Bi_2Se_3, Bi_2Te_3 and Sb_2Te_3 exhibit these topological properties with a very simple electronic structure, namely with only one Dirac cone around Γ [1]. While the TI nature of Bi_2Se_3 and Bi_2Te_3 is well established [2], the phase change material Sb_2Te_3 [3] was rarely probed. The spin chirality and, thereby, the topological nature of the Dirac cone has not been tackled so far.

Spin- and angle-resolved photoemission experiments (spinARPES) have been performed at 300K with electron analyzers Scienta R8000 and SPECS PHOIBOS 150 using linearly polarized synchrotron radiation at BESSY II. Spin resolution is acquired with a Rice University Mott polarimeter operated at 26 kV and capable of recording the two orthogonal spin directions in the surface plane of the sample. The ARPES data has been recorded on a Sb_2Te_3 single crystal, which was cleaved in ultra-high vacuum (base pressure of $1{\cdot}10^{-10}$ mbar) prior the measurement.

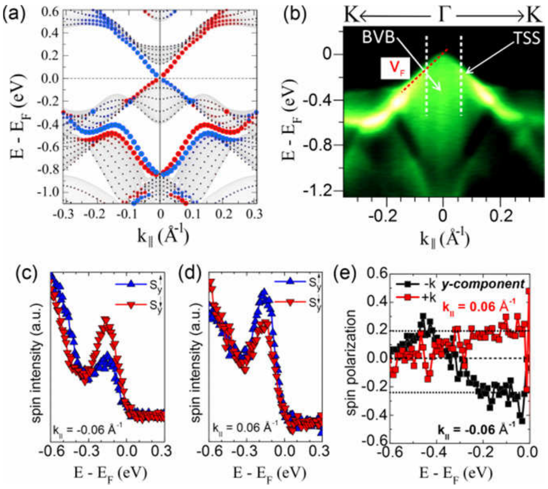

FIG. 1: (a) Band structure in Γ-K direction as calculated by DFT including SO coupling; states resulting from a film calculation are shown as circles with the color (blue or red) indicating different spin directions and the size of colored circles marking the magnitude of the spin density; shaded areas are projected bulk bands originating from a bulk calculation. (b) ARPES measurement of the lower Dirac cone along Γ-K with topological surface state (TSS) and bulk valence band (BVB) marked; hν = 55 eV; red, dashed line is a guide to the eye from which the Fermi velocity vF is deduced. (c), (d) EDCs for the spin component perpendicular to $k_\parallel$ recorded at $k_\parallel$ -values as indicated and marked by dashed lines in (b); different colors mark different spin directions; hν = 54.5 eV. (e) Resulting spin polarization as a function of energy for the two different $k_\parallel$ as indicated.

Fig. 1(a) shows the band structure from DFT calculations of a six QL film including SO interaction. The spin-polarized states are displayed as colored circles being blue or red for the different spin orientations with respect to a direction perpendicular to $k_\parallel$ and the surface normal. A single Dirac cone around Γ with Dirac point at E_F and overlap of the occupied states with bulk states (shaded area) is visible. Another bulk band gap exists around $E\text{-}E_F = -400$ meV. It houses two spin-polarized states exhibiting a Rashba-type spin splitting $\Delta E = \alpha \cdot |k_\parallel|$ with the wave number parallel to the surface $k_{\|}$ and the Rashba coefficient $\alpha \approx 1.4$ eVÅ, at least, up to $k_{\|} \approx 0.05$ Å^{-1}. The measured bandstructure presented in Fig. 1(b) shows the energy dispersion of Sb_2Te_3 around Γ in more detail. Indeed, we identify a band exhibiting a linear dispersion and which crosses at the Fermi level. The linear dispersion is fitted by $E\text{-}E_F = \hbar v_F |k_{\|}|$ resulting in Fermi velocity $v_F = (3.8 \pm 0.2)\cdot 10^5$ m/s, which agrees reasonably with $v_F = 3.2\cdot 10^5$ m/s obtained by DFT. In order to verify the chiral spin polarization of the Dirac cone, we use spinARPES sensitive to the spin components within the surface plane. Fig. 1(c), (d) show the spin-resolved energy distribution curves (EDCs) as measured at $k_{\|} = -0.06$ Å^{-1} and $k_{\|} = 0.06$ Å^{-1} as marked for the spin component perpendicular to $k_{\|}$ and the surface normal. This spin component exhibits an intensity difference between spin up and spin down component which reverses for the two opposite wave numbers. In contrast, the spin component parallel to $k_{\|}$ shows no spin polarization (not shown here). The spin thus points perpendicular to $k_{\|}$ and rotates counterclockwise for the lower part of the Dirac cone in agreement with DFT. The resulting spin polarization [Fig. 1(e)] deduced from the EDCs has a value of $P_y \approx 20\%$ with opposite sign for the surface states of opposite momenta, thus proving evidence for the spin-polarized nature of the topological surface states.

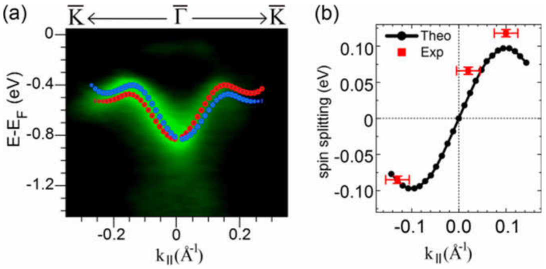

FIG. 2: (a) ARPES dispersion of the Rashba type surface state along Γ-K direction (green color scale); hν = 22 eV; band structure from DFT is superposed as blue and red dots.(b) Calculated spin splitting of the Rashba state in comparison with measured spin splitting.

Beside the topological surface state, we demonstrate that Sb_2Te_3 exhibits an additional spin split surface state originating from SO interactions. Fig. 2(a) shows ARPES data along Γ-K, superimposed by the DFT band structure of the Rashba-type band. Based on the excellent concurrence, we conclude that the ARPES data reveal these bands. We determine their spin splitting at several $k_{\|}$-values using spinresolved EDCs for the spin direction perpendicular to $k_{\|}$. Reasonable agreement between theoretical and experimental ΔE_{SO} is found [Fig. 2(b)]. Moreover, as expected for a Rashba-type spin splitting, the spin direction for upper and lower peak inverts by inverting the $k_{\|}$ direction.

Differently from the Rashba bands found so far [4], the DFT calculations shown in Fig. 1(a) predict that the different spin branches disperse into different projected bulk continuum bands. Thus, each spin branch connects the upper and the lower bulk band surrounding the gap by dispersing from $k_{\|} = -0.28$ Å^{-1} to $k_{\|} = 0.28$ Å^{-1}. At Γ, the surface state is spin degenerate as requested by time reversal symmetry.

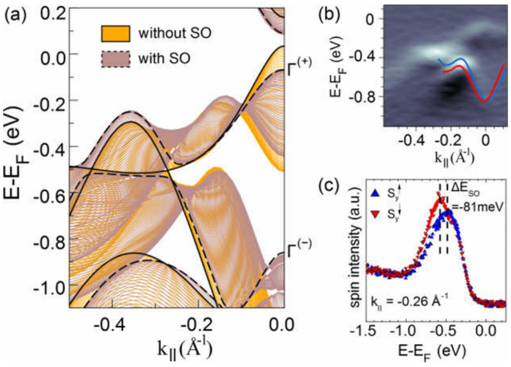

FIG. 3: (a) Bulk band structure along Γ-K calculated with (gray lines) and without (yellow lines) SO interaction; black lines mark the band edge with (dashed) and without (solid) SO interaction;with SO interaction a gap opens near the center of the graph around E=-0.5 eV and $k_{\|} = \pm 0.26$ Å^{-1}; Γ (-), Γ (+) mark the parity of the two bands at the Γ point; (b) ARPES data including the Rashba state at higher $|k_{\|}|$; hν = 54.5 eV; for better visibility, the derivative with respect to E is shown; $E(k_{\|})$ curves from DFT calculation are superposed (colored lines). (c) Spin resolved EDCs measured at the position of the SO gap; hν = 54.5 eV; peak positions as determined from Lorentzian fits (solid lines) are indicated by dashed lines; the resulting ΔE_{SO} is marked.

Fig. 3(b) shows the measured band structure close to the point where the Rashba bands merge with the bulk bands according to DFT. Indeed, a band moving upwards and a band moving downwards are discernible up to about $|k_{\|}| = 0.27$ Å^{-1}. Fig. 3(c) shows that a spin splitting of about 80 meV is still visible at $|k_{\|}| = 0.26$ Å^{-1}, i.e., close to the point where merging of surface bands and bulk bands is obtained in the calculation and the photoemission intensity of the surface band disappears. The origin of this remarkable behavior is illustrated in the main part of Fig. 3(a), where the calculated bulk band structure with and without SO interaction is shown. Obviously the SO interaction opens a gap between the projected bulk states originating from a band $\Gamma_{(+)}$ near the Fermi level and a lower-lying $\Gamma_{(-)}$ band, where (+) and (-) marks the parity of the states. The gap is found at $k_{\|} = 0.26$ Å^{-1} along the line Γ-Σ of the bulk band structure. In such a SO gap, according to a theoretical argument given by Pendry and Gurman [5], at least one surface state (with two spin channels) must exist. The requirement is that the gap is not located at a high symmetry point of the Brillouin zone as in our case. Thus, the observed Rashba split surface state is protected by the SO gap. Similarly to the topologically protected Dirac cone, it connects the lower and the upper bulk bands, which are inverted by SO interaction.

---

[1] H. Zhang *et al.*, Nature Phys. 5, 438 (2009).
[2] D. Hsieh *et al.*, Nature 460, 1101 (2009).
[3] D. Lencer *et al.*, Nature Mat. 7, 972 (2008).
[4] S. LaShell *et al.*, Phys. Rev. Lett. 77, 3419 (1996).
[5] J. B. Pendry *et al.*, Surf. Sci. 49, 87 (1975).

Selective Adsorption of C_{60} on Ge/Si Nanostructures

S. Korte[1], K. Romanyuk[1], B. Schnitzler[1], V. Cherepanov[1], B. Voigtländer[1], S. Filimonov[2]

[1]Peter Grünberg Institut-3, Forschungszentrum Jülich
[2]Department of Physics, Tomsk State University, Tomsk, 634050 Russia

Selective adsorption of C_{60} on nanoscale Ge areas can be achieved, while neighboring Si(111) areas remain uncovered, if the whole surface is initially terminated by Bi. Fullerene chemisorption is found at Bi vacancies which form due to partial thermal desorption of the Bi surfactant [1]. The temperature dependence of the C_{60} adsorption was measured using scanning tunneling microscopy (STM). The selectivity of the C_{60} adsorption can be traced back to an easier vacancy formation in the Bi layer on top of the Ge areas compared to Si areas. Furthermore, it is also possible to desorb C_{60} from Ge areas, allowing to use C_{60} as a resist on the nanoscale.

Nanostructuring using epitaxial growth processes can lead down to sizes in the single digit nano-meter range or even ultimately to the single molecule/atom range which is not accessible by lithography. Serious challenges in these efforts are size fluctuations during the growth process and the ability to place self assembled nanostructures at desired positions. A great help in these nanostructuring attempts is the ability to directly inspect the nanostructure formation by chemically sensitive surface imaging techniques. For instance, in our previous studies it has been shown that the use of Bi as surfactant not only largely suppresses Si/Ge intermixing but also allows the distinction between Si and Ge on the nanometer scale [2]. Using step flow growth mode during Bi mediated Ge epitaxy on a vicinal Si(111) substrate we successfully fabricated an array of 4 nm wide one atomic layer high Ge nanowires. These nanowires could serve as templates for growth of even more complicated nanostructures based on different material combinations. However, attempts to either desorb Bi selectively from Ge areas or decorate the Ge nanowires by a metal failed so far. The fundamental reason for this lack of selectivity is that Si and Ge are, in fact, chemically very similar materials. To achieve the selectivity a physical mechanism has to be found that would enhance the material difference.

We show that the use of surfactants is a means to control the selectivity of C_{60} adsorption and leads to new nanostructuring opportunities. Deposition of C_{60} on a Bi terminated surface results in selective replacement of Bi by C_{60} in Ge surface areas (Fig. 1 (a)). Our analysis shows that the high selectivity of C_{60} adsorption is made possible due to a complex mechanism of C_{60} adsorption, involving the formation of vacancies in the Bi layer followed by vacancy mediated chemisorption of C_{60} on Ge surface areas only [1].

Fig. 1 (a) shows an STM image of a Si(111) sample on which Ge nanowires have been grown at step edges using Bi mediated epitaxy. The borders between the Si and the Ge areas (each with 1 ML Bi on top), which show different apparent heights in the STM images [2], are highlighted by dashed lines. Subsequently 5 ML of C_{60} were deposited onto this Ge nanowire template at 440°C. Only a small fraction of the C_{60} actually remains on the surface whereby C_{60} adsorbs selectively on the Ge areas. The selectivity is perfect in the sense that virtually no C_{60} adsorbs on the Si, however, the Ge nanowires are not completely covered by C_{60}. When no Ge area is present on the surface, deposition of C_{60} on Bi:Si(111) leads to selective adsorption of C_{60} at Si step edges (Fig. 1 (b)).

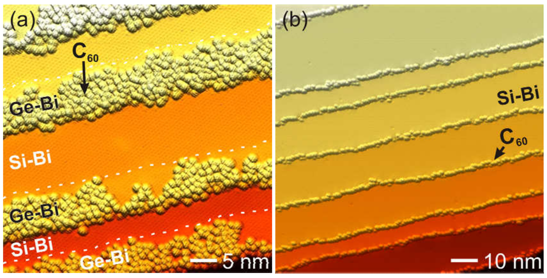

FIG. 1: (a) Selective growth of C_{60} on Ge areas, while Si areas remain uncovered. The slight height difference between Si and Ge areas is highlighted by dashed lines at the Si/Ge boundaries. The C_{60} are seen as round protrusions with intramolecular structure on the Ge areas. (5 ML C_{60} deposited at 440°C during 10 min) (b) Selective adsorption of C_{60} at Si step edges (2 ML C_{60} deposited at 420°C during 10 min).

In order to identify the reason for the selective adsorption of C_{60} on Ge areas we analyzed the C_{60} adsorption as function of temperature, which shows a different behavior on the surfactant terminated surface than on clean Si or Ge [3]. The results are summarized schematically in Fig. 2. At room temperature C_{60} adsorbs on top of the Bi layer and forms large two-dimensional islands consisting of well-ordered hexagonally arranged C_{60} molecules. The observed height of the C_{60} islands above the Bi layer of ~ 8 Å suggests a weak van der Waals bonding of C_{60} to Bi:Ge/Si(111) and Bi:Si(111) surfaces. In this weakly bound physisorption state C_{60} shows no selectivity and grows both on Si and on Ge areas. After short annealing at 200°C the physisorbed C_{60} layer completely desorbs, restoring the Bi covered surface. Depositing C_{60} in a temperature range of 200-400°C does not lead to any adsorption of C_{60} (Fig 2 (b)).

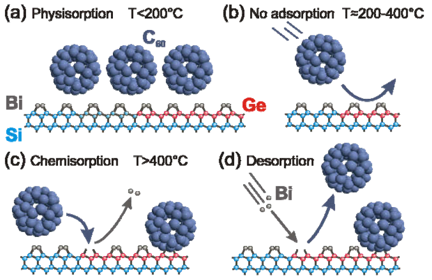

FIG. 2: Schematic of the C_{60} adsorption on Si(Ge) as function of temperature. (a) at room temperature C_{60} adsorbs in a weakly bound physisorption state on top of the Bi layer, (b) at 200-400°C no C_{60} adsorption occurs, (c) above 420°C chemisorption of C_{60} occurs at Bi vacancies on Ge. (d) under Bi flux C_{60} desorbs from the Ge surface.

At temperatures above 420°C adsorption of C_{60} could be seen on Ge, and starting from about 460°C also on Si terraces. At Si step edges the adsorption occurs already at somewhat lower temperatures, c.f. Fig. 1 (b). However, in this high temperature range the adsorption mechanism differs considerably from that observed at room temperature. At submonolayer surface coverages most of the C_{60} adsorb either as single molecules, or forming small irregular clusters. The measured apparent height of the C_{60} above the surrounding Bi layer is only 4 Å, suggesting that at elevated temperatures C_{60} adsorbs directly to Si (Ge), i.e. without Bi below C_{60} (Fig. 2 (c)). The irregular arrangement of the C_{60} clusters hints at strong covalent bonding of C_{60} to the underlying Si (Ge) surface, which also occurs for C_{60} adsorption on clean Si(111) and Ge(111) surfaces [3].

Direct bonding of C_{60} to Si and Ge surfaces may occur either at vacancies in the Bi layer or via displacement of Bi atoms by C_{60}. To experimentally prove the vacancy mediated chemisorption of C_{60} on the Bi terminated Si(111) surface, we deposited the same amount of C_{60} in two different ways. In the first experiment, 1.3 ML of C_{60} was deposited continuously for 5 min at 480°, while in the second experiment the sample was first annealed for 5 min at 480°C and then the same amount of C_{60} was deposited in a burst of only 10 sec at a low temperature of 350°C. Both the amount of C_{60} that actually stick to the surface (ca. 0.3 % of the deposited C_{60}) and the density of C_{60} clusters are almost identical in both cases. This indicates that the annealing phase, lasting the same time as the continuous deposition experiment, determines the island density and not the actual C_{60} deposition.

The major effect of the annealing is a partial desorption of Bi and formation of vacancies in the Bi layer which can be directly seen in STM images after annealing. Therefore, we conclude that the chemisorption of C_{60} occurs at vacancies in the Bi layer which are formed by thermal desorption of Bi. A more detailed analysis shows that a single vacancy where only one Bi trimer of the $\sqrt{3}\times\sqrt{3}$ Bi reconstruction has converted to a Bi monomer is not enough to trigger C_{60} adsorption, but larger vacancy islands with reduced Bi coverage are needed as nucleation centers for C_{60}.

As an additional check for the proposed adsorption mechanism of C_{60} on Bi:Si(111) we have performed C_{60} deposition supplying a Bi flux to prevent Bi desorption. In this case the formation of Bi vacancies is inhibited (deposited Bi fills the vacancies), and the vacancy mediated C_{60} chemisorption should be suppressed, which is confirmed experimentally.

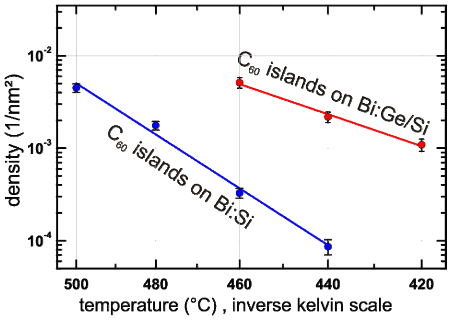

FIG. 3: Temperature dependence of the C_{60} island density on a 1ML Bi:Si(111) and on a Bi:Ge/Si(111) surface for deposition of 0.8 ML C_{60} during 2 min. The smaller slope indicates a lower vacancy formation energy for Bi on Ge than for Bi on Si.

An Arrhenius type temperature dependence was found for the C_{60} island density as shown in Fig. 3. From this data we obtain a much higher vacancy formation energy for Bi on Si (3.2±0.3 eV) than for Bi on Ge (1.7±0.3 eV). This explains the selectivity of the C_{60} chemisorption. One can tune the temperature so that Bi vacancies form readily at the Ge areas, which can serve as nucleation centers for C_{60}, while on the neighboring Si areas the activation energy for a Bi vacancy formation is so high that no Bi vacancies form. There might be additional factors that enhance C_{60} adsorption selectivity even further.

C_{60} can also be removed again from the Ge(1ML)/Si(111) surface. Annealing at 420°C in a flux of Bi leads to desorption of C_{60} according to the mechanism sketched in Fig. 2 (d). The Bi substitutes the C_{60} and fills the vacancies in the Bi termination layer. An almost complete C_{60} desorption from Ge can be achieved, leaving less than 1 % of the C_{60} bound to the surface.

In conclusion, selective adsorption of C_{60} at Ge areas and at Si step edges has been achieved. The mechanism for the selective adsorption is the nucleation and growth of C_{60} at Bi vacancies which form preferentially on Ge areas due to the lower vacancy formation energy compared to Si. It is possible to selectively cover Ge nanowire templates with C_{60} (and to remove it afterwards) in order to use C_{60} as a resist in further nanostructuring steps.

[1] S. Korte, K. Romanyuk, B. Schnitzler, V. Cherepanov, B. Voigtländer, and S. Filimonov, Phys. Rev. Lett. 108, 116101 (2012).

[2] M. Kawamura, N. Paul, V. Cherepanov, and B. Voigtländer, Phys. Rev. Lett. 91, 096102 (2003).

[3] P.J. Moriarty, Surf. Sci. Rep. 65, 175 (2010).

Transport in coupled graphene-nanotube quantum devices

S. Engels[1,2], P. Weber[1,2], B. Terrés[1,2], J. Dauber[1,2], C.Volk[1,2], C. Meyer[2], S. Trellenkamp[2], U. Wichmann[1], and C. Stampfer[1,2]

[1]II. Institute of Physics B, RWTH Aachen University, 52074 Aachen
[2]Peter Grünberg Institute (PGI-6/8/9), Forschungszentrum Jülich, 52425 Jülich

We report transport measurements on carbon nanotube quantum dots with graphene charge detectors and graphene source, drain leads. Individual charging events in the quantum dot lead to conduction changes of up to 20% in the graphene nanoribbon acting as a charge detector. Furthermore, the observed Coulomb effect in a graphene-contacted nanotube quantum dot leads to the conclusion that a tunneling barrier is present at the graphene carbon nanotube interface.

Carbon nanomaterials, such as graphene and carbon nanotubes (CNTs) attract increasing interest mainly due to their promises for flexible electronics, high-frequency devices and spin-based quantum circuits. Both materials consist of sp^2-bound carbon and exhibit unique electronic properties. In particular the weak hyperfine interaction makes graphene and CNTs interesting host materials for quantum dots (QDs) which promise the implementation of spin qubits. Here, we present quantum devices based on both graphene and carbon nanotubes, which combine the advantages of prospectively clean quantum dot systems in CNTs [1] and the ability to pattern graphene into the desired geometries [2,3]. In particular, we discuss (i) a carbon nanotube QD with a capacitively coupled graphene nanoribbon acting as electrostatic gate and charge detector and (ii) a nanotube QD with both source and drain graphene leads. Thus, a quantum dot device exclusively built of carbon nanomaterials.

The fabrication process is based on chemical vapour deposition (CVD) growth of carbon nanotubes and subsequent deposition of mechanically exfoliated natural graphite. Electron beam lithography and reactive ion etching is used to pattern the graphene flake. Metallic contacts are fabricated by electron beam lithography and lift-off.

Fig. 1(a) shows a scanning force micrograph (SFM) of an all-carbon device consisting of a carbon nanotube lying in the close vicinity to an etched graphene nanoribbon (GNR) which acts as a charge detector (CD). From a Raman spectrum the nanoribbon is identified to be bilayer graphene and from a SFM profile the nanotube is determined to be a single-walled nanotube. Both carbon nanostructures are separated by roughly 150 nm, the nanoribbon has a width of around 100 nm and the CNT quantum dot is defined by two metal electrodes (indicated in magenta) which are separated by 350 nm. As illustrated in Fig. 1(a) we apply a symmetric bias voltage (V_{CNT} and V_{GNR} respectively) to both structures and the overall Fermi level can be tuned by the back gate voltage V_{BG} applied to the highly doped Si substrate. Additionally, we can use the CNT as a lateral gate for the GNR by applying a reference potential V_{REF}.

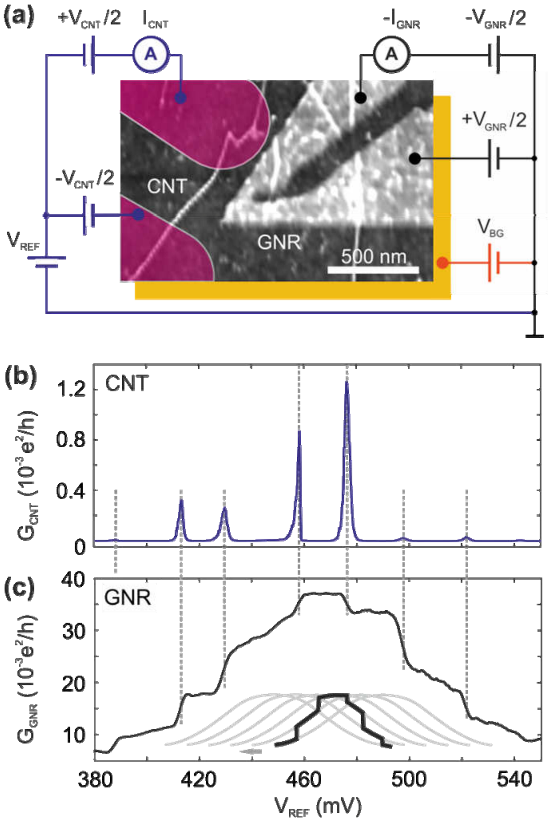

FIG. 1: (a) Scanning force micrograph of the investigated graphene-carbon nanotube hybrid device. (b), (c) Simultaneuosly measured conductance through the nanotube (CNT) quantum dot (b) and through the graphene nanoribbon (GNR) (c).

All measurements taken on the presented device were performed in a pumped ^{4}He-cryostat at a base temperature of $T \approx 1.5$ K. Figs. 1(b) and 1(c) show the simultaneously measured low-bias $V_{CNT}=0.5$ meV conductance through the nanotube G_{CNT} and the nanoribbon G_{GNR} as function of V_{REF} respectively. G_{CNT} exhibits Coulomb peaks which are indicating single charging events in the CNT QD. In the simultaneously measured trace of the GNR we observe distinct steps in the conductance at the exact positions of the CNT QD charging events. The steps in conductance can measure up to 20% of the total resonance amplitude and are due to the capacitive coupling of both nanostructures. Increasing the reference potential V_{REF} and decreasing V_{BG} both leads to a higher chemical potential in the QD and subsequently to a lower occupation number at every event. Consequently, the GNR resonance shifts to lower values of V_{REF} giving rise to the unconventional shape of the charge detection resonance in Fig. 1(c) as illustrated by the inset.

Finally, we discuss a carbon nanotube device where both metal leads (source and drain) are substituted by two graphene flakes (see inset of Fig. 2(a)). In order to measure the conductance of the nanotube, Cr/Au metal contacts are deposited on each graphene flake. Fig. 2(a) shows the back gate dependence of the current I_{CNT} through the nanotube. The absence of a V_{BG}-regime where the current is fully suppressed suggests the presence of a metallic nanotube. Further investigation of the transport through the graphene nanotube hybrid device is shown in Fig. 2(b). Here, we plot the current through the nanotube I_{CNT} on a logarithmic scale as function of the bias voltage V_{BIAS} (applied to the graphene flakes) and V_{SG}. For the entire measurement the back gate voltage is kept at a fixed value of V_{BG}=35.15 V (see black arrow in Fig. 1(a)). The illustrated plot exhibits clear diamond shaped patterns which can be attributed to Coulomb blockade. From the addition energies of 1-1.5 meV the quantum dot length in the nanotube can be estimated to be 0.9-1.5 µm. A comparison of the geometrical length of the nanotube in between the graphene of 1.2 µm and the estimated length of the quantum dot shows good agreement. This circumstance, as well as the fact that we tune the dot system with the closely positioned side gate leads to the conclusion that the quantum dot is sitting in the nanotube and extends over its full length in between the graphene. Moreover, due to the existence of the quantum dot given by the spacing of the graphene leads, the presence of tunnel barriers at the interface of both carbon allotropes is shown. Hence, an all carbon quantum circuit which not only implements gate structures, charge detectors or quantum dots but also includes a contacting scheme, can be fully realized exclusively using carbon components.

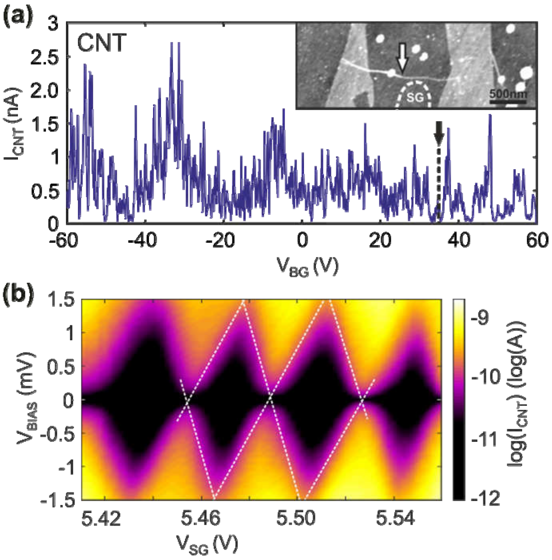

FIG. 2: (a) Back gate characteristic of the device shown in the inset. (b) Coulomb diamond plot of the CNT QD measured by varying the side gate (SG) voltage applied to the metal electrode indicated by the dashed lines in the inset of (a).

In summary, we present the fabrication and characterization of carbon nanotube graphene hybrid devices. We show an example of a structure where a nanotube quantum dot is capacitively coupled to a graphene nanoribbon. Sharp resonances in the graphene nanoribbon gate characteristics give rise to clear detection signals. In a further investigation we study a device where both allotropes are now electrically coupled. Here, we find that the interface between the graphene and the carbon nanotube resembles a tunnel barrier. Consequently, we can use the two dimensional graphene to contact a nanotube quantum dot [4]. Both results open the road to more sophisticated devices which are entirely fabricated out of carbon nanostructures and exploit the different advantages of these materials.

---

[1] S. Sapmaz, P. Jarillo-Herrero, J. Kong, L. P. Kouwenhoven, and H. van der Zant, Phys. Rev. B., **71,** 153402 (2005)**.**

[2] B. Terrés, J. Dauber, C. Volk, S. Trellenkamp, U.Wichmann, and C. Stampfer, Appl. Phys. Lett. **98**, 032109 (2011).

[3] C. Volk, S. Fringes, B. Terrés, J. Dauber, S. Engels, S. Trellenkamp, and C. Stampfer, Nano Lett., **11**, 3581 (2011).

[4] S. Engels, P. Weber, B. Terrés, J. Dauber, C. Meyer, C.Volk, S. Trellenkamp, U. Wichmann, and C. Stampfer, submitted (2012).

Physisorption versus local chemical interactions: Graphene on Ir(111)

Nicolae Atodiresei[1], Predag Lazic[2], Vasile Caciuc[1], Stefan Blügel[1]

[1]Peter Grünberg Institut-1, Forschungszentrum Jülich, 52425 Jülich
[2] Massachusetts Institute of Technology, Cambridge, 02139 Massachusetts, USA.

By using state of the art theoretical first principles calculations including the van der Waals interactions, we reveal the bonding mechanism and the adsorption geometry of graphene on Ir(111) surface. Importantly, we obtained an excellent agreement between the calculated mean height h=3.41 Å of the C atoms with their mean height h=3.38±0.04 Å as measured by X-ray standing wave experiments (XSW). The graphene-Ir(111) bonding mechanism is dominated mostly by the van der Waals interactions, but surprisingly we find that locally, a polar covalent-like chemical interaction occurs. This local bonding arises from the charge transfer from the graphene to metal surface and the subsequent charge accumulation at the interface in the fcc- and hcp- regions of the moiré superstructure.

From a theoretical point of view, a quantitative description of the interaction between π-conjugated systems like graphene and metal substrates is a challenge in density functional theory (DFT) when employing the most commonly used exchange-correlation functionals like local density approximation (LDA) and generalized gradient approximation (GGA) since these (semi)local functionals lack the nonlocal-correlation effects responsible for the van der Waals (vdW) interactions. In particular, in the case of graphene on Ir(111) surface the GGA predicts a non-bonding interaction [1] while the weak chemisorption predicted by LDA [2] is questionable due to the tendency of this functional to overbind which wrongly mimics the vdW interactions. Recently, the first truly nonlocal correlation functional vdW-DF [3] was developed and successfully applied to vdW-bonded systems [4]. Despite the numerical effort inherent in evaluating the six-dimensional real-space [5] integral to obtain the non-local correlation energy, this functional opens a new perspective to arrive at a conclusive physical picture for systems with significant vdW bonding.

Our *ab initio* DFT calculations have been performed by using the projector augmented wave method in combination with the GGA functional as implemented in VASP code. To obtain a reliable relaxed adsorbate-surface geometry [4] we have implemented the vdW forces in VASP using the semi-empirical method DFT-D, where the Ir C_6 coefficient was determined by comparing DFT-D and nonlocal vdW-DF calculations for several adsorption geometries of benzene on Ir(111). For the final relaxed graphene-Ir(111) geometry, the total energy was calculated with vdW-DF in a post-processing approach using the JuNoLo code [5]. The system was modeled by (10 × 10) surface unit cell of graphene on (9 × 9) cell of Ir resulting in a ratio of the surface unit cell lengths of $a_C/a_{Ir} = 1.111$, close to the experimental value of $a_C/a_{Ir} = 1.107$ for flakes with an average size of 1000 Å.

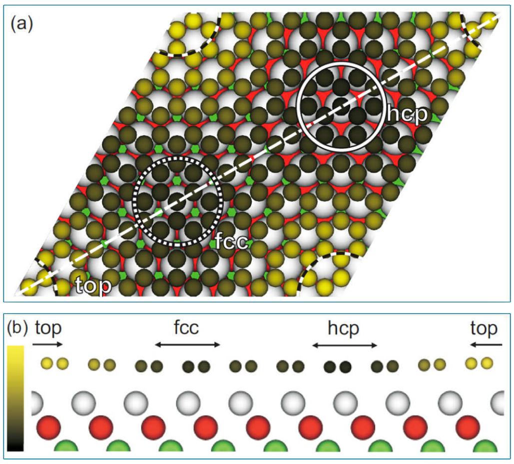

FIG. 1: (a) top view and (b) side view of the relaxed structure of graphene/Ir(111) obtained by DFT including the van der Waals interactions. The different regions (fcc, hcp and top) are marked by white circles.

As already mentioned, when using GGA, the graphene does not bind to the Ir(111) surface. However, by including vdW into the DFT-GGA calculations the graphene layer is brought closer to the Ir(111) substrate. The final relaxed geometry is plotted in Fig. 1, where the color variation of the C atoms from dark to yellow in the top view of the moiré unit cell visualizes their height variation. It is also directly visible in the cross section along the unit cell diagonal in Fig. 1 (b). The largest height of 3.62 Å is found in regions where the center of the C hexagon is located on top of an Ir atom (top region) and the lowest height of 3.27 Å in the hcp-region (center of C hexagon above threefold coordinated hcp site), slightly lower than the one of 3.29 Å in the fcc-region. The mean height is h = 3.41 Å, in excellent agreement with the experimental value [6]. For the relaxed geometry shown in Fig. 1 (a), the GGA binding energy contribution is repulsive (≈ +20 meV/C) while the binding energy contribution containing the non-local correlation effects is attractive (≈ -70 meV/C) leading to the total vdW-DF binding energy E_b = -50 meV/C.

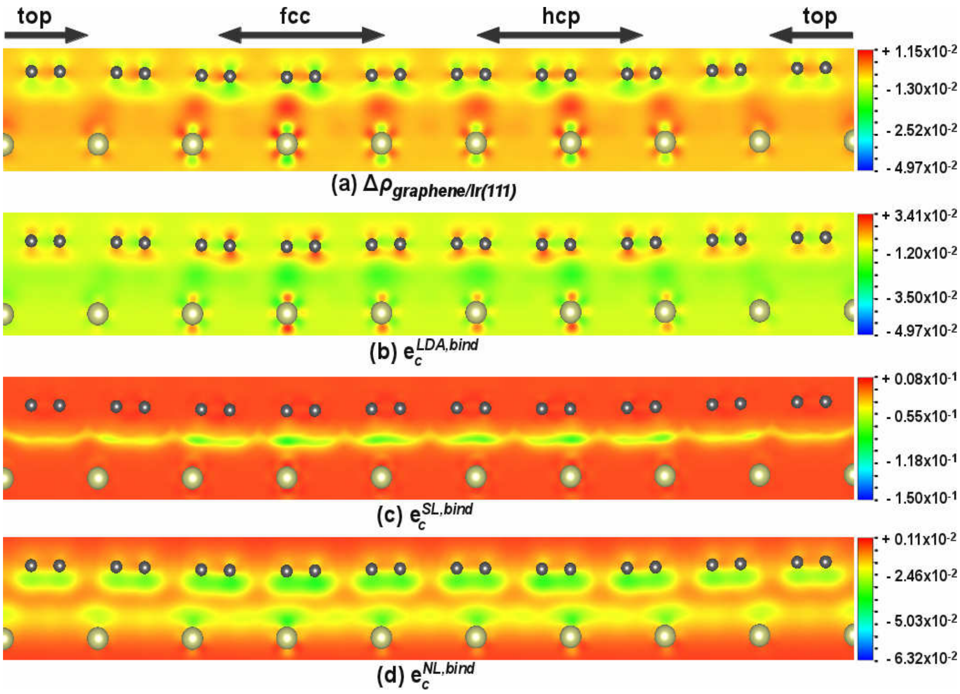

FIG. 1: *(a) The charge density difference* $\Delta\rho_{\text{graphene/Ir(111)}}$, *(b) the LDA correlation binding energy density* $e_c^{LDA,\ bind}$, *(c) the semi-local (SL) correlation binding energy* $e_c^{SL,\ bind}$ *and (d) the non-local (NL) correlation binding energy density* $e_c^{nl,\ bind}$ *plotted for the graphene on Ir(111) surface (for details on the definitions of these binding energy densities are given in Ref. [6]). The plane used to plot these quantities is marked by the white line in Fig. 1(a).*

Contrary to the impression given by the large difference between these energy contributions, the bonding mechanism is not purely physisorption, although it is dominated by van der Waals (see below). The distribution of the nonlocal correlation binding energy density $e_c^{nl,\ bind}$ (for details see Ref. [6]), caused by adsorption is shown in Fig. 2. Note that, as compared to the LDA and semilocal (SL) correlation binding energy densities (which depend on the charge density (LDA) and its gradient (SL) at a given point), the $e_c^{nl,\ bind}$ is a non-local quantity as its value at a given point depends on the interaction of the charge density at this point with the one at all other points.

One can observe that this energy density is *delocalized* below the graphene layer and shows that the polarization effects responsible for the vdW interactions are spread over the entire graphene sheet which is a clear fingerprint for a vdW bonded π-conjugated system [4, 6]. However, on the metal surface this nonlocal binding energy is mainly *localized* only in specific regions close to certain Ir atoms where the charge density transfer from graphene to substrate occurs. This indicates which sites at the metal substrate become more polarizable upon adsorption due to the graphene-surface interaction. Interestingly, in the hcp- and fcc-regions [see Fig. 1], a small charge transfer from graphene to substrate take place which leads to a charge accumulation at the hybrid graphene-Ir(111) interface [Fig. 2]. This surprisingly indicates the formation of a local bonding with a polar covalent character. In total, graphene has lost charge (≈ -0.01 electrons per C atom) that results in slight p-doping. The largest charge accumulation is above the Ir atoms which are directly on top an C atom (i.e. in the center of the hcp and the fcc regions. However, in graphene the largest charge depletion is observed at the nearest neighbors of these C atoms situated on top of the Ir atoms.

To summarize, by performing *ab initio* calculations that include state of the art methods to account for the van der Waals interactions we precisely determined the graphene-Ir(111) mean height as h = 3.41 Å which is in excellent agreement with the XSW experiments. The binding of the graphene to the metal is dominated by van der Waals interactions although, locally, a polar covalent-like chemical interaction takes place due to the charge accumulation at the interface in the fcc- and hcp-regions of the moiré superstructure.

The calculations have been performed on JUROPA and JUGENE supercomputers operated by the Jülich Supercomputer Centre (Forschungszentrum Jülich, Germany).

---

[1] P. Lacovig *et al.*, Phys. Rev. Lett. 103, 166101 (2009).

[2] A. T. N'Diaye *et al.*, Phys. Rev. Lett. 97, 215501 (2006).

[3] M. Dion *et al.*, Phys. Rev. Lett. 92, 246401 (2004).

[4] N. Atodiresei *et al.*, Phys. Rev. Lett. 102, 136809 (2010).

[5] P. Lazic *et al.*, Comput. Phys. Commun. 181, 371 (2010).

[6] C. Busse *et al.*, Phys. Rev. Lett. 107, 036101 (2011).

Magnetic and transport properties of graphene decorated with heavy transition-metal adatoms

Hongbin Zhang, Stefan Blügel and Yuriy Mokrousov[1]

[1]IAS-1: Institute for Advanced Simulation – Quantum Theory of Materials and JARA-SIM and JARA-HPC

Since the day graphene was isolated and produced as a two-dimensional material [1], it abruptly altered the research direction of nanoelectronics with the aim of exploring its fascinating transport properties. One common feature for those transport properties is the nontrivial topological origin, resulting in dissipationless quantized charge or spin current carried by edge states. To avoid the constraints of quantum (spin) Hall effect in graphene, while keeping the benefit of topologically protected quantized transport, the long-sought quantum anomalous Hall effect (QAHE) could be a perfect solution. The essence of the QAHE lies in the quantization of the transverse charge conductivity in a material with intrinsic nonvanishing magnetization. The fact that the magnetization in ferromagnets can be manipulated experimentally much easier than large magnetic fields in dia- or paramagnets makes the QAHE extremely attractive for applications in spintronics and quantum information. However, at present the QAHE is merely a generic theoretical concept.

The spin-orbit interaction couples the spin degree of freedom of electrons to their orbital motion in the lattice. This leads to many prominent physical phenomena in conventional ferromagnets. It is also the key interaction in the newly found quantum topological phase in topological insulators, where the quantum spin Hall effect was observed experimentally, and the quantum anomalous Hall effect was predicted to exist. Since the orbital motion can be manipulated with external electric fields, spin-orbit coupling (SOC) opens a route to electrical control of magnetic properties, playing a crucial role in future spintronics applications.

Owing to their strong spin-orbit coupling, heavy 4d and 5d transition-metals (TMs) display fascinating physical properties for desirable spintronic applications, especially when combined with a nonvanishing magnetization. However, magnetism of 5d TMs proved difficult to achieve, even for low-dimensional structures, because their valence d wave functions are more delocalized than those of Fe, Co, and Ni. Moreover, the interfacial diffusion and strong d-d hybridization suppress magnetism upon the deposition of 5d TMs on commonly used noble-metal substrates. From this point of view, using sp-substrates is more promising. In fact, 4d ferromagnetism was first observed in a Ru monolayer deposited on the graphite (0001) surface.

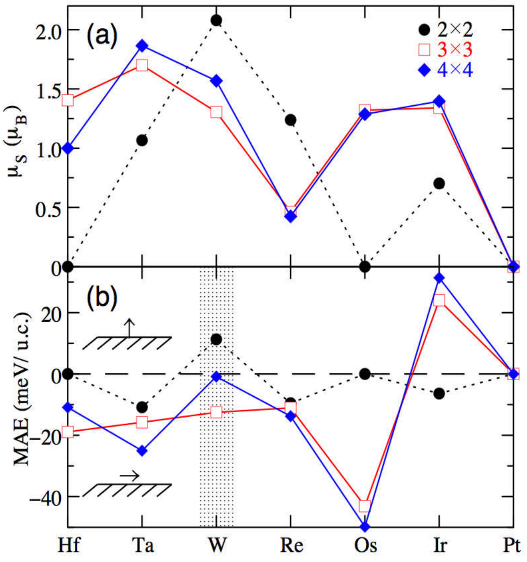

FIG. 1: Magnetic moments and MAE of 5d TMs on graphene. (a) Magnetic moments calculated without SOC and (b) the MAE of 5d TM adatoms on graphene in 2x2, 3x3 and 4x4 superlattice geometry. Positive (negative) values of MAE imply an out-of-plane (in-plane) easy axis of the spin moments, i.e. perpendicular to (in) the plane of graphene. Taken from [3].

From our calculations for deposited 5d TM adatoms on graphene, we predict that all 5d TMs (except for Pt and 2x2 Hf and Os) are magnetic, with sizable magnetic moments ranging between 0.5 and $2\mu_B$. Unique to the 5d TMs is the property that the SOC and the intra-atomic exchange are of the same magnitude, which is manifested by the colossal values of the magnetic anisotropy energy (MAE), defined as the total-energy difference between the magnetic states with spin moments aligned in the plane and out of the graphene plane directions. For the systems considered, the calculated MAEs are very large, typically in the range of 10–30 meV per TM (see Fig. 1) [3]. The MAE presents one of the most fundamental quantities of any magnetic system as its sign defines the easy magnetization axis and its magnitude provides an estimate of how stable the magnetization is. A large MAE makes the magnetization stable but also difficult to manipulate.

Striking is the magneto-electric response of our systems to an external electric field, which we applied in our calculations perpendicularly to the graphene plane. Varying the electric field in the experimentally achievable range, the spin moments of the adatoms can be tuned quite significantly. The magneto-electric coefficient, which characterizes the response of the TM spin moment to the applied electric field, is order of magnitude larger for 5d TMs on graphene than for Fe and Co thin films. Even more surprising is the effect of the electric field on the MAE: as can be seen from Fig. 2, e.g. for 4x4 W it results in a switch in the easy axis of the magnetization. Similar effect can be also observed for Hf, while for other TMs the effect of the electric field on the MAE is gigantic [3]. We explain such remarkable magneto-electric properties by electric field mediated redistribution of the spin density among the d-states of the transition metal [3], see inset in Fig. 2.

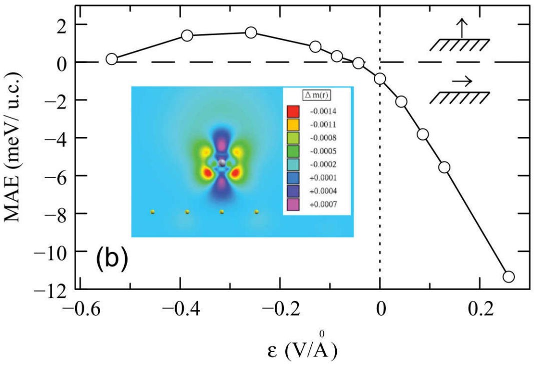

FIG. 2: Dependence of the MAE on the magnitude of applied to graphene electric field E for 4x4 W on graphene. Negative values of E corresponds to the electric field in the z direction, i.e., the direction from graphene towards the adatoms. The inset displays the difference between spin densities for the system without and with an electric field of 0.13 V/Angstrom. Taken from [3].

The most promising feature of our systems is opening of the multiple QAHE gaps in the spectrum of each of the TM on graphene due to spin-orbit interaction. Each of these gaps can be characterized by so-called Chern number C, equal to the quantized value of the transverse conductivity. And although for 4x4 W the QAHE gap opens right at the Fermi energy, such nontrivial topological QAHE states occur also for all other 5d adatoms (except Pt) on graphene in 4x4 geometry, and for several of them (Ta, W, Re, and Ir) in 2x2 geometry, with QAHE gaps of large magnitude away from the Fermi energy.

For example, graphene with Re deposited in 4x4 geometry, see Fig. 3, exhibits three C = +2 QAHE gaps at −1, −0.15, and +0.67 eV, with the corresponding gap size of 38, 63, and 98 meV, respectively. Also, for 4x4 Os, there exist two QAHE gaps with C of +2 and -2 at −0.38 and +0.15 eV, with corresponding gap sizes of 11 and 80 meV, respectively.

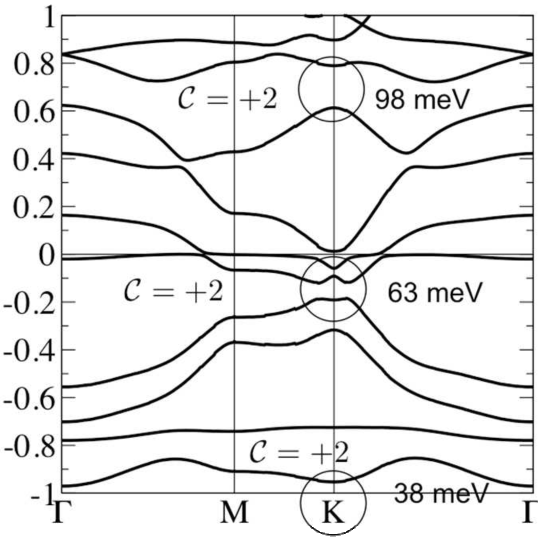

FIG. 3: Bandstructure of 4x4 Re adatoms on graphene with an out-of-plane magnetization. Due to SOC, topologically non-trivial gaps open at +0.67, -0.15 and -1.0 eV. The transport properties of the system can be characterized with a Chern number C, providing the quantized value of the transverse charge conductivity and indicating the occurence of the so-called quantum anomalous Hall effect.

The fact that several QAHE gaps with different Chern numbers at different energies can occur in the same material makes these systems a rich playground for topological transport studies. For such systems, the creation of the QAHE gaps occurs not at time-reversal symmetric points of the Brillouin zone, and the gaps are determined by 5d orbitals of TMs. Most importantly, due to strong SOC of 5d TMs, the magnitude of the QAHE gaps is increased by an order of magnitude, when compared to all QAHE systems suggested before, guaranteeing a strong topological protection against defects, structural disorder of the adatoms or thermal fluctuations, and thus opening a route to QAHE at room temperature.

---

[1] A.H. Castro Neto *et al.,* Rev. Mod. Phys. 81, 109 (2009)

[2] R. Yu *et al.,* Science 329, 61 (2010)

[3] H. Zhang, C. Lazo, S. Blügel, S. Heinze and Y. Mokrousov, Phys. Rev. Lett. 108, 056802 (2012)

Electronic Hybridization in a Rope of Carbon Nanotubes

K. Goss[1], S. Smerat[2], M. Leijnse[3], M. R. Wegewijs[1,4], C. M. Schneider[1], and C. Meyer[1]

[1]Peter Grünberg Institute (PGI-6), Forschungszentrum Jülich, 52425 Jülich
[2]Physics Department, Arnold Sommerfeld Center for Theoretical Physics, Ludwig-Maximilians-Universität München, 80333 München
[3]Niels Bohr Institute & Nano-Science Center, University of Copenhagen, Universitetsparken 5, 2100 Copenhagen
[4]Institute for Theory of Statistical Physics, RWTH Aachen, 52056 Aachen

It is our goal to gain a fundamental and comprehensive understanding about the influences of molecular interactions on electronic transport in low-dimensional systems. Here, we demonstrate low-temperature transport through carbon nanotube quantum dots. The transport measurements can be used as a spectroscopic tool to analyze interactions between carbon nanotubes bundled in a rope. We have shown that the electronic states of carbon nanotube quantum dots can hybridize. This effect is very similar to the hybridization of molecules. We show that this hybridization can be selectively suppressed in a magnetic field due to spin effects.

Molecular electronics and spintronics aim at exploiting the chemical versatility of molecules to control charge and magnetism in nanoscale devices. However, the assembly of molecular structures in junctions for electric and magnetic manipulation is a challenging task [1]. Carbon nanotubes (CNTs) are particularly promising as building blocks of new devices for nanoelectronics, which exhibit interesting spin properties and can be useful for quantum information processing. Fundamental aspects of single-molecule devices require an understanding of strong perturbations by environmental effects, for example, the interaction with contacts or neighboring molecules. These interactions can, in principle, be studied on a single-molecule level using scanning probe techniques as for instance scanning near-field optical microscopy, tip-enhanced Raman spectroscopy or scanning tunneling spectroscopy (STS). However, in situ characterization of actual devices, for example, field-effect transistors, is difficult to implement and only STS can detect spin-dependent phenomena.

As an alternative approach, one may exploit the differential electrostatic gating effect, which was found to occur for contacted CNTs filled with fullerenes [2] and for single molecules in nanojunctions [3]. In this respect, bundled CNTs are interesting: Within a rope one expects the individual strands to be at a different potential and to respond differently to the external electric fields due to electrostatic effects. Low-temperature transport spectroscopy is sensitive to these potential variations on the sub-meV scale, allowing the study of interactions between coupled nanoscale conductors.

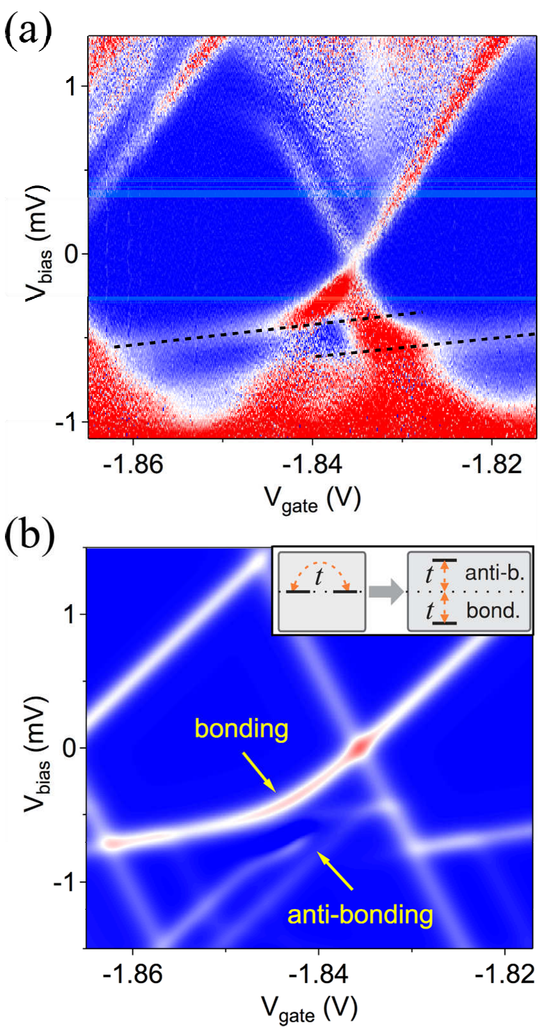

FIG. 1: Differential conductance plotted versus gate and bias voltage. Additional resonances appear in the measurement (a), which belong to a parallel quantum dot. The simulation of the data (b) shows that the current is carried by the bonding states. The electronic states of the quantum dot split, due to tunnel coupling between the two dots (inset), which leads to an anticrossing of the diamond edges.

The CNTs were grown on a Si/ SiO_2 substrate by chemical vapor deposition at 920 °C using a Fe/Mo catalyst and methane as precursor. At these temperatures the process results mainly in single-walled CNTs and few double-walled CNTs [4].

Source and drain electrodes (5 nm Ti/ 60 nm Au) were patterned by electron beam lithography to form a QD of length 360 nm with the highly doped Si substrate acting as back gate. The height profile of an atomic force micrograph of the quantum dot (QD) region shows a CNT height of ~ 7 nm, evidencing that the device consists of a CNT rope rather than an individual tube.

Low-temperature transport properties were measured in a dilution refrigerator at a base temperature of ~30mK. In the plot of the differential conductance (Fig. 1), Coulomb blockade in a QD is observed by the typical diamond-shaped signatures together with excited states, which imply size quantization. Two salient features are observed in Fig. 1(a): First, additional conductance peaks appear within the region of Coulomb blockade. These secondary resonances exhibit a weak gate voltage dependence (small slope) and do not appear symmetrically at positive and negative bias voltage (dashed lines). Proceeding from one Coulomb diamond to the next, the positions of these resonances jump in voltage. Second, anticrossings are observed whenever the secondary resonances meet with a main resonance of the Coulomb diamonds with the same slope. In the vicinity of these points the secondary resonances show an enhanced conductance. As we have shown, this indicates that several coupled QDs are formed in the rope and contacted in parallel [5].

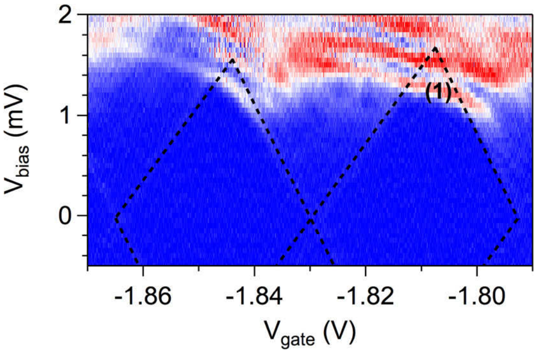

FIG. 2: Differential conductance plotted versus gate and bias voltage at B = 10 T. Dashed lines indicate extrapolated diamond edges of the main QD. (1) marks a clear crossing among the anticrossings proving that the ground states of the electron spins are different for the main QD and the side QD. For this occupation of the main QD, the ground state of the side QD hybridizes with an excited state of the main QD, which results in an anticrossing of these state.

When the electrochemical potentials of two parallel QDs are at resonance, hybridized bonding and anti-bonding states are generated, which are split in energy by 2|t| (inset Fig. 1(b)). If the hybridization amplitude t is significant on the scale of the energy difference between the two orbitals, anticrossings of excitation lines should appear. Fig. 1(b) shows that the calculations reproduce the experimentally observed features of the measurement in Fig. 1(a) very well. The calculations also reveal that the current is mainly carried by the bonding states.

In order to investigate a possible influence of the spin degrees of freedom on the hybridization within the rope, the transport spectrum was measured in an applied magnetic field. Compared to the measurements at B = 0 T, the transport through the main dot is strongly suppressed at B = 10 T (Fig. 2) and the secondary resonances at positive bias voltage appear as the most prominent feature. Again, the anticrossings show an enhancement of the bonding state. The energy offset, hybridization integral, and gate coupling are the same as in zero field, evidencing that these resonances indeed originate from the same CNT strand as the ones at B = 0 T.

Furthermore, Fig. 2 shows additional resonances involving excited states of the side dot, which exhibit the same weak gate voltage dependence and anticrossings as the initial secondary resonances. Amidst these anticrossings a clear crossing [marked (1)] appears, when the chemical potential μ^s for adding an electron to the ground state of the side dot is at resonance with the chemical potential of the main dot μ^m for the ground-state transition from N to N+1 electrons. This crossing reveals that the resonant states of the coupled QD system containing in total N+1 electrons have different quantum numbers, most probably different spins, preventing the states from hybridizing.

In summary, we measured quantum transport through several parallel QDs, formed in different CNT strands within a rope. We have shown that the molecular hybridization within a CNT rope can be detected and manipulated both by electric and magnetic fields. Such tunability of the hybridization is a key element in accessing localized charges and spins in coupled molecular systems, realized also in, for example, graphene or single molecules.

---

[1] L. Bogani, R.Maurand, L. Marty, C. Sangregorio, C. Altavilla, and W. Wernsdorfer, J. Mater. Chem. 20, 2099 (2010).

[2] A. Eliasen, J. Paaske, K. Flensberg, S. Smerat, M. Leijnse, M. R. Wegewijs, H. I. Jørgensen, M. Monthioux, and J. Nyågrd, Phys. Rev. B 81, 155431 (2010).

[3] E. A. Osorio, K. Moth-Poulsen, H. S. J. van der Zant, J. Paaske, P. Hedegård, K. Flensberg, J. Bendix, and T. Bjørnholm, Nano Lett. 10, 105 (2010).

[4] C. Spudat, C. Meyer, K. Goss, and C. M. Schneider, Phys. Status Solidi B 246, 2498 (2009).

[5] K. Goß, S. Smerat, M. Leijnse, M. R. Wegewijs, C. M. Schneider, C. Meyer, Phys. Rev. B 83, 201403(R) (2011).

Development and Characterization of Carbon Nanotube Sensors

V. Sydoruk[1], M. Petrychuk[2], F. Gasparyan[3], A. Offenhäusser[1] and S. Vitusevich[1]

[1] Peter Grünberg Institut-8, Forschungszentrum Jülich, 52425 Jülich
[2] Taras Shevchenko National University, Kiev, Ukraine
[3] Yerevan State University, Yerevan, Armenia

The main aim of the project "Development and characterization of carbon nanotube sensors" is developing low-noise high-speed test device structures on the basis of single-wall carbon nanotubes (SWNTs) for biosensor applications. The noise spectroscopy results allow us to analyze the mechanisms of conductivity in fabricated carbon nanotube structures. Furthermore, we showed that functionalization of the electrolyte-insulator-semiconductor (EIS) structure with multilayers of polyamidoamine dendrimer and single-walled carbon nanotubes leads to an essential reduction of the 1/*f* noise compared with noise in a bare EIS device. Thus the control of molecular architecture is important to obtain the enhanced performance of multilayer structures interfacing with electrolyte.

Carbon nanotubes are unique materials due to the high degree of ordering of carbon atoms on the surface of the tube, which represents a very uniform channel for high-speed electron transport. Therefore CNTs are very promising for various applications, including extremely sensitive biosensors. Noise spectroscopy is a powerful method for studying the transport properties, performance and reliability of material structures, especially scaled down to the nanoscale [1]. The fluctuation phenomena contain important information on the material performance and may be utilized as a valuable method for the characterization of nanoscaled materials and devices.

We studied the phenomena of charge transport in structures consisting of bundles of carbon nanotubes [2] prepared by applying uniaxial pressure. The Raman spectra data demonstrate that the bundles mainly consist of single-walled nanotubes. Low-frequency noise and transport properties of the structures were studied for samples fabricated in the form of dumbbells, containing a constriction with a characteristic size of 100×100 μm^2 in a cross-sectional area and a length of about 200 μm. In the temperature range from 20 K to 200 K the measured data demonstrate the characteristic for Luttinger liquid temperature dependence of resistance $R \sim T^{-\alpha}$ with exponent of $\alpha = 0.4$. At the temperatures higher than 200 K, the measured dependence deviates from this simple function. At lower temperatures, $T \approx (4.2 - 20)$ K the resistance follows an exponential function: $R \sim \exp(T_0/T)^{0.25}$. Exponential dependence of the resistance versus the sample temperature with an exponent of 0.25 indicates the hopping mechanism of conductivity with variable hopping length. The noise spectra of the sample have $1/f$ dependence, which is a characteristic function of flicker noise. To analyze the nature of the noise current in the nanotube bundles, we measured the spectral density of current noise, as a function of the current, $S_I \sim I^{\beta}$, at different temperatures in the range from 4.2 K to 300 K. Based on these results, we found the dependence of the coefficient on the temperature.

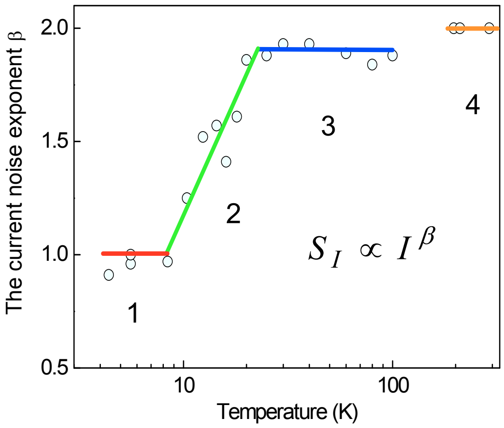

FIG. 1: The current noise exponent, β, of power function $S_I \sim I^{\beta}$ determined from measured noise spectra as a function of temperature, corresponding to: (1) hopping mechanism of conductivity; (2) transition region (see for details [2]); (3) Luttinger liquid conductivity; (4) diffusion conductivity.

A transition region is recorded in the temperature range T = (8 - 25) K, which indicates the transition from hopping conductivity to Luttinger liquid conductivity. Our experiment showed that the conductivity of Luttinger liquid is less "noisy" than the conductivity of the Fermi liquid. A sharp increase of noise in this latter region can be explained by increased phonon scattering and, as a result, decreasing of mean free path of carriers. At the same time, the conductivity of Luttinger liquid up to the temperature $T \approx 200$K is of a ballistic nature and is characterized by a low noise level, weakly dependent on temperature.

On the other hand, noise spectroscopy is a very sensitive method for the analysis of the semiconductor/insulator interface quality as well as for characterization of the quality of functionalization/ passivation layers in liquid environments. We studied the low-frequency noise properties of a capacitive field-effect electrolyte-insulator-semiconductor (EIS) structure functionalized with polyamidoamine (PAMAM) dendrimer/SWNT multilayers (Fig.2) and compared with noise of a bare EIS device [3].

In contrast to transistor structures, capacitive EIS sensors are simple in layout and cost-effective in fabrication (usually, no photolithographic process steps or complicated encapsulation procedures are required). Capacitive Al-p-Si-SiO_2-Ta_2O_5 structures with a 30 nm thermally grown SiO_2 and a 55 nm Ta_2O_5 layer were fabricated. The Ta_2O_5 layer has been prepared via electron-beam evaporation of 30 nm Ta followed by thermal oxidation at 515 °C for about 30 min. As contact layer, a 300 nm Al film was deposited on the rear side of the Si wafer and then, the wafer was cut into single chips of 10 mm x 10 mm size. The EIS sensor was mounted into a home-made measuring cell and sealed by an O-ring to protect the side walls and backside contact of the chip from the electrolyte solution. The contact area of the EIS sensor with the solution was about 0.5 cm^2.

The LF noise spectra were measured in buffer solutions of pH 3, pH 7, and pH 11 in accumulation, depletion and inversion regions of the EIS structure by applying different gate voltages. We have observed that the pH value of the buffer solution did not significantly influence the noise spectral density. This is in agreement with results obtained on pH ion sensitive field-effect transistors (ISFETs) previously. It has been reported that the gate-referred $1/f$ noise in a channel current of pH ISFETs is also independent of the pH, and the origin of LF noise in these ISFET devices is the trapping/detrapping of carriers at the Si-SiO_2 interface.

Moreover, it has been discussed that the ionic strength of the solution does not affect the noise magnitude of liquid-gated SWNT transistors. These results may suggest that the interface between the solution and the gate insulator does not or not significantly contribute to the $1/f$ noise. It has been observed that the gate current noise in EIS structures with thin gate oxides is increased with increasing the gate voltage or leakage current. This has been attributed to the more slow-trap states available for a trap-assisted tunneling with increasing gate voltage. The noise spectral density exhibits an $1/f^{\gamma}$ dependence with the power factor γ of 0.8 and (0.8 – 1.8) for the bare and functionalized EIS sensor, respectively.

It has been revealed that functionalization of the EIS structure with multilayers of polyamidoamine dendrimer and single-walled carbon nanotubes multilayer leads to considerable reduction of the $1/\mathbf{f}$ noise.

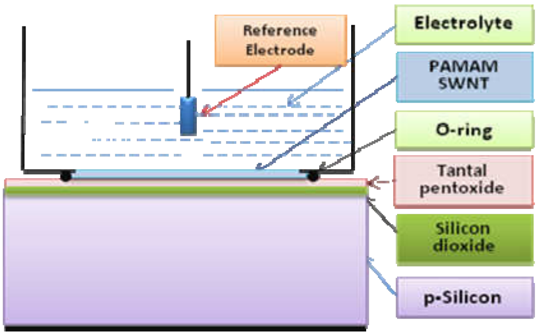

FIG. 2: Electrolyte-insulator-semiconductor (EIS) bio-sensor functionalized with a multilayer of polyamidoamine (PAMAM)/SWNTs. See details in [3].

The gate-current noise behavior in bare and functionalized EIS devices has been modeled. The experimentally observed gate-voltage dependence of the noise in capacitive EIS structures is explained by the gate-voltage-dependent changes in the occupancy of the oxide trap levels resulting in a modulation of the conductivity of current paths or charge carriers passing through the EIS structure. Physical processes in the semiconductor, insulator and electrolyte medium responsible for low-frequency charge fluctuations are discussed based on an electrical equivalent scheme for the capacitive EIS structure [4].

Thus, CNTs offer new perspectives for development of biosensors. We demonstrated that noise can be used to investigate transport phenomena and factors determining the performance of electrolyte-insulator-semiconductor structures. Biomolecules and biological object contain as backbone carbon atoms. Therefore interfacing living systems with nanocarbon materials is promising direction for biosensor applications.

---

[1] S.Vitusevich, F.Gasparyan: Low-frequency noise spectroscopy at nanoscale: carbon nanotube materials and devices. in "Carbon Nanotubes Applications on Electron Devices", edited by J.M.Marulanda, ISBN 978-953-307-496-2, InTech publisher, 257-298 (2011) .

[2] B.A.Danilchenko et al. Carbon, 49,5201 (2011).

[3] F.V.Gasparyan et al.: IEEE Sensors Journal. 11,142 (2011).

[4] F.V.Gasparyan, S.A.Vitusevich, A.Offenhäusser, M.J.Schöning. Modern Physics Letters B, 25, 831 (2011).

Towards batch fabrication of graphene based spin valve devices

T.-Y. Yang[1], A. Avsar[2], S.-K. Bae[3], J. Balakrishnan[2], F. Volmer[1], M. Jaiswal[2], Z. Yi[2,3], S.R. Ali[1], G. Güntherodt[1], B.-H. Hong[3], B. Özyilmaz[2,4,5], and B. Beschoten[1]

[1]II. Institute of Physics, RWTH Aachen University, 52074 Aachen
[2]Graphene Research Center & Department of Physics, National University of Singapore, 2 Science Drive 3, Singapore 117542, Singapore
[3]SKKU Advanced Institute of Nanotechnology (SAINT) and Center for Human Interface Nanotechnology (HINT), Department of Chemistry, Sungkyunkwan University, Suwon, 440-746, Korea
[4]Nanocore, National University of Singapore, Faculty of Engineering, Engineering Block A, EA, Level 4, Room No.27, Singapore 117576, Singapore
[5]NUS Graduate School for Integrative Sciences and Engineering (NGS), 05-01, 28 Medical Drive, Singapore 117456, Singapore

We demonstrate injection, transport and detection of spins in spin valve arrays patterned in copper based chemical vapor deposition (Cu-CVD) synthesized wafer scale bilayer graphene (BLG). We observe spin relaxation times comparable to those reported for exfoliated graphene samples demonstrating that CVD specific structural differences such as nano-ripples and grain boundaries do not limit spin transport in the present samples. Our observations make Cu-CVD graphene a promising material of choice for large scale spintronic applications.

The demonstration of micrometer long spin relaxation length in exfoliated single [1] and in bilayer [2] graphene even at room temperature (RT) and spin relaxation times in the order of nanoseconds may pave the way to realize several of the recently proposed spin-based device concepts. However, for realistic device applications it remains to be seen, if such impressive spin transport properties can also be achieved in wafer scale CVD graphene. Equally important, spin transport studies based on micromechanically exfoliated graphene sheets are often too time-consuming for the quick exploration of the basic spin properties of graphene and for testing potential device architectures. The recent progress in the Cu-based CVD growth of graphene has a strong impact on charge based graphene device applications [3]. However, CVD graphene has a large number of structural differences when compared to exfoliated graphene such as grain boundaries. In addition, the current growth and transfer process introduces residual catalysts, wrinkles and quasi-periodic nanoripple arrays. Despite all of these defects, charge mobilities in CVD graphene field effect transistors (FETs) have been comparable to what has been reported for most exfoliated graphene FETs on Si/SiO$_2$ substrates [4]. Whether this synthesis route will also play an important role for spin transport studies and large scale spin-based device applications depends on how the same defects affect the spin relaxation times.

We demonstrate spin transport in Cu-CVD grown BLG transferred on conventional Si/SiO$_2$ substrates and discuss the role of nano-ripples, a ubiquitous surface structure of Cu-CVD graphene. Spin valves are fabricated by first patterning isolated BLG stripes by means of a PMMA etch mask. A second e-beam lithography step is used to pattern the device electrodes. Next, we deposit in the same run a ~ 2 nm thick MgO layer followed by 35 nm thick Co electrodes [2]. This approach allows the batch fabrication of large arrays of lateral spin valves with a fast turn-around time well suited for studying device physics [5]. An optical image of a 5 × 5 array of such devices is shown in Fig. 1B together with a scanning electron microscopy image (Fig. 1A) of multiple spin-valve junctions showing the specific electrode configuration at a single site.

For simplicity we discuss RT spin transport results. Sweeping the in-plane magnetic field $B_{||}$ (Fig. 1C) changes the relative magnetization directions of the Co electrodes and hence the spin accumulation between the injector and detector electrodes.

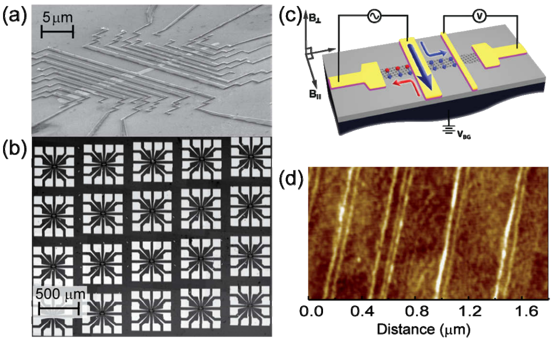

FIG. 1: A. Scanning electron micrograph of CVD spin valve sample with multiple nonlocal spin valve devices. Electrode widths range from 0.3 to 1.2 µm. B. Optical image of a 5 × 5 device array. CVD graphene allows the fabrication of large arrays of identical lateral spin valves. C. Schematics for a graphene based non-local spin-valve. D. High-resolution contact mode AFM image of CVD graphene after transfer onto a Si/SiO$_2$ wafer revealing the presence localized nanoscale ripples of high density.

This leads to a clear bi-polar non-local spin signal with a change in resistance of ΔR ≈ 0.15 Ω (Fig. 2A). The origin of the spin signal is confirmed by conventional Hanle spin precession measurements. For this purpose, the magneti-zation of the electrodes are first aligned parallel (anti-parallel) to each other by the in-plane magnetic field $B_{\|}$. This is followed by a magnetic field perpendicular to the graphene plane forcing the spins to precess about the latter (Fig. 2B). As expected, this also yields ΔR ≈ 0.15 Ω. The width of the Hanle curve determines the transverse spin relaxation time $\tau_s \approx 180$ ps.

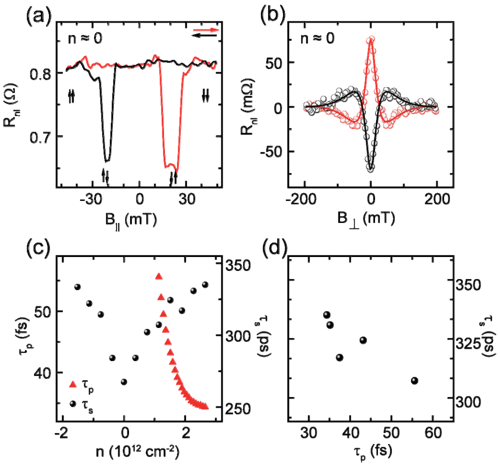

FIG. 2: Spin transport measurements on CVD BLG non-local spin-valve at room temperature. A. Bipolar spin signal obtained near the charge neutrality point. B. Corresponding Hanle spin precession measurement. C. Electron carrier density dependence of τ_s and τ_p at RT. D. Scaling of τ_s with τ_p indicates DP type spin scattering as the dominant spin scattering mechanism in CVD BLG.

We next discuss the dominant spin scattering mechanisms, which can be evaluated from the functional dependence of τ_s on τ_p. For the Elliott-Yafet (EY) mechanism, spin dephasing occurs during momentum scattering. Therefore, the spin relaxation time is directly proportional to the momentum scattering time ($\tau_s \propto \tau_p$). On the other hand, the D'yakonov-Perel' (DP) mechanism refers to the case where spin dephasing takes place between momentum scattering events, which may result from random Bychkov-Rashba like spin-orbit fields. This leads to a spin relaxation time, which is inversely proportional to the momentum scattering time ($\tau_s \propto \tau_p^{-1}$). Away from the charge neutrality point, the electric field effect in graphene provides a convenient tool to correlate τ_s and τ_p [2,5]. Provided that both quantities show a strong density dependence, such a correlation can be used to identify the limiting spin dephasing mechanism as has been demonstrated for exfoliated graphene samples. Using this approach at RT, the dominant spin scattering mechanism for exfoliated BLG spin valves with spin injection through pin-hole contacts has been identified to be of DP type. In case of CVD BLG, τ_s increases with increasing electron density *n* from 265 ps to 335 ps (Fig. 2C). However, τ_p shows a decreasing trend with increasing *n* as extracted by $\tau_p = m^*\sigma/e^2n$, where m^* is the effective mass of the charge carrier (Fig. 2C). Therefore, correlating τ_s and τ_p, we obtain for BLG an inverse scaling (Fig. 2D), i.e. $\tau_s \propto \tau_p^{-1}$. These results summarize the key findings of our experiments: At room temperature the typical spin parameters in CVD graphene differ neither quantitatively nor qualitatively from exfoliated graphene. Hence, the limiting spin dephasing mechanisms at RT remain of DP type in CVD BLG.

This result is at first surprising, since the high temperature growth of CVD graphene leads to single-crystal terraces and step edges in Cu, which in turn gives rise to additional nano-ripples in graphene after transfer. They are best seen in high resolution contact mode AFM images after transfer onto Si/SiO$_2$ substrates (Fig. 1D). Such double peak structures of 0.2 – 2 nm height, ~ 100 nm width and ~ 300 nm separation are quasi-periodic across an area (≥ 10 μm^2) much larger than the actual spin valve size. Assuming for example a channel area of ~ 1 × 1 μm^2, there will be approximately three such features present independent of their relative orientation with respect to the ferromagnetic electrodes. Thus, current growth conditions and transfer processes cause local curvature in graphene which may affect spin-orbit coupling. In carbon nanotubes (CNT), local curvature has been shown to strongly enhance spin-orbit coupling. However, it is important to note that the radius of curvatures in CNT and our samples differ greatly. The average radii of curvatures in quasi-periodic nano-ripples is ~ 200 nm, which leads to a much weaker spin-orbit coupling strength of ~ 3 μeV [5]. A comparison with the intrinsic spin-orbit coupling of graphene (~ 25 μeV) suggests that the nano-ripples in the present samples cannot set a limit for spin transport. Thus, under current growth conditions, neither grain boundaries nor nano-ripples, which are the two key differences of Cu-CVD graphene with respect to exfoliated graphene, have a limiting effect on spin transport. The main spin scattering mechanism in Cu-CVD samples seems to originate from the same source as in the case of spin valves based on exfoliated samples: adatoms, scattering from the tunneling barrier interface and the supporting substrate.

This work was supported by the Singapore National Research Foundation, by NUS NanoCore, by DFG, by JARA-FIT, and by the National Research Foundation of Korea (NRF).

---

[1] N. Tombros *et al.*, Nature 448, 571 (2007).

[2] T.-Y. Yang *et al.*, Phys. Rev. Lett. 107, 047206 (2011).

[3] S. Bae *et al.*, Nat. Nanotechnol. 5, 574 (2010).

[4] X.S. Li *et al.*, Nano Lett. 10, 4328 (2010).

[5] A. Avsar *et al.*, Nano Lett., 11, 2363 (2011).

Properties of Metal-Graphene Contacts

J. Knoch[1], Z. Chen[2], J. Appenzeller[2]

[1]Institute of Semiconductor Electronics, RWTH Aachen University
[2]Department of Electrical and Computer Engineering, Purdue University

We present a study on the metal-graphene contact properties. Utilizing a dual-gate field-effect transistor device, an energetic separation between the Fermi level and the Dirac point in the contact areas can be adjusted by applying a front gate voltage that can be compensated by an opposite large-area back-gate voltage thereby mimicing the metal induced doping effect. A back-gate voltage sweep enables identifying two distinct resistance peaks - a result of the combined impact of the graphene cones in the contact and in the channel re-gion. Comparing our experimental data with simu-lations allows extracting the coupling strength bet-ween metal and graphene and also estimating the magnitude of the metal induced doping concentra-tion in the case of palladium contacts. In contrast to conventional metal-semiconductor contacts, our simulations predict a decreased on-current for increased coupling strength in graphene field-effect transistors (GFETs).

Graphene is currently attracting increasing attention as an alternative material for future nanoelectronics devices. However, to realize high-performance devices, it is very important to form adequate, highly transmissive metal-graphene contacts. The effect of metal-semiconductor contacts on the performance of an electronic device can in principle be characterized by the position of the Fermi level with respect to the conduction/valence bands and the coupling strength between metal and semiconductor. But since the coupling strength impacts the position of the Fermi level, it is difficult to obtain information on both quantities separately. In contrast to conventional metal-semiconductor contacts, the graphene underneath a contact metal can still be influenced by a gate suggesting a moderate metal-graphene coupling. Due to the importance of contact electrodes for electronic devices it is therefore necessary to study the contact properties in much greater depth.

Dual-gate GFETs were fabricated by growing a 300nm SiO_2 film onto a heavily doped silicon substrate [1]. After exfoliation, a mono-layer of graphene is contacted using Ti/Pd/Au (0.5nm/ 20nm/20nm) electrodes followed by the deposition of a 10nm Al_2O_3 employing atomic layer de-position. The devices are finalized by the formation of a Ti/Au (1nm/40nm) front-gate electrode. Figure 1 shows a scanning electron micrograph and a schematic of the cross-sections of the devices, respectively. Device B consists of a channel that is entirely controlled by both gates and it is this fact that allows studying the contact properties.

Applying a constant front-gate voltage V_{fg} results in an energetic separation of the Dirac points in the channel and the contact area. Compensating V_{fg} in the channel by applying an appropriate opposite back-gate voltage V_{bg} leads to a V_{fg}-dependent separation ΔE_f in the contact areas. Two resistance peaks, occurring when either the Dirac point in the channel or the Dirac point in the contacts is aligned with the Fermi level, dominate the resistance R versus V_{bg} characteristics [1].

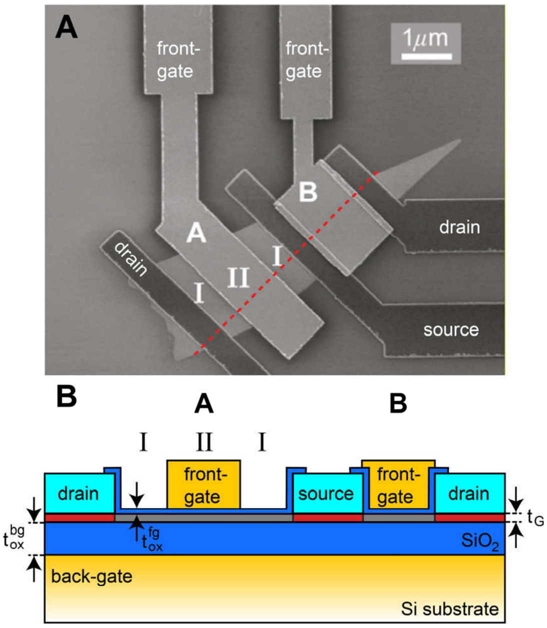

FIG. 1: A. Electron micrograph of the graphene device structure under investigation. A cross section of the devices of type A and B is shown in B.

Figure 2A displays experimental R-V_{bg}-charac-teristics for several V_{fg}. For sufficiently large ΔE_f (i.e. large V_{fg}) a second resistance peak can clearly be identified (black curve in Fig. 2A). If on the other hand, V_{fg} is too small, the second resistance peak is superimposed by the main resistance peak and thus disappears.

In order to investigate the metal-graphene coupling, simulations are performed and compared with the experimental data. Our simulations are based on a self-consistent solution of Poisson's and Schrödinger's equation. For the electrostatics a surface potential method is employed as appropriate for an ultra-thin body transistor such as a GFET. The non-equilibrium Green's function formalism (NEGF) on a finite difference grid is used to calculate the charge in and current through the device. An independent mode-space approach is employed to calculate the 2D graphene sheet by summing-up the charge and current contributions of appropriate one-dimensional subbands (see inset of Fig. 2B). The metal-graphene contacts are taken into account by attaching Buettiker probes at each node of the finite difference grid within the contact area over a certain contact length (see inset of Fig. 2B). The metal-graphene coupling strength is described by a coupling constant γ=0..1. Different coupling strengths are a result of a varying metal-graphene separation or a varying height of the potential barrier in-between the metal and the graphene. The present approach has been applied successfully to study the properties of metal-carbon nanotube contacts.

Resistance versus V_{fg}- and V_{bg}-characteristics are simulated and compared with experiments [1]. In order to reproduce the main experimental features, the back-gate voltage dependence was simulated as a function of the metal-graphene coupling strength. In particular, the second resistance peak is of interest since a comparison with the experiments allows estimating the coupling strength γ. Figure 2B shows the resulting curves for several γ. A small coupling leads only to a small modification of the graphene DOS and hence yields a pronounced second resistance peak (see Fig. 2B). Upon increasing γ, the second resistance peak becomes less pronounced and eventually vanishes completely for $\gamma>0.05$.

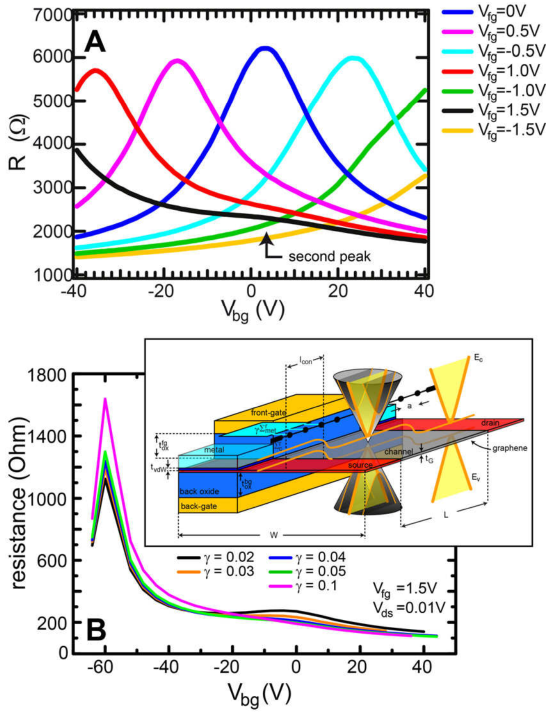

FIG. 2: A. Experimental resistance versus back-gate voltage for several V_{fg}. B. Simulated resistance versus back-gate voltage for several coupling strengths. Inset: Schematics of the simulated device structure. An independent mode-space approach is employed as illustrated by the three intersections between the cone and the planes of constant k-values quantized along the direction of W.

Comparing experimental and simulated curves, we estimate $\gamma\sim$0.02-0.03. Note that this coupling yields a life time broadening of the electronic states in the expected range of 50-75meV. With γ=0.02 we simulated R-V_{fg}- (for different V_{bg}) and R-V_{bg}-characteristics (for several V_{fg} and were able to reprocude all experimental features such as the resistance asymmetry, the decreasing peak resistance for increasing V_{bg} and in particular the broadened second resistance peak; note, that the deviation of the absolute resistance values between simulation and experiment is due to scattering in the graphene channel in the experimental case. As a result, we are now in a position to explore the impact of the coupling on the characteristics of GFETs in greater detail.

The dual-gate device structure allows creating different ΔE_f within the contacts mimicing the metal-induced doping effect of various metal-graphene work-function differences. However, the second resistance peak is only observable for sufficiently large front-gate voltages corresponsing to a ΔE_f ~125meV. For smaller ΔE_f the main and second resistance peaks cannot be observed. From the experimental data, however, ΔE_f ~100meV can be extracted consistent with the findings by other authors. This means that in a single-gate device a second resistance peak is not expected to be observable for the coupling strengths present between graphene and metal contact. This is an important finding since there has been a debate about the coupling strength and other authors have assumed a rather weak coupling which immediately implies that the second peak is smeared out completely due to a large variation of ΔE_f that goes along with a variation of the distance between metal and graphene [2]. However, if such a large variation of contact properties actually existed, a second resistance peak would not be observable even for larger ΔE_f as accessible with our dual-gate device structure. The fact that we do observe experimentally the second resistance peak by creating various ΔE_f shows that the metal-graphene contact properties are not determined by a large variation and rather weak coupling but instead can be described by a larger coupling consistent with theoretical predictions of the life-time broadening in metal-nanotube contacts.

We studied the impact of the metal-graphene coupling on the performance of GFETs with experiments and simulations. We found that the metal-graphene coupling strength is moderate resulting in a modification of the graphene DOS underneath the contacts small enough so that Fermi level pinning does not occur. On the other hand, the coupling is strong enough yielding a substantial broadening of the second resistance peak.

---

[1] J. Knoch, Z. Chen, J. Appenzeller, IEEE Trans. Nanotechnol. 10.1109/TNANO.2011.2178611.

[2] F. Xia, V. Perebeinos, Y.-M. Lin, Y. Wu, Ph. Avouris, Nature Nanotechnol., 6, 179 (2011).

Instabilities of interacting electrons on the honeycomb bilayer

M. M. Scherer[1], S. Uebelacker[1], C. Honerkamp[1]

[1]Institute for Theoretical Solid State Physics, RWTH Aachen University

In bilayer graphene, the Coulomb interaction between the electrons might lead to the breakdown of the semi-metallic state at low temperatures. In this context, we investigated the instabilities of interacting electrons on the honeycomb bilayer by means of the functional renormalization group. Taking model parameters as determined by ab-initio calculations puts the system close to the boundary between antiferromagnetic and quantum spin Hall instabilities. The energy scales for these instabilities found by this theoretical modeling are large compared to the scales revealed by recent experiments. Thus deviations from the basic model are expected to play a major role in real bilayer graphene and need to be understood in further investigations.

Recently, a number of experiments have addressed the ground state properties of bilayer graphene [1,2], trying to clarify possible signatures for the interaction between the electrons. So far, however, the precise nature of the ground state and whether the spectrum is gapped or gapless remain under controversial discussions. In theory, a number of competing instabilities of the semi-metal, e.g. toward a gapped antiferromagnetic (AF) state, a gapless nematic phase and even toward gapped topological phases as the quantum anomalous and quantum spin hall states are debated and compared to the experimental findings. All these theoretical studies indicate that the ground state properties may depend decisively on the profile of the interaction. In this context it is important to notice that the effective interaction parameters and their spatial dependence for the usual low-energy models of graphene and graphite have been calculated [3] by ab-initio techniques using the constrained random phase approximation (cRPA) that takes into account the screening due to bands further away from the Fermi level. In this work we use a functional RG (fRG) scheme [4] for an unbiased investigation of the instabilities of the Bernal stacked bilayer honeycomb lattice. Our approach can be regarded as quantitative, as we integrate out the four p_z-derived bands fully from the band edges toward the Fermi energy and as we use the ab-initio interaction parameters given in Ref. [3]. This way we strongly reduce the variety of possibilities depending on the model parameters and get closer toward a realistic picture of bilayer graphene. We start with a tight-binding model for the Bernal stacked graphene bilayer at the charge neutrality point, cf. Ref. [5] and see Fig. 1. Within both layers, we include a nearest-neighbor (n.n.) hopping with amplitude t. The interlayer hopping t_p is defined between the sites of the sublattices A in both layers that lie on top of each other. Diagonalizing the tight-binding Hamiltonian results in 4 bands. Two of them have two inequivalent quadratic band crossing points (BCP) K and K' at the Brillouin zone (BZ) corners at the Fermi level. The nonzero density of states ate the Fermi level allows interaction-driven instabilities for arbitrarily small couplings. We ignore trigonal warping terms for the time being, but comment later on the effect of perturbations on the quadratic BCPs.

As interactions, we account for an onsite repulsion U, a n.n. density-density interaction V_1 and a second-n.n. density-density interaction V_2. For these terms, cRPA values are listed in Ref. [3]. In addition, for checking the robustness of our results, we consider a third-n.n. repulsion V_3.

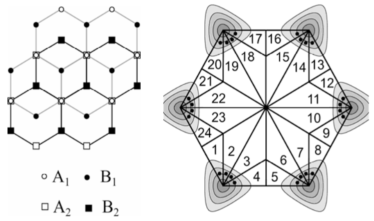

FIG. 1: Left panel: Lattice structure of bilayer graphene. Right panel: Patching scheme of the BZ in the fRG.

For the detection of instabilities, we employ a functional renormalization group (fRG) approach [4] for the one-particle-irreducible vertices of a fermionic many-body system. In this scheme, an infrared regulator is introduced into the bare propagator [4]. Here, the flowing interaction vertex is described by a coupling function V with a discretized momentum dependence for incoming and outgoing quantum numbers which include a wavevector, a Matsubara frequency, a spin projection, and band-, or orbital indices. As one is interested in groundstate properties, external frequencies are set to zero. Furthermore, in order to keep the calculations doable, we neglect self-energy corrections. This approximate fRG scheme then amounts to an infinite-order summation of one-loop particle-particle and particle-hole terms of second order in the effective interactions. It allows for an unbiased investigation of the competition between various correlations, by analyzing the components of V that create instabilities by growing large at a critical scale which can be understood as energy scale for the modification of the spectrum, typically by a gap. With the approximations mentioned above, this procedure is well-controlled for small interactions. At intermediate interaction strengths we still expect to obtain reliable results. The discretization of the interaction vertex V is implemented by dividing the BZ into N patches with constant wavevector-dependence within one patch. The representative momenta for the patches are chosen to lie at or close to the Fermi level, see Fig. 1. Each of the four momenta in the interaction vertex is additionally equipped with a sublattice index and a layer index. Momentum conservation fixes one of the four wavevectors resulting in a 44 × N3 component coupling function V.

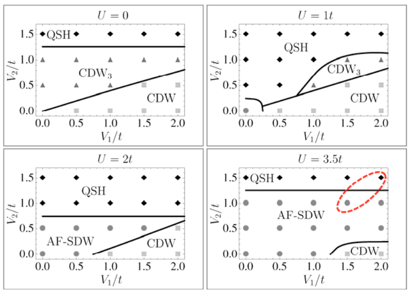

FIG. 2 : Tentative fRG phase diagram for t_p=0.1t.

Here we present fRG results at zero temperature for interlayer hopping t_p =0.1*t*. The next-neighbor hopping *t* ~ 2.8eV sets the energy unit. We study the parameter space spanned by U, V_1 and V_2 up to the cRPA parameters in Ref. [3]. We find flows to strong coupling with non-zero critical scales for all choices of non-vanishing interaction terms. By identifying the leading tendencies, i.e. the strongest class of divergent couplings, we encounter rich tentative phase diagrams as shown in Fig. 2. The observed phases are discussed in the following. *Antiferromagnetic (AF) spin density wave (SDW) instability.* In the fRG, the flow towards the AF-SDW is seen as a leading divergence of interaction components with zero momentum transfer in the spin channel with AF sublattice structure. The effective interaction is infinitely-ranged due to its sharpness in momentum space. A mean-field decoupling results in an AF spin alignment in each layer where a net spin (e.g. 'up') moment is located on the A_1- and B_2-sublattices, and an opposite net spin ('down') moment on the B_1- and A_2-sublattices.

Charge density wave (CDW) instability. Here we encounter diverging interactions in the density channel, again with zero momentum transfer. The sign-structure between the layers favors an enhanced occupancy of the A_1 and B_2- sublattices and a reduced occupancy on the B_1 and A_2 sublattices or vice versa. The electronic spectrum is gapped. *Quantum Spin Hall (QSH) instability*. This phase breaks spin-rotational symmetry, whereas time reversal symmetry is conserved. In the fRG, spin interactions with zero wavevector transfer diverge, with a sign structure that alternates between K and K' points, and between the sublattices. In a mean-field treatment, a purely imaginary Kane-Mele order parameter is induced. In the fRG, the chirality of the state comes out the same in the two layers for the same spin, i.e. there should be two edge modes with the same propagation direction per spin. Hence, the edge states would not be topologically protected, in contrast with the single-layer case [6]. We found another instability for smaller U and V2/t < 1.0, which so far seems not to be mentioned in the literature. Here a site-centered CDW tendency with a finite momentum transfer Q=K-K'=K' grows during the flow. In a variational treatment, the corresponding effective interaction is minimized by complex expectation values. These break the translational symmetry by density modulations. Each sublattice is broken up into three. This state should be observable directly in scanning tunneling experiments. The fermionic spectrum is gapless and has 4 Dirac cones near the center of the new reduced BZ. Now we discuss the relation to bilayer-graphene. In Ref. [3] the interaction parameters for single-layer graphene and graphite were estimated by ab-initio methods. We expect bilayer graphene to interpolate between these cases. The area of these ab-initio interaction parameters is shown as a red dashed line in Fig. 2 (d). In the fRG for this parameter range SDW and QSH instabilities compete. As both states have a non-zero single-particle-gap, they are compatible with the gapped experimental spectra of Refs. [1]. Note that the instability scales deduced for these realistic parameters are huge (up to ~ *t*), due to the perfect nesting between the two bands forming the quadratic BCPs. The experimental energy gaps in Refs. [1] ~ 2 meV or ~ 10^{-3} *t* are orders of magnitude smaller than the gaps one gets theoretically in this simple modeling. This poses an important question for further research. We cannot guarantee that our method still works quantitatively in this regime. However, a recent QMC analysis confirms our fRG result of high critical scales [7]. Hence, a quantitative understanding remains to be found. In summary, we have presented a fRG study of interaction driven instabilities in the honeycomb bilayer model. Besides a novel gapless CDW state, we found that using ab-initio estimates for the band-structure and non-local interaction parameters for bilayer graphene leads to a narrow competition of quantum-spin-Hall and AF-SDW instabilites, making them the two main candidates for the experimental search. Details might decide what the actual groundstate is. Important quantitative information from our study is the high energy scale for the breakdown of the gapless state. At present, these high scales are not reflected in the experiments, and more research is needed to understand this discrepancy.

---

[1] J. Velasco Jr. et al., Nature Nanotechnology 7, 156 (2012); F. Freitag et al., Phys. Rev. Lett. 108, 076602 (2012).

[2] R. T. Weitz, M. T. Allen, B. E. Feldman, J. Martin, and A. Yacoby, Science 330, 812 (2010).

[3] T. O. Wehling et al., Phys. Rev. Lett. **106**, 236805 (2011).

[4] W. Metzner et al., Rev. Mod. Phys. **84**, 299 (2012).

[5] A. H. Castro Neto et al., Rev. Mod. Phys. 81, 109 (2009).

[6] R. Raghu, et al, Phys. Rev. Lett. 100, 156401 (2008).

[7] T. C. Lang et al., *in preparation*

From Majorana Fermions to Topological Order

Barbara M. Terhal[1], **Fabian Hassler**[1], **and David P. DiVincenzo**[2]

[1]Institute for Quantum Information, Physikzentrum RWTH Aachen, 52056 Aachen
[2]Dept. Theoretical Nanoelectronics, PGI, Forschungszentrum Jülich, 52425 Jülich

While there is now striking evidence that Majorana Fermions exist in nanowire systems, there is no indication yet that they can make exceptionally coherent qubits. Our work starts with the premise that they will in fact permit us to realize “ordinary" qubits, which are susceptible to decoherence due to coupling to their environment. We propose here a network structure that will efficiently protect these qubits from decoherence, and will permit effective error correction. The nanostructured network that we propose permits a natural implementation of several equivalent many-body systems of interest for condensed matter physics: the Kitaev toric code model, and the transverse-field square-lattice Ising model with frustration.

We consider a physical system corresponding to a 2D network of links between Majorana fermions on superconducting islands. We show that the fermionic Hamiltonian modeling this system is topologically-ordered in a region of parameter space. More precisely we show how Kitaev’s toric code emerges in 4th-order perturbation theory. By using a Jordan-Wigner transformation we can map the model onto a family of signed Ising models in a transverse field where the signs (FM or AFM) are determined by additionalsign or gauge qubits. Our mapping allows an understanding of the non-perturbative regime and the phase-transition to a non-topological phase. We discuss the physics behind a possible implementation of this model and argue how it can be used for topological quantum computation by adiabatic changes in the Hamiltonian.

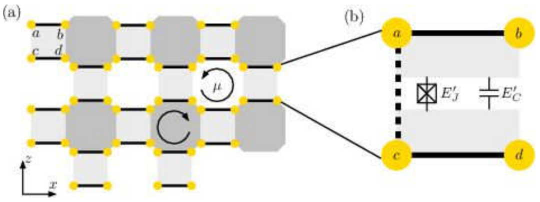

FIG. 1: (a) Toric code on a $L \times L$ *lattice with* $2L^2$ *qubits on vertices and periodic boundary conditions in both directions. The Hamiltonian is a sum over white and grey plaquette operators* $A_\mu = Z_{\mu+\hat{z}} Z_{\mu-\hat{z}} X_{\mu+\hat{x}} X_{\mu-\hat{x}}$. *(b) The Hamiltonian in which the hatched plaquettes are omitted has ground space degeneracy of 8 in the topologica; phase, hence encodes an additional qubit. The logical operators of this qubit are depicted by the blue and red lines. We can call this a white hole qubit as it is obtained by omitting plaquettes in the Hamiltonian, i.e. making a hole in the lattice, which are centered on a white plaquette.*

Kitaev’s well-known toric code [1] is a toy model Hamiltonian which demonstrates the concept of topological order in two dimensions; it features a 4-dimensional groundspace whose degeneracy is topologically-protected from sufficiently small perturbations. Thus one can imagine storing a qubit in this groundspace of such model such that at low temperature T compared to the gap, dephasing of such qubit is exponentially suppressed with growing lattice size. In the theory of quantum error correction this surface code architecture has emerged [2] as one of the more plausible routes towards fault-tolerant quantum computation. In this architecture the protection is due to the topological nature of the encoding and the sufficiently frequent error-correction. We consider the following fermionic Hamiltonian $H = H_0 + V$ where $H_0 = \sum_i^{2L^2} H_0^i$ and i labels the square islands in Fig. 1. For simplicity in the analysis, the lattice in Fig. 1 has periodic boundaries conditions in both directions (see the end of the paper for a discussion of the model on a 2D surface).

Each H_0^i acts on two fermionic modes or four Majorana modes as

$$H_0^i = -\Delta \sum_i c_a^i c_b^i c_c^i c_d^i. \qquad (1)$$

In addition we have $V = \lambda \sum_{i,j} V_{i,j}$ where i, j represents the interaction between two Majorana fermions on adjacent islands i and j, i.e. $V_{i=\mu\pm\hat{z},j=\mu\pm\hat{x}}$ equals

$$V_{\mu+\hat{z},\mu-\hat{x}} = \pm i c_b^{\mu-\hat{x}} c_c^{\mu+\hat{z}}, V_{\mu-\hat{z},\mu-\hat{x}} = \pm i c_a^{\mu-\hat{z}} c_d^{\mu-\hat{x}},$$

$$V_{\mu-\hat{z},\mu+\hat{x}} = \pm i c_c^{\mu+\hat{x}} c_b^{\mu-\hat{z}}, V_{\mu+\hat{z},\mu+\hat{x}} = \pm i c_d^{\mu+\hat{z}} c_a^{\mu+\hat{x}}. \qquad (2)$$

Clearly, all link operators $V_{\mu\pm\hat{z},\mu\pm\hat{x}}$ mutually commute. The ± signs of these terms will be fixed according to the consistent orientation in Fig. 1, i.e. the link on the top-left of a white plaquette μ represents the interaction $V_{\mu+\hat{z},\mu-\hat{x}} = i c_b^{\mu-\hat{x}} c_c^{\mu+\hat{z}}$. Physically, the signs depend on the overlap of the wave function of the Majorana bound state and thus these signs are random but fixed. We can easily find an extensive set of operators which commute with all terms of H and *which all mutually commute*. These are, first of all, weight-8 fermionic plaquette operators $\{C_\mu^g, C_\mu^w\}$ (where g(w) stands for gray (white) plaquettes μ) which are the product of four link operators around a plaquette:

$$C_\mu^{g/w} = c_d^{\mu+\hat{z}} c_a^{\mu+\hat{x}} c_c^{\mu+\hat{x}} c_b^{\mu-\hat{z}} c_a^{\mu-\hat{z}} c_d^{\mu-\hat{x}} c_b^{\mu-\hat{x}} c_c^{\mu+\hat{z}} . \quad (3)$$

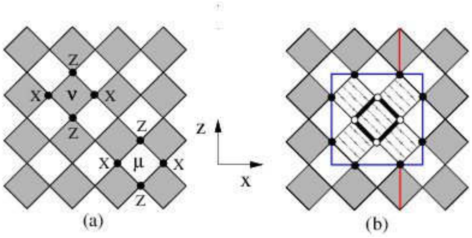

FIG. 2: (a) Toric code on a L×L lattice with 2L² qubits on vertices and periodic boundary conditions in both directions. The Hamiltonian is a sum over plaquette operators $A_v = Z_{v+\hat{z}} Z_{v-\hat{z}} X_{v+\hat{x}} X_{v-\hat{x}}$*.The lattice can be colored in checkerboard fashion so that we can speak of white and gray plaquettes. In Fig. (b) the dashed plaquettes represent plaquettes which have been omitted from the Hamiltonian, so that an additional qubit with logical operators depicted by the blue and red lines, can be encoded in the groundspace.*

ial closed loops γ_1, γ_2 and the loop operators $C_{\gamma_{1/2}} = \Pi_{(i,j)\in\gamma_{1/2}} V_{i,j}$ commute with all link $V_{i,j}$ and

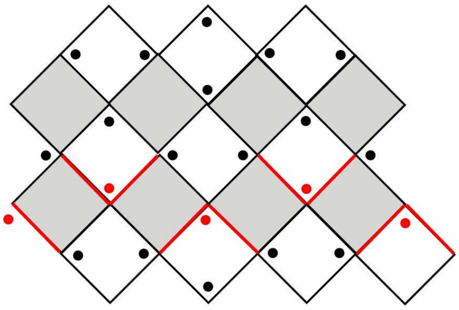

FIG. 3: The gauge qubits σ set the Ising interactions to FM (black edges) except for an AFM (red edges) loop around the torus. This AFM boundary will be felt in the FM phase, but not in the PM phase of the model leading to the topological degeneracy. A loop operator C_γ in the fermionic model becomes a product of Ising edges which winds around the torus; note that for the depicted sign pattern the loop operator which crosses this domain wall will have -1 eigenvalue.

island operators H_0^i. Thus the Hamiltonian is block-diagonal with respect to subspaces ('sectors') characterized by the eigenvalues $c_\mu^{g/w} = \pm 1$ of $\{C_\mu^{g/w}$ and $C_{\gamma_{1/2}} = \pm 1\}$. There is one linear dependency between the plaquette operators i.e. $C_{\text{all}} = \Pi_\mu C_\mu^g = \Pi_\nu C_\nu^w$ where C$_{\text{all}}$ is the (properly ordered) product of all 8*L*² Majorana operators. We can analyze the model in the perturbative regime where Δ››λ using a self-energy expansion or Schrieffer-Wolf perturbation theory. The groundspace of *H* at λ=0 is characterized by $\{c_a^i c_b^i c_c^i c_d^i = +1\}$, and thus the groundspace on each island is a two-dimensional subspace, a qubit. By a choice of convention one can define the logical *X* and *Z* operator on this island qubit as

$$X_i = i c_c^i c_a^i \equiv i c_d^i c_b^i, Z_i = i c_c^i c_d^i \equiv i c_b^i c_a^i . \quad (4)$$

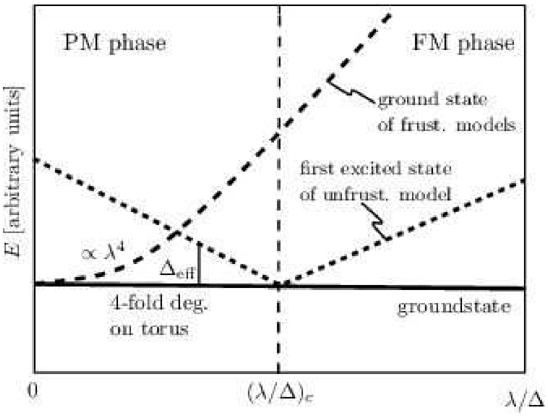

FIG. 4: Sketch of the spectrum of system as a function of λ/Δ. For small λ, the system is in a topological state with a four-fold groundstate degeneracy on the torus. In terms of the TF 2D Ising models, the topological phase corresponds to the paramagnetic side of the phase transition. The first excited states for small λ are Ising models with frustration labeled by the gauge qubits. All these models are degenerate for λ = 0 and the degeneracy lifts in forth order perturbation theory in λ, see Eq. (5). The gap of the frustrated model increases monotonically for increasing λ. The phase transition towards a state without topological order happens at the transition point (λ/Δ)$_c$ of the unfrustrated Ising model. At the point of the quantum phase transition the gap of the Ising model closes and the degeneracy of the topological states vanished.

Let $P_- = 2^{-2L^2} \Pi_{i=1}^{2L^2} (I + c_a^i c_b^i c_c^i c_d^i)$ be the projector onto this 2^{2L^2}-dimensional groundspace and $P_- + P_+ = I$. Let $V_{\pm\mp} = P_\pm V P_\mp$ and let $G_+(z=0) = P_+ G_0(z=0) P_+ = -P_+ \frac{1}{H_0} P_+$ where we have redefined *H₀* as *H₀+2ΔL²* such its lowest-eigenvalue is 0. In the self-energy expansion all terms with odd number of perturbations *V* vanish. The second-order term $V_{-+} G_+ V_{+-}$ contributes a term proportional to *I* whereas the fourth-order term

$$V_{-+} G_+ V_{++} G_+ V_{++} G_+ V_{+-} = -\frac{5\lambda^4}{16\Delta^3} \sum_{\mu=1}^{2L^2} A_\mu , \quad (5)$$

where $A_\mu = Z_{\mu+\hat{z}} X_{\mu+\hat{x}} Z_{\mu-\hat{z}} X_{\mu-\hat{x}}$, i.e. the plaquette terms of the toric code in Fig. 2. Note that $P_- C_\mu^{g/w} P_- = A_\mu^{g/w}$ and hence the four-dimensional toric code groundspace of *H* when Δ››λ lies in the $\{c_\mu^{g/w} = +1\}$ sector. When Δ=0 the ground-state of *H* is unique since we are in a state of fixed link parity $\{V_{i,j}$ = -1}. Clearly this state also lies in the $\{c_\mu^{g/w} = +1\}$ sector since each $C_\mu^{g/w}$ is a product of four link operators $V_{i,j}$.

Further details may be found in [3].

---

[1] A. Yu. Kitaev, Ann. Phys. (NY), 2 (2003).

[2] D. P. DiVincenzo, Phys. Scr. T, 014020 (2009).

[3] B. M. Terhal, F. Hassler, and D. P. DiVincenzo, arXiv:1201:3757.

A Bonding Indicator for Plane-Wave Based Quantum Simulations of Solids

V. L. Deringer[1], S. Maintz[1], A. L. Tchougréeff[1,2], R. Dronskowski[1]

[1]Institute of Inorganic Chemistry, RWTH Aachen University
[2]Poncelet Laboratory, Independent University of Moscow, Moscow Center for Continuous Mathematical Education, Russia

Despite its conceptual simplicity and long tradition in the quantum chemistry of solids, a local, orbital-based interpretation of state-of-the-art density-functional theory (DFT) computations is increasingly difficult, and the reason is simple: today, many DFT simulations rely on plane-wave (PW) basis sets, which describe solids in an efficient but ultimately *non*-chemical way. To allow for chemical interpretation of such PW-based wave functions, we propose the projected crystal orbital Hamilton population (pCOHP) technique, related to the well-known COOP and COHP approaches.

Chemistry, like all sciences, is permanently subject to change—which is advantageous in most cases. Some especially useful concepts, however, have persevered through time: one of them surely is the "chemical bond" formed (in the simplest case) between two adjacent atoms. In the solid state, this notion is especially useful because one has to deal with three-dimensionally extended crystal structures. And while chemists explore more and more complex solid-state materials (tailor-made doped semiconductors, data storage alloys, the next generations of steels, to name but a few), simple, yet powerful chemical-bonding concepts keep them from getting lost in complexity [1].

Let us start with some analogies. In a molecule, atoms combine their atomic orbitals (AOs) to build the molecular orbitals (MOs), which are usually drawn along an "energy ladder", and the resulting MO scheme is filled with electrons from the bottom to the top. In molecular hydrogen (H_2), the simplest example, two 1s orbitals (denoted ϕ) give one bonding ($\phi_1+\phi_2$) and one antibonding but empty MO ($\phi_1-\phi_2$). In solids, crystal orbitals (COs) result in a comparable way, but in this case, a tiny crystal already contains some 10^{20} atoms and even more AOs and COs. Luckily, the latter are easily condensed into a densities-of-states (DOS) plot which is the solid-state counterpart of an MO diagram. The DOS indicates *where* to find electronic states but not their *character* (are they bonding, antibonding, or do they not contribute at all?). One needs another tool to extract this crucial information.

A simple recipe was proposed by Hughbanks and Hoffmann already in 1983 [2]: Draw the bonding DOS contributions to the right side of the energy ladder, and those that are antibonding to the left. To determine if a pair of neighboring orbitals engages in bonding or antibonding interaction, one takes the overlap between the two AOs as a measure: a bonding interaction (in the hydrogen molecule, $\phi_1+\phi_2$) will give a positive overlap and thus a positive "crystal orbital overlap population" (COOP). For antibonding interaction, the COOP curve takes negative values, identifying the de-stabilizing interaction at one glance.

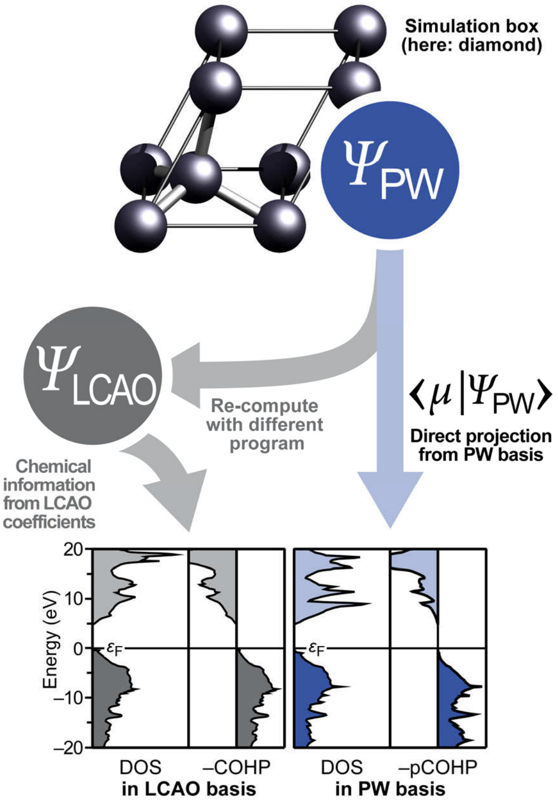

FIG. 1: Schematic depiction of the two routes leading to COHP-like analysis of plane-wave (PW) computation results. Traditional COHP and novel pCOHP routine arrive at the same result [4]: the filled states in diamond (below ε_F) are all bonding (drawn to the right), while the unoccupied states (above ε_F) are strictly antibonding.

The COOP technique has found many followers, both in chemistry and physics, and it has been built into several codes (often of the semiempirical extended Hückel type). Within DFT, an analogue was proposed in 1993 [3]: the crystal orbital Hamilton population (COHP), which takes the bonding information not from the overlap matrix elements $S_{\mu\nu} = \langle\mu|\nu\rangle$ but from the Hamiltonian matrix with $H_{\mu\nu} = \langle\mu|\hat{H}|\nu\rangle$. This time, the expectation value of the Hamiltonian $\hat{H}$ indicates the bond strength. The bottom left part of Fig. 1 shows DOS and COHP plots for diamond, a classical test case for solid-state theorists.

All such orbital-resolved approaches, however, fail when one uses one of today's plane-wave electronic-structure codes. The latter expand the crystal's electronic wavefunction into a large number of plane waves, which has several methodological advantages but practically "abolishes" the chemical picture of atoms and bonds. So far, the usual way out [5] has been to re-compute the crystal's wave function using a completely different approach, namely, tight-binding linear muffin-tin orbital theory within the atomic-spheres approximation (TB-LMTO-ASA), sketched on the left of Figure 1.

To take a different route and extract COHP-like information *directly* from a plane-wave computation, we project the plane-wave function onto an auxiliary, minimal atomic basis (for the diamond example, one s and three p orbitals at each atom suffice; see references in [4] for details). Once the overlap $<\mu|\Psi_{PW}>$ between the plane waves and an auxiliary orbital μ is known, we can reconstruct a "projected Hamilton matrix" with the elements $H_{\mu\nu} = <\mu|\hat{H}^{(PW)}|\nu>$, and then define the "projected COHP" (pCOHP) in the auxiliary basis, using a simple formulation. Applied to the diamond example, we obtain a qualitatively similar picture directly from the plane-wave computation, and the resulting pCOHP plot is shown on the right of Fig. 1. Other test cases have been described, including covalently bound, ionic and metallic systems [4].

A more current example is shown in Figure 2. Barium pernitride, BaN_2, contains dinitrogen entities in its crystal structure, and chemical intuition suggests a ionic compound to be written as $BaN_2 = Ba^{2+} + (N_2)^{2-}$, so that the pernitride unit will be isoelectronic to molecular oxygen, O=O, and contain a double bond. The bonding in the isolated O=O and $(N{=}N)^{2-}$ molecules is characterized by a half-filled set of π* orbitals giving a bond order of two [5]. Does this also hold in the solid state? It does, as is easily visualized through the pCOHP shown in Fig. 2. Note that, while the DOS contains all electronic states within the crystal structure, the pCOHP selectively shows the pairwise interaction of the nitrogen valence orbitals, so that the highest (more Ba-dominated) bands above 2 eV are visible in the DOS plot but have almost no influence on the N–N pair interaction in the pCOHP.

The charge state of the pernitride anion is not too surprising and could be expected; there is no Ba^{3+} ion. Much to the contrary, transition-metal cations *can* exist in different oxidation states: take platinum, which is encountered both as Pt^{2+} and Pt^{4+}. That being said, platinum pernitride PtN_2 can unambiguously be identified as the "+4" compound $PtN_2 = Pt^{4+} + (N_2)^{4-}$ [5], and in this case, the π* states at nitrogen are completely filled, as a quick look at the N–N COHP of PtN_2 affirms [5]. There are many more examples of energy-partitioning schemes like the COHP providing direct chemical insight into materials of current research interest.

Besides the methodological advantage of being based *directly* on the original PW wave function, where is the advantage of the newly developed pCOHP approach? It is technical but very important.

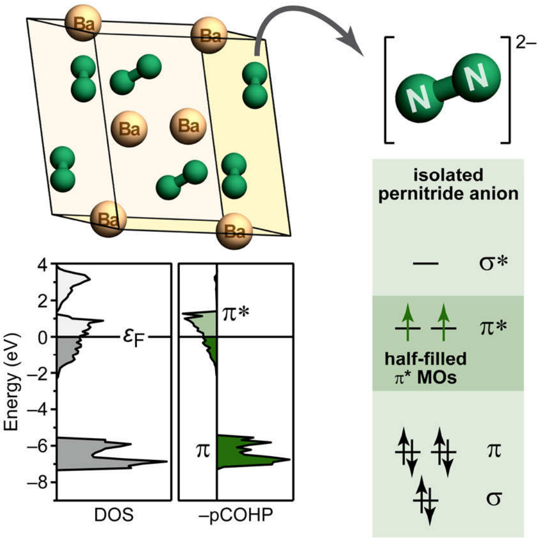

FIG. 2: A glimpse into recent work [5], re-interpreted using the pCOHP tool. The unit cell of BaN_2 is shown together with DOS and –pCOHP plots that have been computed, this time, in a plane-wave framework (VASP; see references in [4]). The scheme on the right yields the MOs of an isolated "$(N_2)^{2-}$" ion, and the correspondence to the pCOHP is obvious.

The traditional COHP, computed in the tight-binding approximation, requires densely packed crystal structures throughout. If at all possible, open or lower-dimensional structures must then be treated by including "empty spheres" [3]. Plane-wave basis sets, on the other hand, are often the method of choice for supercell computations, allowing facile access to complex scenarios like adsorption on surfaces or a chemical modeling of nanotubes. The pCOHP method promises to extend the range of possible application to many of these systems beyond densely packed solids, and we assume that a lot of interesting chemistry waits to be explored. Accordingly, a program including the pCOHP routines and more advanced projection techniques will be made public in due course.

V.L.D. gratefully acknowledges a scholarship from the German National Academic Foundation, and A.L.T. thanks the Russian Foundation for Basic Research for partial support.

---

[1] R. Hoffmann, *Angew. Chem. Int. Ed. Engl.* 26, 846 (1987).

[2] T. Hughbanks, R. Hoffmann, *J. Am. Chem. Soc.* 105, 3528 (1983).

[3] R. Dronskowski, P. E. Blöchl, *J. Phys. Chem.* 97, 8617 (1993).

[4] V. L. Deringer, A. L. Tchougréeff, R. Dronskowski, *J. Phys. Chem. A* 115, 5461 (2011).

[5] M. Wessel, R. Dronskowski, *J. Am. Chem. Soc.* 132, 2421 (2010).

Mechanism for large thermoelectric power in molecular quantum dots

S. Andergassen[1,2], T. A. Costi[3], V. Zlatić[4,5]

[1]Institut für Theorie der Statistischen Physik, RWTH Aachen University
[2]Faculty of Physics, University of Vienna, Austria
[3]Peter Grünberg Institut and Institute for Advanced Simulation, Forschungszentrum Jülich, 52425 Jülich
[4]Institute of Physics, Zagreb, Croatia
[5]J. Stefan Institute, Ljubljana, Slovenia

We investigate with the aid of numerical renormalization group techniques the thermoelectric properties of a molecular quantum dot described by the negative-*U* Anderson model. We show that the charge Kondo effect provides a mechanism for enhanced thermoelectric power via a correlation-induced asymmetry in the spectral function close to the Fermi level. We show that this effect results in a dramatic enhancement of the Kondo-induced peak in the thermopower with Seebeck coefficients exceeding 50 *μV/K* over a wide range of gate voltages.

Thermoelectric devices on the nanoscale such as quantum dots or molecules are envisaged as possible alternatives to present realizations using bulk materials. Besides the potential of low-temperature applications as on-chip cooling of microprocessors or low-temperature refrige-ration, a major advantage consists in the scalability and the high degree of tunability (e.g., via a gate voltage) allowing them to be operated at optimal thermoelectric efficiency. Here we investigate the thermal transport properties of molecular quantum dots, since a diverse range of such systems can be fabricated and investigated for interesting thermoelectric properties [1].

The theoretical description of electrical and thermal transport through quantum dots represents a challenging task in presence of strong correlation effects. A prominent example is the spin Kondo effect arising in presence of a large local Coulomb repulsion with respect to the coupling to the leads [2]. The latter dramatically affects transport, resulting, for example, in the lifting of Coulomb blockade at low temperatures for a wide range of gate voltages V_g and an enhanced conductance close to the unitary limit, $G \approx G_0 = 2e^2/h$, for symmetric coupling to the leads [3]. Recent studies showed that the spin Kondo effect only moderately affects the thermoelectric properties of quantum dots [4,5]. Here, we consider a quantum dot with an attractive onsite Coulomb interaction $U < 0$, resulting from the screening by electrons in metallic leads [6], or from local electron-phonon interactions [7,8]

$$H = \sum_{\sigma} \varepsilon_d n_{d\sigma} + U n_{d\uparrow} n_{d\downarrow} + \sum_{k\alpha\sigma} \varepsilon_{k\alpha} c^{\dagger}_{k\alpha\sigma} c_{k\alpha\sigma} + \sum_{k\alpha\sigma} (t_\alpha c^{\dagger}_{k\alpha\sigma} d_\sigma + h.c.),$$

where, ε_d is the energy of the molecular level, σ the spin, and $U < 0$ the local Coulomb interaction.The coupling to the lead $\alpha = L, R$ are denoted by $\Gamma_\alpha(\omega) = 2\pi\rho_\alpha(\omega)|t_\alpha|^2$, where $\rho_\alpha(\omega)$ is the lead density of states. At the particle-hole symmetric point the negative-*U* Anderson model in the absence of a local magnetic field can be mapped onto the positive-U symmetric Anderson model in a finite local magnetic field $B = 2\varepsilon_d + |U| = -2V_g$ [9]. The role of spin-up and spin-down states in the conventional spin Kondo effect are here played by the non-magnetic empty and doubly occupied states of the dot [10] giving rise to a charge Kondo effect, where $T_K = \sqrt{|U|\Gamma/4}\, e^{-\pi|U|/4\Gamma}$ is the relevant low-energy Kondo scale [2].

The linear response transport properties can be calculated from the single-particle spectral function of the dot $A_\sigma(\omega, T)$. The thermopower S is given by [5]

$$S = -\frac{1}{|e|T} \frac{\int d\omega\, \omega T(\omega)(-\partial f/\partial\omega)}{\int d\omega T(\omega)(-\partial f/\partial\omega)},$$

where f is the Fermi function, e the electronic charge, and $T(\omega) = 2\pi\Gamma(\omega)\sum_\sigma A_\sigma(\omega)$ the transmission with $\Gamma(\omega) = \frac{\Gamma_L(\omega)\Gamma_R(\omega)}{\Gamma_L(\omega)+\Gamma_R(\omega)}$. At low T, the Sommerfeld expansion reads

$$S(T) = -\frac{\pi^2 k_B}{3|e|} k_B T \left(\frac{\Gamma'(\varepsilon_F)}{\Gamma(\varepsilon_F)} + \frac{\sum_\sigma A'_\sigma(\varepsilon_F)}{\sum_\sigma A_\sigma(\varepsilon_F)} \right)$$

where $\varepsilon_F = 0$ is the Fermi level of the leads. In the absence of a magnetic field the spectral function is spin independent. A large S at low T can be achieved by either tailoring the band structure of the leads to give a highly asymmetric $\Gamma(\omega)$ at ε_F with a large slope $\Gamma'(\varepsilon_F)$ or tailoring correlations to yield a highly asymmetric $A(\omega)$ at ε_F with a large slope $A'(\varepsilon_F)$, or both. We focus on the latter which is robust to details of the lead density of states.

The ω- and T-dependence of the spectral function is calculated by using the numerical renormalization group (NRG) method [11]. At $T = 0$ the spectral function (Fig. 1) with a Kondo resonance of width $O(T_K)$ and two Hubbard satellite peaks is symmetric at $V_g = 0$. A finite V_g induces a splitting analogous to a

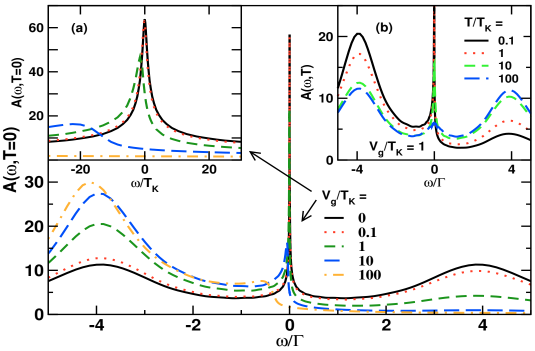

Figure 1: Spectral function for U/Γ = -8

magnetic field in the conventional spin Kondo effect, with n_d changing substantially from its “perfectly screened” value of $n_d = 1$ [12]. The resulting pronounced asymmetry in the spectral function with a large slope at ε_F for both spin components (reduced for $T \gg T_K$) is the origin of the large values of S.

Figure 2 shows the dramatic enhancement of the Seebeck coefficient induced by a finite $V_g \geq T_K$ exceeding 50 $\mu V/K$ for $V_g \geq 2T_K$. The maximum of S occurs on a temperature scale which correlates with V_g and is therefore highly tunable. Corresponding Seebeck coefficients for $U > 0$ in the Kondo regime are insignificant (see inset). The large enhancement in S is due to the correlation-induced asymmetry in the spectral function at finite V_g. At low T

$$S(T) = -\frac{\pi\gamma T}{|e|}\cot(\pi n_d / 2)$$

with $\gamma T \ll 1$, and γ the linear coefficient of specific heat [2]. A finite $V_g \sim T_K$ polarizes the charge Kondo state, leading to $n_d \sim 2$ for $V_g > 0$. This enhances S by a factor cot $(\pi n_d/2) \gg 1$.

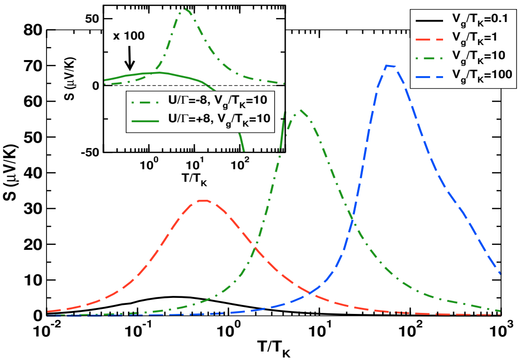

Figure 2: Thermopower S

The V_g-dependence of S and electrical conductance G is shown in Fig. 3. Except at $T \leq T_K$, a large Seebeck coefficient exceeding 50 $\mu V/K$ can always be realized by a suitable choice of V_g. By tuning the V_g to positive or negative values about the charge Kondo state at $V_g = 0$ one can realize the p-type or n-type legs of a thermoelectric device. Note the absence of a Kondo plateau in $G(V_g)$ at $T \ll T_K$, which contrasts with the $U > 0$ case, and the rapid drop on a scale $V_g \sim T_K$ of $G(V_g)$ due to the suppression of the Kondo state by the finite V_g acting as a magnetic field in the conventional Kondo effect [13,7].

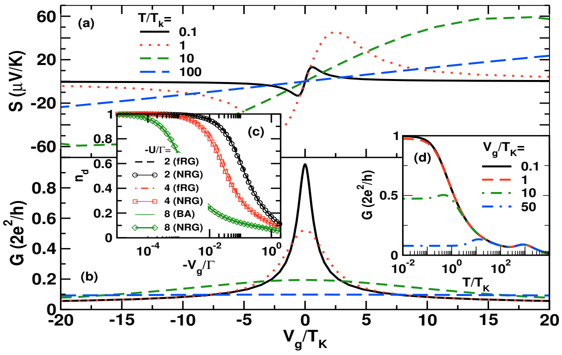

Figure 3: Thermopower S, conductance G, and dot occupation number n_d

For $T = 0$, we compared the NRG results for occupation numbers n_d with those from functional renormalization group (fRG) [14] and Bethe ansatz (BA) [15] techniques.

Results for the power factor $P = S^2G$ relevant for future comparison with experiments show that for each V_g the power factor exhibits a maximum at a temperature which is related to V_g [16]. As a consequence, high tunability of the device allows for large power factors at virtually any temperature by a suitable choice of gate voltage.

[1] P. Reddy et al., Science 315, 1568 (2007).

[2] A.C. Hewson, The Kondo Problem To Heavy Fermions, Cambridge Studies in Magnetism (Cambridge University Press, Cambridge, UK, 1997).

[3] L. I. Glazman and M. E. Raikh, JETP Lett. 47, 452 (1988); T.-K. Ng and P. A. Lee, Phys. Rev. Lett. 61, 1768 (1988); D. Goldhaber-Gordon et al., Phys. Rev. Lett. 81, 5225 (1998); S. M. Cronenwett et al., Science 281, 540 (1998); W. van der Wiel et al., Science 289, 2105 (2000).

[4] T. A. Costi & V. Zlatić, Phys. Rev. B 81, 235127 (2010); R. Scheibner et al., Phys. Rev. Lett. 95, 176602 (2005).

[5] T-S. Kim & S. Hershfield, Phys. Rev. Lett. 88, 136601 (2002).

[6] I. E. Perakis and C. M. Varma, Phys. Rev. B 49, 9041 (1994); T. A. Costi, Phys. Rev. B 55, 6670 (1997).

[7] P. S. Cornaglia et al., Phys. Rev. Lett. 93, 147201 (2004).

[8] A. C. Hewson et al., Eur. Phys. J. B 40, 177 (2004).

[9] G. Iche and A. Zawadowski, Solid State Commun. 10, 1001 (1972); A. C. Hewson et al., Phys. Rev. B 73, 045117 (2006).

[10] A. Taraphder and P. Coleman, Phys. Rev. Lett. 66, 2814 (1991).

[11] K. G. Wilson, Rev. Mod. Phys. 47, 773 (1975); R. Bulla, T. A. Costi, and T. Pruschke, ibid. 80, 395 (2008).

[12] A. Rosch, T. A. Costi, J. Paaske, and P. Wölfle, Phys. Rev. B 68, 014430 (2003).

[13] J. Koch et al., Phys. Rev. B 75, 195402 (2007).

[14] W. Metzner, M. Salmhofer, C. Honerkamp, V. Meden, and K. Schoenhammer, Rev. Mod. Phys. 84, 299 (2012).

[15] A. M. Tsvelick and P. B. Wiegmann, Adv. in Physics 32, 453 (1983); N. Andrei, Phys. Lett. 87A, 299 (1982).

[16] S. Andergassen, T. A. Costi and V. Zlatić, Phys. Rev. B 84, 241107(R) (2011).

Spin-quadrupoletronics: transport and accumulation of spin anisotropy

M. Baumgärtel[1], M. Hell[1], S. Das[3], M. R. Wegewijs[1,2]

[1] Peter Grünberg Institut-2, Forschungszentrum Jülich, 52425 Jülich
[2] Institute for Theory of Statistical Physics, RWTH Aachen University
[3] Department of Physics and Astrophysics, University of Delhi, India

We demonstrate that the description of an elementary situation in spintronics, the detection and manipulation of an impurity spin using a quantum-dot spin-valve, requires a new physical concept, bringing together the fields of molecular magnetism and spintronics. We show that besides spin-polarization, *spin anisotropy* can be also transferred to an *spin-isotropic* system by *transport* of spin quadrupole moment. We derive a quadrupole moment current operator and continuity equation and illustrate its crucial importance for a spin valve structure consisting of two ferromagnets coupled to a quantum dot probing an impurity spin. For large polarizations of the ferromagnets – envisaged in spintronics – the quadrupole back-action on the spin significantly affects the *charge current* through the quantum dot and plays a vital role in its physical description.

The field of spintronics is driven by the desire to use the intrinsic dipole moment of the electron as an information carrier. Great progress has been achieved in understanding the accumulation of spin dipole moments, their manipulation by, e.g., current induced spin torques, and their readout by electrical transport measurements. Recently these studies have been extended to quantum dot (QD) devices. In particular the predicted [1] interplay of virtual tunneling, spin polarization and Coulomb interaction has been experimentally demonstrated [2]. In molecular magnetism, in addition to the spin-dipole moment, the spin-orbit induced spin anisotropy is known to be of great importance. This anisotropy provides an energy barrier preventing unwanted spin reversal in molecular scale spin manipulation. This is a key motivation for further progress in synthesis of ever more anisotropic molecules. This spin anisotropy in a given quantum state of a system can be quantified by the average of the quadrupole moment tensor operator

$$\hat{Q}_{ij} = \frac{1}{2}\left(\hat{S}_i\hat{S}_j + \hat{S}_j\hat{S}_i\right) - \frac{1}{3}\hat{\mathbf{S}}^2\delta_{ij} \qquad (1)$$

where $\hat{S}_i$ is the *i=x,y,z* component of the spin operator $\hat{\mathbf{S}}$. This report illustrates that in a simple QD, which by itself is spin isotropic, a non-equilibrium spin-quadrupole moment (SQM) can accumulate by connecting it to ferromagnets. This is a new concept, both in spintronics – where so far only spin-dipole currents have been considered – as well as in molecular magnetism – where spin-anisotropy is not a transport quantity.

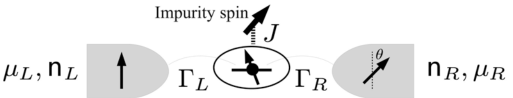

FIG. 1: Quantum dot spin-valve, exchange-coupled to an impurity spin.

To illustrate this we consider the simplest realization of an isotropic, high-spin QD in a spintronics setup sketched in the above figure. The high-spin quantum dot is composed of a single redox orbital that is tunnel coupled to noncollinearly polarized ferromagnets (FM). An electron visiting this orbital is ferromagnetically exchange coupled to impurity spin (s´=½) with an isotropic interaction *J*>0. This represents several experimentally feasible situations, e.g., a QD coupled to a magnetic impurity, a fullerene, an asymmetrically gated double QD or even a hyperfine coupled single nuclear spin in a molecule. Close to the QD resonance, only two adjacent discrete electronic states dominate the transport, giving a Hamiltonian with a nonzero spin in both these charge states:

$$H = \varepsilon\hat{N} + U\hat{N}_{\uparrow}\hat{N}_{\downarrow} - J\,\hat{\mathbf{s}}\cdot\hat{\mathbf{s}}'. \qquad (2)$$

Here ε denotes the orbital energy, tuneable by a gate voltage, and $\hat{N} = \sum_\sigma \hat{N}_\sigma$ the occupation operator ($\hat{N}_\sigma = d^\dagger_\sigma d_\sigma$ with σ=↑,↓) and $\hat{\mathbf{s}} = \frac{1}{2}\sum_{\sigma\sigma'} d^\dagger_\sigma \sigma_{\sigma\sigma'} d_{\sigma'}$ the electron spin (Pauli-matrix vector σ). We consider the limit of weak tunnel coupling Γ_r, finite transport bias V_b and strong local interactions, $U \gg J \gg V_b$, $T \gg \Gamma_r$; where the electron number N is restricted to 0 or 1 (due to the Coulomb charging energy U) with spin ½ and 1, respectively (the N = 1 singlet state is inaccessible). Spintronics comes in through the tunnel coupling to noncollinearly polarized ferromagnets (FM) with a energy-independent, spin polarized density of the states k (DOS) $\nu_{r\tau}$ where τ=↑,↓ refers to the spin of the electrons along the polarization vector $\mathbf{n}_r$ of he respective FM electrode $r = L,R$. The tunneling through junction r is assumed to conserve spin and occurs with an amplitude t_r, thereby setting the tunnel rates Γ_r. The electrodes are held at temperature T and the transport is controlled by (i) biasing the electro-chemical potentials $\mu_r = \pm V_b/2$, (ii) gating the QD, i. e. $\varepsilon = -V_g$ and (iii) adjusting the relative polarization angle between $\mathbf{n}_L$ and $\mathbf{n}_R$.

To describe the detection of the impurity spin $\mathbf{s}'$ by the charge transport one would expect that the change in the particle number and the spin of the QD would provide the complete physical picture. The continuity equations $\dot{\hat{N}} = \sum_r \hat{I}_N^r$ and $\dot{\hat{\mathbf{S}}} = \sum_r \hat{\mathbf{I}}_\mathbf{S}^r$ relate these changes to the injected particle and spin currents that emanate from the FM, respectively.

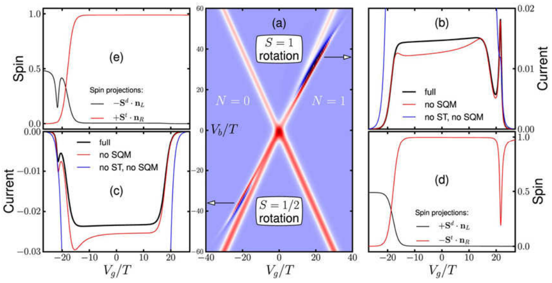

FIG. 2: (a) dI/dV_b vs. V_g; V_b (red = positive, dark blue = negative) for $\Gamma_\mathrm{L} = 2\Gamma_{\mathrm{R}\text{-}0.2\mathrm{T}}$, D=U=500T, polarization strength 99% and angle 0.99π. (b),(c): I vs. V_g for V_b = ±36T normalized to the maximal current achievable for V_b 0 and $^{=}$zero angle. Black: full result, red: neglecting the SQM, blue: additionally neglecting the spin-transfer (ST). (d),(e): spin accumulations $\pm\mathbf{S}^\mathrm{d}\mathbf{n}_\mathrm{T}$ and $\mp\boldsymbol{S}^t\mathbf{n}_R$ in the N = 0,1 charge state, resp. vs. V_g.

These derive from the conservation of the charge and spin of the total system in a tunneling process and their local conservation on the spin-isotropic QD. This picture of the spintronic operation is however, incomplete: the average of the local quadrupole tensor (1) can become nonzero even though electrons only have an intrinsic spin-dipole moment. Still, transport of quadrupole moment does occur: the transport of correlated pairs of dipoles from the spin-anisotropic FM results in transport of quadrupole moment onto the QD. Thus, in the spin triplet state the QD becomes anisotropic in addition to spin polarized. Similar to spin-polarization, this spin-quadrupole accumulation is caused by injection: from quadrupole conservation during tunneling, a continuity equation follows:

$$\dot{\hat{\mathbf{Q}}} = \sum_r \hat{\mathbf{I}}_\mathbf{Q}^r, \qquad (3)$$

It indicates that the spin-quadrupole currents associated with electrodes r = L,R are responsible for this injection: $\hat{\mathbf{I}}_\mathbf{Q}^r = \frac{1}{2}(\hat{\mathbf{I}}_\mathbf{S}^r\hat{\mathbf{S}} + \hat{\mathbf{S}}\hat{\mathbf{I}}_\mathbf{S}^r) - (\frac{1}{3}\hat{\mathbf{I}}_\mathbf{S}^r \cdot \hat{\mathbf{S}})\hat{1} + \text{h.c.}$. This is a new, independent transport quantity that must be treated on the same footing with the charge currents $\hat{I}_N^r$ and spin-currents $\hat{\mathbf{I}}_\mathbf{S}^r$. To obtain this non-equilibrium accumulation of charge, spin and SQM on the QD the reduced density operator p of the QD must be calculated from a kinetic (generalized master) equation describing its time-evolution. One can specify p by the quantum-statistical averages of a complete set of physical operators: for our model these are the charge occupancies p^d, p^t of the doublet and triplet state respectively, the corresponding spin accumulations $\boldsymbol{S}^d$, $\boldsymbol{S}^t$ and the triplet SQM $\boldsymbol{Q}^t$. A diagrammatic calculation to the first order in Γ_r gives the following coupled equations:

$$\dot{p}^d = -3\gamma^+ p^d + 2\gamma^- p^t - 2\gamma^+ \cdot \mathbf{S}^d + 2\gamma^- \cdot \mathbf{S}^t$$

$$\dot{p}^t = 3\gamma^+ p^d - 2\gamma^- p^t + 2\gamma^+ \cdot \mathbf{S}^d - 2\gamma^- \cdot \mathbf{S}^t$$

$$\begin{aligned}\dot{\mathbf{S}}^d = &-\frac{1}{2}\gamma^+ p^d + \frac{1}{3}\gamma^- p^t - 3\gamma^+ \mathbf{S}^d + \gamma^- \mathbf{S}^t \\ &+ \mathbf{S}^d \times \beta + 2\,\mathbf{Q}^t \cdot \gamma^-\end{aligned}$$

$$\begin{aligned}\dot{\mathbf{S}}^t = &\frac{4}{2}\gamma^+ p^d - \frac{4}{3}\gamma^- p^t + 4\gamma^+ \mathbf{S}^d - 2\gamma^- \mathbf{S}^t \\ &+ \mathbf{S}^t \times \beta - 2\,\mathbf{Q}^t \cdot \gamma^-\end{aligned}$$

$$\begin{aligned}\dot{\mathbf{Q}}^t = &\left[\frac{4}{2}\left(\mathbf{S}^d\gamma^+ + \gamma^+\mathbf{S}^d\right) - \frac{4}{3}(\mathbf{S}^d \cdot \gamma^+)1\right] \\ &- \left[\frac{1}{2}\left(\mathbf{S}^t\gamma^- + \gamma^-\mathbf{S}^t\right) - \frac{1}{3}(\mathbf{S}^t \cdot \gamma^-)1\right] \\ &- 2\gamma^-\mathbf{Q}^t + \mathbf{Q}^t \times \beta - \beta \times \mathbf{Q}^t\end{aligned}$$

Here $\gamma^\pm$ and $\gamma_r^\pm$ are charge (scalar) and spin (vector) tunneling rates and β is the electrically tunable exchange field arising from Coulomb interaction and coherent virtual electron tunneling processes into FMs [1], causing a precession of the spin-accumulations $\boldsymbol{S}^d$ and $\boldsymbol{S}^t$. See [3] for details. In the stationary limit the time-derivatives on the left hand sides are zero and these explicit equations reveal that the spin-dipole accumulations couple to the spin-quadrupole accumulation (through the last term $\pm 2\boldsymbol{Q}^t$) which is driven by quadrupole current injection from the ferromagnets. This finite SQM results in a back-action on the spin-accumulations, and thereby also on the charge occupancies and the measurable charge current through each junction r:

$$I^r = 3\gamma_r^+ p^d - 2\gamma_r^- p^t + 2\gamma_r^+ \cdot \mathbf{S}^d - 2\gamma_r^- \cdot \mathbf{S}^t. \qquad (4)$$

Whenever large spin polarizations $(\nu_{r\uparrow} - \nu_{r\downarrow})/(\nu_{r\uparrow} + \nu_{r\downarrow})$ (in excess of ~ 50%) are involved – a central objective in spintronics – a correct description of the charge and spin dynamics requires full account of the transport of the spin-quadrupole moment. We checked that failing to do so may result in unphysical particle currents running opposite to the voltage bias direction. The above theory describes the detection of the side-coupled impurity spin by nonlinear transport measurements: Fig. 3(a-c) depicts a sharp, anomalous current peak in the thermally broadened regime where usually the SET current through the QD switches on. Fig. 3(d)-(e) show that in both cases the current peak directly measures a significant precession of the spin accumulation on the QD, which is actuated by the exchange field β: It is aligned perpendicular to the spin accumulation for (i) asymmetric tunnel coupling and (ii) similar FMs with nearly anti-parallel polarizations. Furthermore, (iii) the onset of the Coulomb blockade suppresses the spin relaxation, allowing for a highly voltage-sensitive resonant spin-precession effect.

[1] J. König and J. Martinek, PRL 90, 166602 (2003).

[2] J. R. Hauptmann et al., Nature Phys. 4, 373 (2008).

[3] M. Baumgärtel et al., PRL, 107:087202, (2011).

Time scales in the dynamics of an interacting quantum dot

L. D. Contreras-Pulido[1], J. Splettstoesser[1], M. Governale[2], J. König[3], and M. Büttiker[4]

[1] Institut für Theorie der Statistischen Physik, RWTH Aachen University
[2] School of Physical and Chemical Sciences and MacDiarmid Institute for Advanced Materials and Nanotechnology, Victoria University of Wellington, Wellington 6140, New Zealand
[3] Theoretische Physik, Universität Duisburg-Essen & CeNIDE, D-47048 Duisburg
[4] Département de Physique Théorique, Université de Genève, CH-1211 Genève 4, Switzerland

We consider a single-level quantum dot with Coulomb interaction, tunnel coupled to a single electronic reservoir and driven out of equilibrium by a fast switching. We analyze the time scales governing the exponential decay of the quantum dot states to the new equilibrium. In addition to the charge and spin relaxation times there is a third time scale which is independent of the level position and the Coulomb interaction, emerging in the time evolution of quantities sensitive to two-particle processes. We propose different methods to read out these rates. We compare the charge relaxation rate of the quantum dot, playing the role of a quantum capacitor, to the inverse *RC* time in linear response to an ac modulation.

The control and manipulation of single electrons in mesoscopic systems constitutes one of the key ingredients in nanoelectronics. A single-level quantum dot (QD) coupled to a single electronic reservoir takes the role of a mesoscopic capacitor [1]. It can serve as the building block of high-frequency single-electron sources, see for example [2], with potential applications in quantum electron optics experiments, in metrology, and in quantum information processing based on fermionic systems. It is therefore important to study the response characteristics of such a system to an external driving. In some of the realizations [2], the Coulomb interaction is weak; however, in small-sized QDs the Coulomb repulsion is, in general, strong and it is therefore desirable to include it in the theoretical analysis.

We study the relaxation behavior of a QD weakly tunnel coupled to a single electronic reservoir. We focus here on the exponential decay of the dot states towards a new equilibrium after the dot has been brought out of equilibrium by applying, e.g., a step pulse to the gate voltage [3,4], see Fig. 1. The dot is assumed to have a single spin-degenerate level with energy ε; two electrons occupying the dot are subject to the Coulomb repulsion U. The coupling to the lead is taken to be spin- and momentum-independent; it is characterized by the tunneling rate Γ.

We are interested in the probability of finding the QD empty (p_0), single occupied with spin σ =↑, ↓ (p_σ) or double occupied (p_d), after having integrated out the reservoir degrees of freedom.

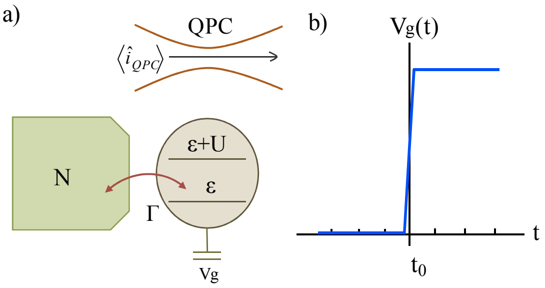

FIG. 1: a) Schematics of the single level QD with Coulomb interaction, U, coupled to a lead with a tunneling strength Γ. The dot occupations can be measured via the current passing through a nearby quantum point contact (QPC). b) The system is brought out of equilibrium by a fast change of, e.g., the gate voltage at $t = t_0$.

The time evolution of these probabilities, stored in the vector $\mathbf{P} = (p_0, p_\uparrow, p_\downarrow, p_d)^{\mathrm{T}}$, obeys the generalized master equation $\dot{\mathbf{P}}(t) = \int_{t_0}^{t} dt' \mathbf{W}(t-t')\mathbf{P}(t')$. Here, the kernel $\mathbf{W}(t\text{-}t')$ describes transitions between dot states due to tunneling to the lead. After the switching time t_0, it depends on the time difference $t\text{-}t'$ only, since the Hamiltonian is then time-independent. We are interested in the exponential decay of the system, which matters at times t distant from t_0 such that the difference $t\text{-}t'$ is much lager than the support of the kernel $\mathbf{W}(t\text{-}t')$. The solution of the kinetic equation is found as $\mathbf{P}(t) = \exp(\mathbf{A}t)\mathbf{P}^{in}$, where $\mathbf{P}^{in}$ is the initial probability vector at the switching time t_0. The matrix $\mathbf{A}$, governing the relaxation, is directly related to the Laplace transform of the Kernel and contains Markovian and non-Markovian effects. We obtain $\mathbf{A}$ by means of a real-time diagrammatic expansion on the tunneling strength, considering processes up to second order in Γ.

The four eigenvalues of $\mathbf{A}$ are the negative of the relaxation rates of the system. One of them equals zero and relates to the equilibrium state. In first order in Γ, the charge and spin relaxation rates, γ_n and γ_s, and a third rate which is fully energy independent, γ_m, are given by

$$\gamma_n = \Gamma\left[1 + f(\varepsilon) - f(\varepsilon + U)\right] \qquad (1)$$

$$\gamma_s = \Gamma\left[1 - f(\varepsilon) + f(\varepsilon + U)\right] \qquad (2)$$

$$\gamma_m = 2\Gamma \qquad (3)$$

with the Fermi function $f(x)$. The quantities decaying with only one of these rates are obtained from the left eigenvectors of **A**: for example the charge decays like

$$<n>(t) = <n>^{in}\, e^{-\gamma_n t} + <n>^{eq}\, (1-e^{-\gamma_n t}),$$

from its initial to its equilibrium ("eq") state.

The relaxation rates, Eqs. (1) to (3), are shown in Fig. 2. Charge and spin relaxation rates depend on the level position ε and differ from each other due to Coulomb interaction. In the region of single occupation, $-U < \varepsilon < 0$, γ_n is enhanced, since the twofold-degenerate single level increases the possibilities to relax to the singly occupied state. In the same region, γ_s is suppressed since spin-flip processes are not allowed. The energy-independent rate γ_m appears in the dynamics of quantities related with *two-particle processes*.

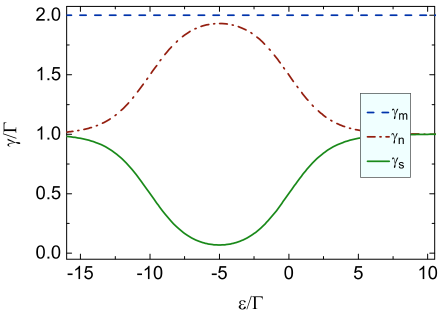

FIG. 2: Relaxation rates of the single level QD, in first order in Γ, for U = 10 Γ and temperature k_BT = 1.5 Γ.

For instance, the mean squared deviations of the charge from its equilibrium value relax to equilibrium partly with the charge relaxation rate γ_n and partly with the rate γ_m. The same is true for the relaxation of the charge when the QD is proximized by an extra superconducting reservoir, which naturally couples electrons and holes [4].

Corrections of the relaxation rates in second order in the tunnel coupling, Γ, are induced by real cotunneling processes and by virtual processes leading to the renormalization of *ε* and Γ. Cotunneling processes influencing the charge relaxation are due to coherent transitions between zero and two particles in the QD; the spin relaxation rate is affected by cotunneling corrections due to spin-flip processes. As a result of the sum of the corrections, both rates are enhanced [3]. In contrast, the rate γ_m does not get corrected at all [4]. This lack of second-order correction confirms the fact that the relaxation with γ_m is not sensitive to the Coulomb interaction.

We finally propose schemes to address the independent relaxation of the full probability vector with only one of the different rates and to further read out these rates [4]. Infinitesimal variations of a magnetic field yield a dynamics of the probability vector **P** governed by the spin relaxation rate. Similarly, infinitesimal variations of the gate potential lead to a decay governed by the rate γ_n.

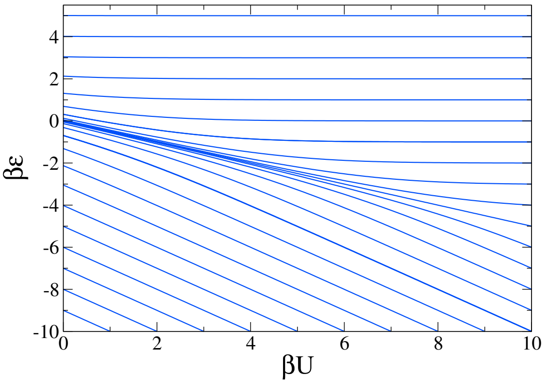

FIG. 3: Field lines describing variations of ε and U that lead to a response of the system with the rate γ_m only.

However, in order to obtain a dynamics of **P** governed by the rate γ_m, variations of the gate need to be accompanied by a modulation of the two-particle term, namely the Coulomb interaction. These variations of *ε* and *U* are visualized in the form of field lines in Fig. 3. If the initial and final values for *U* and *ε* lie on the same field line, the relaxation is governed only by γ_m. This is valid both for the linear and the nonlinear regime. Generic variations of *ε* and *U* deviating from the field lines, result in a relaxation of **P** given by two rates: γ_n and γ_m. Nevertheless, we find that, if merely the occupation probability of a single dot state is read out, variations of the gate voltage alone can be sufficient to obtain either a behaviour governed purely by γ_m or by γ_n, depending on the initial condition and the modulation amplitude. The readout is then achieved by measuring the current passing through a quantum point contact (QPC) located nearby the system, Fig. 1 a).

Since the single-level QD takes the role of a capacitor, it is intriguing to compare the charge relaxation rate discussed above with the inverse of the *RC*-time, extracted from the frequency-dependent response to a slow harmonic modulation of the gate potential [3]. As expected from the classical capacitor, the two rates are equal in lowest order in Γ and they are given by Eq. (1). Importantly, the rates are found to differ in second order in Γ, due to cotunneling processes leaving the state of the dot unchanged. Remarkably, this is in contrast with the result for a classical capacitor, in which both rates are equal.

---

[1] M. Büttiker, H. Thomas and A. Prêtre, Phys. Lett. A 180, 364 (1993).

[2] G. Fève et al., Science 316, 1169 (2007).

[3] J. Splettstoesser, M. Governale, J. König and M. Büttiker, Phys. Rev. B 81, 165318 (2010).

[4] L. D. Contreras-Pulido, J. Splettstoesser, M. Governale, J. König and M. Büttiker, Phys. Rev. B 85, 075301 (2012).

Structural and Magnetic Properties of Phase-Change Materials doped with magnetic impurities

Y. Li[1]**, R. Mazzarello**[1,2]

[1]Institute for Theoretical Solid State Physics, RWTH Aachen University
[2]JARA-FIT and JARA-HPC

Phase-change materials are technologically important due to their ability to undergo fast and reversible transitions between the amorphous and crystalline phase upon heating. In this work we have investigated the structural, electronic and magnetic properties of $Ge_2Sb_2Te_5$, a prototypical phase-change material, doped with Fe impurities, by *ab initio* simulations. We have considered both the amorphous and the crystalline (hexagonal and cubic) phases of $Ge_2Sb_2Te_5$. We have shown that, in the amorphous phase, the magnitude of the local magnetic moments of the Fe impurities is reduced with respect to the crystalline phase: these findings could explain the magnetic contrast between the two phases observed in recent experiments.

The technological importance of Chalcogenide phase-change materials (PCMs) for storage applications stems from the stability of their amorphous and crystalline phases at room temperature, the optical and electronic contrast between the two phases and the high crystallization speeds [1]. PCMs are currently used to store information in rewritable optical media (CD, DVD, Blu-Ray Disc) and electronic Non-Volatile Memories (NVMs). Among PCMs, $Ge_2Sb_2Te_5$ (GST) stands out for its superior performance for NVMs applications.

Recent experimental works and first-principles studies based on density functional theory (DFT) [2,3] have shed light on the structural and electronic properties of the relevant phases of GST, although several questions about the mechanisms responsible for the electronic contrast and the fast crystallization remain open.

Recently, the first magnetic PCM was synthesized by a pulsed laser deposition method [4]. The authors of this paper showed that GST doped with Fe impurities displays phase-change features; moreover, at low temperatures, both the crystalline and amorphous phases are ferromagnetic but have different saturation magnetization (smaller in the amorphous state), thus exhibiting a pronounced magnetic contrast. These findings open up the perspective of exploiting the phase-change behavior of doped GST for fast magnetic switching in future spintronic devices.

We have carried out an *ab initio* DFT study of the structural, electronic and zero-temperature magnetic properties of the stable hexagonal GST (h-GST), the metastable cubic GST (c-GST) and amorphous GST (a-GST) doped with Fe impurities to shed light on the microscopic origin of the contrast [5]. The cubic phase (shown in Fig. 1, together with h-GST) is technologically important, for, upon fast laser irradiation, GST crystallizes into this phase. The supercell method was used: large models of GST containing 199–216 atoms and 7% Fe concentration were employed to describe all the three phases. The Quantum Espresso [6] and CP2K [7] DFT packages were used.

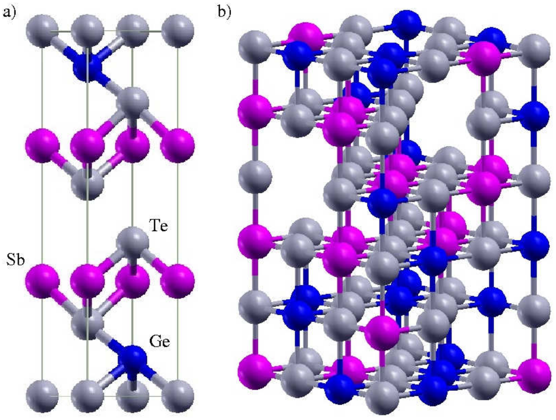

FIG. 1: a) Hexagonal phase of GST. b) Cubic rocksalt phase of GST: Te atoms occupy one sublattice, whereas 40% Ge, 40% Sb and 20% vacancies are randomly arranged in the second one.

The first step was the study of the energetics and the magnetic properties of a single Fe impurity sitting at various substitutional and interstitial sites in both crystalline phases. The most favorable sites turn out to be the Ge and Sb substitutional sites. In these two configurations, the system has large total magnetic moments of 4-5 μ_B. Then we relaxed big models of Fe-doped h-GST and c-GST containing 200-216 atoms and a 7% concentration of Fe placed randomly at the cation Ge and Sb sites. The model of Fe-doped a-GST was generated by fast quenching from the melt.

The resulting structural properties of Fe-doped a-GST are similar to those reported for pure a-GST (see Fig. 2) [2,3]. All Sb and Te atoms and 68% of Ge atoms are in a defective octahedral-like geometry with octahedral bonding angles but a coordination lower than six. The remaining Ge atoms have tetrahedral coordination. The average coordination numbers of Ge, Sb, Te and Fe, defined using the first minimum in the corresponding partial pair correlation functions to set the cutoff distance, are 4.1, 3.5, 2.8 and 5.9, respectively. To summarize, these results confirm that the short-range order in a-GST is very different from that in crystalline GST, also in the presence of Fe doping. On the other hand, the distribution of primitive rings (shown in Fig. 2b) displays a pronounced maximum at four-membered rings, 75% of which have ABAB alternation (A = Ge,Sb; B = Te). In this respect, doped a-GST resembles the atomic arrangement of the cubic rocksalt phase. Since the latter property, together with the large number of voids (also present in Fe-doped a-GST), has been linked to the fast crystallization of pure a-GST [3], our results suggest that the crystallization rate of a-GST should not degrade dramatically upon moderate Fe doping. These results are in line with experiments, which indeed show only a slight decrease in the crystallization rate of Fe-doped a-GST with respect to the clean phase [4].

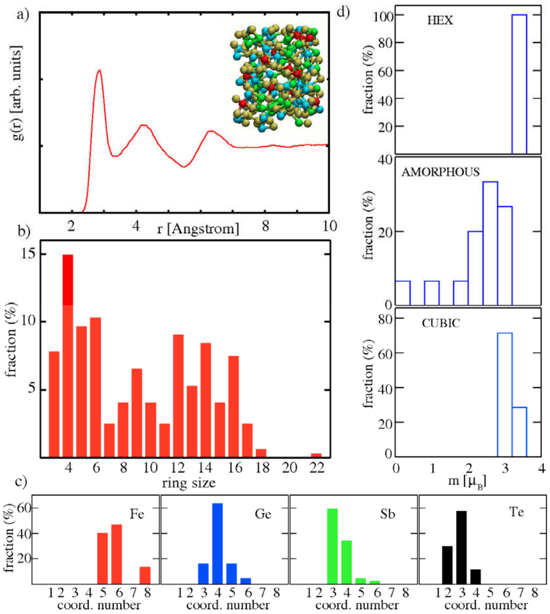

FIG. 2: a) g(r) of the model of Fe-doped a-GST (shown in the inset) generated by quenching from the melt. b) Statistics of irreducible n-fold ring configurations of Fe-doped a-GST. c) Distribution of the coordination numbers of different species. d) Distribution of the local magnetic moments of Fe atoms for each phase.

The distribution of the local moments of Fe (calculated by integrating the magnetization density inside a sphere centered at the Fe atom) in the three phases is shown in Fig. 2d. h-GST and c-GST display large values of the local moments and small fluctuations around the average values. In a-GST, on the other hand, Fe atoms have different local bonding geometries and also different number and type of nearest neighbors with respect to the crystalline phase: in particular, bond lengths of Fe with nearest neighbor atoms fluctuate considerably and, on the average, 25% of Fe neighbors are not Te atoms, in contrast to Fe-doped h-GST and c-GST. As a result, the local magnetic moments of Fe, which depend sensitively on these properties, vary considerably from Fe atom to Fe atom and, on the average, they are smaller than the values found in h-GST and c-GST for the 'optimal' substitutional Ge and Sb sites (see Fig. 2b). This behavior can be ultimately related to the already mentioned differences in the local environment and short-range order between the two phases. Since the peculiar structural properties of the amorphous phase are shared by most PCMs along the pseudobinary line GeTe-Sb2Te3, we predict that the magnetic contrast between the two phases should be a general feature of Fe-doped PCMs along this line.

In conclusion, we have shown that our models of crystalline and amorphous Fe-doped GST exhibit a magnetic contrast stemming from a reduction of the magnitude of the magnetic moments of Fe atoms in a-GST. We have also shown that the presence of Fe does not affect significantly the structural properties of a-GST (presence of four-membered rings and vacancies), which are believed to be responsible for the fast crystallization.

We are currently investigating the magnetic properties of GST doped with other 3d impurities (namely Cr, Mn, Co and Ni), with the goal of finding the best performing magnetic PCMs in terms of phase-change properties and magnitude and stability of the magnetic contrast.

[1] Wuttig M., Yamada N., Nature Mater. **6**, 824 (2007).

[2] Caravati S., Bernasconi M., Kühne T., Krack M., Parrinello M., Appl. Phys. Lett. **91**, 171906 (2007).

[3] Akola J., Jones R. O., Phys. Rev. B **76**, 235201 (2007).

[4] Song W.-D., Shi L.-P., Miao X.-S., Chong C.-T., Adv. Mater. **20**, 2394 (2008); Song W.-D., Shi L.-P., Chong C.-T., J. Nano Nanotechnol. **11**, 2648 (2011).

[5] Li Y., Mazzarello R., Adv. Mater. **24**, 1429 (2012).

[6] Giannozzi P. *et al.*, J. Phys. Condens. Matter **21**, 395502 (2009); http://www.quantum-espresso.org.

[7] VandeVondele J. *et al.*, Comput. Phys. Commun. **167**, 103 (2005); http://cp2k.berlios.de

Magnetic nano-skyrmions in an Fe monolayer on Ir(111)

G. Bihlmayer[1]**, S. Heinze**[2]**, K. v. Bergmann**[3]**, S. Blügel**[1]

[1]Peter Grünberg Institut-1 & Institute for Advanced Simulation-1, Forschungszentrum Jülich
[2]Institut für Theoretische Physik und Astrophysik, Universität zu Kiel
[3]Institut für Angewandte Physik, Universität Hamburg

Topological protection of a magnetic texture occurs when the stability of the structure is a consequence of the lattice as a whole, in contrast to other mechanisms, that rely on the properties of the individual magnetic moments. E.g. ferromagnetism in two dimensions can be stabilized by the magnetic anisotropy of single ions, while we report here on a magnetic skyrmion lattice that gains its robustness against external perturbations from its topological properties. In contrast to previously observed skyrmions, this example is of atomic dimensions, i.e. about 1 nm in diameter as experimentally observed by scanning-tunneling microscopy (STM). Density functional theory (DFT) elucidates the mechanisms that lead to the formation of these structures.

About 50 years ago, the English physicist Tony Skyrme was looking for stable mathematical solutions of field-theoretical equations that can be characterized by their topological properties [1] and are interpreted as particles. A simple, one-dimensional example in Fig. 1a can illustrate the principle: shown is a domain structure of a ferromagnetic chain of atoms. The direction of the magnetization of a single atom is symbolized by an arrow. To the left and right ends of the chain, these arrows point upwards, while in the middle we find a domain with opposite spin-orientations. In between, the magnetization rotates in so-called domain-walls. The walls can have – as in Fig. 1a – either the same rotational sense or (Fig. 1c) an opposite sense of rotation. Mathematically this difference can be described by plotting the angle of the spins with respect to the *z*-axis, θ, on a unit circle. Then, it is observed that in the first case (Fig. 1a) the magnetization describes a full circle, while in the second case (Fig. 1c) it just describes a semicircle before the angle θ returns to zero. A winding number can be defined as

$$S = \frac{1}{2\pi}\int \frac{\partial\theta(x)}{\partial x}\, dx$$

to describe the two cases: in the first situation we find a winding number of unity, in the second case it is zero.

It can be easily seen, that a structure with finite winding number (i.e. a skyrmion) shows a stability that results from its topology. Suppose an external magnetic field in *z*-direction tries to remove the middle domain of the magnetic arrangement shown in Fig.1: while the inner domain shrinks, the domain walls start moving towards each other. In the case shown in Fig. 1b, the angle θ will rotate around the unit circle in increasingly shorter spatial distances, but the inner domain cannot be removed due to a continuous deformation of the lattice in the *(x,z)*-plane. Quite different from this behaviour is the evolution of the magnetic structure shown in Fig. 1d: The curve described by θ contracts to a point and the middle domain disappears. We see that the skyrmion, with its non-zero winding number, is protected against continuous deformations caused by an external magnetic field.

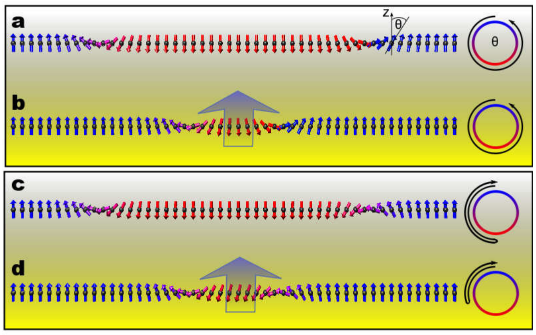

FIG. 1: One-dimensional example of a topologically protected magnetic structure (a,b) and of a topologically trivial one (c,d). On the right the orientation of the spins along the chain direction (x) is shown as a graph θ on the unit circle. In (a) the angle goes once around the circle and the winding number is unity, in (c) it is zero. Under the influence of a magnetic field (b,d) it can be seen that this difference in the topology of the magnetic structures results also in a difference of stability: while in the topologically trivial structure (c,d) the domain is removed, in the non-trival one (a,b) it remains stable.

It is easily realized that the above discussion is only valid, if we only consider the possibility that the directions of the magnetic moments remain confined to the shown *(x,z)*-plane. Spin rotations via the y-direction were not considered. But it is quite easy to extend the above discussion to three-dimensional magnetic structures on a two-dimensional lattice: denoting the magnetization direction in the *(x,y)*-plane with the vector $\vec{n}$, we can define the winding number as

$$S = \frac{1}{4\pi}\int \vec{n}\cdot\left(\frac{\partial\vec{n}}{\partial x}\times\frac{\partial\vec{n}}{\partial y}\right)dxdy.$$

Without performing the integration, the above expression defines a skyrmion density, $S(x,y)$. In a similar fashion, Skyrme extended this concept to four dimensions. He was looking for Hamiltonians that allow for solutions, which are characterized by non-trivial (non-zero) topological numbers. In field theory, many properties of such Hamiltonians are known, e.g. they have to contain higher (at least second) derivatives of the field variables for models in more than one spatial dimension [2].

Considering the particle nature of skyrmions there is a considerable interest to see, whether similar conditions can be realized in magnetic structures so that they can be used as units for information storage. Experimentalists in Hamburg found that a monolayer of iron on the hexagonal iridium (111) surface shows a square-like magnetic contrast in the spin-polarized STM images, like the one shown in the left inset of Fig. 2. A combination of these measurements and DFT calculations in Jülich could confirm that these structures are indeed skyrmions, which arrange on a lattice of atomic scale [3]. These nano-skyrmions are at least one order of magnitude smaller that the magnetic skyrmions found so far [4].

Usually used models, like the Heisenberg Hamiltonian, describe the formation of one-dimensional spin-spirals that might be homogeneous or inhomogeneous as the structure shown in Fig.1a. The essential ingredient to form two-dimensionally modulated spin-structures is, in our example, a higher-order spin interaction, known as four-spin term

$$H_{4\text{-spin}} = \sum_{ijkl} K_{ijkl} \left(\left(\vec{S}_i \cdot \vec{S}_j\right)\left(\vec{S}_k \cdot \vec{S}_l\right) + \left(\vec{S}_j \cdot \vec{S}_k\right)\left(\vec{S}_l \cdot \vec{S}_i\right) - \left(\vec{S}_i \cdot \vec{S}_k\right)\left(\vec{S}_l \cdot \vec{S}_j\right) \right)$$

that couples the one-dimensional (co-planar) spin-spirals to three-dimensional magnetic structures. But, as it turns out, such a superposition of two spin-spirals does not lead automatically to a topologically non-trivial spin structure, rather to a lattice of skyrmions and their anti-particles, the anti-skyrmions. Our calculations show that the finite winding number, the integral over the skyrmion density shown in the right inset of Fig.2, which is observed in the Fe films on Ir(111), result from the combination of the above-mentioned interactions with another, relativistic, two-spin term, the Dzyaloshinskii-Moriya (DM) interaction:

This term favours skyrmions over anti-skyrmions and is, thus, responsible for the topological protection of this spin structure.

It should be noted that the DM interaction also

$$H_{\mathrm{DM}} = \sum_{ij} \vec{D}_{ij} \bullet \left(\vec{S}_i \times \vec{S}_j\right)$$

selects a certain sense of rotation of the spin-spirals, e.g. a situation as shown in Fig. 1a can be more stable than the one shown in Fig.1c, where domain walls of different rotational sense occur. Recently, we have shown that this is indeed realized in ultrathin Fe films on a W(110) substrate [5]. In these one-dimensional examples, the left-rotating wall can be considered the "anti-particle" of the right-rotating wall. In two dimensions, structures with different rotational sense (chirality) can have the same winding number, while the antiparticle is achiral.

Experiments confirmed a high stability of the skyrmion lattice in magnetic fields, as expected from its properties. Furthermore, careful analysis of the data shows that the magnetic structure is not exactly commensurate with the atomic lattice, thus being detached from the periodicity of the supporting atoms.

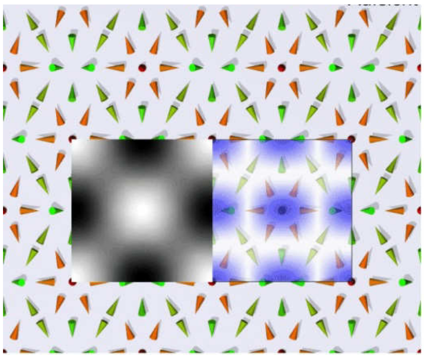

FIG. 2: The tiny vortices formed by only 15 atoms arrange in an almost square lattice. The colored cones indicate the orientation of the magnetic moments directions of the hexagonal iron layer. The inset on the left is a simulated image as it results from scanning tunneling microcopy with a spin-polarized tip with a polarization perpendicular to the film plane. The right inset shows the skyrmion-density, S(x,y), in white (low) and blue (high).

For future applications, e.g. in the field of spintronics, these magnetic skyrmions open completely new possibilities: Nowadays, new storage concepts based on isolated skyrmions realizing a single bit are in the focus of research. But there are many questions that still have to be addressed, e.g. regarding the interaction of electrical currents with the skyrmions. Ideally this would offer a possibility to move and manipulate these magnetic entities. Our work [3] shows, that miniaturization of these concepts might be possible, down to the atomic scale.

We gratefully acknowledge insightful discussions with A. Bogdanov and the grant of computing time by the Jülich Supercomputing Centre (JSC).

[1] T. H. Skyrme, *A non-linear field theory*. Proc. R. Soc. Lond. Ser. A 260, 127-138 (1961).

[2] G .H. Derrick, J. Math. Phys. 5, 1252 (1964).

[3] S. Heinze, K. von Bergmann, M. Menzel, J. Brede, A. Kubetzka, R. Wiesendanger, G. Bihlmayer, and S. Blügel, *Spontaneous atomic-scale magnetic skyrmion lattice in two dimensions.* Nature Physics 7, 713 (2011).

[4] S. Mühlbauer, B. Binz, F. Jonietz, C. Pfleiderer, A. Rosch, A. Neubauer, R. Georgii, und P. Böni, Science 323, 915-919 (2009).

[5] M. Heide, G. Bihlmayer and S. Blügel, Phys. Rev. B 78, 140403(R) (2008).

Magnetism in the family of Fe-based super-conductors containing rare-earth elements

Y. Xiao[1], S. Nandi[1], Y. Su[2], S. Price[1], Th. Brückel[1, 2]

[1] Jülich Centre for Neutron Science JCNS-2 and Peter Grünberg Institute PGI-4: Scattering Methods
[2] Jülich Centre for Neutron Science JCNS at FRM II

The discovery of iron-pnictide superconductors has triggered extensive research on their physical properties and mechanism of high-temperature superconductors [1,2]. During last few years, we have investigated extensively on the lattice dynamics [3,4], magnetic order [5,6] and spin dynamics [7] of the family of Fe-based superconductors. Similar to high-Tc cuprates, superconductivity in iron pnictides is in proximity to magnetism. The magnetism is more complicated in compounds which contain both iron and rare earth elements. Scattering methods such as x-ray scattering and neutron scattering have played an important role in the understanding of the magnetism in superconducting systems. We have used x-ray resonant magnetic scattering (XRMS) and neutron scattering methods to disentangle the two magnetic moment sublattice contributions in the parent compounds SmFeAsO [8] and $EuFe_2As_2$ [9].

Most of the research on pnictide superconductors has focused on $RFeAs(O_{1-x}F_x)$ with R=La, Nd, or Sm, etc. and AFe_2As_2 with A=Ba, Ca, or Eu, etc., the so called “1111” and “122” families. These two families are closely related since both of them adopt a layered structure with a single FeAs layer in the unit cell of 1111 and two such layers in the unit cell of 122. The superconducting state can be achieved either by electron or hole doping of the parent compounds. Apart from carrier doping, the application of hydrostatic pressure or chemical pressure can also induce superconductivity. Considering that the electronic states near the Fermi surface are dominated by contributions from Fe and As, it is believed that the FeAs layers are responsible for superconductivity in these compounds.

Regarding to the SmFeAsO parent compound, XRMS experiments were performed for the Sm L_2, L_3 and Fe K absorption edge. Below T = 110 K, both Sm and Fe magnetic moments order with a magnetic propagation vector (1 0 1/2), as observed by the enhancement of XRMS intensities at Sm $L_{2,3}$ and Fe K edges, respectively. By exploiting the peculiar polarization dependence and site selectivity of XRMS we have determined the magnetic structure of the Sm sublattice, by collecting integrated intensities of a series of magnetic reflections measured at the Sm L_2-edge. Similarly, the magnetic structure of Fe sublattice was determined in the temperature range 5 K ≤ T ≤ 110 K and the final magnetic structure is shown in Fig. 1.

The temperature dependence of the sublattice magnetizations is represented in Fig. 2, where the Fe shows a typical magnetization curve and Sm follows a quite unusual behaviour, with a sharp increase of the intensity below 50 K, followed by a second magnetic phase transition at 5 K. This unusual temperature dependence of the Sm sublattice can be explained with a ground-state doublet crystal-field level, split by an exchange field, and can be modelled by taking into account only the ground-state doublet and a splitting [Δ(T)] proportional to the effective field [Beff(T)] produced by the Fe sublattice [see Fig. (2b), red line]. We obtained Beff (T=0) = 56.4±1.9 Tesla characterising the strength of interaction between the two sublattices, which indicates a strong coupling between these two sublattices. Below 5 K a magnetic phase transition arises on both sublattices, as deduced by a drop of the Fe XRMS intensity [inset of Fig. 2(a)] and the switch of the XRMS intensities at Sm L2 edge from (3 0 7.5) reflection to the charge (−2 0 6) reflection, signalling a change in the magnetic order of Sm with the magnetic unit cell equal to the chemical unit cell. Our finding reveals that the magnetisms of Sm and Fe in the SmFeAsO compound are strongly correlated.

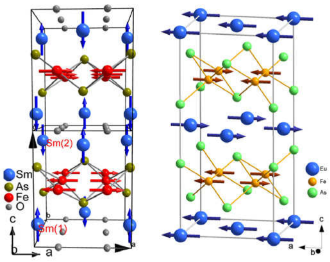

FIG. 1: Illustration of the magnetic structures of SmFeAsO in the temperature range 5K≤T≤110K and $EuFe_2As_2$ at 2 K [5,8].

For EuFe2As2, we have determined its low temperature magnetic structure by using neutron diffraction method [5]. Here we report a single-crystal neutron-diffraction study of the T-H phase diagram for $EuFe_2As_2$ under a magnetic field up to 3.5 T. As shown in Fig. 3(a), application of a field along a axis strongly weakens the (201) magnetic reflection and suppresses it totally at the critical field H_{Crit}^{Eu} of 0.8 T at 2 K. On the other hand, the increase in intensity at (006) nuclear reflection indicates that the Eu spins gradually reorientate to the (100) direction. The field-induced magnetic phase transition takes place from antiferromagnetic, via a canted configuration, to the ferromagnetic structure. These results suggest that the Eu spins will orient to the direction of the applied magnetic field once the field strength is greater than the critical field. The temperature dependence of ferromagnetic reflections was measured afterwards to determine the ordering temperature of the Eu moments. According to the neutron measurement results, the magnetic phase transition temperatures are determined and plotted in Fig. 3(c).

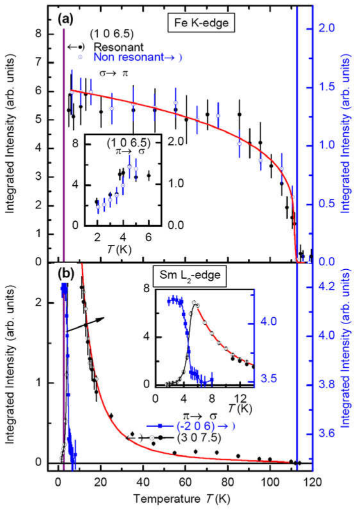

FIG. 2: (a) Temperature dependence of the (1 0 6.5) reflection measured in both resonant and nonresonant conditions near Fe K edge in polarization channel σ-π. The inset shows the change of Fe magnetic order below 5 K in π-σ channel. (b) Temperature dependencies of the (3 0 7.5) and (−2 0 6) reflections measured in resonant condition at the Sm L₂ edge. The inset shows the Sm phase transition below 5K.

Besides of Eu order, we also examined the Fe order under the applied field along a axis. In contrast to the reorientation of the Eu spins, the antiferromagnetic spin density wave order of Fe is found to be robust and it persists till fields up to 3 T. Surprisingly, it is found that the integrated intensity of the (101) magnetic reflection decreases slightly and then sharply increases with increasing magnetic field, as shown in Fig. 3(b). It is known that a twinning structure may exist in orthorhombic $EuFe_2As_2$ phase due to the interchange of the orthorhombic a and b axes. The variation of (101) magnetic reflection exhibits the same behavior as (400) nuclear reflection, which indicated that the twin populations are redistributed with applying magnetic field. The critical fields for twin structure evolution are determined at different temperatures and plotted in Fig. 3(c). It is interesting that the critical field of the twin redistribution is closely correlated with the field that induces the antiferromagnetic to ferromagnetic transition of Eu magnetic sublattice. The energy difference between two twins seems strongly related with the total energy of the Eu magnetism. Moreover, in-plane magnetotransport properties of $EuFe_2As_2$ are also investigated by angular dependent magnetoresistance measurement [10]. Strong anisotropy in magnetotransport properties is observed and it exhibits intimate correlation with the ordering states of both Eu and Fe spins in $EuFe_2As_2$, which provides a direct evidence of the coupling between itinerant electrons and ordered spins.

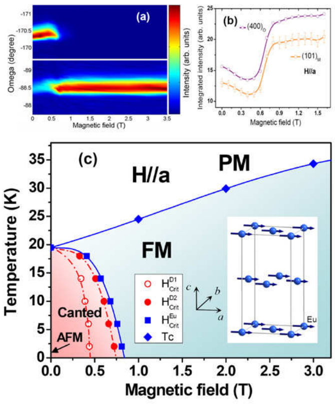

FIG. 3: (a) Magnetic field dependence of (201) magnetic and (006) nuclear reflections in two dimensional plots. (b) Field dependence of integrated intensities of (400) and (101) reflections. (c) Magnetic phase diagram for EuFe₂As₂ with applied field parallel to the crystallographic a axis. The inset shows the schematic view of the magnetic structure. Note that only Eu atoms are shown.

In summary, by using neutron and x-ray scattering methods, we found field induced spin reorientation and strong spin-charge-lattice coupling in $EuFe_2As_2$ compound. Surprisingly, we achieved detwinning in rather low external field without the need to apply uniaxial pressure. We also found an intricate interplay between the magnetism of Sm and Fe in the SmFeAsO compound, which sheds light on the currently debated importance of the rare-earth-iron interaction in the family of iron-based superconductors.

We would like to acknowledge our international collaborators for their valuable help and support on our research works. Lists of all collaborators are given as co-authors in our publications.

---

[1] Y. Kamihara et al., J. Am. Chem. Soc. 130, 3296 (2008).

[2] D. C. Johnston, Advances in Physics **59**, 803(2010).

[3] R. Mittal et al., Phys. Rev. Lett. **102**, 217001(2009).

[4] R. Mittal et al., Phys. Rev. B **79**, 214514(2009).

[5] Y. Xiao et al., Phys. Rev. B **81**, 174424(2009).

[6] Y. Xiao et al., Phys. Rev. B **81**, 094523(2010).

[7] Y. Su et al., to be submitted.

[8] S. Nandi et al., Phys. Rev. B **84**, 054419(2011).

[9] Y. Xiao et al., Phys. Rev. B **81**, 220406(R)(2010).

[10] Y. Xiao et al., Phys. Rev. B **85**, 094504(2012).

Magnetization Distribution and Self-Assembly of Magnetic Nanoparticles

S. Disch[1], R. P. Hermann[1,2], E. Wetterskog[3], G. Salazar-Alvarez[3], L. Bergström[3], Th. Brückel[1]

[1] JCNS-2: Jülich Centre for Neutron Science
[2] Faculty of Science, University of Liège, B-4000 Liège, Belgium
[3] Department of Materials and Environmental Chemistry, Arrhenius Laboratory, Stockholm University, S-10691 Stockholm, Sweden

The physical properties of magnetic nanoparticles are intensely investigated for both fundamental and technological reasons. A broad interest is attributed to their manifold possible applications in magnetic data storage, magnetic imaging, or biomedical applications. With regard to these applications, the two main aspects of fundamental interest are (i) the magnetic anisotropy and the related magnetization distribution in individual nanoparticles and (ii) the interparticle interactions leading to ordered assemblies of nanoparticles. Our study of the magnetization distribution in iron oxide nanoparticles as well as the shape induced symmetry in their assemblies using advanced X-ray and neutron scattering techniques aims at a better understanding of such fundamental nanoparticle properties.

The determination of the spatial magnetization distribution in magnetic nanoparticles represents a long standing challenge in nanomagnetism. Evidence for spin disorder at the particle surface was found by macroscopic measurements as well as simulations. Reduced magnetization values in nanoparticles as compared to the bulk material as well as excess susceptibility in high applied fields are commonly attributed to a magnetic dead layer at the nanoparticle surface. In order to determine the spatial distribution of the magnetization microscopically, we performed a polarized small-angle neutron scattering (SANS) study on iron oxide nanoparticles [1].

Well-dispersed solutions of non-interacting nanospheres and nanocubes with a 9 nm diameter and 8.5 nm edge length, respectively, were chosen as a model system. The excellent monodispersity of the samples with lognormal size distributions of 5.5(1) % and 7.2(2) % FWHM is an important requirement for the investigation of surface effects such as surface spin disorder. Polarized SANS experiments were performed at D22/ILL using 6 Å neutron wavelength and a horizontal magnetic field of ≤ 1.5 T. Polarized SANS gives quantitative access to the magnetic particle form factor, which is directly correlated with the spatially resolved microscopic magnetization distribution through Fourier transformation. We find a constant magnetization density in the nanoparticle core, which decreases close to the nanoparticle surface (see Fig. 1), thus giving the first experimental evidence of surface spin canting in non-interacting nanoparticles.

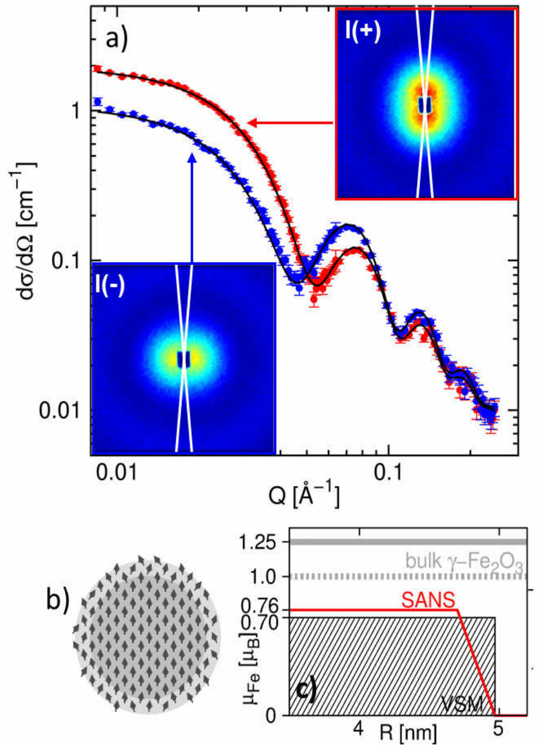

FIG. 1: Polarized SANS by iron oxide nanospheres a) Scattering cross sections obtained by magnetic contrast variation. Insets: 10° sectors used for integration. b) Schematic of the magnetization distribution model with surface spin canting. c) Quantitative magnetization distribution obtained by SANS compared to macroscopic measurements (VSM) and the bulk magnetization (dashed line).

Such spin canting may result from local structural deviations and broken symmetry at the particle surface. We further observe a substantial influence of the particle shape with a significantly larger surface thickness for the nanocubes. This is likely a direct consequence of the cubic shape anisotropy, related to a larger spin canting at the cube corners. Consequently, the magnetization decrease in the particle shell is attributed to a combination of both surface and shape anisotropies. Surface spin canting might be assumed to explain the reduced magnetization found macroscopically in nanoparticles. However, our quantitative analysis reveals that even the atomic magnetic moments in the nanoparticle core are significantly lower than expected (see Fig. 1c). The lower magnetization density observed in nanoparticles as compared to the bulk material thus results partially from spin canting at the surface, but to a much larger extent from reduced magnetic moments inside the uniformly magnetized nanoparticle core.

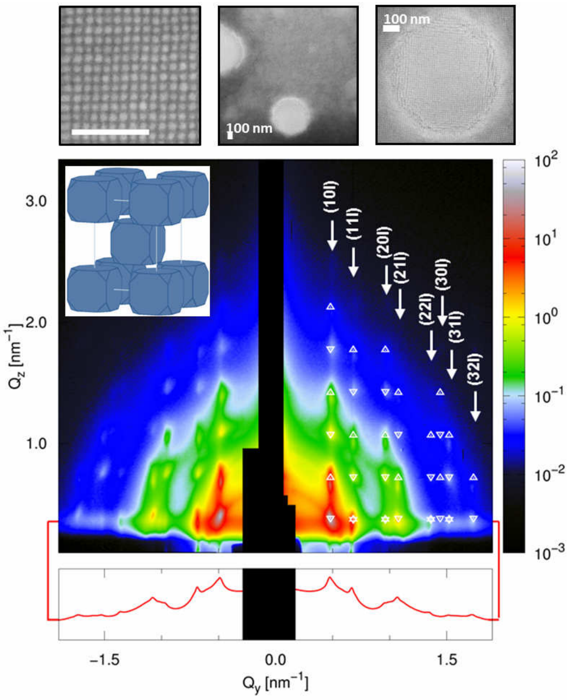

FIG. 2: GISAXS pattern of iron oxide nanocubes assemblies. Reflections are indexed according to a bct *packing of nanocubes (inset). Bottom: In plane scattering intensities displayed on a logarithmic scale. Top: SEM images of the mesocrystal arrangements.*

For investigation of interparticle interactions, nanoparticle assemblies provide suitable model systems. Self-assembly of nanocrystals is a widely investigated phenomenon, as its understanding promises new routes for the formation of large-scale ordered structures for nanotechnology. Most investigations focus on spherical nanoparticles or binary superlattices composed of different particle sizes or compositions. Because the interactions between the nanocrystal facets are important for self-assembly, slight variations in the nanocrystal shape an influence their arrangements on the mesoscale. We have studied the self-assembly of iron oxide nanocubes with a slight degree of truncation of the cubes corners and report on the influence of the nanoparticle shape on the obtained structure [2].

Deposition in an applied magnetic field yields highly ordered mesocrystals with a micrometer lateral size and several hundred nm in height. A square lateral order with face to face arrangement of the nanocubes is evident from scanning electron microscopy (SEM, see Fig. 2). Grazing-incidence small-angle X-ray scattering (GISAXS), performed at ID01/ESRF, allows for determination of the three dimensional mesocrystal structure. The in plane scattering contribution (red line in Figure 2) is in agreement with the square lateral order observed by SEM. By indexing of all *hkl* reflections in the GISAXS pattern shown in Figure 2, we derive a tetragonal body centered (*bct*) lattice with face to face arrangement of the nanocubes. This is different from the simple cubic (*sc*) arrangement reported for cubic Fe nanoparticles [3], which can also be inferred from the square symmetry observed by SEM.

Based on the precise knowledge of interparticle separation distances from GISAXS, TEM, and SEM, we were able to calculate the van der Waals energies for the different types of interparticle interactions found in the mesocrystal structure [2]. Comparing the energy needed to remove a nanocube from either *bct* or *sc* lattice revealed that the degree of truncation of the nanocubes corners is an essential parameter for the lattice type preference. The ratio between the interaction energies calculated for both lattice types indicates that the *sc* lattice is favoured at a low degree of truncation, whereas the *bct* lattice dominates at moderate truncation as observed for the nanocubes under study. The interaction energy estimates thus support the observed preference of a *bct* lattice and identify the degree of truncation to be crucial for the mesocrystal structure.

In combination, the presented studies contribute to the understanding of fundamental physical properties such as a possible spin canting close to the nanoparticle surface. The strong nanoparticle shape dependence of the observed mesocrystal structure types further illustrates the sensitivity of the interparticle interactions on nanoparticle shape anisotropy. With the structure-directing influence of the anisotropic nanoparticle shape as opposed to the spherical atoms in conventional crystal structures, a new dimension of crystallography has been established.

[1] S. Disch, E. Wetterskog, R. P. Hermann, A. Wiedenmann, U. Vainio, G. Salazar-Alvarez, L. Bergström, Th. Brückel, New J. Phys. 14 (2012), 013025.

[2] S. Disch, E. Wetterskog, R. P. Hermann, G. Salazar-Alvarez, P. Busch, Th. Brückel, L. Bergström, S. Kamali, Nano Lett. 11 (2011), 1651.

[3] A. Demortière, P. Launois, N. Goubet, P. Albouy, C. Petit, J. Phys. Chem. B 112 (2008), 14583.

Dynamical magnetic excitations of nanostructures from first-principles

S. Lounis[1], **A. T. Costa**[2], **R. B. Muniz**[2], **and D. L. Mills**[3]

[1] Peter Grünberg Institut and Institute for Advanced Simulation, Forschungszentrum Jülich
[2] Instituto de Física, Universidade Fedeal Fluminense, 24210-340 Niterói, Rio de Janeiro, Brazil and
[3] Department of Physics and Astronomy, University of California Irvine, California, 92697 USA

Within time-dependent density functional theory, combined with the Korringa-Kohn-Rostoker Green functions, we devise a real space method to investigate spin dynamics. Our scheme enables one to deduce the Coulomb potential which assures a proper Goldstone mode is present. We illustrate with application to 3d adatoms and dimers on Cu(100).

Very recently new experimental methods, e.g. the spin polarized electron energy loss spectroscopy (SPEELS) [1] and inelastic scanning tunneling microscopy (STM) [2,3,4], for the study of magnetic excitations in the nanoscale and subnanoscale length regime have appeared. The quantity probed is the transverse susceptibility χ that, in linear response, describes the amplitude of the transverse spin motion produced by an external magnetic field B_{ext} of frequency ω. To calculate χ is a major computational challenge, if one wants to employ time dependent density functional theory (TD-DFT) [5] or many-body perturbation theory (MBPT) based on DFT [6]. Thus one sees very few DFT based calculations even for bulk systems [7,8,10,9]. There are studies that use empirical tight binding theory (ETB) [11,12,13] based on MBPT. In all schemes, a similar master equation must be solved. Its solution maybe be written in schematic notation,

$$\chi = \chi_0(1 - U\chi_0)^{-1} \qquad (1)$$

In TD-DFT [5], χ_0 is the Kohn-Sham susceptibility and χ, the total susceptibility, is exact in principle if the full exchange and correlation kernel U is known. In practice, one often invokes the adiabatic local spin density approximation (ALDA); U can also be viewed as a parameter whose value is in the range of $1eV/\mu_B$ for 3^d transition elements [14]. In the ETB MBPT, U is the effective Coulomb interaction that is the local exchange splitting divided by the magnetic moment. In DFT based methods, the Goldstone theorem is violated in numerical studies. So, for instance, zero wave vector spin waves have no zero frequency with spin orbit coupling set aside . One then adjusts U in an ad hoc manner so χ is compatible with the Goldstone theorem. We introduce a scheme that constrains U so no adjustment are needed [15].

We developed a new computationally attractive method [15] that allows us to address magnetic excitations from first-principles. We use the Korringa-Kohn-Rostoker single particle Green function (KKR-GF) [16] which contains an ab-initio description of the electronic strucutre. Such a method is required to describe spin-excitations in metallic systems where hybridization of electronicstates play a crucial role and where a Heisenberg model of the type used in ref. [3] would fail qualitatively. Our scheme is readily applied to bulk materials, to surfaces with adsorbed films, and it is a real space formalism ideal for diverse small nanostrucures. As an initial application, below we explore the spin dynamics of single adatoms and dimers on the Cu(100) surface.

To illustrate our scheme, we investigate the magnetic excitations of 3^d adatoms and dimers deposited on Cu(001) surface with the theoretical LDA lattice parameter (6.64 a.u.). First we examine the spin dynamics of the magnetic moment bearing adsorbates Cr, Mn, Fe and Co. The atoms are positioned in the fourfold hollow sites with the first nearest neighbors around every adatom included when evaluating the full real space Green function.

We note that many years ago the spin dynamics of a moment embedded in a paramagnetic host was described [17] within a framework conceptually similar to that used here. The local response displays a g shifted Zeeman resonance, broadened very substantially by decay of the coherent spin precession to particle hole pairs, whereas the total moment of the system precesses with g=2 and zero linewidth. Our calculations explore the local response of the moment. Local probes such as STM thus examine aspects of spin dynamics inaccessible to spectroscopy based on excitation by long wavelength radiation such as microwaves or light; these sense the precession of the total moment.

In Fig. 1(a), we show our calculations of the resonant response of the local moments for the four adatoms we have investigated. The resonant frequency scales linearly with the applied DC field, as does the width of the structure. For this reason, we can apply a DC field of sufficient strength to move the resonance up to frequencies that allow numerical study. A simple scaling reduces the results to the regime of physical applied fields. The g shift can be positive (Co) or negative (Cr, Mn and Fe) (For the field we have applied, a g value of 2 would provide a resonance at 13.6 meV). The width of the resonances is controlled by the local density of states [17], and is thus influenced by the position of the d levels relative to the Fermi energy.

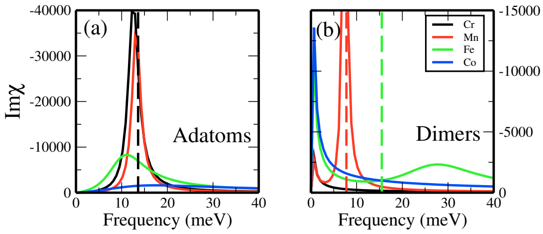

FIG. 1: In (a) the imaginary part of χ is plotted for every adatom when applying an additional magnetic field along the z -direction corresponding to a Larmor frequency of 13.6 meV (dashed line). In (b) are shown Imχ calculated for the four dimers. The optical modes, estimated for Mn and Fe from a Heisenberg model, are represented as dashed lines.

Thus the Co and Fe resonances are quite broad, since their minority spin levels intersect the Fermi level, whereas those for Mn and Cr are much sharper since for these adatoms the Fermi level lies between the majority and minority states.

We have also explored nearest neighbor dimers of the 3^d adatoms discussed above, assuming a ferromagnetic ground state. For the dimer, there are two resonances, a zero frequency acoustical mode, and a high frequency optical mode that is damped by decay toStoner excitations. The position of the optical mode provides information on the stability of the assumed ground state. We find the optical mode at negative frequency for Cr and Co. This informs us the ferromagnetic ground state is unstable, whereas for the Fe and Mn dimer the mode resides at positive frequency so ferromagnetism is stable. We have calculated adiabatic exchange integrals J in an effective Hamiltionian we write as $-J\vec{e}_1\cdot\vec{e}_2$, with $\vec{e}_1$ and $\vec{e}_2$ unit vectors. [18] We find J negative for Cr (J =-19.8 meV) and Co (J =-14.9 meV), consistent with instability of ferromagnetism in the ground state, while positive values were obtained for Fe (J =30.4 meV) and Mn (J =16.3 meV) so we confirm ferromagnetism is stable. For positive frequencies we plot the imaginary part of the susceptibility in Fig. 1(b). For Cr, Mn, Fe and Co the Heisenberg model gives -19.7 meV, 15.4 meV, 39.2 meV and -33.1 meV for the optical mode frequencies, respectively.

To conclude, we have shown that a simple approach, based on TD-DFT and the KKR-GF method, can be used to extract dynamics magnetic susceptibilities. As an application, 3^d adatoms and dimers deposited on Cu(001) surface were investigated from first-principles.

Research supported by the A.v. Humboldt Foundation, the HGF-YIG Programme VH-NG-717 (Functional nanoscale structure and probe simulation laboratory-Funsilab) and U. S. Depart. of Energy through grant No. DE-FG03-84ER-45083. R.B.M. acknowledges support from CNPq and FAPERJ, Brazil.

---

[1] Kh. Zakeri, Y. Zhang, J. Prokop, T.-H. Chuang, N. Sakr, W. X. Tang, and J. Kirschner, Phys. Rev. Lett. , 137203 (2010)

[2] T. Balashov, T. Schuh, A. F. Takacs, A. Ernst, S. Ostanin, J. Henk, I. Mertig, P. Bruno, T. Miyamachi, S. Suga, and W. Wulfhekel, Phys. Rev. Lett. , 257203 (2009)

[3] C. F. Hirjibehedin, C.-Y. Lin, A. F. Otte, M. Ternes, C. P. Lutz, B. A. Jones, A. J. Heinrich, Science , 1199 (2007)

[4] A. A. Khajetoorians, S. Lounis, B. Chilian, A. T. Costa, L. Zhou, D. L. Mills, J. Wiebe1, and R. Wiesendanger, Phys. Rev. Lett. , 037205 (2011)

[5] E. Runge, E. K. U. Gross Phys. Rev. Lett. 52, 997 (1984); E. K. Gross, W. Kohn, Phys. Rev. Lett. , 2850 (1985).

[6] F. Aryasetiawan, K. Karlsson, Phys. Rev. B , 7419 (1999)

[7] S. Y. Savrasov, Phys. Rev. Lett. , 2570 (1998).

[8] J. B. Staunton, J. Poulter, B. Ginatempo, E. Bruno, and D. D. Johnson, Phys. Rev. Lett. , 3340 (1999)

[9] P. Buczek, Spin-dynamics of complex itinerant magnets, PhD thesis, Martin-Luther University, Halle-Wittenberg (2009)

[10] E. Sasioglu, A. Schindlmayr, C. Friedrich, F. Freimuth, and S. Blügel, Phys. Rev. B , 054434 (2010)

[11] J. F. Cooke, J. A. Blackman, T. Morgan, Phys. Rev. Lett. , 718 (1985)

[12] R. B. Muniz, D. L. Mills, Phys. Rev. B , 224414 (2003)

[13] A. T. Costa, R. B. Muniz, D. L. Mills, Phys. Rev. Lett. , 137203 (2005)

[14] F. J. Himpsel, J. Magn. Magn. Mater. , 261 (1991)

[15] S. Lounis, A. T. Costa, R. B. Muniz, and D. L. Mills, Phys. Rev. Lett. , 187205 (2010); ibid. Phys. Rev. B , 035109 (2011)

[16] N. Papanikolaou, R. Zeller, P. H. Dederichs, J. Phys.: Condens. Matter , 2799 (2002)

[17] P. Lederer, D.L. Mills, Phys. Rev. , 590 (1967)

[18] A. I. Lichtenstein, M. I. Katsnelson, V. P. Antropov, and V. A. Gubanov, J. Magn. Magn. Mater. , 65 (1987)

A mathematical account on Thiele's equation for magnetic vortices

Christof Melcher

Lehrstuhl I für Mathematik, RWTH Aachen University

A pioneering reformulation of Landau-Lifshitz-Gilbert equations, aiming to facilitate the dynamic description of magnetic domains, has been introduced by A. A. Thiele in 1973 and used by D. L. Huber in 1982 in the context spin vortices, and is nowadays a common tool for predicting the dynamics of various types of topological defects in magnetism. In this note, we shall report on recent analytical results, developed in collaboration with M. Kurzke (Bonn), R. Moser (Bath), and D. Spirn (Minneapolis), that establish a mathematically rigorous derivation of Thiele's equation in some specific situations.

The Landau-Lifshitz-Gilbert equation (LLG) is the fundamental evolution law in ferromagnetism, governing the dynamics of discrete or continuous spin systems expressed in terms of direction fields $\boldsymbol{m}$ having values on the unit sphere $\boldsymbol{S}^2$. In suitable units it reads

$$\frac{\partial \mathbf{m}}{\partial t} = \mathbf{m} \times \left(\alpha \frac{\partial \mathbf{m}}{\partial t} + \gamma \nabla E(\mathbf{m}) \right),$$

where $\nabla E(\boldsymbol{m})$ is the functional L^2-gradient of the underlying interaction energy $E = E(\mathbf{m})$. Due to its hybrid structure combining gyrotropic precession and relaxation dynamics, LLG mixes properties of Hamiltonian flows and gradient flows and exhibits at least two different time scales. In a basic micromagnetic model for a soft ferromagnet, the effective field $\boldsymbol{h}_{\mathrm{eff}} = -\nabla E(\boldsymbol{m})$ combines short-range exchange forces and long-range stray-field effects, giving rise to the formation of magnetic microstructures. In planar magnets or thin-film geometries, these structures are build up from of domain walls and vortices emerging as topological defects. Magnetization fields $\boldsymbol{m}$, however, can only give an implicit description of these structure elements, and an ultimate goal is to extract effective dynamic laws for walls and vortices reflecting the gyrotropic-dissipative nature of LLG.

Assuming magnetization dynamics can be expressed in terms of a steady state $\boldsymbol{M} = \boldsymbol{M}(x)$ and a collective coordinate $X = X(t)$, i.e. $\boldsymbol{m}(x,t) = \boldsymbol{M}(x-X(t))$, Thiele introduced an ordinary differential equation for X that is consistent with LLG. A generalized version of Thiele's equation stemming from a more general ansatz $\boldsymbol{m} = \boldsymbol{M}(x-X(t),\dot{X}(t))$, taking into account structural changes depending on the speed $\dot{X}$, reads

$$M\ddot{X} + D\dot{X} + G \times \dot{X} + F = 0.$$

The constants M and D are referred to as effective mass and damping, respectively, G is a gyrovector, and $F = F(X)$ a forcing term stemming from external and self-interaction. These quantities depend explicitly on material and geometric parameters. Implicitly they also incorporate information about the steady state $\boldsymbol{M}$ which is, once it exist, an unknown of the problem.

A particular interesting feature of geometric evolution equations such as LLG is the occurrence of finite time blow-up. In the two-dimensional case, this phenomenon, called bubbling, is well-understood and typically accompanied by a change of topological type. The subtle connection between bubbling of generalized solutions on the one hand and the creation, collision and annihilation of vortices in planar spin system or magnetic thin-films on the other hand is a matter of ongoing research. The crucial quantity in order to control the topology of planar vortex systems is the vorticity

$$\omega(\mathbf{m}) = \left\langle \mathbf{m}, \frac{\partial \mathbf{m}}{\partial x_1} \times \frac{\partial \mathbf{m}}{\partial x_2} \right\rangle,$$

where $\langle \cdot,\cdot \rangle$ denotes the inner product on $\boldsymbol{R}^3$. In fact, if $\Omega \subset \boldsymbol{R}^2$ is a simply connected domain bounded by the smooth contour Γ, then, if $\mathbf{m} : \Omega \rightarrow \boldsymbol{S}^2$ maps Γ to the equator, i.e. if $m_3(\Gamma) = 0$, the integral $q = \frac{1}{4\pi}\int_\Omega \omega(\mathbf{m})\, dx$ is the topological charge. In mathematical terms, q is the half-integer valued $\boldsymbol{S}^2$-degree, i.e. the oriented number of covers of the sphere $\boldsymbol{S}^2$ by the map $\boldsymbol{m}$. In particular, for a simple vortex or anti-vortex, i.e. a cover of one hemisphere, we have $q = \frac{1}{2}dp$, where $d \in \{\pm 1\}$ are the winding number ($\boldsymbol{S}^1$-degree) and $p = \mathrm{sgn}\,(m_3)$ the polarity, respectively. Note that, for $\boldsymbol{m} = (m,m_3)$, we have $d = \frac{1}{2\pi}\int_\Gamma m \times \frac{\partial m}{\partial \tau}$. In a global picture, the total topological charge and the total winding number of a map $\boldsymbol{m}$ are the sum of local topological charges and winding numbers, respectively.

In the presence of a strong confining potential, stemming e.g. from shape-anisotropy, the vorticity is expected to concentrate near the vortex center X, i.e. $\omega(\boldsymbol{m}) \sim 4\pi q \delta_X$, where δ_X is the Dirac function centered at X. For a mathematically rigorous approach we shall consider, for a simply connected domain $\Omega \subset \mathbf{R}^2$ and $\varepsilon > 0$, a family of interaction energies

$$E_\varepsilon(\mathbf{m}) = \frac{1}{2}\int_\Omega |\nabla \mathbf{m}|^2 + \left(\frac{m_3}{\varepsilon}\right)^2 dx$$

as a simplified model for a planar nanomagnet. We denote the associated energy density by $e_\varepsilon(\mathbf{m})$, which we also expect to concentrate near vortex locations X, i.e., more precisely, $e_\varepsilon(\boldsymbol{m}) \sim \pi \log(1/\varepsilon)\delta_X$. The scaling parameter $\varepsilon \ll 1$ appears as the coherence length (core size) of a vortex featured in this model. The connection between vorticity, energy density, and LLG with underlying energy $E_\varepsilon(\boldsymbol{m})$ are the conservation laws

$$\frac{\partial\omega(\mathbf{m})}{\partial t} = \operatorname{curl}\operatorname{div}(\nabla\mathbf{m}\otimes\nabla\mathbf{m}) - \alpha\operatorname{curl}\left\langle\frac{\partial\mathbf{m}}{\partial t},\nabla\mathbf{m}\right\rangle$$

and

$$\frac{\partial e_\varepsilon(\mathbf{m})}{\partial t} + \alpha\left|\frac{\partial\mathbf{m}}{\partial t}\right|^2 = \operatorname{div}\left\langle\frac{\partial\mathbf{m}}{\partial t},\nabla\mathbf{m}\right\rangle.$$

We have considered an asymptotic regime of initial configurations $\mathbf{m}_\varepsilon^0$ where, $\varepsilon \to 0$, $e_\varepsilon(\mathbf{m}_\varepsilon^0)$ and $\omega(\mathbf{m}_\varepsilon^0)$ concentrate at N distinct initial vortex locations $X_1^0,\dots,X_n^0$, while initial energies are just large enough to develop N vortices with winding numbers $\mathbf{d} = (d_1,\dots,d_N)$ at $\mathbf{X}^0 = (X_1^0,\dots,X_N^0)$, i.e.

$$E_\varepsilon(\mathbf{m}_\varepsilon^0) = N\pi\log(1/\varepsilon) + W(\mathbf{X}^0,\mathbf{d}) + o(1)$$

for the renormalized energy $W=W(\mathbf{X},\mathrm{d})$, see below. Assuming in addition to these well preparedness assumptions an appropriate small damping condition, i.e. $\alpha_\varepsilon \log(1/\varepsilon)$ has a finite limit D/π as $\varepsilon \to 0$, we proved in [1] on the basis of the above conservation laws the following result:

Theorem *Given a family* $\{\mathbf{m}_\varepsilon^0\}$ *of well-prepared initial data that exhibits N initial vortices at positions* $\mathbf{X}^0 = (X_1^0,\dots,X_N^0)$ *with topological charges* $(q_1,\dots,q_N) \in \{\pm\tfrac{1}{2}\}^N$ *and winding numbers* $(d_1,\dots,d_N) \in \{\pm 1\}^N$, *there exists a corresponding family* $\{\mathbf{m}_\varepsilon\}$ *of solutions of LLG that are smooth up to some terminal time* $T > 0$ *such that, for* $0 < t < T$,

$$\alpha_\varepsilon e_\varepsilon(\mathbf{m}_\varepsilon(,t)) \to D\sum_{j=1}^N \delta_{X_j(t)}$$

and

$$\omega(\mathbf{m}_\varepsilon(,t)) \to 4\pi\sum_{j=1}^N q_j\delta_{X_j(t)}$$

in the sense of distributions as $\varepsilon \to 0$. *Vortex trajectories* $\mathbf{X} = (X_1,\dots,X_N)$ *satisfy, for* $G_j = 4\pi q_j\hat{\mathbf{e}}_z$, *Thiele's equation*

$$G_j \times \dot{X}_j + D\,\dot{X}_j + \frac{\partial W}{\partial X_j}(\mathbf{X},\mathbf{d}) = 0$$

with $\mathbf{X}(0) = \mathbf{X}^0$.

The renormalized energy $W = W(\mathbf{X},\mathbf{d})$ coincides with the Kirchhoff-Onsager functional arising in Euler point vortices

$$W(\mathbf{X},\mathbf{d}) \square -\pi\sum_{j\neq k} d_j d_k \log|X_j - X_k|.$$

In particular, vortex pairs (X_j, X_k) of equal winding number interact repulsively while vortex-antivortex pairs ($d_j\ d_k$ = -1) interact attractively. The terminal time T in the Theorem is the time when the solution to Thiele's equation collapses, i.e. when the first vortex-antivortex pair collides (for otherwise we have global existence T = ∞). The nature of LLG dynamics subsequent to the collision of a vortex-antivortex pair depends on corresponding polarities. While the total winding number $d = \sum d_j$ is determined by the boundary degree and remains unaltered, a (local) change of topological charge occurs if polarities are antiparallel ($p_j \cdot p_k$ = -1), i.e. $p_j + p_k$ = ±1 drops to 0 which corresponds to the annihilation of a full cover of $\boldsymbol{S}^2$ (magnetic bubble). In this situation, a burst of spin waves has first been observed by Hertel and Schneider [2] by means of numerical simulations of the full LLG system and has later been attributed, by Tretiakov and Tchernyshyov [3], to a sudden change in topological charge - as predicted by the Thiele equation in our Theorem. Understanding the dissipation of corresponding excess energy and extending the dynamical law of vortices passed collisions remains a major mathematical challenge.

The analysis extends to models for vortex excitation by electric currents, refereed to as spin-transfer torque. In case of an in-plane current **v**, the additional terms in the governing Landau-Lifshitz-Slonczewski equation are $-(\mathbf{v}\cdot\nabla)\mathbf{m}$ and $\beta\,\mathbf{m}\times(\mathbf{v}\cdot\nabla)\mathbf{m}$ referred to as adiabatic and non-adiabatic term, respectively, and with a coefficient β of the order of the damping factor α, see [4]. In [5] we have obtained the modified Thiele equation

$$G_j \times \left(\dot{X}_j - \mathbf{v}\right) + D\left(\dot{X}_j - \xi\,\mathbf{v}\right) + \frac{\partial W}{\partial X_j}(\mathbf{X},\mathbf{d}) = 0,$$

where $\xi = \lim_{\varepsilon\to 0}\beta_\varepsilon/\alpha_\varepsilon$.

We remark that in our limit of vanishing core size, inertial contribution, i.e. effective vortex masses, are not visible. To this end we would need to take into account not only finite core size but also structural changes depending on velocity. In case of a single planar Néel wall driven by an applied field $H = H(t)$, a damped harmonic oscillator

$$M\ddot{X} + D\dot{X} + \nabla W(X) = H(t)$$

can be obtained from the dissipative wave equation

$$m \times \left(\frac{1}{\gamma^2}\frac{\partial^2 m}{\partial t^2} + \frac{\nu}{\gamma}\frac{\partial m}{\partial t} - h_{\text{eff}}\right) = 0$$

that we identified in [6] as a thin-film limit of LLG on a intermediate time scale and in the absence of topological defects.

[1] Kurzke, M., Melcher, C., Moser, R., Spirn, D.: Ginzburg-Landau vortices driven by the Landau-Lifshitz-Gilbert equation, *Arch. Ration. Mech. Anal.* 199 (3), 843–888 (2011)

[2] Hertel, R., Schneider C. M.: Exchange Explosions: Magnetization Dynamics during Vortex-Antivortex Annihilation, Phys. Rev. Lett. 93, 177202 (2006)

[3] Tretiakov, O. A., Tchernyshyov, O.: Vortices in thin ferromagnetic films and the skyrmion number, Phys. Rev. B 75, 012408 (2007)

[4] Zhang, S., Li, Z.: Roles of non equilibrium conduction electrons on the magnetization dynamics of ferromagnets, Phys. Rev. Lett. 97, 127204 (2004)

[5] Kurzke, M., Melcher, C., Moser, R.: Vortex motion for the Landau-Lifshitz-Gilbert equation with spin-transfer torque, SIAM J. Math. Anal. 43 (3), 1099–1121 (2011)

[6] Melcher, C.: Thin-film limits for Landau-Lifshitz-Gilbert equations, SIAM J. Math. Anal. 42 (1), 519–537 (2010)

Probing the timescale of the exchange interaction in a ferromagnetic alloy

Roman Adam[1], Patrik Grychtol[1], Stefan Mathias[2], Chan La-O-Vorakiat[3], Patrick Granitzka[2], Emrah Turgut[3], Justin M. Shaw[4], Hans T. Nembach[4], Mark E. Siemens[3], Steffen Eich[2], Claus M. Schneider[1], Thomas J. Silva[4], Martin Aeschlimann[2], Margaret M. Murnane[3], and Henry C. Kapteyn[3]

[1]Peter Grünberg Institut PGI-6, Forschungszentrum Jülich, 52425 Jülich
[2]University of Kaiserslautern and Research Center OPTIMAS, 67663 Kaiserslautern
[3]Department of Physics and JILA, University of Colorado and NIST, Boulder, CO, USA
[4]Electromagnetics Division, National Institute of Standards and Technology, Boulder, CO, USA

The underlying physics of all ferromagnetic behavior is the cooperative interaction between individual atomic magnetic moments that results in a macroscopic magnetization. We use extreme femtosecond pulses of laser higher harmonics in the extreme ultraviolet spectral range as an element-specific probe of ultrafast, optically driven, demagnetization in a ferromagnetic $Ni_{0.8}Fe_{0.2}$ (Permalloy). We show that for times shorter than the characteristic timescale for exchange coupling, the magnetization of Fe quenches more strongly than that of Ni [1]. Then, as the Fe moments start to randomize, the strong ferromagnetic exchange interaction induces further demagnetization in Ni, with a characteristic delay determined by the strength of the exchange interaction. We also show that we can further enhance this delay by lowering the exchange energy by diluting the NiFe with Cu. Our measurements probe how the fundamental quantum mechanical exchange coupling between Fe and Ni in magnetic materials influences magnetization dynamics in ferromagnetic alloys.

Progress in magnetic information storage and processing technology is intimately associated with complex materials that are engineered at the nanometer scale. Next-generation devices require that the magnetic state of materials is manipulated on fast timescales and at the nanometer level. However, a complete microscopic understanding of magnetization dynamics that involves the correlated interactions of spins, electrons, photons, and phonons on femtosecond timescales has yet to be developed.

In our work, we experimentally answered the fundamental question of whether the magnetization dynamics of individual elements in a ferromagnetic alloy can differ on ultrafast timescales [1]. This is a very important fundamental question that has not been addressed either theoretically or experimentally to date, the answer to which reveals how the exchange interaction affects the ultrafast dynamics of elemental spin subsystems in complex materials.

To answer this question, we rapidly excite permalloy with a train of ultrashort (≈25 fs) laser pulses and probe the demagnetization dynamics with XUV pulses that allow to explore the involved spin dynamics *element specifically*.

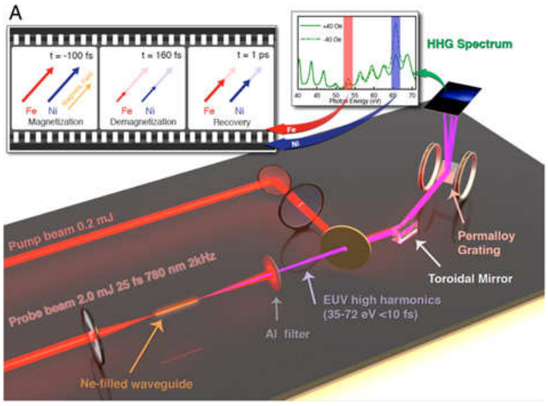

FIG. 1: Schematics of the experimental setup for XUV pump-probe measurement. XUV pulses (<10fs) are reflected from a permalloy grating sample, forming a spectrum on a CCD camera. The reflected HHG intensity at the Fe and Ni M-shell absorption edges (red and blue) depends on the magnetization direction. After rapid excitation of the electron system by a femtosecond laser pulse, various scattering processes between electrons and phonons (with and without spin-flips) determine the dynamical response of the system. First, the strongly excited electron gas thermalizes by predominantly electron-electron scattering to a Fermi-Dirac distribution. The ferromagnet starts to demagnetize because of spin-flip scattering events during this thermalization process. Electron-phonon scattering processes transfer energy from the excited electron gas to the lattice, and thermal equilibrium is typically reached on picosecond timescales. Finally, on nanosecond timescales, the material cools by thermal diffusion. The red and blue arrows in the lower boxes show the observed distinct demagnetization dynamics of Fe and Ni in permalloy.

To reach the required temporal resolution in our experiment, sub-10 fs XUV light pulses from high-harmonic generation (HHG) are produced by focusing 2 mJ femtosecond laser pulses into a Ne-filled waveguide. The generated harmonic photon energies of 35 to 72 eV include the *M* absorption edges of Fe (54 eV) and Ni (67 eV).

In the transverse magneto-optical Kerr-effect (T-MOKE) geometry used for these measurements, the intensity of the reflected HHG light is directly proportional to the sample magnetization transverse to the plane of incidence [6].

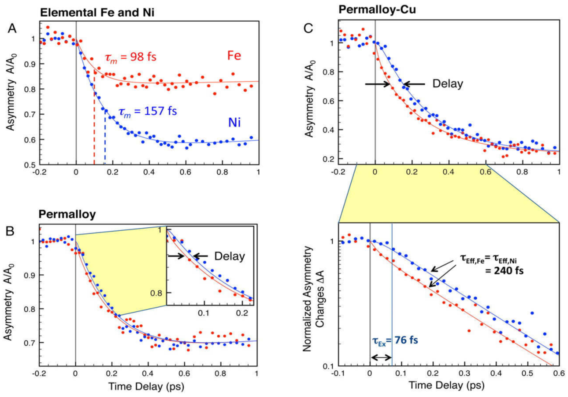

FIG. 2: Ultrafast demagnetization of Fe (red dots) and Ni (blue dots) for elemental Fe and Ni (A), in permalloy (B), and in permalloy-Cu (C). Fits to the model (solid lines) are used to extract the intrinsic demagnetization times for Fe and Ni in the alloys, τ_{Fe} *and* τ_{Ni}*, as well as the exchange time* τ_{Ex}*, after which the Fe and Ni spin baths return to equilibrium with respect to each other with an effective demagnetization time constant of* τ_{Eff}*. The data for permalloy-Cu (C) is also shown in log-scale as a function of the normalized asymmetry changes* $\Delta A(t) = (A(t)-A_{min})/(A_0-A_{min})$*, where* A_0 *is the asymmetry amplitude and* A_{min} *the minimum asymmetry reached in the demagnetization process.*

We probe the magnetization by reflecting the XUV beam from the sample, as shown in Fig.1. To gain insight into element sensitive dynamics, we used gratings patterned in three different ways: (*i*) alternating elemental Fe and Ni stripes to probe the behavior of the pure materials; (*ii*) permalloy ($Ni_{0.8}Fe_{0.2}$); (*iii*) permalloy-Cu ($(Ni_{0.8}Fe_{0.2})_{0.6}Cu_{0.4}$). The HHG spectrum diffracted from the sample grating is focused onto an X-ray CCD camera. In order to determine the T-MOKE asymmetry, the change in reflected intensity of the XUV light at the *M*-absorption edges is monitored while the magnetization direction of the sample is reversed. After taking the spectra, the T-MOKE asymmetry parameter *A* is calculated from the experimental data as

$$A = \frac{I_r(H^{\uparrow}) - I_r(H^{\downarrow})}{I_r(H^{\uparrow}) + I_r(H^{\downarrow})}$$

where $I_r(H^{\uparrow})$ and $I_r(H^{\downarrow})$ denote the reflected XUV intensities for the two magnetization directions. More details of the measurement method can be found in Refs. [1-6]. We note that the demagnetization data for Fe and Ni are collected *at the same time* in this measurement, precluding any mismatch between the two elements in the determination of time-zero between pump and probe laser pulses.

The superior time resolution of our experiment allows us to observe that the magnetization dynamics of Fe and Ni are *transiently delayed* with respect to each other by about 18 fs in pure permalloy and 76 fs in Cu-diluted permalloy (Fig.2). We ascribe this transient decoupling in the magnetic behavior to the finite strength of the fundamental quantum exchange interaction between Fe and Ni atoms in the material. Specifically, for times shorter than the characteristic timescale for exchange coupling, the magnetization of Fe quenches more strongly than that of Ni. Then, as the Fe moments start to randomize, the strong ferromagnetic interatomic exchange interaction between Fe and Ni induces further demagnetization in Ni, with a characteristic delay determined by the strength of the Fe-Ni exchange interaction. Interatomic exchange energies of transition metal alloys are in the 10–100 meV range, yielding characteristic exchange times in the femtosecond range which corresponds to finite spin-flip scattering times of 10–100 fs. Our findings provide crucial information for open questions in femtosecond magnetization dynamics in the case of metallic, multispecies, exchange-coupled systems.

In summary, we explore the consequences of the fundamental quantum exchange interaction in strongly coupled ferromagnetic systems, showing that quantitatively *different magnetization dynamics of the individual elements can be observed on timescales shorter than the characteristic exchange timescale*. On longer timescales, the dynamics are dominated by the faster one of the two species. Analysis of our data indicates that the observed differences in demagnetization rate are primarily determined by intrinsic properties of the material. This fact has significant impact for fundamental models of ultrafast magnetism, and for the dynamical magnetic behavior for all types of exchange-coupled materials, including both the alloys and multilayer structures that are widely used for data storage.

---

[1] Mathias, S., La-O-Vorakiat,C, Grychtol,P., Granitzka, P., Turgut, E., Shaw, J.M., Adam, R., Nembach, H.T., Siemens, M., Eich, S., Schneider, C. M., Silva, T., Aeschlimann, M., Murnane, M.M. & Kapteyn, H., PNAS 109, 4792 (2012)

[2] La-O-Vorakiat, C., Turgut, E., Teale, C.A., Kapteyn, H.C., Murnane, M.M., Mathias, S., Aeschlimann, M., Schneider, C.M., Shaw, J., Nembach, H. & Silva, T., Physical Review X 2, 011005 (2012)

[3] Adam, R., Grychtol, P., Cramm, S. & Schneider, C.M. Journal of Electron Spectroscopy and Related Phenomena 184, 291 (2011)

[4] Grychtol, P., Adam, R., Valencia, S., Cramm, S., Bürgler, D.E. & Schneider, C.M., Phys. Rev. B 82, 054433 (2010)

[5] La-O-Vorakiat, C., Siemens, M., Murnane, M., Kapteyn, H., Mathias, S., Aeschlimann, M., Grychtol, P., Adam, R., Schneider, C. M., Shaw, J., Nembach, H. & Silva, T., Phys. Rev. Lett. 103, 257402 (2009)

[6] Hecker, M., Oppeneer, P.M., Valencia, S., Mertins, H.-Ch. & Schneider, C.M., Journal of Electron Spectroscopy and Related Phenomena 144–147, 881 (2005)

Double-vortex spin-torque oscillators

V. Sluka[1,2], A.M. Deac[1,2], A. Kákay[1], R. Hertel[3], D. E. Bürgler[1], and C. M. Schneider[1]

[1]Peter Grünberg Institut (PGI-6), Forschungszentrum Jülich
[2]Institute of Ion-Beam Physics and Materials Research, Helmholtz-Zentrum Dresden-Rossendorf
[3]Institut de Physique et Chimie des Matériaux de Strasbourg, Université de Strasbourg

The interaction of spin-polarized currents with a magnetic system – the spin-transfer torque – provides a novel handle on magnetization dynamics, which enables the operation of spin-torque oscillators (STO). Here, we realize and study STO comprising two stacked magnetic vortices. These double-vortex STO (DV-STO) are a promising application for spin-transfer torque physics. The major challenge is to increase the microwave output power by synchronizing an array of DV-STO. We demonstrate phase-locking of a DV- STO to an external high-frequency signal as a prerequisite for DV-STO synchronization.

Typical STO are pillar-shaped structures comprising a ”fixed” ferromagnetic (FM) layer acting as a polarizer for the electric current and a second ”free” FM layer, the magnetization of which is dynamically excited under the impact of the spin-polarized current. Fixed and free layers are separated by a non-magnetic (NM) spacer layer with a thickness in the nanometre range such that the FM/NM/FM trilayer shows giant or tunnelling magnetoresistance (GMR, TMR). The magnetoresistive response reflects the relative magnetization alignment of the two FM layers and turns the nanometre-scaled pillar structures into sources for high-frequency (HF) signals in the GHz range. The frequency is tuneable via the applied direct current (DC) and/or the external magnetic field. However, the HF output power of an individual all-metallic STO is very low (typically < 1 nW). A promising strategy to increase the HF output power is to operate STO in the vortex mode, i.e. by exciting the gyrotropic vortex motion with a DC current [1]. This is most efficiently realized in a double-vortex (DV) configuration [2,3]. Advantages of vortex STO are high tunability, narrow linewidths, and that they intrinsically operate in zero external field.

However, to achieve a usable microwave power (several µW) one still needs large arrays of DV-STO radiating coherently. The excitation of an array of DV-STO in a coherent, phase-locked manner delivers a significant power increase, as N coherently coupled oscillators can emit up to the N^2-fold power. There are two ways to achieve STO-STO coupling, which is a requirement for synchronization. The first method employs spin waves in a common FM layer (e.g. the bottom FM layer). The fast decay of spin waves renders this interaction short-range, such that the STO-STO separation must be of the order of the STO's diameter, i.e. clearly below 1 µm. The second coupling mechanism operates via microwaves that propagate in common electrodes [4]. The negligible losses of electrical microwave signals over long distances allows for macroscopic STO separation. Experimentally, the electrical coupling via microwaves can be addressed by injection locking experiments, which study the interaction of a STO with an external applied electrical HF signal. In general, oscillators that are subjected to an external periodic driving force tend to tune their frequency to that of the external force, building up a constant phase relationship. Necessary conditions for phase-locking are oscillator-oscillator coupling of suitable strength and that the detuning between the external frequency and the auto oscillator eigenfrequency is sufficiently small. Here we demonstrate for the first time phase-locking of the vortex dynamics in the DV state of a pillar STO [5]. We fabricate our samples from epitaxial (001)-oriented Fe 30 nm/Ag 6 nm/Fe 15 nm trilayers grown by beam epitaxy on a GaAs(001)/Fe 1 nm/Ag 150 nm buffer system and capped with 50 nm Au. Cylindrical pillars of 150 nm diameter are fabricated by means of optical and electron beam lithography combined with ion beam etching, reactive ion etching, and lift-off. We etch through the Fe/Ag/Fe multilayer, such that the pillar comprises two FM disks stacked on top of each other [inset of Fig. 1]. The electrode layout allows for contacting by two microwave probes via coplanar waveguides. One is used to inject an HF current (frequency f_{ext}) from a network analyzer and the other is connected to a 30 dB amplifier and a spectrum analyzer. A DC current that excites the magnetization dynamics and enables GMR measurements is applied via a bias-T that decouples the DC current from the HF equipment. The experiments were conducted at room temperature. The preparation of a DV state is rather involved as two degrees of freedom of the vortex structure, vorticity and core polarity, allow for 16

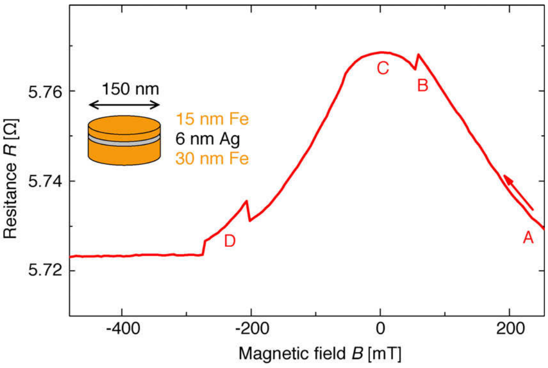

FIG. 1: The GMR field cycle for a weak current flowing perpendicular to the layers (i.e. along the pillar axis) indicates different magnetization configurations labelled by letters. The magnetic field was tilted 27° out of plane. Similar behaviour is observed for strictly in-plane fields.

different DV states. Here, we are interested in a configuration with opposite vorticities and arbitrary core polarizations.

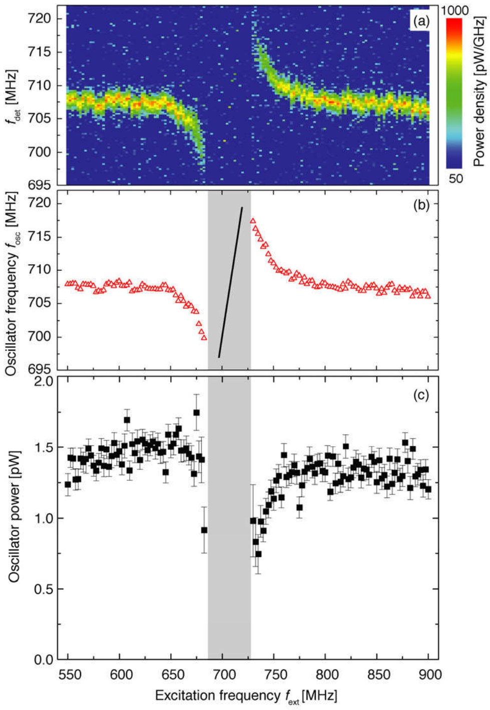

FIG. 2: Locking behaviour of a DV-STO. (a) Power spectrum and (b) extracted peak positions of the current-induced magnetization dynamics as a function of the HF excitation frequency f_{ext},. The HF excitation amplitude is -4 dBm and I_{DC} = −9 mA. No magnetic field is applied. Background subtraction is applied to remove the excitation signal [black line in (b)] from the spectra. (c) Oscillator power obtained from Lorentzian fits.

We start the state preparation by applying a positive in-plane saturating field and a DC current of I_{DC} = +15mA (i.e. electron flow from the top to the bottom disk). After ramping the field to zero, while keeping I_{DC} constant, vortices have nucleated in both disks. Both vorticities are counter-clockwise as defined by the Oersted field of the positive I_{DC}. Next we tune I_{DC} to -10 mA and again increase the field to +254 mT, i.e. a value between the two fields, for which the two vortices are expelled from their disks. The vortex in the thinner top disk is expelled, while the vortex in the bottom disk is retained. In this state A we start the measurement shown in Fig. 1. For each field value we measure the DC resistance and simultaneously a HF spectrum (not shown). Upon reducing the field to below 100 mT the resistance increases and in state B we observe excitations with frequencies around 1.13 GHz. The small step in the resistance at 59 mT is accompanied by a sharp drop of the excitation frequency by 480 MHz (state C), which indicates the formation of the DV state. The new vortex in the top disk forms with a vorticity according to the actual Oersted field, which for negative I_{DC} circulates clockwise. The resistance difference between state C and saturation is 45 mΩ, which is close to the difference of 50 mΩ between parallel and antiparallel aligned homogeneously magnetized layers. This is expected for a DV configuration with opposite vorticities, because for this situation top and bottom magnetizations are locally antiparallel. As the field is swept towards negative values, the cores of the two vortices shift into opposite directions, which reduces the resistance monotonically. The discontinuity at -202 mT is caused by expelling of one of the vortices. The comparison with simulations and the similar field dependences of the resistance in states A and D suggest that the remaining single-vortex state is due to a vortex in the bottom disk. Finally, at -271 mT saturation is reached.

For the injection-locking experiment we prepare the DV state [state C in Fig. 1] and apply I_{DC} = −9 mA. In Fig. 2 we sweep the frequency f_{ext} from 550 to 900 MHz. The power at the output socket of the network analyzer is -4 dBm. We record spectra for each value of f_{ext}. For large detuning, the STO frequency f_{osc} remains undisturbed at f_0 = 708 MHz. As f_{ext} approaches that of the oscillator, the latter clearly tunes its frequency towards that of the source. Thus, the DV-STO is phase-locked between 695 and 720 MHz. Lorentzian fits to the background-subtracted spectra yield precise peak positions of the STO signal f_{osc} as a function of the external frequency f_{ext} [Fig. 2(b)]. The fitted STO power (at the amplifier input) is plotted in Fig. 2(c). We observe a decrease of up to 50% in oscillator power as the detuning (f_{det} − f_0) is driven towards zero, indicating that the oscillator cannot anymore be regarded as weakly forced. In that limit, one would instead expect the external signal to mostly affect the oscillator phase, while its power should remain unperturbed. After the frequency scan, we measure a field loop at I_{DC} = −10 mA. The obtained GMR and frequency versus field profiles confirm that the sample still is in the initially prepared DV state.

In conclusion, we have clearly demonstrated phase-locking of the current-induced dynamic mode of a DV-STO confirming that DV states are nonlinear oscillators [5]. Injection-locking of this sort is a prerequisite for the synchronization of DV-STO via microwaves that propagate in common electrodes. The rich dynamic properties of DV-STO, which still needs to be explored in detail, makes them promising candidates for future technology ingredients.

[1] R. Lehndorff, D.E. Bürgler, S. Gliga, R. Hertel, P. Grünberg, and C.M. Schneider, Phys. Rev. B **80**, 054412 (2009).

[2] A.V. Khvalkovskiy, J. Grollier, N. Locatelli, Y.V. Gorbunov, K.A. Zvezdin, and V. Cros. Appl. Phys. Lett. **96**, 212507 (2010).

[3] V. Sluka, A. Kákay, A.M. Deac, D.E. Bürgler, R. Hertel, and C.M. Schneider. J. Phys. D: Appl. Phys. **44**, 384002 (2011).

[4] J. Grollier, V. Cros, and A. Fert. Phys. Rev. B **73**, 060409 (2006).

[5] D.E. Bürgler, V. Sluka, R. Lehndorff, A.M. Deac, A. Kákay, R. Hertel, and C.M. Schneider. SPIE Proc. **8100**, 18 (2011).

The Planar Hall Effect in a Modern Ferromagnet with Potential for Sensor Applications

Klaus M. Seemann

Peter Grünberg Institut (PGI-6), Forschungszentrum Jülich, 52425 Jülich

Detecting the minute stray field of magnetic nanoparticles lays down challenging requirements for spintronic sensors. Demands for ultra-high sensitivity combined with robustness propose sensor principles based on nanocrystalline soft-magnetic alloys. Cobalt-Iron-Boron (CoFeB) alloys offer considerable advantages over conventional permalloy (Py) with this respect. The nanocrystalline morphology of CoFeB maintains the coherence of the magnetization in exchange-biased systems and allows for a maximal spin-dependent electron transport signal in planar Hall effect (PHE) devices. From a fundamental physical perspective the planar Hall effect was proven to have its origin in the well-known anisotropic magnetoresistance, which is an effect that is accessible in single layers of ferromagnetic metals. This in combination with the antiferromagnetic exchange-bias mediating the coherence of the localized spins of CoFeB forms the basis for the robustness required in spintronic sensor applications urgently sought for especially in the biomedical field.

Spintronic sensors for magnetic nanoparticle detection in fluids bridge the gap between large scale fluorescence arrays for DNA analysis, the Lab-on-a-Chip-type biomedical applications, drug loaded magnetic nanoparticle carriers and nanoparticle based bio-catalysis.

Spintronic devices based on the planar Hall effect offer high sensitivity and the robustness required in fluidic media. The nanocrystalline $Co_{60}Fe_{20}B_{20}$ alloy prepared to a single magnetic domain state by exchange-bias that is facilitated through antiferromagnetically ordered $Ir_{20}Mn_{80}$ has been used as a model system (Fig. 1). The physical relation between the well-known anisotropic magneto-resistance and the transverse electron transport effect, i.e. the PHE has been a focus of investigations.

The morphology provided by CoFeB nanocrystals of a grain size of approximately 5 nanometers of arbitrary crystallographic orientation within the layer of 50 nm thickness does not affect the ferromagnetic coupling of the localized spins across several neighbouring CoFeB nano-grains. Hence the formation of a ferromagnetically ordered single-domain state over the entire micron-sized device geometry is mediated by the ex-change bias effect of the antiferromagnetic Iridium-Manganese alloy and takes place in an unhindered way. As a consequence of this long-range coherence of the localized spins within CoFeB, a transverse voltage signal similar to the Hall effect builds up upon sourcing a current. The transverse signal becomes maximal for an angle of 45° coherent rotation of the collinear spins in CoFeB against the direction of the current. However, the maximal field sensitivity of the planar Hall device has been shown to be around zero magnetic field, i.e. minute elongations of the collinearly rotating magnetization cause a significant variation of the transverse voltage, in the present case in the sound range of several microvolts. Due to the vanishing magneto-crystalline anisotropy of nanocrystalline CoFeB, this sensitivity of the planar Hall device for external magnetic fields is considerably enhanced over similar devices based on permalloy, a NiFe-alloy of non-vanishing magneto-crystalline anisotropy.

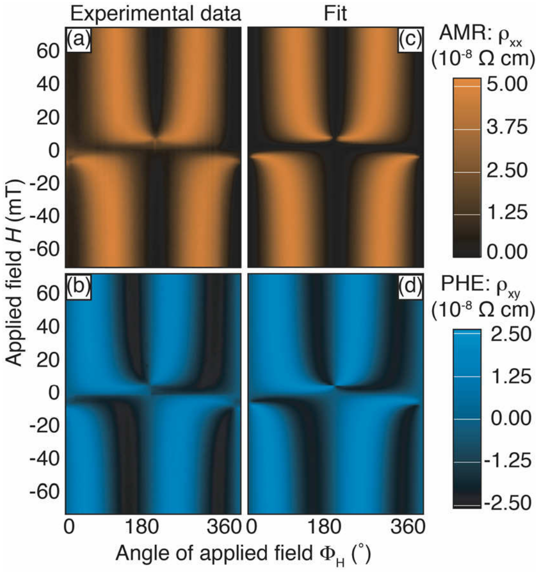

FIG. 1: The planar Hall effect (b: experiment and d: theory) is closely related to the anisotropic magneto-resistance (a: experiment and c: theory) [1]. In the softmagnetic cobalt-iron-boron alloy the planar Hall effect yields a magnetic sensitiviy of an order of magnitude higher than in conventional permalloy.

The fact, that a collinear rotation of the single-domain state was achieved in CoFeB planar Hall effect devices upon applying magnetic fields in the film plane is promising for sensoric applications. The robustness of a metallic structure that consists of a coupled antiferromagnet-ferromagnet bi-layer that can be sealed for example against a fluidic medium without detrimentally affecting the sensor functionality is to be considered advantageous for the detection of magnetic nanoparticles in liquid suspensions.

The sensor principle employing the planar Hall effect on the basis of a soft-magnetic CoFeB alloy is versatile and robust solution to detect magnetic nanoparticles in fluidic media. Other alternative approaches utilize the anomalous Hall effect in perpendicularly magnetized Cobalt-Platinum multi-layers sandwiched by thin layers of Magnesium-Oxide to enhance the sensitivity of such Hall bar devices to a magnetic field [2]. However, while the strong spin-orbit interaction strength induced by the heavy Platinum atoms increases the scale of the anomalous Hall effect dramatically [3], the sensitivity in the zero-field region important for magnetic nanoparticle detection is detrimentally affected in such devices.

A lower spin-orbit interaction strength as present in the magnetic Iron-Palladium-alloys are more favorable with this respect and also offer reliable spintronic functionality at room temperature. Especially the controlled introduction of disorder into the epitaxially ordered L1o-phase of the Iron-Palladium alloy gives rise to a favorably enhanced domain wall magneto-resistance effect. Moreover, the perpendicularly magnetized L1o-alloys provide for a high spin-polarization of the diffusive current combined with magnetic domain walls of extremely narrow widths of approximately 10 nanometers. [4, 5].

The electrical resistance due to magnetic domain walls has its origin in the spin-torque effect of conduction electrons and hence also belongs to the spin-dependent transport phenomena in transition metal ferromagnetic materials. However, magnetic domain walls are considered to be more suitable for future logic devices or mass data storage rather than magnetic sensors for nanoparticle detection in fluids, since the immobilization of magnetic particles at domain walls is believed to hinder the detection process.

In comparison, the coherent rotation of the collinear magnetization found in micron-sized planar Hall devices upon applying external fields is favorable for spintronic sensor devices. The detection of individual nanoparticles of only few nanometers in diameter is a most competitive goal to reach, yet. The difference in magnetic stray field originating from a variable concentration of nanoparticles in a fluid or a variable area density of nanoparticles attached to the surface of micron-sized objects in liquid suspension however is achievable.

From a fundamental physical perspective, it is the coherence of the ferromagnetic coupling of the localized spins of CoFeB persistent on a long range and mediated by antiferromagnetic IrMn that at the same time transgresses the manifold grain boundaries of the nano-crystalline morphology and gives rise to its enhanced soft-magnetic behaviour.

The random orientation of the CoFeB nanocrystallites hinders the formation a residual magneto-crystalline anisotropy. At the same time however, the planar Hall effect was shown in exchange-biased CoFeB to be closely related to the anisotropic magneto-resistance effect, which in most transition metal ferromagnetic alloys is based on the magneto-crystalline anisotropy. In exchange-biased CoFeB it is found that the collinear orientation of the localized spins, i.e. the magnetization, is due to a decoupling of spins and lattice induced by exchange bias. This effectively reduces the absolute scale of the anisotropic magneto-resistance in comparison to epitaxial ferromagnets, but also significantly reduces the coercivity field leading to an enhanced soft-magnetic behaviour, which is paramount for sensor applications for instance.

The preservation of the angular dependence of the electron transport signals detected in the planar Hall devices in the longitudinal case (Fig. 1. a: experiment, c: theory) and the transversal case (Fig. 1. b: experiment, d: theory) [1] despite the exchange bias driven decoupling of localized spins and the random orientation of the nano-grain lattices of CoFeB is an interesting quantum feature observable at room temperature. The robustness and comparative simplicity of the planar Hall effect devices may open up new routes to integrated solutions in the biomedical field.

---

[1] K.M. Seemann, F. Freimuth, H. Zhang, S. Blügel, Y. Mokrousov,, D.E. Bürgler, and C.M. Schneider, Phys. Rev. Lett. 107, 086603 (2011).

[2] S.L. Zhang, J. Teng, J.Y. Zhang, Y. Liu, J.W. Li, G.H. Yu, and S. G. Wang, Appl. Phys. Lett. 97, 222504 (2010)

[3] K.M. Seemann, Y. Mokrousov, A. Aziz, J. Miguel, F. Kronast, W. Kuch, M.G. Blamire, A.T. Hindmarch, B.J. Hickey, I. Souza, and C.H. Marrows, Phys. Rev. Lett., 104, 076402, (2010)

[4] K.M. Seemann, M.C Hickey, V. Baltz, B.J. Hickey, and C.H. Marrows, New J. Phys. 12, 033033 (2010)

[5] K.M. Seemann, V. Baltz, M. MacKenzie, J.N. Chapman, B.J. Hickey, and C.H. Marrows, Phys. Rev. B, 76, 174435 (2007)

Model Systems for Molecule-Electrode Contacts in Molecular Spintronics

B. Botar[1], C. Besson[1,2], M. Speldrich[2], X. Fang[3], P. Kögerler[1,2]

[1]Peter Grünberg Institut-6, Forschungszentrum Jülich
[2]Institut für Anorganische Chemie, RWTH Aachen University
[3]Ames Laboratory, Iowa State University

Two molecular magnets constructed from polyoxotungstate cluster anions and cationic $Mn^{III/IV}_4O_4$ cubane-based spin polytopes illustrate the significant influence of charge distribution on the molecular magnetic anisotropy. In turn, the magnetic characteristics observed for these model systems are consequential for the magnetic properties of molecular magnets attached to metallic or metal oxide electrodes, i.e. contact modes potentially characterized by pronounced electrical field gradients at the sites of the spin polytope.

The integration of individual molecular magnets into electronic devices, resulting e.g. in a molecular transistor, mandates reliable contacts between the molecule and both conducting metallic (source and drain) and non-conducting (gate) metal oxide electrodes. The generation of reliable and reproducible molecule-electrode contacts remains a pressing challenge, which we aim to address via numerous molecular functionalization steps, which amounts to a bottom-up alternative to the conventional top-down approach using break junctions. A second fundamental aspect yet to be elucidated concerns the magnetic consequences of the binding of molecules to metallic and non-metallic surfaces. In this context, we target to mimic several scenarios of surface-attached spin polytopes, employing molecular metal oxide clusters as model systems for gate electrode surfaces. Specifically, magnetically functionalized polyoxometalate cluster anions can ideally recreate various electrical field environments that act upon the attached spin polytopes [1,2]. In this context polyoxometalates exhibit several benefits: their negative charge can be localized at specific lacunary defect sites; their rigid coordination environments facilitate targeted design of magnetic core structures; as ligands coordinating to spin centers they can also induce strong axial magnetic anisotropy. Our strategy of replacing organic bridging groups on preformed manganese carboxylate clusters with polyoxometalate ligands has resulted in a range of cationic polynuclear Mn(III/IV) spin clusters attached to polyoxotungstate groups that exhibit high-spin ground states but strongly differ in their magnetic anisotropy, which is tentatively assigned to the arrangement of the negatively charged polyanion building blocks.

A tetranuclear $[Mn^{III}_3Mn^{IV}O_4]$ cubane-type spin cluster can be obtained from reaction of the single-molecule magnet $\{Mn^{III/IV}_{12}\text{-acetate}\}$ with the (diamagnetic) polyoxotungstate $[\alpha\text{-}P_2W_{15}O_{56}]^{12-}$. The magnetic core of the resulting complex $[(\alpha\text{-}P_2W_{15}O_{56})Mn^{III}_3Mn^{IV}O_3(CH_3COO)_3]^{8-}$ (**1**) coordinates to the heptadentate $\{P_2W_{15}\}$ ligand on one side and three bridging acetate groups situated on the opposite site of the Mn_4O_4 cube (Fig. 1). Analogous to other $\{Mn^{III}_3Mn^{IV}\}$ single-molecule magnets of the cubane type, **1** has an $S = 9/2$ spin ground state due to antiferromagnetic exchange between a Mn^{IV} ($S = 3/2$; $^4A_2$) apex and a triangle of three ferromagnetically coupled Mn^{III} ($S = 2$; $^5B_{1g}$) ions. However, **1** does not constitute a single-molecule magnet and is surprisingly characterized by a *positive* axial anisotropy parameter ($D = +0.36\ \text{cm}^{-1}$) that leads to the absence of an energy barrier between the zero field-split $m_S = +9/2, +7/2, \ldots, -7/2, -9/2$ substates and therefore an absence of slow relaxation of the magnetization at low temperatures.

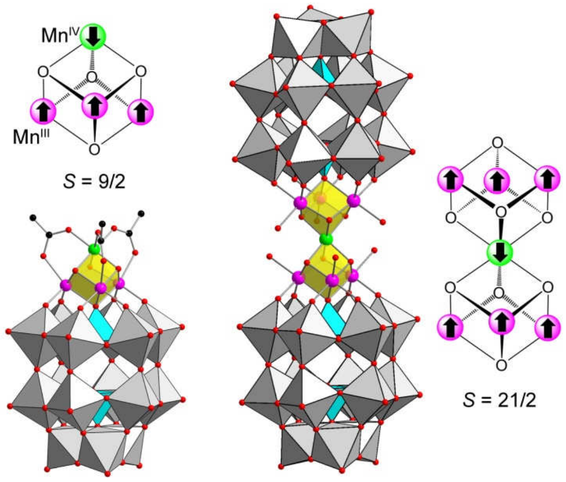

*FIG. 1: Structures of the polyoxometalate complexes **1** (left; approx. C_{3v}) and **2** (right; approx. D_{3h}) with their cubane-based magnetic core structures highlighted in yellow. The $[\alpha\text{-}P_2W_{15}O_{56}]^{12-}$ groups are shown in polyhedral representation. The schematic diagrams for the Mn_4O_4 (**1**) and Mn_7O_8 (**2**) subgroups indicate the ground state spin alignments. Mn^{IV}: green; Mn^{III}: purple; O: red; C: black; WO_6: gray octahedra; PO_4: blue tetrahedra. Hydrogen omitted for clarity.*

A closely related cluster, based on a $\{Mn^{III}_3Mn^{IV}Mn^{III}_3\}$ spin polytope featuring two corner-sharing Mn_4O_4 cubane units, can be realized by reducing the concentration of acetate ligands in the reaction solution, which effectively terminate the spin cluster coordination sites in **1**. An accordingly adapted synthesis procedure then yields the cluster anion $[(\alpha\text{-}P_2W_{15}O_{56})_2Mn^{III}_6Mn^{IV}O_6(H_2O)_6]^{14-}$ (**2**). This cluster anion now features two trans-positioned $\{P_2W_{15}\}$ groups that attach to the opposite ends of the central $\{Mn^{III}_3Mn^{IV}Mn^{III}_3\}$ group (Fig. 1). The bridging acetate groups in **1** are now replaced with terminal H_2O ligands that complete the octahedral geometry of the Jahn–Teller distorted Mn^{III} centers and defining the orientation of their elongation axes. The angles between the elongation axes and the C_3 axis of the molecule (avg. 54.59°) deviate minimally from those in **1** (avg. 56.36°). The removal of acetate bridges between Mn^{III} and Mn^{IV} ions also results in slightly longer $Mn^{III}\cdots Mn^{IV}$ distances (avg. 2.855 vs. 2.801 Å in **1**) and a concomitant decrease in $Mn^{III}\cdots Mn^{III}$ distances (avg. 3.092 vs. 3.152 Å). Overall, cluster anion **2** is approximate D_{3d}-symmetric, and the Mn^{IV} ion defines the inversion center.

The geometric similarity of the magnetic core structures in **1** and **2** implies similar superexchange, i.e. ferromagnetic Mn^{III}–Mn^{III} and antiferromagnetic Mn^{III}–Mn^{IV} contacts. For **2**, this produces a ground state configuration with the spins of the six Mn^{III} ions aligned parallel, and antiparallel to the central Mn^{IV} ion, i.e. an $S = 21/2$ ground state (in a spin-only approximation). Based on the approximate D_{3d} point group symmetry of **2**, the exchange interactions can be grouped in Mn^{III}–Mn^{IV} (J_1) and Mn^{III}–Mn^{III} (J_2) contacts, each mediated by two μ-O sites. Least-squares fitting to the low-field susceptibility data for **2** in order to parameterize the magnetic interactions within the $\{Mn^{III}_3Mn^{IV}Mn^{III}_3\}$ spin polytope in **2** relies on modeling all relevant single-ion effects as well as Heisenberg-type exchange coupling. Fitting to temperature- and field-dependent susceptibility data [3] then results in $J_1 = -18.8$ cm^{-1} and $J_2 = 12.5$ cm^{-1}. Compared to **1**, J_2 is little changed (10.2 cm^{-1} in **1**) whereas the J_2 is considerably weakened (–31.3 cm^{-1} in **1**), emphasizing the influence of acetate bridging ligands on the superexchange energies. On the other hand, the ligand field parameters in **2** are in line with the analogous values for compound **1**. Importantly, and contrary to **1**, below 3 K cluster **2** exhibits the frequency-dependent ac susceptibility characteristics of a single-molecule magnet, where the m_S substates of the $S = 21/2$ ground state multiplet now form a parabolic energy barrier separating the highest ($m_S = \pm 21/2$) substates. This in turn causes a slowing of the magnetization relaxation upon a field change. For **2**, the total zero-field splitting of 15.7 cm^{-1} of the ground state relates to a *negative* empirical axial anisotropy parameter $D = -0.143$ cm^{-1}.

The two drastically different zero field-splitting energies derived for cluster anions **1** and **2** imply important postulates for molecular magnets in highly anisotropic environments, such as that of a charged molecular magnet attached to a metallic surface or to a electron density-rich defect site of a metal oxide surface: In **1**, the $\{Mn^{III}_3Mn^{IV}O_4\}$ substructure – a crucial structural feature of numerous $S = 9/2$ SMMs – is characterized by an “inverted” parabola of m_S substates, leaving the $m_S = \pm 1/2$ substates the energetically lowest. Comparing these results to compound **2**, where the geometric parameters relevant to the molecular magnetic anisotropy (e.g. the alignment between the Jahn Teller axes) are very similar, we tentatively attribute this unexpected sign change in D to the pronounced dipole moment of **1** vs. the absence of a dipole moment in **2**. The electrical dipole moment caused by the $[Mn^{III}_3Mn^{IV}O_4(AcO)_3]^{4+}$ group and the $[P_2W_{15}O_{56}]^{12-}$ polyoxometalate likely influences the spin-orbit coupling which fundamentally depends on the electrical field gradient. Correspondingly, the absence of a significant net dipole moment in **2**, as well as in all other known polyoxometalate-based single-molecule magnets, appears to preserve the energy barrier in m_S states originating from zero field-splitting. Such variations in the electrical field gradients that molecular magnets experience upon surface attachment, caused e.g. by mirror charges, surface defect sites, or simple reorganization of counter ions, will therefore have to be taken into account for the interpretation of spin-dependent transport through such contacted molecular magnets.

---

[1] X. Fang, P. Kögerler, M. Speldrich, H. Schilder, M. Luban, Chem. Commun., 48, 1218 (2012).

[2] X. Fang, M. Speldrich, H. Schilder, R. Cao, K. P. O’Halloran, C. L. Hill, P. Kögerler, Chem. Commun., 46, 2760 (2010).

[3] M. Speldrich, H. Schilder, H. Lueken, P. Kögerler, Isr. J. Chem., 51, 215 (2011).

Metal / Molecule Contacts: From Electronic Properties to Charge Transport

S. Soubatch[1], R. Temirov[1] P. Puschnig[2], E.-M. Reinisch[2], T. Ules[2], G. Koller[2], M. Ostler[3], L. Romaner[4], C. Toher[5], F. Pump[5], A. Greuling[6], M. Kaczmarski[6], M. G. Ramsey[2] C. Ambrosch-Draxl[4], G. Cuniberti[5], M. Rohlfing[6], F. B. Anders[7], F. S. Tautz[1]

[1]Peter Grünberg Institut-3, Forschungszentrum Jülich, 52425 Jülich
[2]Universität Graz
[3]Universität Erlangen
[4]Montanuniversität Leoben
[5]TU Dresden
[6]Universität Osnabrück
[7]TU Dortmund

Any progress toward the vision of molecular electronics requires a thorough understanding of current conduction through single molecules. For this reason, an intense effort has been focused recently on transport experiments in metal/molecule/metal junctions. However, before transport data can be understood quantitatively, a few prerequisites have to be fulfilled: The geometric and the electronic structures of the metal/molecule contact have be known, and electron correlation effects have to taken into account. Here we present new experimental and theoretical approaches to tackle these challenges. All experiments and simulations reported here have been carried out on the prototypical PTCDA molecule on silver surfaces.

Electronic structure of metal-molecule contacts

The valence bands of large conjugated molecules consist of a multiplicity of closely spaced molecular states, and their correct assignment is challenging both experimentally and theoretically. Experimentally, energy positions of molecular orbitals in organic molecular layers can be studied by ultraviolet photoemission spectroscopy (UPS). However, UPS spectra of thin molecular layers on metals often show only weak and rather broad features and are, therefore, not always conclusive. Also, UPS data depend on the experimental geometry, molecular orientation, and photon energy, which further complicates the assignment of the measured peaks. Therefore, calculated densities of states (DOSs) from ab initio electronic-structure calculations are commonly used to complement and interpret UPS data. However, this is problematic, for various reasons: For example, in density-functional theory (DFT) calculations, both the orbital energies and the orbital-energy order rely on approximations made for exchange-correlation effects, and thus the functional chosen. In ref. [1] we present a tomographic analysis of angle resolved photoemission spectroscopy (ARPES) that provides a solution to the problem of assigning spectral features in UPS to specific molecular states.

We collect ARPES data in the full half-space above the sample surface. This data set contains a complete momentum- and energy-resolved DOS of the sample in the measured binding-energy range. To assign emissions to specific molecular states, we evaluate tomographic cross sections through the momentum-resolved data set and search for momentum space patterns that are characteristic for the corresponding molecular orbitals. This analysis is based on a simple plane-wave approximation for the final state in the photoemission process that has been shown to be appropriate for many π -conjugated organic molecules since scattering effects have been demonstrated to be negligible. In this approximation, the ARPES intensity distribution from a molecular state is related to the respective molecular orbital's Fourier transform.

The combination of these simulated momentum maps with experimental tomographs (Fig. 1) allows the quantitative deconvolution of a spectrum into contributions from individual molecular states beyond the limits of intrinsic line broadening and instrumental energy resolution, thus even if its deconvolution based on conventional peak fitting is impossible. This is achieved by carrying out the deconvolution in k-space, thereby making use of the full momentum space information of the molecular orbitals. The so-obtained orbital projected DOS provides a stringent test for electronic-structure theories including density functional calculations as well as wave-function-based approaches.

Comparison of ab-initio transport simulations to experiments in controlled geometries

Unfortunately, most single-molecule transport experiments to date do not allow the structural characterization of the junction independent of its transport properties. In this respect, STM-based approaches offer advantages. For example, in a recent publication, we have shown that a surface-adsorbed molecule can be chemically bonded to an

STM tip at a defined position within the molecule and peeled off the surface by tip retraction. Spectroscopic data recorded during tip retraction revealed a *mechanical gating effect*, in the sense that one of the molecular orbitals responds to the structural change and shifts with respect to the Fermi level of the substrate.

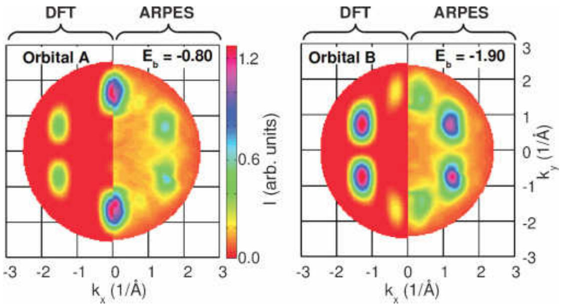

Fig. 1 Orbital Tomographs of PTCDA/Ag(110) [1].

In ref. [2] we present more comprehensive data of this experiment and compare the experimental data to an *ab initio* study of transport through this gated molecular wire. To describe the conduction through a molecule theoretically from first principles, three demanding quantum mechanical problems have to be addressed, namely, the geometric and electronic structures of the junction and the non-equilibrium current between two biased reservoirs across the molecular bridge. For the first two, we employ density functional theory (DFT), while the transport problem is solved by the non-equilibrium Green's function (NEGF) formalism.

Our analysis starts with a simulation of the contacting process during tip approach and the molecule-substrate bond-cleaving process during tip retraction. This yields structural and energetic data which can be compared to experimental results. In the second step, the transport calculations are carried out for the experimentally validated geometries and compared to experimental transport data. In this way, we can separately compare structure and transport simulations to experiment. Moreover, the comparison is not limited to a single point in the configuration space of the molecular junction, but includes a wide range of systematically and controllably varied configurations for each of which experimental transport data exist. The experiments thus provide a critical test of the theoretical methodology by effectively eliminating the possibility of fortuitous agreements between theory and experiments.

We find that DFT fully confirms structural aspects of the contacting and bond-cleaving scenarios deduced from experiment, while the transport simulations exhibit several differences compared to experiment. These can be understood as a failure of the DFT-NEGF platform with the local density approximation (LDA) to account for the dynamical nature of electron-electron correlations in the transport orbital of the molecule.

The role of electron correlations in molecular transport

The interrelation between the structure of the junction and its transport spectra was studied in ref. [2] in terms of transport theory disregarding the dynamical correlation mechanisms. However, we concluded in ref. [2] that the mechanical gating is subject to subtle details of electronic correlation, e.g., screening of the intramolecular Coulomb repulsion by the electrodes, which is not described by conventional density functional theory (DFT). In ref. [3] we therefore apply the following strategy: DFT (in the local density approximation LDA) addresses the atomistic details of the junction structure but does not provide reliable, well-founded spectral data. To evaluate the electronic spectrum, we combine DFT with many-body perturbation theory (MBPT) for nonlocal correlation and with numerical renormalization group (NRG) theory for correlation dynamics beyond the mean-field level. Among these three approaches, MBPT constitutes the essential link between DFT and NRG. Most NRG studies so far have been based on empirical model parameters. MBPT spectra, on the other hand, provide better-founded NRG input data.

MBPT for large and complex systems such as, for example, the tip/PTCDA/Ag junction, which combines metallic with non-metallic screening and shows partial occupancy of the most important molecular level, is computationally very expensive. For such systems, the commonly employed GW approximation of MBPT thus requires further simplification. Here we introduce the so-called "LDA+GdW" as an efficient and systematic implementation of MBPT.

Within this framework of LDA + GdW + NRG, we can correctly describe the mechanical gating of the molecular wire, and we reproduce the evolution of a Kondo resonance in the initially non-magnetic molecule. Moreover, we have presented an approach to calculating electronic spectra that systematically includes nonlocal and dynamic correlation effects. Because of its computational efficiency, this state-of-the-art approach to electronic spectra should be widely applicable.

---

[1] P. Puschnig, E.-M. Reinisch, T. Ules, G. Koller, S. Soubatch, M. Ostler, L. Romaner, F. S. Tautz, C. Ambrosch-Draxl, M. G. Ramsey, Phys. Rev. B 84 235427 (2011), Editor's Selection

[2] C. Toher, R. Temirov, A. Greuling, F. Pump, M. Kaczmarski, G. Cuniberti, M. Rohlfing, F. S. Tautz, Phys. Rev. B 83 155402 (2011), Editor's Selection

[3] A. Greuling, M. Rohlfing, R. Temirov, F. S. Tautz, F. B. Anders, Phys. Rev. B 84 125413 (2011)

Single Molecule and Single Atom Sensors for Atomic Resolution Imaging of Chemically Complex Surfaces

G. Kichin[1], **C. Weiss**[1], **C. Wagner**[1], **F. S. Tautz**[1], **R. Temirov**[1]

[1]Peter Grünberg Institut-3, Forschungszentrum Jülich, 52425 Jülich

Individual Xe atoms as well as single CO and CH_4 molecules, adsorbed at the tip of a scanning tunnelling microscope (STM), function as microscopic sensors that change the tunnelling current in response to the forces acting from the surface. The STM equipped with any of these sensors images the short-range Pauli repulsion and so resolves the inner structure of large organic molecules. Differences in the performance of the three studied sensors suggest that the sensor functionality can be tailored by tuning the interaction between the sensor particle and the STM tip.

Recently we demonstrated that condensing molecular hydrogen or deuterium (H_2 or D_2) in the junction of a low-temperature scanning tunneling microscope (STM) it is possible to resolve the inner structure of molecular adsorbates [1,2] and directly image intermolecular interactions [3]. To explain the new imaging mechanism, named Scanning Tunneling Hydrogen Microscopy (STHM) it has been proposed that a single (H_2 or D_2) molecule in the tunneling junction acts as a static nanoscale force sensor and signal transducer [2]: Interactions with the sample surface change the position of the sensor molecule relative to the STM tip, thus varying the strength of Pauli repulsion between the tip and the molecule; this is the “sensor” action.

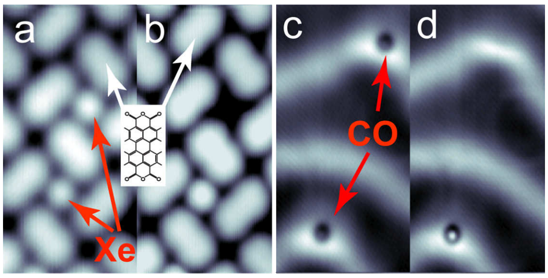

FIG. 1: (a). 5x2.5 nm² STM image of PTCDA/Au(111) with the two Xe atoms residing in the layer, measured with the clean Au tip. The chemical structure formula of PTCDA is shown in the inset. (b). The same as (a), but made after picking up the upper Xe atom with the tip. (c). 5x10 nm² STM image of the two CO molecules adsorbed on the clean Au(111) surface. (d). The same as (c), but made after picking up the upper CO molecule with the tip.

The “transducing” effect is based on the coupling of the Pauli force to the tunneling conductance; the coupling occurs because an increasing repulsion between tip and sensor molecule progressively depletes the tip’s density of states close to the Fermi level.

However, since neither H_2 nor D_2 can be imaged in the STM, the assumed structure of the nanoscale force sensor was up to now inferred from the properties of the STHM contrast itself, rather than determined independently. In these circumstances, an unambiguous proof for the idea that a single molecule acts as the force sensor has remained elusive. In our latest experiments we used Xe, CO and CH_4 to demonstrate directly that a single atom or molecule that decorates the STM tip indeed produces an STHM-like resolution [4]. Utilizing known recipes we were able to transfer single Xe atoms and CO molecules between the tip and the surface reproducibly (Fig. 1a-d). This has allowed us to study the imaging properties of the decorated STM tips systematically.

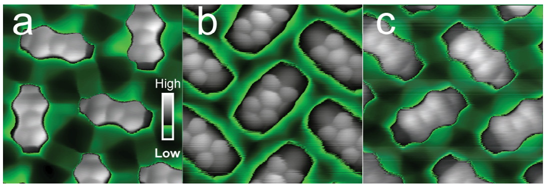

FIG. 2: (a). 2.5x2.5 nm² constant height image of the PTCDA/Au(111) recorded with the Xe-tip. The color palette is shown in the inset. Brightness scale: I_{low} =-0.4 nA, I_{high} =-8 nA. (b). The same as (a), but recorded with CO-tip. (c). The same as (a), but recorded with CH_4-tip.

When scanned at ordinary tunneling conditions, decorated tips yield a slight enhancement of spatial image resolution (Fig. 1b,d). However, when moved closer to the surface, these tips develop a new type of contrast (Fig. 2a-c). Comparing Fig. 2a to Fig. 1c from the ref. 3, we see that the contrast generated by the Xe-tip is almost identical to the STHM contrast obtained with D_2. Thus, the experiments with Xe allow significant progress in our understanding of STHM: Because the structure of the Xe-tip is known, it becomes unambiguously clear that the STHM-type contrast is produced by a single particle (Xe or D_2) which is bound to the apex of the STM tip, from where it interacts with the sample and thus senses the force exerted on it by the surface. The comparison between D_2-sensors and Xe-sensors shows that the mass of the involved particle has limited (if any) influence on the image contrast obtained. Therefore, also the static model of the STHM force sensor that was proposed in our earlier work is confirmed.

Study of different sensor particles (Xe, CO and CH_4) helped us to explore the possibility of tailoring the sensor properties by tuning the tip-particle interaction strength. Similar to Xe, all CO-terminated tips were able to resolve the inner structure of organic molecules (Fig. 2b). At the same time we found characteristic differences between the images recorded with different sensors: the CO-sensor yields better resolution of the aromatic backbone. On the other hand, the contrast in the spaces between the molecules, related to the intermolecular hydrogen-bond network [3], is much better reproduced with Xe and CH_4.

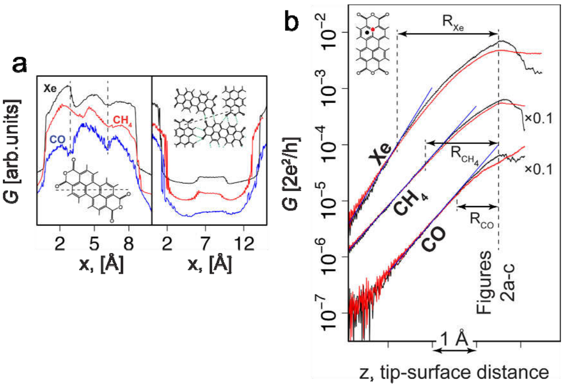

FIG. 3: (a). Conductance line profiles measured along the path marked by the dashed lines in the respective insets. The black curve was extracted from Fig. 2a measured with Xe, the red curve from Fig. 2c measured with CH_4, and the blue curve from Fig. 2b measured with CO. (b). The G(z) spectra of the Xe, CO, and CH_4 sensors. The curves were shifted along the z-axis such that the tip-surface distances, at which the Fig. 2a-c were scanned, coincide.

Fig. 3a compares the contrasts obtained with different types of sensors. The left panel of Fig. 3a shows that the “Pauli repulsion images” recorded with the Xe- and CH_4-sensors are laterally distorted: e.g. in both cases, the three aromatic rings along the profile appear to have different sizes. This happens due to the deformations of the tip-sensor complex that occur during imaging. Notably, the contrast generated by the CO-sensor is much less distorted. This property of the CO-sensor may be rationalized by the stiffer bonding of CO to the tip, as compared to Xe and CH_4.

Looking at the signal above the hydrogen bonds (Fig. 3a, right), we see that the imaging performance is reversed: Here, the Xe- and CH_4-sensors provide a higher contrast than the CO-sensor. To rationalize this observation we inspect the conductance versus distance G(z) spectra measured while the decorated tip approaches the surface. All G(z) curves plotted in Fig. 3b exhibit pronounced non-exponential behavior at small tip-sample distances. Earlier we proposed that the observed deviation from the exponential behavior is related to the depletion of the tip DOS by Pauli repulsion acting between the tip and the sensor molecule adsorbed at the apex.

Recording G(z) spectra above a carbon atom (red curve) and a C_6 ring (black curve), we can directly observe that each sensor molecule indeed achieves its optimal imaging resolution of the carbon backbone (shown in Fig. 2a-c) at the distance where the difference between the red and the black G(z) spectra is pronounced. At the same time the G(z) behavior of all three sensors is slightly different manner: It is apparent that the tip-surface distance range in which the sensors are sensitive to any influence whatsoever from the sample surface (and thus their conductance deviate from exponent) differs substantially between the three sensor particles. This range can be quantified by the parameter R which is defined as the difference between the distance at optimal contrast and the distance at which the particular G(z) curve starts to deviate form exponential growth.

According to Fig. 3b, the values R_{Xe} and R_{CH4} are noticeably larger than R_{CO}, which means that the Xe- and CH_4-sensors produce detectable output in a wider range of tip-surface distances, while the sensitivity of the CO-sensor decays faster as the tip is moved away from the sample surface. Thus the CO-sensor has a substantially shorter sensitivity range than Xe- and CH_4-sensors and at the same time it yields the poorest hydrogen bond contrast. We suggest that this is not a mere coincidence, but that the shorter-range sensitivity of the CO-sensor is indeed the reason for its poor hydrogen bond resolution. Based on the fact that, in the area between the molecules where the hydrogen bond network is located, the effective tip-surface distance is larger than on top of PTCDA (we note again that all STHM images reported in this paper have been measured in constant height mode); because of their short-range sensitivity, the increased tip-surface distance above the interstitial areas must affect the performance of CO-sensors in a more pronounced way than of the Xe- and CH_4-sensors. This finding demonstrates the possibility of tuning the imaging performance of single atom and molecule sensors by tuning the interaction of the particle with the STM tip.

---

[1] R. Temirov, S. Soubatch, O. Neucheva, A. Lassise, F.S. Tautz, New J. Phys. 10, 053012 (2008).

[2] C. Weiss, C. Wagner, C. Kleimann, F. S. Tautz and R. Temirov, Phys. Rev. Lett. 105, 086103 (2010)

[3] C. Weiss, C. Wagner, R. Temirov and F. S. Tautz, J. Am. Chem. Soc, 132, 11864 (2010)

[4] Kichin, C. Weiss, C. Wagner, F. S. Tautz, and R. Temirov, J. Am. Chem. Soc. 133, 16847 (2011)

Arylthio-substituted coronenes as tailored building blocks for molecular electronics

Peter Kowalzik[1], Nicolae Atodiresei[2], Vasile Caciuc[2], Stefan Blügel[2], Marc Gingras[3], Rainer Waser[1], and Silvia Karthäuser[1]

[1]Peter Grünberg Institut-7, Forschungszentrum Jülich, 52425 Jülich
[2]Peter Grünberg Institut-1, Forschungszentrum Jülich, 52425 Jülich
[3]CNRS, Aix-Marseille University, UPR 3118 CINAM, 13288 Marseille Cedex 09, France

The electron transport through molecules in molecular devices is typically influenced by the nature of the interfaces with the contacting electrodes and by the interactions between neighbouring molecules. It is a major goal of molecular electronics to adjust the electronic function of a molecular device by tailoring the intrinsic molecular properties and the interfacial and intermolecular interactions. Here, we report on the tunability of the electronic properties of coronene derivatives, namely dodecakis(phenylthio)-coronenes (DPTCs) , which are found to exhibit a three-dimensional aromatic system. Scanning tunnelling microscopy (STM), spectroscopy (STS) and simulations based on the density functional theory (DFT) are employed to characterize the structural and electronic properties of these molecules deposited on Au(111) surfaces. It is shown that modifications of the peripheral aryl-groups allow to specifically affect the self-assembly and the charge transport characteristics of the molecules. Molecular assemblies like supramolecular wires with highly delocalized orbitals and single molecules with molecular "quantum dot" characteristics are obtained in this way.

The development of future nanoelectronic devices based on single molecules or well-defined molecular assemblies is driven by the vision that a great variety of functionalities may be implemented by using the appropriate chemical design. In this study, we report on a molecular system based on a polycyclic aromatic hydrocarbon core, substituted thoroughly by phenylthio-groups, i. e. dodecakis-(phenylthio) coronene (DPTC). DPTC can be seen as nanosized system with a three-dimensional delocalized electronic network. Further systematic substitution of DPTCs, i. e. with electron-with-drawing trifluoromethyl-moieties or electron-donating methoxy-moieties, leads to the compounds DFPTC and DMPTC, respectively [1-3].

The monolayer of DFPTC deposited on Au(111) shows ordered domains consisting of parallel chains which are surrounded by a disordered region. The columnar arrangement of DFPTC (Fig. 1(a)), is in line with findings made for discotic liquid crystals. Molecules with strongly electronwith-drawing groups form stable columnar mesophases over a broad temperature range. These observations are explained by the stabilization of a π–π-stacking between aromatic molecules due to the fact that electron-withdrawing groups help to minimize the repulsive interactions between adjacent aromatic π-systems. A comparable structural arrangement is observed in the case of the molecular building block DPTC [2]. The columnar structures of both, DFPTC and DPTC, can be described by a stacked arrangement of molecules with an edge-on orientation (Fig. 1). Depending on the structural arrangement of the DFPTC molecules, we experimentally observed three different electron transport characteristics [1] (Fig. 1(b)).

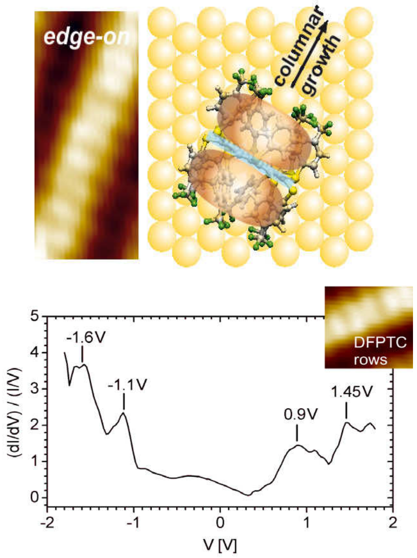

FIG. 1: (a) STM image and corresponding schematic of a DFPTC columnar structure on Au(111). The molecules are observed to form supramolecular columns along the [11-2] direction of the underlying gold surface. The distance between bright intracolumnar features has the average value a_{STM} *= (0.47 ± 0.05) nm. (b) STS characteristics measured on top of the columnar DFPTC structure.*

To gain insight into the detailed molecular structure and possible intermolecular interactions, respectively, we performed DFT calculations including long range van der Waals (vdW) interactions. In the first instance, we investigated the geometrical structure and the stability of several conformers of the isolated single molecules. Three different stable conformations were obtained (Fig. 2): (i) in the *up-down* conformer adjacent aryl groups alternate between the position above and below the plane of the coronene unit, (ii) in the *2up-2down* conformer alternately two adjacent aryl groups are located above and below the plane, and (iii) in the *up-up* conformer all 12 aryl groups are located above the coronene plane. The *ab initio* calculations reveal that the *up-up* conformer of all investigated DPTCs is significantly less stable than the other two conformers (Table 1). This suggests that the columnar structures should consist of molecules having a conformation with an alternating pattern of the substituents above and below the coronene core, that is a conformation close to *up-down* or *2up-2down*. During the aggregation into the columnar structure, a geometrical reorganization of the peripheral groups is expected to occur and enable a commensurable growth on the Au(111) surface.

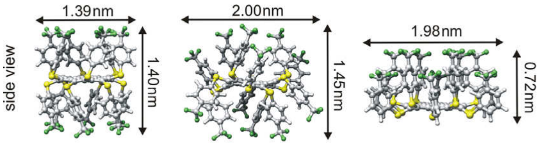

FIG. 2: Top and side views of the optimized geometries of the DFPTC conformers: (a) up-down, (b) 2up-2down, and (c) up-up conformer.

Table 1 Total energies in eV of DPTC conformers.[a]

	up-down	*2up-2down*	*up-up*
DFPTC	+ 0.16	0	+ 0.77
DPTC	0	+ 0.19	+ 0.68
DMPTC	0	+ 1.15	+ 1.18

[a] The total energy of the most stable conformer is set to the reference value 0 eV for all three DPTC molecules.

Comparing experimental and theoretical results several important statements should be noted: (i) The topographic appearance and the corresponding energy gap of single DFPTC molecules within the disordered layer fits best to the DFT results of the up-down conformer. (ii) DFPTC molecules with a threefold symmetric appearance can be assigned to the 2up-2down conformer since the experimentally measured intramolecular features and the energy gap fit almost perfectly to the theoretical values [1,3]. (iii) STS of DFPTCs within the columnar structure exhibit distinctly different features when compared to the characteristics of single non-aggregated molecules. The observed set of HOMO/LUMO levels is explained by the overlap between the peripheral groups within the DFPTC columns which should enable charge delocalization and thus lead to the build up of one-dimensional charge transport channels.

An opposed behaviour is observed in the case of the DMPTC molecules adsorbed *face-on* on Au(111) (Fig. 3). The impact of the methoxy-functionalization is twofold. Firstly, these groups seem to anticipate a stacking of the molecules and, secondly, they point towards the surface and therewith act as distance defining (insulating) spacers giving rise to a tunneling barrier between the substrate and the three-dimensional aromatic/delocalized electronic system of the molecules (Fig. 3). A double-barrier tunnel junction is formed in this way and leads to the occurrence of single electron tunnelling effects in STS measurements.

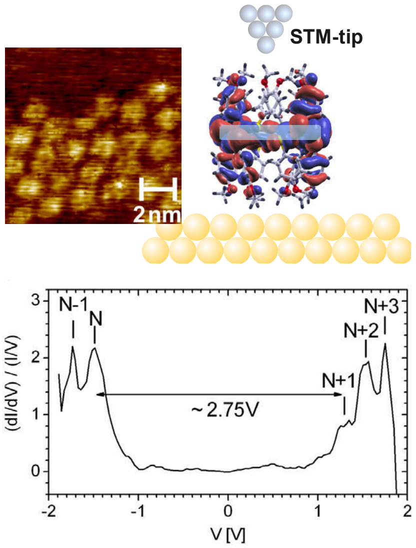

FIG. 3: (upper part) STM image of DMPTC molecules and a sketch showing that the methoxy groups pointing towards the substrate act as spacers, giving rise to an additional tunnelling barrier between the substrate and the three-dimensional aromatic system of DMPTC. (lower part) STS data of DMPTC adsorbed on Au(111) in face-on *configuration showing peaks related to subsequent charge states of the molecule. [3]*

We conclude that by using systematically substituted phenylthio-moieties the self-assembly behaviour of DPTC-derivatives was directed into different regimes. Thus the tendency to form columnar structures of molecules in edge-on configuration was strongly enhanced when using electron-withdrawing CF3 substituents (DFPTC). The face-on adsorption of DMPTC together with not fully delocalized molecular orbitals, on the other hand, is accompanied by an electronic decoupling of the aromatic system from the substrate. This goes along with the creation of a double-barrier tunnel junction configuration and the occurrence of single electron transport features visible in the tunnelling spectroscopy. In conclusion, the investigated DPTC system can be tailored in such a way that quite different advantageous electronic functionalities are achieved.

[1] P. Kowalzik, N. Atodiresei, M. Gingras, V. Caciuc, N. Schnaebele, J.-M. Raimundo, S. Blügel, R. Waser, and S. Karthäuser, Phys. Chem. Chem. Phys. 14, 1635-1641 (2012).

[2] P. Kowalzik, S. Rathgeber, S. Karthäuser, R. Waser, N. Schnaebele, J. –M. Raimundo and M. Gingras, New J. Chem. 36, 477-483 (2012).

[3] P. Kowalzik, N. Atodiresei, M. Gingras, V. Caciuc, S. Blügel, R. Waser, and S. Karthäuser, J. Phys. Chem C 115, 9204-9209 (2011).

Commensurate Registry and Chemisorption at a Hetero-organic Interface

Benjamin Stadtmüller, Tomoki Sueyoshi, Georgy Kichin, Ingo Kröger, Sergey Soubatch, Ruslan Temirov, F. Stefan Tautz, and Christian Kumpf

Peter Grünberg Institut-3, Forschungszentrum Jülich, 52425 Jülich

We have investigated the hetero-organic interface between molecular layers of copper-II-phthalocyanine (CuPc) and 3,4,9,10-perylene-tetracarboxylic-dianhydride (PTCDA) that were stacked on Ag(111). A commensurate registry between the two molecular layers and the substrate, i.e., a common crystallographic lattice for CuPc and PTCDA films as well as for the Ag(111) surface, was found. It indicates that the growth of the upper layer is dominated by the structure of the lower. Photoemission spectroscopy clearly reveals a gradual filling of the lowest unoccupied molecular orbital of PTCDA due to CuPc adsorption. This finding proves a partly chemisorptive bonding between the single molecular layers.

The applicability of organic molecules as active materials in electronic devices such as organic light-emitting diodes, field-effect transistors, or solar cells strongly depends on the properties of the interfaces between different materials. While organic-metal contacts – model systems like PTCDA and Metal-Pcs in particular [1] – are intensively investigated in this context, organic-organic heterojunctions are characterized only seldom, even though such interfaces are at least of similar importance for organic electronic devices. Maybe this is due to the common belief that interfaces between different organic materials are generally dominated by very weak, van der Waals interaction, an assumption that will be proven to be incorrect.

We have investigated the geometric and electronic structure of the hetero-organic interface between the prototypical molecules CuPc and PTCDA [2]. The heterojunction is formed by adsorbing CuPc molecules on top of a closed layer of PTCDA on Ag(111). Figure 1 shows a high-resolution low-energy electron-diffraction (LEED) image of the so-called "stacked bilayer structure" (SB-structure). The image was recorded at 100 K for a CuPc coverage of 0.6 ML, but the same structure is observed at higher CuPc coverages (close to 1 ML) and room temperature (for details see [2]).

The LEED pattern of the SB structure can be explained unambiguously by one single structural model. In the upper right half of Fig. 1 the PTCDA diffraction spots are marked by red circles whereas in the lower left the spots stemming from the CuPc cell are indicated in blue. Note that all PTCDA spots can also be indexed as CuPc spots. This immediately shows that the structure of the CuPc overlayer is commensurate with the PTCDA monolayer structure. Consequently, the superstructure matrices describing the unit cell of the CuPc/PTCDA stacked bilayer structure have integer numbers only:

$$\begin{pmatrix}\vec{A}\\ \vec{B}\end{pmatrix}_{\mathrm{SB}}=\begin{pmatrix}3 & 1\\ -2 & 1\end{pmatrix}\begin{pmatrix}\vec{A}\\ \vec{B}\end{pmatrix}_{\mathrm{PTCDA}}=\begin{pmatrix}3 & 16\\ -12 & -9\end{pmatrix}\begin{pmatrix}\vec{A}\\ \vec{B}\end{pmatrix}_{\mathrm{Ag}}$$

The appearance of commensurate structures is usually an indication for a relatively strong interaction of organic molecules with the underlying substrate. Commensurability across an organic-organic heterojunction is therefore very unexpected and stands in contrast to the structure formation reported for such interfaces so far. However, in our case, commensurability is a very characteristic feature with important consequences for the formation of the CuPc film: In contrast to almost squared unit cells generally found for CuPc, and rectangular cells for PTCDA (both reflecting the fourfold or two-fold symmetry of the molecule), the SB structure has an oblique unit cell. This indicates that commensurability is not just the result of an arbitrary coincidence of similar lattices of the isolated PTCDA and CuPc layers. There must be a significant interaction across the heterojunction which dominates the structure formation and forces the CuPc layer in an unusual structure which otherwise would not be formed.

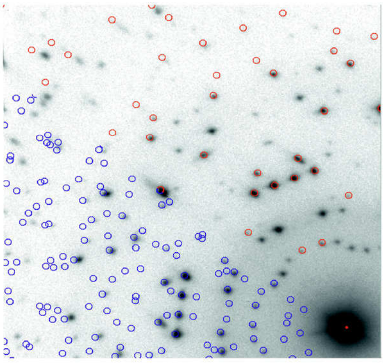

FIG. 1: High-resolution LEED image of 0.6 ML CuPc on a closed layer of PTCDA/Ag(111), recorded at 100 K. Red and blue circles mark calculated positions of diffraction spots from the PTCDA-monolayer structure and the CuPc/PTCDA stacked-bilayer (SB) structure, respectively.

We used low-temperature scanning tunneling microscopy (STM) in order to determine positions and orientations of the molecules in the unit cell. Figure 2 shows constant-current images recorded at 10 K. In panel (a) the edge of a CuPc island on the PTCDA monolayer is visible with submolecular resolution in both regions: the PTCDA monolayer (lower part) and the CuPc island on top (upper part). It can be seen that CuPc homogeneously overgrows the PTCDA monolayer. The unit-cell dimensions obtained from SPA-LEED are confirmed by the STM images. Translating the well-known PTCDA superlattice (indicated by the red grid in the lower part of Fig. 2(a)) onto the CuPc island in the upper part and comparing it with the unit cell of that region (indicated by the blue grid) illustrates matching of the periodicities of the SB and PTCDA-monolayer phases.

CuPc molecules all show the typical crosslike STM contrast, even though their wings differ in apparent height. In Fig. 2(b), the positions of the underlying PTCDA molecules are marked as dotted ellipses. This plot reveals that the CuPc wings that appear bright are located directly above the PTCDA molecules, while dark wings are bridging the PTCDA molecules; i.e., they lie above the "gaps" in the lower layer. This finding indicates that the different contrast of the molecular wings is caused by an electronic coupling between the molecular layers. It appears as if the underlying PTCDA molecule facilitates electronic transport through that part of the CuPc molecule that lies exactly above the central part of the PTCDA molecule.

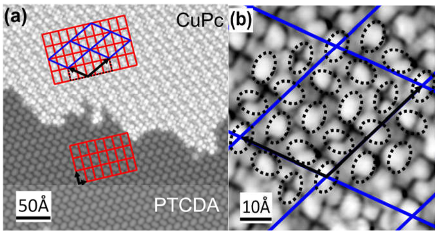

FIG. 2: STM images of the SB phase at 10 K (0.75 V, 18 pA). (a) A CuPc island (bright contrast) has condensed on a closed PTCDA monolayer on Ag(111). PTCDA and CuPc lattices are indicated by red and blue lines, respectively. (b) Dotted ellipses indicate the positions of PTCDA molecules under the CuPc layer. Bright STM contrast is found where CuPc wings lie above the PTCDA core.

We also used UPS to gain more insight into the electronic interaction between the substrate and the molecular layers. Figure 3 shows He Iα UPS data recorded for different submonolayer CuPc coverages between 0 and 0.9 ML at RT. In the spectra of the bare PTCDA monolayer (lowest curves labeled "0.0 ML"), the highest occupied molecular orbital (HOMO) and a second state close to the Fermi level, the former lowest unoccupied molecular orbital (F-LUMO), can be seen. The F-LUMO is partially filled due to charge transfer from the substrate into the molecule. This directly indicates chemisorptive interaction between the Ag(111) substrate and the PTCDA molecule which is well-known for many organic molecules adsorbing on noble metal surfaces.

Upon adsorption of CuPc on top of the PTCDA layer, new peaks appear in the spectra (the HOMO and HOMO-1 states of CuPc) and some peak shifts are detected. However, the most important change in the spectra is the shift of the F-LUMO state of PTCDA. As illustrated by the vertical dashed lines in Fig. 3, this state shifts continuously by as much as 120 meV. This indicates an additional filling of the PTCDA F-LUMO induced by the adsorption of CuPc molecules, i.e., an increase of the charge transfer between substrate and adsorbate (and/or between both organic layers). This implies an enhancement of the chemisorptive interaction between the CuPc and PTCDA adsorbate layers and the substrate, and is in strong contrast to previous studies which reported only very weak interactions across organic-organic interfaces [3].

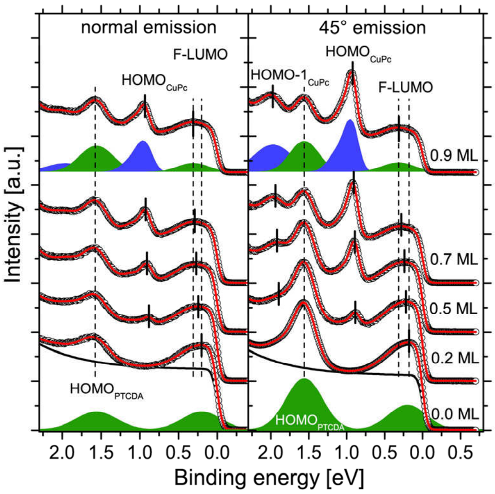

FIG. 3: UPS data of CuPc on PTCDA on Ag(111) for different CuPc coverages at RT. The red curves represent least-square fits to the data. For the lowermost and uppermost curves the fitting model consisting of up to four independent peaks is shown; PTCDA and CuPc states are displayed in green and blue, respectively. A background curve is shown as a black solid line with the lowermost curve.

In conclusion, we have presented evidence for an unexpectedly strong interaction (namely, a weak chemisorption) at the organic heterojunction between CuPc and PTCDA on Ag(111). The chemisorptive character is indicated (1) by the formation of a commensurate registry between the CuPc and PTCDA superstructures, consistently found by SPA-LEED and STM, (2) by the STM contrast of the CuPc benzene-wings which strongly depends on their position relative to the underlying PTCDA molecule, and (3) by the gradually increasing filling of the F-LUMO state of PTCDA upon adsorption of CuPc. Against common belief, these results prove that rather strong, chemisorptive interaction can occur also at hetero-organic interfaces. This aspect will have significant impact on the understanding and designing of molecular electronic devices.

---

[1] F.S. Tautz, Prog. Surf. Sci. 82, 479 (2007), A. Hauschild at al., Phys. Rev. B 81, 125432 (2010); I. Kröger et al., J. Chem. Phys. 135, 234703 (2011); C. Stadler et al., Nature Phys. 5, 153 (2009); I. Kröger et al., New J. Phys. 12, 083038 (2010).

[2] B. Stadtmüller et al., Phys. Rev. Lett. (2012).

[3] M. Häming et al, Phys. Rev. B 82, 235432 (2010); W. Chen et al., J. Phys. Chem. C 112, 5036 (2008); F. Sellam et al., Surf. Sci. 478, 113 (2001).

Lattice Dynamics in Thermoelectric Antimonides

A. Möchel[1,2], D. Bessas[1,2], W. Schweika[1], J. Voigt[1], Sergueev I[2], and R. P. Hermann[1,3]

[1] Jülich Centre for Neutron Science JCNS-2 and Peter Grünerg Institute PGI-4
[2] Faculty of Science, University of Liège, B-4000 Liège, Belgium
[3] European Synchrotron Radiation Source

The lattice dynamics in several thermoelectric antimonides were studied by a combination of inelastic neutron scattering, synchrotron radiation nuclear inelastic scattering, and several macroscopic techniques. Combining the results obtained by these methods, detailed insights into microscopic vibrational properties were obtained. The different mechanisms which lead to the observed low thermal conductivity in skutterudites and in the thermoelectric Zintl phase $Yb_{14}MnSb_{11}$ were identified, and the calculations of the lattice properties including electron phonon coupling in the giant Seebeck coefficient material $FeSb_2$ were validated. The gained knowledge will prove useful in order to search for and enhance new efficient thermoelectric materials.

Direct conversion of thermal-to-electric energy and vice-versa by thermoelectric devices is attracting increasing interest in times where energy efficiency is a crucial issue. Advanced thermal management for future information technology or energy harvesting for processes where waste heat cannot be avoided are the main fields of application. Notably energy recovery from the exhaust gas system in the automotive industry is a strong driving force for research. Optimizing thermoelectric conversion efficiency is a balancing act involving improving the electric transport by doping and impeding the thermal transport by various mechanisms. Our research aims at an understanding on the atomic- and nanoscale of the influence on thermal transport for exaemple of nanostructuration and grain boundary scattering, of inclusion of rattling guests in cage-like structures, and of complex large unit cell materials, with less effectively transporting modes.

Our investigations of the lattice dynamics are based essentially on the well known inelastic neutron scattering technique and on the phonon assisted nuclear resonant absorption by Mössbauer active nuclei. The recent development of this technique for new isotopes such as Sb or Te [1] has widened the technique and made it particularly attractive for investigating antimony based thermoelectrics, as it gives access to the element specific density of phonon states and a host of quantities such as the microscopic speed of sound, the force constants, and the vibrational entropy.

The lattice dynamics of the unfilled and filled skutterudites $FeSb_3$, $CoSb_3$ and $YbFe_4Sb_{12}$ were studied and compared [2,3]. We have shown that the skutterudite $FeSb_3$, a metastable compound that can only be synthesized by thin film methods, is significantly softer than the isostructural compound $CoSb_3$. The phonon states are shifted towards lower energies and the velocity of sound is lower in $FeSb_3$ than in $CoSb_3$ [2]. Thus, beside the reduction of the thermal conductivity by the filler atoms, so called “rattlers”, the low thermal conductivity in filled RFe_4Sb_{12} skutterudites, such as $YbFe_4Sb_{12}$, might more fundamentally be related to the soft $[Fe_4Sb_{12}]$ framework. We have also shown, that the lattice dynamics of the $[Fe_4Sb_{12}]$ framework is only slightly affected by filling the structure. Furthermore, our investigations have related the anomalous softening around 50 K of $YbFe_4Sb_{12}$ and the rearrangement of the spectral weight in the density of phonon states of $YbFe_4Sb_{12}$, a phenomenon that is very likely explained by the observed change in the Yb valence state[3].

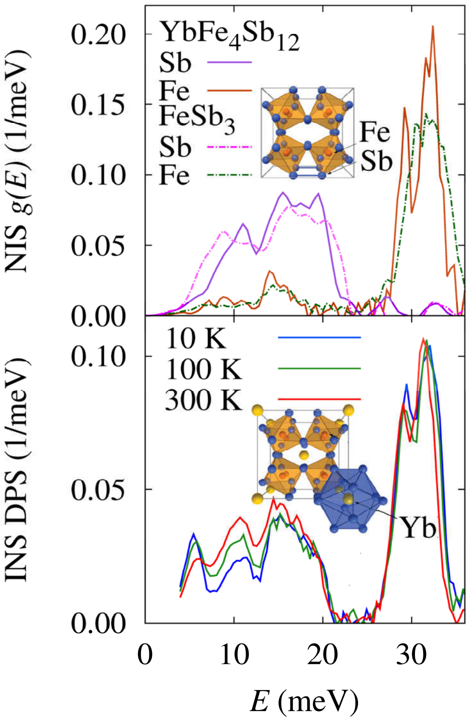

FIG. 1: Density of phonon states (DPS) in the filled $YbFe_4Sb_{12}$ and unfilled $FeSb_3$ skutterudites. Top: Sb and Fe element specific DPS (ESRF ID18 and ID22N), inset: unfilled structure. Bottom: neutron weighted DPS in $YbFe_4Sb_{12}$ (SNS, ARCS), inset: filled structure.

Inelastic scattering by the new high temperature thermoelectric Zintl phase $Yb_{14}MnSb_{11}$ reveals that all phonon modes have energies below 25 meV. The low mean force constants, and the related low velocity of sound, have been identified as one reason for its low thermal conductivity. Furthermore, $Yb_{14}MnSb_{11}$ has a very large unit cell, and thus the ratio of acoustic modes to optical phonon modes is quite small. As the number of modes that contribute to the thermal transport is thus small, the thermal conductivity is strongly reduced [4]. For comparison, in another Zintl phase, Zn_4Sb_3, which exhibits similar thermal conductivity at room temperature, the low thermal conductivity in Zn_4Sb_3 is caused by a small phonon mean free path due to vibrational subunits [5] or Zn-interstitial disorder [6].

Finally, the density of phonon states and the elastic response was investigated in $FeSb_2$, a material with a record Seebeck coefficient at low temperature that has been ascribed to electron phonon interactions. In a first study we have investigated the low temperature density of states in order to validate density functional theory calculations of the electronic and lattice dynamic properties. Our measurements reveal excellent agreement with calculations that include spin-orbit corrections and electron-phonon coupling. Further, our ultrasound spectroscopy measurements indicate that activation of the charge carries in this semi-conductor leads to a small lattice softening at 150 K [7].

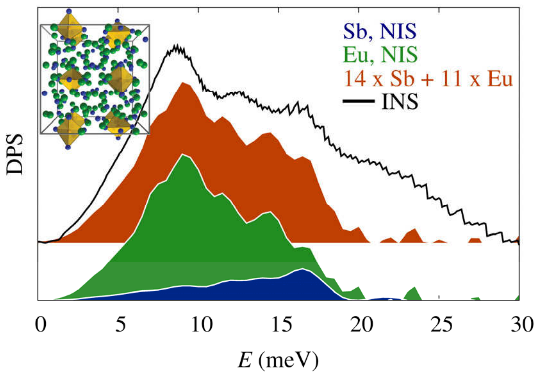

FIG. 2: Density of phonon states (DPS) in the $Yb_{14}MnSb_{11}$ Zintl phase, as obtained by inelastic neutron scattering (FOCUS, SINQ) and by nuclear inelastic scattering (NIS) by Sb and Eu (ID22N, ESRF). Eu is used as a substitute for Yb which is not accessible by NIS. Inset: $Yb_{14}MnSb_{11}$ body-centered unit cell with 208 atoms and a 6000 Å3 volume; Mn in yellow.

In summary, our measurements of the phonon properties in several antimonide thermoelectrics have revealed that a reduced lattice thermal conductivity in bulk materials can be achieved by several mechanisms. In cage structures, such as skutterudites, both the guests atoms and the framework dynamics play a role. In large volume cell structures an essential limitation comes from the number of effectively transporting modes. In the future we hope to improve on our understanding of the microscopic mechanisms at work including the interactions of the electronic and lattice degrees of freedom.

The European Synchrotron Radiation Facility, the Institut Laue-Langevin, the Spallation Neutron Source, and the Swiss Spallation Neutron Source, and the corresponding local contacts, are acknowledged for provision of beatime at ID18-ID22N, IN6, ARCS, and FOCUS, respectively.

The Helmholtz Association of German Research Centers is acknowledged for funding of the “Lattice Dynamics in Emerging functional Materials” Young Investigator Group.

---

[1] Sergueev I., Wille H.-C., Hermann R. P., Bessas D., Shvyd'ko Yu.V., Zając M., and Rüffer R., J. Synchr. Rad. 18, 802 (2011).

[2] Moechel A., Sergueev I., Nguyen N., Long Gary J., Grandjean F., Johnson D. C., and Hermann R. P., Phys. Rev B 84, 064302 (2011).

[3] Moechel A., Sergueev I., Wille H.-C., Juranyi F., Schober H., Schweika W., Brown S. R., Kauzlarich S. M., and Hermann R. P., Phys. Rev B 84, 184303 (2011).

[4] Moechel A., Sergueev I., Wille H.-C., Voigt J., Prager M., Stone M.B., Sales B.C., Guguchia Z., Shengelaya A., Keppens V., and Hermann R.P., Phys. Rev B 84, 184306 (2011). Editor's Suggestion.

[5] Schweika W., Hermann R. P., Prager M., Perßon J., and Keppens V., Phys. Rev. Lett. 99, 125501 (2007).

[6] Snyder G. J., Christensen M., Nishibori E., Caillat T., and Iversen B. B., Nature Materials 3, 458-463 (2004).

[7] Diakhate M. S., Hermann R. P., Moechel A., Sergueev I., Sondergaard M., Christensen M., and Verstraete M. J., Phys. Rev. B 84, 125210 (2011)

Competing Magnetic Phases and Absence of Ferroelectricity in $LuFe_2O_4$

J. de Groot[1], S. Adiga[1], T. Mueller[1], W.J.H. Borghols[2,3], K. Schmalzl[2,4], W. Schweika[1], Y. Su[2,3], M. Angst[1]

[1] Peter Grünberg Institut and Jülich Centre for Neutron Science, JCNS, Forschungszentrum Jülich, 52425 Jülich
[2] Jülich Centre for Neutron Science JCNS, Forschungszentrum Jülich GmbH, 52425 Jülich
[3] JCNS Outstation at FRM II, D-85747 Garching,
[4] JCNS Outstation at ILL, BP 156, 38042 Grenoble, France

Magnetoelectric multiferroics with large electric polarizations and magnetoelectric coupling are of strong interest for novel storage devices. Because the traditional mechanism of ferroelectricity is incompatible with magnetism, increasing attention is focused on various unconventional mechanisms, such as ferroelectricity originating from charge order (CO). In this field $LuFe_2O_4$ is often cited as a prototypical material for CO based multiferroic materials. Here both charge and (Ising) spin orders are localized at the Fe sites, which are contained in triangular Fe-O bilayers, a highly frustrated arrangement. Thus, this is an ideal system to study frustration effects. We identified two nearly degenerate spin structures by neutron and soft x-ray diffraction, establishing $LuFe_2O_4$ as a new model system for metamagnetic materials. Furthermore the crystal structure could be refined with a new CO configuration incompatible with ferroelectricity.

Above $T_{CO} \sim 320$K observed diffuse x-ray scattering was linked to competing CO instabilities which could be addressed to geometrical frustration [1,2]. Similar frustration effects can also be expected for the magnetism. Below T_{CO} sharp CO reflections were interpreted as a CO configuration of Fe^{2+} and Fe^{3+} valences which renders the Fe-O bilayers polar, making $LuFe_2O_4$ ferroelectric or antiferroelectric [1,2]. Mainly for this reason, but also due to unrelated magnetic effects blow $T_N \sim 240$K [3] such as giant coercivity and various glassy states, this system is currently attracting increasing attention. Strong sample to sample variations in magnetic behavior are found, which could be attributed to tiny variations in oxygen stoichiometry. We focused our work on the type of samples showing the sharpest features in magnetization, where diffraction reveals sharp CO and magnetic reflections indicating 3D long range charge and spin orders, i.e. the best approximation for intrinsic defect-free magnetic behavior in $LuFe_2O_4$.

The magnetic field (H) - temperature (T) phase diagram underlying the above unusual behaviors has now been established. In the following we focus on the region just below the magnetic ordering temperature T_N (Fig.1 [4]). Here, a sharp first-order metamagnetic transition separates an antiferro- (AFM) and a ferrimagnetic (fM) phase in low-H and high-H region, respectively. In a wide H -T region (hatched area) both phases can be stabilized, depending on the sample history.

In contrast to previous work we found by neutron and soft x-ray diffraction studies magnetic contributions on reflections where for the spin structure proposed in [3] no magnetic intensity should be present. Taking these additional reflections into account, the spin structures of both AFM and fM phases could be refined.

Interesting is the geometrical relation between the fM solution in Fig.2(a), which is identical to the AFM solution in Fig.2(b), except that all Ising-spins of one particular Fe-O bilayer flip their sign. This leads to the overall 2:1 configuration of ↑ and ↓ spins in the fM phase and zero net moment in the AFM phase, consistent with observations.

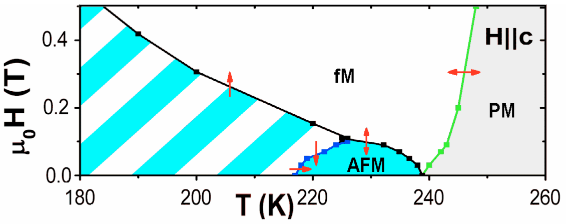

FIG.1: H - T phase diagram, which exhibits a para-magnetic (PM) an antiferromagnetic (AFM) and a ferrimagnetic (fM) phase, extracted from various M(H) and M(T) curves. The hysteretic region where either fM or AFM can be stabilized is hatched. Arrows across phase lines indicate for which measurement direction the particular transition is observed. After [4].

Phase competition and metamagnetic transitions between antiferro- and ferro-stacking of net bilayer moments are expected for layered magnets with very strong Ising-anisotropy. Such a behavior has already been observed in a few model systems at low temperatures [5]. Intriguingly, and in contrast to the expectations in the simple model systems, for $LuFe_2O_4$ the AFM-fM metamagnetic transition extrapolates to $H = 0$ for $T \rightarrow T_N$ as clearly seen in Fig.1. This means that at T_N and $H = 0$ the two phases seem to be essentially degenerate.

Given the particular differences between the two nearly degenerate spin-structures, just above T_N we may expect a random stacking of the net moments of bilayers that are still medium range ordered, i.e. a

2D-order. Magnetic diffraction would consequently results in a strong diffuse scattering line through (⅓ ℓ) above T_N, still reasonably sharp in-plane, but featureless along the ℓ direction. This was indeed observed in Fig.3, visible even up to 280K.

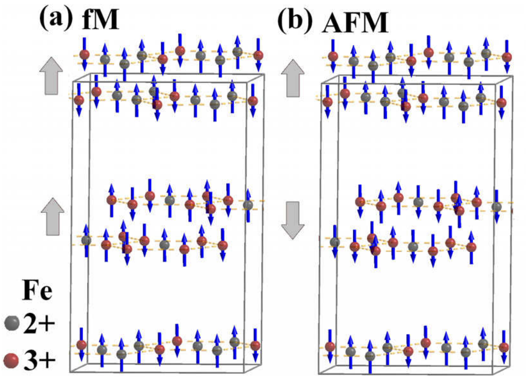

FIG.2: Charge order and Spin structure of the AFM (a) and fM phase (b). Gray arrows indicate bilayer net magnetization. For better visibility an additional Fe layer is shown above the unit cell.

The AFM / fM metamagnetism presented by us [4] is resolvable only in the highest quality samples but it has strong ramifications for all specimens of this material. For example, if disorder, e.g. due to oxygen off-stoichiometry, is added to the competing interactions, glassy freezing may be expected to replace long-range spin order at T_N, as observed in some samples.

Beside the spin structure we also refined the crystallographic structure in the charge ordered phase from which follows a totally new CO pattern involving charged bilayers (Fig.2). This new CO configuration is further collaborated by XMCD measurements [6] and moment-dependent spin structure refinements [4], which additionally provide a strict coupling between the charge and the spin order (Fig.2). The charged bilayers are *not polar* and this new CO is therefore incompatible with the generally accepted mechanism of CO-based ferroelectricity [1]. All these findings cast strong doubt on the CO based ferroelectric behavior of $LuFe_2O_4$.

In summary, we have elucidated the magnetic phase diagram of $LuFe_2O_4$ close to T_N and determined a ferrimagnetic and an antiferromagnetic spin configuration which are almost degenerate at T_N in zero magnetic field. Such a phase competition was up to now not observed in classical metamagnetic materials. Therefore our results could establish $LuFe_2O_4$ as a simple model system for frustrated layered magnets. Furthermore, the charge order pattern for this material could be firmly established from crystal structure refinements. In contrast to the widely accepted charge order configuration with polar bilayers our new result exhibits charged bilayers coupled to the spin order. The absence of polar bilayers casts strong doubt on the "ferroelectricity from charge order" scenario of $LuFe_2O_4$. Hence, a clear example of an oxide material with ferroelectricity originating from charge order has yet to be identified.

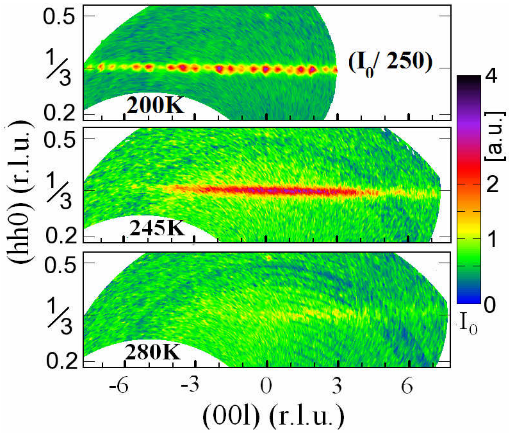

FIG.3: Reciprocal space map of the scattered intensity (logarithmic scale) in the (hhℓ) plane by polarized neutrons in the spin flip channel (DNS) at different T.

We would greatly acknowledge our collaborators: K. Marty, M.D. Lumsden, A.D. Christianson, S.E. Nagler, Z. Yamani, S. R. Bland, R. de Souza, U. Staub, R.A. Rosenberg, D.J. Keavney, Z. Islam, and J.-W. Kim.

---

[2] N. Ikeda *et al.,* Nature 436, 1136 (2005).

[2] M. Angst *et al.*, Phys. Rev. Lett. 101, 227601 (2008).

[3] A. D. Christianson *et al.*, Phys. Rev. Lett. 100, 107601 (2008).

[4] J. de Groot *et al.*, Phys. Rev. Lett. 108, 037206 (2012).

[5] E. Stryjewski *et al.*, Adv. Phys. 26, 487 (1977).

[6] J. de Groot *et al.*, Accepted for publication in Phys. Rev. Lett.; arXiv:1112.0978v1 (2012).

Infrared-optical Detection of Buried Nanostructures with scattering-type Near-field Microscopy

B. Hauer, A. P. Engelhardt, T. Taubner

I. Institute of Physics (IA), RWTH Aachen University

We investigate the resolution and contrast of buried structures in scattering-type scanning near-field optical microscopy (s-SNOM) both in experiment and by developing a model that quantitatively describes the tip-sample interaction. We find that metallic particles of only 30 nm in size can be detected through a dielectric layer of up to 50 nm. An extended layer can be investigated through dielectric films of more than 100 nm thickness. We have thus shown that s-SNOM is a non-destructive method to locally analyze dielectric properties even below the surface. We envision s-SNOM application on the characterization of buried nanostructures and thin films that are otherwise not accessible.

An s-SNOM is based on an atomic force microscope (AFM) with an additional illumination of the tip and the detection of the scattered light. The high spatial resolution in s-SNOM is realized by localized light fields at the apex of a metalized tip that is illuminated from the side and acts as an optical antenna [1]. Due to this principle the spectral range that can be covered by s-SNOM is expanded to mid-infrared and even terahertz frequencies, where conventional aperture SNOMs are not applicable since the power-loss in the sub-wavelength aperture would be far too high. Our s-SNOM is set up with tunable lasers covering most of the wavelength range between 5.3 µm and 11.2 µm. This wavelength range covers many characteristic phononic and molecular absorption bands, which allows for a chemical identification of materials. Also structural properties, such as phase boundaries or strain can be addressed.

In s-SNOM the evanescent electric fields at the apex of the tip are used to probe the dielectric function of a sample with a sub-wavelength resolution. The near-field interaction between tip and sample is not restricted to the immediate surface but it is sensitive to the three-dimensional composition of the sample. In an earlier work by Taubner et al. [2], it has been demonstrated that infrared s-SNOM can detect metallic structures in a depth of more than 50 nm below a polymeric capping layer. We now determined the limits in resolution and quantified the effect of cover layers on the s-SNOM signal by developing a model that describes the interaction of the tip with layered systems.

In our latest work [3] we have investigated resolution and contrast of nanoparticles below silicon-nitride (Si_3N_4) membranes, which can be regarded as a model system for samples where metallic nanostructures are embedded into dielectrics and thus are not directly accessible. We prepared samples in which spherical gold particles with a diameter of 30 nm were drop-casted on the backside of a membrane. The system was imaged from the top (Fig. 1a). The membranes had a thickness of 30 nm and 50 nm. The radius of the s-SNOM tip was 30 nm. Therefore the imaged gold particles and all the other dimensions are clearly of sub-wavelength size. In Fig. 1b and 1c, the scan images of the topography (left) and of the optical amplitude signal (right) are shown. The topography is flat and does not show any indications of the particles on the backside. Therefore a clear separation between optical and mechanical effects can be guaranteed. In the optical images, bright spots can be identified that stem from the near-field coupling between the tip and the nanoparticles through the membrane.

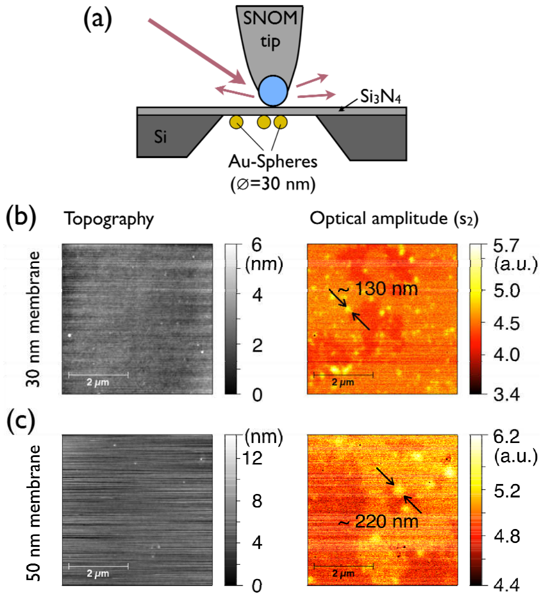

FIG. 1: a) Illustration of the experiment. Gold nanoparticles are attached to the backside of a silicon-nitride membrane. The SNOM tip is scanned across the membrane on the other side. b) and c) Topography and optical amplitude signals for membranes with a thickness of 30 nm (b) and 50 nm (c). The arrows in the optical images indicate the statistically evaluated resolution of the gold particles.

We further developed a statistical approach to discriminate between single particles and aggregates. For this we recorded reference scans on samples where the nanoparticles were drop-casted directly onto a substrate. With the same statistical process we evaluated the resolution depending on the membrane thickness. The full with half maximum of the spots is ~130 nm through the 30 nm membrane and ~220 nm through the 50 nm membrane. A simple model can explain this behavior: The tip is represented by a sphere as illustrated in Fig. 1a and the coupling between this sphere and the gold nanoparticles is described by an electrostatic dipole-dipole interaction. The tip and the particles are polarized by the illuminating light and by their interaction. By scanning the tip over a particle in a given height the total polarization of the system changes in a similar way as the measured results. This gives a good understanding of the broadening of the spot sizes with increasing membrane thickness.On a more technical side, we were able to enhance the visibility of buried objects by optimizing the experimental conditions to subsurface imaging. We found that maximizing the visibility requires a trade-off between high contrasts at cost of higher noise and vice versa [3].

In order to get a more quantitative understanding of the near-field between a metallic tip and a vertically inhomogeneous sample, we developed an accurate model for the prediction and analysis of s-SNOM signals on layered systems [4]. In this description we follow an example in literature [5], where the charge separation within the tip is described analytically by introducing several point charges, which approximate a realistic field between the tip and the sample. We extended this so-called finite dipole model to layered systems with no lateral structure.

With this newly developed model we can describe the experimentally obtained signals very precisely. This is because the near-field decay is described more realistically than in commonly used models where the tip is represented by a point dipole [6]. The coupling between the tip and the sample can be well characterized by recording so-called approach curves, where the scattered light is measured depending on the vertical distance *H* between the tip and the sample surface. In Fig. 2 we show approach curves on five samples consisting of silicon substrates and a polymer cover layer of different thickness *d*. The experimental curves are plotted in blue. Our theoretical curves (black) coincide very well, indicating a good description of the distance-dependent near-field decay. The points where the tip is in contact with the surface ($H = 0$) are marked with blue bullets and error bars that indicate the uncertainty. These points show a trend to lower values when the film thickness is increased. Theoretically they are described by the red curve. This curve shows that even a non-metallic substrate (in this case silicon) has a significant impact on the tip-sample coupling on length-scales of more than 100 nm.

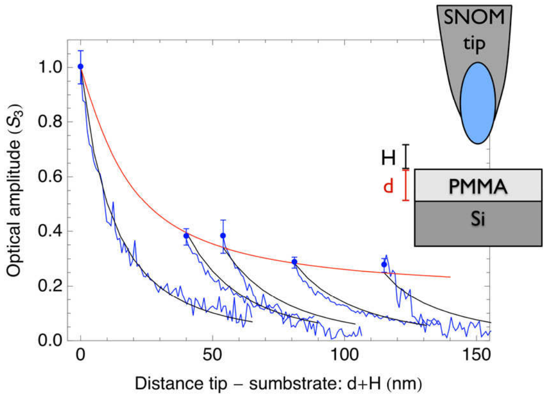

FIG. 2: Approach curves on silicon samples with polymer cover layers of different thickness. Blue: experimental curves, black: calculated curves, red: calculated signal depending on the layer thickness when the tip is in contact with the surface. The blue bullets mark the points where the tip is in contact with the sample. The error bars mark the uncertainty in their experimental determination.

Our model is based on an analytic calculation and does not contain any fit parameters. We can therefore use it both for the prediction and the analysis of signals on layered samples. In this way we can locally extract variations in the film thickness or in the dielectric function of thin films and covered materials. The model can also be applied to spectrally resolved measurements and describes a resonant coupling between the tip and the sample when the dielectric function of the sample matches the resonance condition.

Together our work on subsurface resolution and signal strength is a huge step towards the quantitative understanding of s-SNOM experiments on vertically inhomogeneous samples. We can employ our findings for the non-destructive investigation and spectroscopy of buried nanostructures and materials under a capping layer with infrared light. Another further possible application is the local quality control of thin films.

Our work was supported by the German Excellence Initiative, the Ministry of Innovation NRW, and the DFG under SFB 917.

---

[1] F. Keilmann, R. Hillenbrand, Philos. Trans. R. Soc. Lond A 362, 787 (2004).

[2] T. Taubner, F. Keilmann, R. Hillenbrand, Opt. Exp., 13, 8893 (2005).

[3] A. P. Engelhardt, Master Thesis, RWTH Aachen University (2012).

[4] B. Hauer, A. P. Engelhardt, T. Taubner, *submitted* (2012).

[5] A. Cvitkovic, N. Ocelic, R. Hillenbrand, Opt. Exp., 15, 8550 (2007).

[6] J. Aizpurua, T. Taubner, F. J. G. de Abajo, M. Brehm, R. Hillenbrand, Opt. Exp., 16, 1529 (2008).

Bulk Electronic Band Structure Measurements Using Hard X-ray Photoemission

L. Plucinski[1], J. Minar[2], J. Braun[2], A. X. Gray[3,4], S. Ueda[5], Y. Yamashita[5], K. Kobayashi[5], H. Ebert[2], C.S. Fadley[3,4], and C.M. Schneider[1,6]

[1]Peter Grünberg Institut PGI-6, Forschungszentrum Jülich, 52425 Jülich
[2]Department of Chemistry, Ludwig Maximillian University, 81377 Munich
[3]Department of Physics, University of California Davis, Davis, CA 95616, USA
[4]Materials Sciences Division, Lawrence Berkeley National Laboratory, Berkeley, CA 94720, USA
[5]NIMS Beamline Station at SPring-8, Nat. Inst. for Mat. Science, Hyogo 679-5148, Japan
[6]Fakultät für Physik, University of Duisburg-Essen, 47057 Duisburg

Traditional ultraviolet/soft X-ray angle-resolved photoemission spectroscopy (ARPES) may in some cases be too strongly influenced by surface effects to be a useful probe of bulk electronic structure. Going to hard X-ray photon energies and thus larger electron inelastic mean-free paths should provide a more accurate picture of bulk electronic structure. Special effects occurring in a higher-energy ARPES experiment must be considered, such as photon momentum, phonon-induced zone averaging effects, and the degree of cryogenic cooling required, which can be estimated via appropriate Debye-Waller factors.

ARPES is the most powerful tool to study the valence band electronic structure of solid, giving direct access to the k-resolved electronic bands in the direction parallel to the measured surface. In the widely used vacuum ultraviolet and soft x-ray regions ($h\nu$ = 10-1000 eV) photoemission is surface sensitive due to the electron mean free path of 5-10 Å. This surface sensitivity is advantageous in case one is interested in surface-relates features, however, it commonly disturbs the interpretation ofthe bulk related properties such as the magnitude of the fundamental gap or the shape of three-dimensional Fermi surface. The only certain way to increase the electron mean free path, and in turn increase the bulk sensitivity, is to increase kinetic energy of the valence band electrons by increasing the photon energy.

The recent advent of new high-energy third-generation synchrotron facilities and the development of new high-energy electron analyzers makes it possible to attempt such novel angle-resolved experiments extending deep into the hard x-ray regime. The overall energy resolutions (down to 50 meV), as well as the angular resolutions of these newly-developed facilities (down to 0.2-0.3°) in principle make it possible to perform meaningful studies of dispersive energy bands up to e.g. 3-6 keV excitationenergies. A key advantage of such energies lies in increasing the inelastic mean-free path of the electrons by a factor of about 10-20, thereby markedly enhancing the bulk sensitivity of the measurement, and also permitting it to study, in some cases, deeply buried layers.

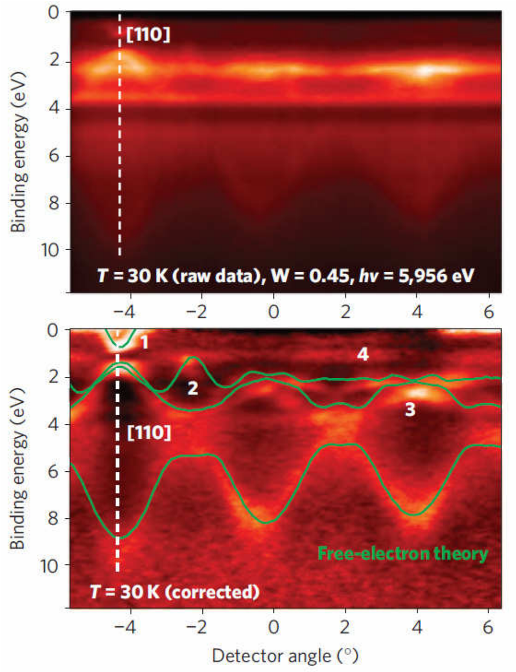

FIG. 1: HAXPES results for W(110) surface measured using 5956 eV photons at 20K [1]. Upper panel: raw data, Lower panel: data corrected for inelastic background and photoelectron diffraction effects, together with free-electron final state model simulation using DFT ab-initio bulk band structure [5].

We have pushed ARPES into the hard x-ray regime using photon energies 3-6 keV, which enhances the probing depth up to 30-60 Å [1], and such hard x-ray photoemission (HAXPES) results for (110) face of the W single crystal at $h\nu$ = 6 keVare shown in Fig. 1. Upper panel shows the raw data which contains contribution from direct and indirect transitions:

$$I_{tot} = W(T)I_{DT} + (1\text{-}W(T))I_{NDT}$$

where I_{DT} is the intensity of the wave-vector-conserving direct transitions, which gives the momentum dependent information of the band structure, and I_{DT} describes indirect transitions, where the creation or annihilation of phonons accompanies the photoemission process, which in first approximation can be modeled by the density of states (DOS) [2], while more elaborate derivationa have also been performed [3]. The photoemission Debye-Waller factor $W(T) = e^{-(1/3)|k_f k_i|^2\langle u^2(T)\rangle}$ in this equation originates from the de-phasing of the initial and final state electron wave functions by lattice displacements, where $|k_f - k_i|$ is the electron wave-vector difference (equal to a reciprocal lattice vector $\mathbf{g}$ in the usual interpretation of ARPES), and $\langle u^2(T)\rangle$ is the mean-square thermal displacement of the atoms. This shows that reducing the temperature helps inimproving the I_{DT} / I_{NDT} ratio. Furthermore $I(angle)$ in the raw data in Fig. 1 is modulated by the photoelectron diffraction effects, and in the corrected spectra in the lower panel both of these effects are corrected by dividing the raw data image by averaged intensities in both energy and angular directions. The details of the band dispersions and spectral weights can be understood using a simple free-electron final state model, or accurate one-step photoemission calculations [1,3].

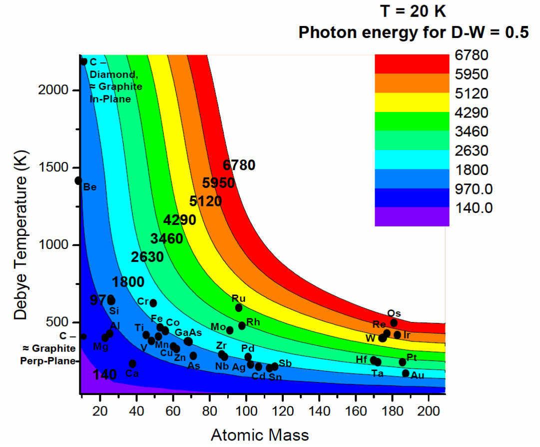

FIG. 2: Plot of the photon energies yielding valence-band Debye-Waller factors of 0.5, as a rough estimate of 50% direct-transition behavior, at a 20 K measurement temperature, as a function of atomic mass and Debye temperature. The points show various elements. This plot can be used to estimate the feasibility of high-energy ARPES experiments for other materials.

As an approximate way to assess the degree of phonon-induced Brillouin-zone averaging for various systems, we show in Fig. 2 the photon energies yielding Debye-Waller factors of 0.5 at 20 K (a reasonable measuring temperature for many current cryocooled sample holders) as a function of atomic mass and Debye temperature, with points for several elements indicated [4]. Other elements or compounds can be estimated from this plot. From this consideration of approximately 40 elements, we conclude that fruitful ARPES measurements should certainly be possible for many materials in the 1-3 keV range. For other materials, and/or with correction procedures such as this used for Fig. 1 (right panel), or better methods allowing more precisely for phonon effects, even higher energies up to 6 keV should be possible. An additional consideration in hard x-ray ARPES (HARPES) measurements is the effects of recoil on energy positions and resolution. In the limit of free-atom recoil, the recoil energy can be estimated from:

$$E_{recoil} = \frac{\hbar^2 k_f^2}{2M} \approx 5.5 \cdot 10^{-4} [\frac{E_{kin}(eV)}{M(amu)}],$$

Where M is the effective mass of the atom(s) involved [4]. Here again, with typical resolutions of ~ 100 meV that can already be achieved with soft and hard x-ray ARPES systems, we find that most elements should be capable of study up to 4 keV, if not higher.

---

[1] A. X Gray, C. Papp, S. Ueda, B. Balke, Y. Yamashita, L. Plucinski, J. Minar, J. Braun, E. R. Ylvisaker, C. M. Schneider, W. E. Pickett, H. Ebert, K. Kobayashi, and C. S. Fadley, “Probing Bulk Electronic Structure with Hard-X-Ray Angle-Resolved Photoemission: W and GaAs”, Nature Materials 10, 759 (2011).

[2] Z. Hussain, C. S. Fadley, S. Kono, and L. F. Wagner, “Temperature-dependent angle-resolved x-ray photoemission study of the valence bands of single-crystal tungsten: Evidence for direct transitions and phonon effects”, Phys. Rev. B 22, 3750 (1980).

[3] L. Plucinski, J. Minar, B.C. Sell, J. Braun, H. Ebert, C.M. Schneider, and C.S. Fadley, “Band mapping in higher-energy x-ray photoemission: Phonon effects and comparison to one-step theory”, Phys. Rev. B 78, 035108 (2008).

[4] C. Papp, L. Plucinski, J. Minar, J. Braun, H. Ebert, and C. S. Fadley, “Band mapping in x-ray photoelectron spectroscopy: an experimental and theoretical study of W(110) with 1.25 keV excitation”, Phys. Rev. B 85, 045433 (2011).

[5] P. Blaha, K. Schwarz, G. K. H. Madsen, D. Kvasnicka, and J. Luitz, An Augmented Plane Wave + Local Orbitals Program for Calculating Crystal Properties (Karlheinz Schwarz, Techn. Universität Wien, Austria) ISBN 3-9501031-1-2 (2000)

Electrically Conducting Gold Nanopatterns on Structured SAMs by Chemical e-Beam-Lithography

P. A. Schaal[1], M. Noyong[1], A. Besmehn[2], E. Maynicke[3], B. Beschoten[3], U. Simon[1]

[1] Institute of Inorganic Chemistry (IAC), RWTH Aachen University
[2] Central Division of Analytical Chemistry (ZCH), Forschungszentrum Jülich, 52425 Jülich
[3] II. Institute of Physics, RWTH Aachen University

We demonstrate the fabrication of electrically conducting Au nanopatterns by a combination of bottom-up and top-down techniques. Therefore, organic self-assembled monolayers with sulfonic acid head groups were locally reduced to thiol groups by means of chemical e-beam lithography. These thiol patterns were decorated with 15 nm gold nanoparticles, which acted as nucleation seeds for electroless Au deposition from solution in subsequent enhancement steps. Electrical characterisation of these structures was then performed with an *in situ* nanomanipulator setup operated in a scanning electron microscope.

In order to meet the current interest of metal nanoparticles (NPs) in electronic, optoelectronic, sensor and biological applications, it is necessary to reproducibly generate versatile patterns of NPs. [1, 2] A promising approach is the combination of top-down and bottom-up techniques, e.g. chemical e-beam lithography (CEBL) and self-assembly processes.[3-5]

We used wet-chemical silanisation in absolute toluene to produce self-assembled monolayers (SAMs) of 2-(4-chlorosulfonylphenyl)ethylsilane (CSPETCS, see fig. 1). The formed CSPETCS-SAMs were analysed by ellipsometry and contact angle measurements. Film thicknesses were determined to be about 1.3 nm ± 0.1 nm and contact angles were calculated to be 62° ± 6°.

These SAMs were lithographically exposed to an electron beam with a pattern generator controlled SEM. The e-beam induced reduction at 2 kV of the sulfonic acid head groups to thiol groups was proven by XPS measurements of the S2s orbital, showing a shift in binding energy from ≈232.5 eV to ≈228.0 eV.

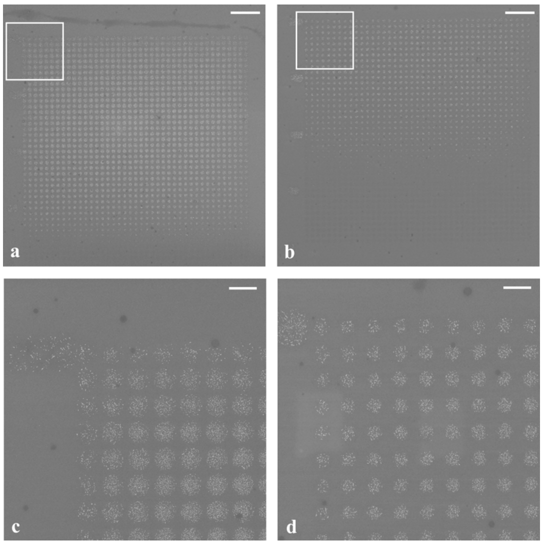

Fig. 2: SEM pictures of lithographic patterns of different size and dose, decorated with 15 nm AuNP. Scale bar equals 5 µm (a, b) and 1 µm (c, d), respectively. Adapted with permission from Langmuir 2012, 28, 2448. Copyright 2012 American Chemical Society.

Lithographic spot patterns of different size were selectively decorated with 15 nm gold nanoparticles (AuNPs) resulting in patterns like those shown in fig. 2. Diameters of all written spots

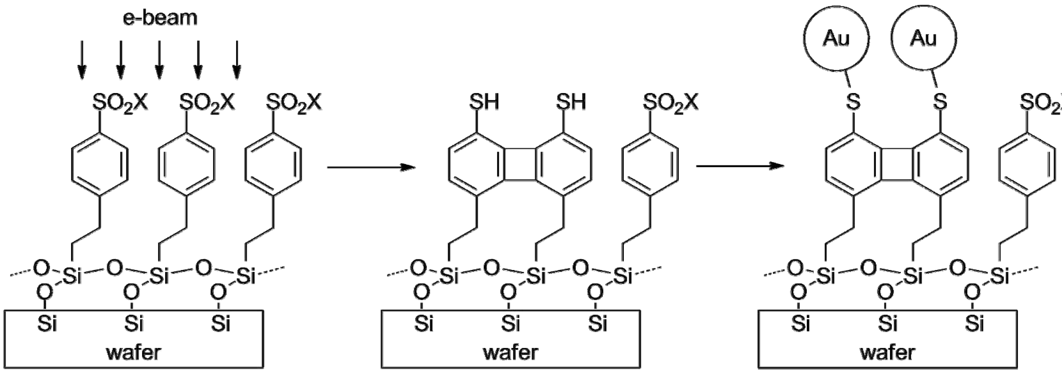

Fig. 1: CEBL on 2-(4-chlorosulfonylphenyl)ethylsilane SAMs (X = Cl, OH) and decoration of generated thiol patterns with AuNPs. Adapted with permission from Langmuir 2012, 28, 2448. Copyright 2012 American Chemical Society.

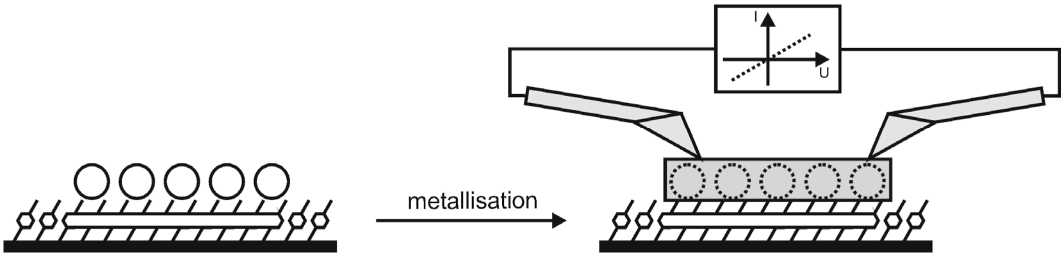

Fig. 3: Electroless metallisation of AuNP and subsequent electrical characterisation via in situ nanomanipulator measurements. Adapted with permission from Langmuir 2012, 28, 2448. Copyright 2012 American Chemical Society.

were about two times bigger than intended, viz. 830 nm ± 20 nm instead of 400 nm in fig. 2a and 550 nm ± 30 nm instead of 200 nm in fig. 2b. This enlargement is most probably caused by large-area electron back-scattering. Furthermore all patterns show size depended threshold doses for immobilisation of AuNPs.

Subsequent electroless plating for 180 s with Au(I)/hydroquinone [6, 7] solution resulted in almost filled, circular gold island, shown in fig. 4. Using an *in situ* nanomanipulator setup (schematically drawn in fig. 3) these gold islands were electrically characterised. In order to exclude electrical conductance through the substrate neighbouring islands were contacted and measured. *I(U)* characteristics showed negligible conductance within the measuring range of ± 1 mV. In contrast to that measurements on one single island (see fig. 4b) showed ohmic *I(U)* behaviour between ±500 µV (current compliance of 5 µA was used). Electrical measurements of different islands yielded an average resistance *R* of 170 Ω ± 40 Ω. Including individual tip distance and radii the resistivity ρ was calculated to values within the range from 4×10^{-7}Ωm to 3×10^{-6} Ωm, which are in accordance to values for granular gold structures reported in literature.[8, 9]

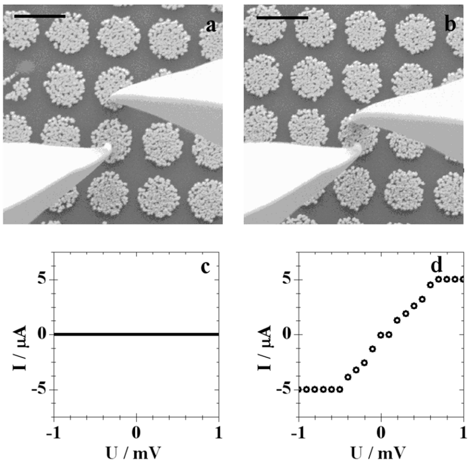

Fig. 4: SEM images (a, b) of electrical characterisation with in situ nanomanipulator setup (scale bar equals 1 µm) and corresponding I(U) characteristics (with compliance of 5 µA) reprinted with permission from Langmuir 2012, 28, 2448. Copyright 2012 American Chemical Society.

This approach can be considered as a proof-of-concept for the formation of versatile thiol patterns on silicon wafers. By combination of this top-down process with the metallisation of the formed structures, fabrication of future electrical devices becomes possible.

This work was supported by the Excellence Initiative of the German federal and state governments (Seed fund of the faculty). We thank A. Gölzhäuser and A. Beyer, University of Bielefeld (Germany) for kind support.

---

[1] Schmid, G., Ed. *Nanoparticles - From Theory to Application*; Wiley-VCH Verlag GmbH & Co.KGaA, 2010.

[2] Mendes, P. M.; Preece, J. A. In *Micromanufacturing and Nanotechnology*; Mahalik, N. P., Ed.; Springer GmbH, Berlin, Germany, 2006, 383–396.

[3] Mendes, P. M.; Jacke, S.; Critchley, K.; Plaza, J.; Chen, Y.; Nikitin, K.; Palmer, R. E.; Preece, J. A.; Evans, S. D.; Fitzmaurice, D. *Langmuir* 2004, *20*, 3766–3768.

[4] Beyer, A.; Godt, A.; Amin, I.; Nottbohm, C. T.; Schmidt, C.; Zhao, J.; Gölzhäuser, A. *Phys. Chem. Chem. Phys.* 2008, *10*, 7233–7238.

[5] Lud, S. Q.; Neppl, S.; Richter, G.; Bruno, P.; Gruen, D. M.; Jordan, R.; Feulner, P.; Stutzmann, M.; Garrido, J. A. *Langmuir* 2010, *26*, 15895–15900.

[6] Fischler, M.; Simon, U.; Nir, H.; Eichen, Y.; Burley, G. A.; Gierlich, J.; Gramlich, P. M. E.; Carell, T. *Small* 2007, *3 (6)*, 1049–1055.

[7] Braun, E.; Eichen, Y.; Sivan, U. S. Patent 2006/0211136 A1, 2006.

[8] Keren, K.; Krüger, M.; Gilad, R.; Ben-Yoseph, G.; Sivan, U.; Braun, E. Science 2002, 297, 72–75

[9] Harnack, O.; Ford, W. E.; Yasuda, A.; Wessels, J. M. *Nano Lett.* 2002, *2*, 919–923

Assembly of gold nanoparticles on patterned chemical templates

S. Gilles[1,3], C. Kaulen[2], M. Pabst[1], U. Simon[2], A. Offenhäusser[1], D. Mayer[1]

[1]Peter Grünberg Institute (PGI-8), Forschungszentrum Jülich
[2]Institut of Inorganic Chemistry, RWTH Aachen University
[3]Present address: Institute of Inorganic Chemistry, RWTH Aachen University

We fabricated defined assemblies of gold nanoparticles by using chemical patterns on silicon surfaces as template structures. These templates were produced by means of a stepwise process comprising soft UV nanoimprint lithography, reactive ion etching, chemical functionalisation with amino groups, and lift-off of imprint resist. 20 nm diameter citrate stabilised gold nanoparticles were immobilised on the chemical patterns from aqueous solution. By reducing the ionic strength of the solution, even one- and zero-dimensional particle assemblies could be generated on sub-100-nm predefined structures.

The defined assembly of nanoscale metallic building blocks such as gold nanoparticles (AuNP) on solid surfaces is relevant for numerous applications in research fields such as sensing [1], biotechnology [2] and nanoelectronics [3]. Here, we report a combination of nanoimprint lithography (NIL) as top-down approach and self-assembly of gold nanoparticles as bottom-up approach to fabricate patterns of gold nanoparticles. Templates having a chemical pattern without bearing a significant topology are fabricated by using soft UV nanoimprint lithography, reactive ion etching, silanisation, and a lift-off process. These template patterns are used for localised immobilisation of gold nanoparticles from solution onto topography free surfaces. By changing the ionic strength of the colloid solution, it is possible to tune the particle density on the structures.

Silicon wafer with an oxide surface were used as substrates for the patterning process shown in figure 1. The substrates were diced into 2 x 2 cm^2 pieces, cleaned thoroughly, further PMMA was spincoated and baked on a hotplate at 150°C resulting in a layer with a thickness of approximately 120 nm. After that UV resist NXR-2010 was applied which lead to a second resist layer of approximately 100 nm thickness. For soft UV-NIL, polymer stamps made of Surlyn 1702 (DuPont) were used [5]. The imprint was carried out in the NX-2000 nanoimprint device working with aircushion principle. The stamp was placed on a resist coated sample and introduced in the imprint machine. At reduced pressure the stamp structures were replicated into the deformable UV resist. The resist was then cured by exposure to UV light. After releasing the pressure, the polymer stamp was peeled off the substrate leaving a negative copy of its surface structure in the cured resist. Next, the defined pattern was transferred to the substrate by reactive ion etching. After etching, the samples were coated by 3-aminopropyl-triethoxysilane via vapor deposition. Subsequently, the NIL resist stack was removed by a lift-off procedure in acetone and samples were blown dry with nitrogen.

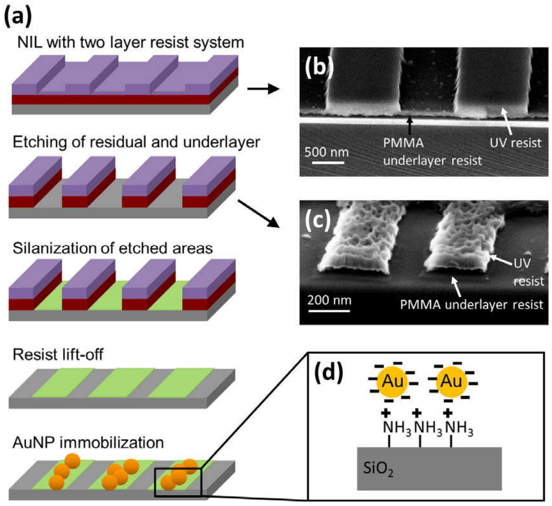

FIG. 1: (a) Schematic representation of the patterning process, (b) SEM measurement (observation angle 60°) of a cross section of a patterned area after imprint, (c) SEM measurement (observation angle 60°) of a cross section of a patterned area after etching residual layer and underlayer resist, (d) schematic representation of electrostatic interaction between an amino modified area and citrate stabilised gold nanoparticles. (Adapted from [4] with permission from IOP Publishing Ltd).

Incubation of the samples carrying the chemical template with a solution of citrate stabilised AuNPs (20 nm diameter) resulted in particle deposition on the structured area. The density of the particles on the surface pattern could be tuned by diluting the colloid solution and by this means changing the ionic strength I of the solution. A reduced ionic strength influences the Debye length κ^{-1} in solution according to the Debye-Hückel theory. Figure 2 shows decreasing particle densities for decreasing ionic strengths of the particle solution. The hydrodynamic radii calculated from Debye-Hückel theory agree well with the experimentally determined interparticle distances. The observed principle and the knowledge of the hydrodynamic particle size were further utilised to create patterns with single particle resolution.

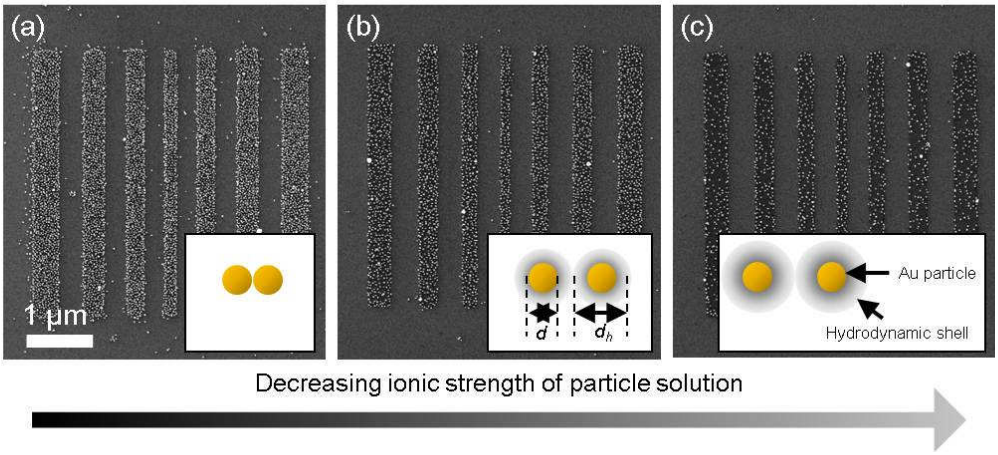

FIG. 2: SEM measurements with widths ranging from 400 to 150 nm decorated with gold nanoparticles fabricated with decreasing particle density by decreasing the ionic strength of AuNP solution (from left to right). The particle densities on the shown structures are (a) 779 µm^{-2}, (b) 432 µm^{-2}, (c) 219 µm^{-2}. The insets show schematically two nearest gold nanoparticles with diameter d and hydrodynamic diameter d_h. (Reprinted from [4] with permission of IOP Publishing Ltd).

Nanoimprint lithography in combination with a highly diluted colloid solution (I = 1.26 mmol L^{-1}) for immobilisation of particles was used to define structures below 100 nm. In this way, 0- and 1-dimensional particle assemblies could be obtained using amino terminated structures. Figure 3b shows a circular pattern with a diameter of about 100 nm. In comparison to the corresponding hydrodynamic diameter of 54 nm the pattern size is small enough to locate a single particle. This approach was also used to generate and analyse 1-dimensional nanoparticle patterns by employing stripe like chemical templates. If the width of the stripes is small enough to obey the one particle criterion, lines of individual particles can be produced, as shown in figure 3a. There the stripes are about 400 nm long and 85 nm wide. The result was a 'chain-like' arrangement of particles on the stripes.

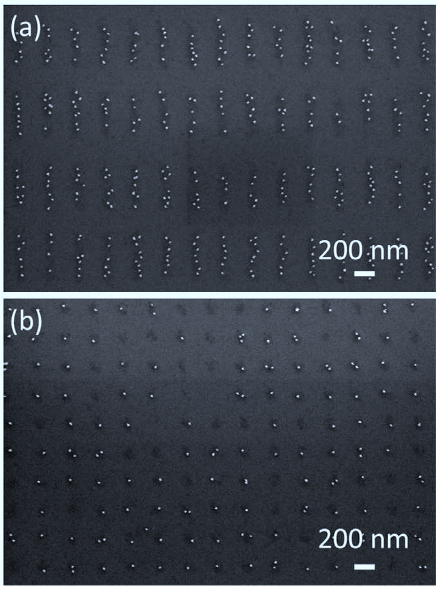

FIG. 3: SEM measurements of (a) rectangular and (b) circular structures decorated with low density of gold nanoparticles. (Adapted from [4] with permission of IOP Publishing Ltd).

The distribution of the particles along the stripes is more or less random. On average, the particles are packed not closer than predicted by their hydrodynamic diameter. It is presumed that by choosing a smaller width of the stripes the particles can be aligned more straight. In principle, more complicated patterns can be envisioned for the assembling of nanoparticles.

In conclusion, we fabricated topography free, amino terminated chemical templates by means of nanoimprint lithography utilising an inexpensive polymer mold. The chemical templates were successfully used for the self-assembly of citrate stabilised gold nanoparticles based on electrostatic template-particle interactions. By using sub-100 nm template structures and low ionic strength, we were able to fabricate 1- and 0-dimensional nanoparticle assemblies on the surface. In this way, we found a rather simple method for the fabrication of high resolution gold nanoparticle assemblies, by combining a bottom-up and a top-down approach. The nanoparticle assemblies may represent precursor structures for local chemical surface modifications, for instance by exchanging the ligands of the gold nanoparticles.

---

[1] N. Nath, A. Chilkoti, Anal. Chem. 76, 5370 (2004)

[2] M. Arnold, V. C. Hirschfeld-Warneken, T. Lohmüller, P. Heil, J. Blümmel, E. A. Cavalcanti-Adam, M. López-García, P. Walther, H. Kessler, B. Geiger, J. P. Spatz, Nano Lett. 8, 2063 (2008)

[3] G. Schmid, U. Simon, Chem. Commun. 6, 697 (2005)

[4] S. Gilles, C. Kaulen, M. Pabst, U. Simon, A. Offenhäusser, D. Mayer, Nanotechnology 22 295301 (2011), doi: 10.1088/0957-4484/22/295301

[5] S. Gilles, M. Meier, M. Prömpers, A. van der Hart, C. Kügeler, A. Offenhäusser, D. Mayer, Microelectronic Engineering, 86, 661 (2009)

Sputtered Platinum-Iridium Layers as Stimulation Electrode Material for Neural Cells

G Ganske[1]**, E Slavcheva**[1, 2]**, W Mokwa**[1]**,and U Schnakenberg**[1]

[1]Institute of Materials in Electrical Engineering I, RWTH Aachen University, 52074 Aachen
[2]Institute of Electrochemistry and Energy Systems, Bulgarian Academy of Sciences, 1113 Sofia, Bulgaria

Co-sputtered layers of platinum-iridium (PtIr) as stimulation electrode material were deposited and compared to sputtered platinum and iridium thin films. The effects of different sputter parameters like working distance, power, and pressure on the morphology and the electrochemical behavior were investigated. It could be shown that films sputtered at the lowest incident energy showed the highest charge delivery capacity (CDC).

Today an increasing number of medical devices are dedicated to the stimulation of neural cells. Best known examples are the heart pacemaker and the cochlea implant. A major obstacle next to autoimmune reactions is the electrode-electrolyte interface between the neuron and the stimulation electrode. The electrical energy has to be transformed to an ionic current which results in a depolarization of the nerve cell evoking an action potential. Typical electrode materials are platinum, platinum-iridium [1], titanium-nitride, iridium, and iridium-oxide [2]. These materials can be differentiated into three groups: a) titanium-nitride which has a pure capacitive charge transfer from the electrode into the electrolyte; b) platinum, iridium, and platinum-iridium where a reversible faradaic reactions take place at the electrode surface in addition to the capacitive charge and c) iridium oxide which transforms into a hydrated oxide film with a high charge injection capacity [3].

Platinum-iridium is used as a material for stimulation electrode because of its increased hardness, corrosion stability and enhanced charge injection capacity compared to platinum. Platinum-iridium can be applied to microelectronic devices by electroplating [4], chemical reaction [5,6], or sputtering techniques [7]. The later method allows the deposition of elements and compounds with adapted performance. Through variation of the sputtering parameters like power, pressure, distance between target and substrate (working distance, WD), and gas flow the composition, roughness, stability, and charge delivery capacity (CDC) can be customized. The parameters pressure, WD, and sputtering power can be combined and calculated into the parameter mean incident energy (E_{inc}). The incident energy of an adatom that reaches the substrate is the most important factor for the film growth [8]. To our knowledge, up to now sputtered platinum-iridium thin films have not been applied for stimulation purposes. Due to its physical and electrochemical

properties this material combination is of interest for the realization of micro electrodes. In our studies three sets of parameters were used that are given in table 1. We will from now on refer to the samples by their incident energy.

E_{inc} [eV]	10.2	1.9	0.2
P [mTorr]	12	68	11
Power [W]	180	1000	180
WD [mm]	78	78	78

Table 1: Sputtering parameters.

SEM pictures of 200 nm PtIr sputtered on silicon substrates are shown in figure 1. The film sputtered at highest energy (figure 1a) shows a straight columnar dense growth with a smooth closed surface. The sample in figure 1b sputtered at medium energy still shows a mainly columnar growth with dislocations. The surface is rougher.

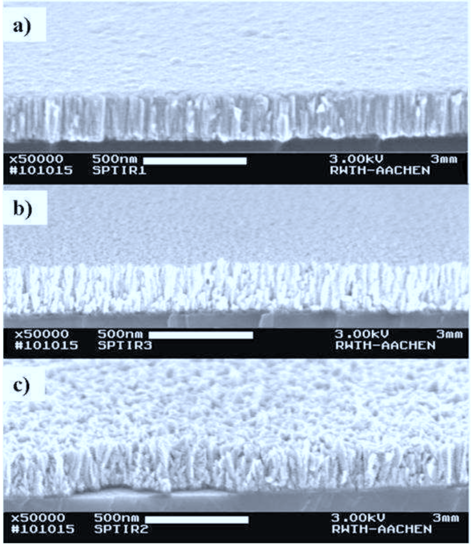

Figure 1: Platinum-Iridium sputtered at different incident energies: a) 10.2 eV; b) 1.9 eV; c) 0.2 eV (thermalized)

Finally, the layer sputtered at the lowest deposition energy (figure 1c) still shows a columnar growth, but the columns are distorted and crooked. The observed cauliflower like outgrowth indicates a non directional growth with visible gaps in the surface and voids between the columns.

In [9] it was shown for sputtered iridium films by simulations and experiments that atoms reaching the substrate with a high energy (E_{inc}) form dense films. This energy results from a high starting energy and a long mean free path with few collisions during the transport from the target to the substrate. When impacting the surface the atoms have long diffusion paths, which result into the formation of tightly packed surfaces. Furthermore, the possibility of resputtering and lattice rearrangement occurrences is also increased. A similar behavior was confirmed here for sputtered PtIr layers. For stimulation purposes a large open porous surface is desired. At low impact energy (figure 1c) the atoms reaching the substrate with just their thermal energy are far less likely to diffuse towards a previously sputtered atom. Thus, the layer is much rougher compared to that of figure 1a, resulting in a dramatically increased surface.

Interestingly, the CV-characteristics of the densest layer sputtered at a incident energy of 10.2 eV is very similar to that of pure platinum (figure 2b). The cathodic peaks of oxygen reduction and hydrogen adsorption as well as the corresponding anodic peaks of hydrogen desorption followed by formation of surface oxygen coverage are clearly depicted. It does not show the broad hydrogen adsorption shoulder starting at -0.4 V which is typical for iridium but instead the small platinum oxygen reduction peak at -0.2 V. This might be a result of the co-sputtering process. Since the substrate rotates beneath the activate targets it is possible that the wafer has passed the platinum target last and the surface of this smooth and dense layer is covered mostly by platinum atoms.

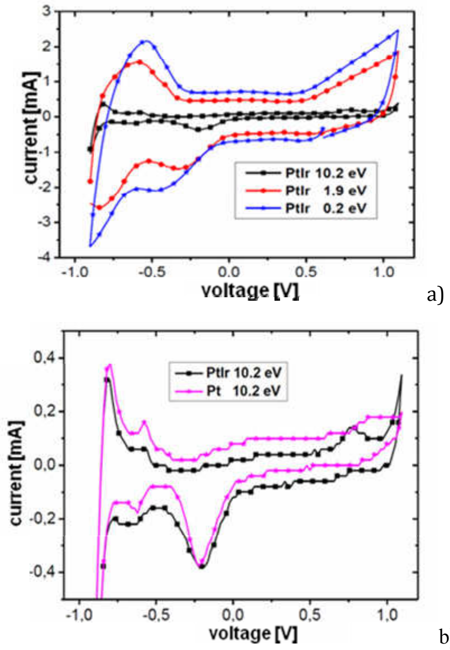

Figure 2: a) CV-curves of PtIr sputtered at different parameters measured in saline solution at a scan rate of 100 mV/s; b) CV-curves of PtIr and Pt sputtered at 10.2 eV (scan rate 100 mV/s).

Such an effect is observed for the CV-curves of the other samples which differ from those of pure platinum or pure iridium (not shown here).

To classify the properties of platinum-iridium as a stimulation electrode coating we compared the layers that show the highest CDC to films of pure iridium and pure platinum sputtered at similar conditions. The results are given in table 2. The CDC value for PtIr is significantly higher than for Pt. Therefore, the combination of platinum and iridium through co-sputtering is a promising technology for fabrication of stimulation electrodes. As for iridium, sputtering at high pressures and low sputter power results in the most porous films. These have the highest charge delivery capacity and are ideal for stimulation purposes. We showed that the positive attributes of both materials can be combined. The used ratio of Pt and Ir is not yet ideal and needs to be optimized. Long term tests showed that on repeated cycling an activation of the material, hence hydroxide incorporation into the iridium part, does take place. The resulting film remains stable and show an increased CDC. A further study of this activation process in sputtered PtIr is necessary to clarify this process.

E_{inc} [eV]	10.2	1.9	0.2
Pt [mC/cm^2]	2.29	10.5	16-18
Ir [mC/cm^2]	2.3	30.6	35-37
PtIr [mC/cm^2]	2.26	17	23-25

Table 2: Anodic charge delivery capacity CDC of layers sputtered at given parameters in saline solution (0.9% NaCl, -0.9 V – 1.1 V, 100 mV/s).

In summary, co-sputtered Platinum-Iridium is a promising candidate for stimulation electrode coatings due to its higher stability in regard to pure iridium, in combination with an increased charge delivery capacity in comparison to pure platinum.

Acknowledgments
The authors wish to thank the DFG for funding the graduate school 1035 “Biointerface” and the German Academic Exchange Service (DAAD) for supporting project PPP D/06/05922.

---

[1] Cogan S F, Troyk PR, Ehrlich J and Plante T D 2005 *Biomedical Engineering, IEEE Transactions on* 52 1612-4

[2] Slavcheva E, Vitushinsky R, Mokwa W and Schnakenberg U 2004 *Journal of the Electrochemical Society* 151 E226-E237

[3] Cogan S R 2008 *Annual Review of Biomedical Engineering* 10 275-309

[4] Ureta-Zanartu M S, Yanez C, Reyes G, Gancedo J R and Marco J F 1998 *Journal of Solid State Electrochemistry* 2 191-7

[5] Ioroi T, Yasuda K 2005 *Journal of the Electrochemical Society* 152 A1917-A1924

[6] Yim S D, Lee W Y, Yoon Y G, Sohn Y J, Park G G, Yang T H and Kim C S 2004 *Electrochimica Acta* 50 713-8

[7] Kuribayashi K, Fujita Y, Isige H and Iwanuma T 2004 *Materials Science and Engineering B-Solid State Materials for Advanced Technology* 109 188-91

[8] Wessling B, Mokwa W and Schnakenberg U 2007 *Journal of the Electrochemical Society* 155 F61-F65

[9] Wessling B, Lusebrink D, Mokwa W and Schnakenberg U 2007 *Journal of the Electrochemical Society* 155

Understanding the role of the local field potential in neuronal network interaction

M. Denker[1], J. Ito[1], T. Tetzlaff[1], M. Diesmann[1,2], S. Grün[1,3]

[1]Institute for Neuroscience and Medicine (INM-6), Computational and Systems Neuroscience, Forschungszentrum Jülich
[2]Computational Neuroscience, Faculty of Medicine, RWTH Aachen University
[3]Theoretical Systems Neurobiology, Faculty I, RWTH Aachen University

The local field potential (LFP) is the low frequency component (1-500Hz) of a extracellularly recorded signal from the brain. Albeit this signal is known since decades, likely due to the simplicity to stably record it, its composition and origin is yet hardly understood. In this contribution we illustrate the role of the LFP as measured in various cortical areas in neuronal processing during every days behavior. In visual cortex the LFP occurs as a short living oscillation locked to the onset of saccades thereby representing top-down information for the integration of incoming visual input (Ito et al, 2011). In data from the motor cortex we were able to show that the LFP reflects coordinated neuronal spiking activity (Denker et al, 2011). Finally, by analytical and network modeling of the LFP we provide an understanding in the composition and spatial extent of the LFP signal (Linden et al, 2011).

During natural vision, primates perform frequent saccadic eye movements, allowing only a narrow time window for processing the visual information at each location. Individual neurons may contribute only with a few spikes to the visual processing during each fixation, suggesting precise spike timing as a relevant mechanism for information processing. We recently found in V1 of monkeys freely viewing natural images, that fixation-related spike synchronization occurs at the early phase of the rate response after fixation-onset, suggesting a specific role of the first response spikes in V1. In [1] we show that there are strong local field potential (LFP) modulations locked to the onset of saccades, which continue into the successive fixation periods. Visually induced spikes, in particular the first spikes after the onset of a fixation, are locked to a specific epoch of the LFP modulation. We suggest that the modulation of neural excitability, which is reflected by the saccade-related LFP changes, serves as a corollary signal enabling precise timing of spikes in V1 and thereby providing a mechanism for spike synchronization (Fig. 1).

While oscillations of the local field potential (LFP) are commonly attributed to the synchronization of neuronal firing rate on the same time scale, their relationship to coincident spiking in the millisecond range is unknown. In [2] we presented first experimental evidence to link the notions of synchrony at the level of spiking and at the mesoscopic scale of observation. Only in time intervals of significant spike synchrony that cannot be explained on the basis of firing rates, coincident spikes are better phase locked to the LFP than predicted by the locking of the individual spikes (Fig. 2). This effect is enhanced in periods of large LFP amplitudes. To understand these findings, we embedded our measurements in a quantitative

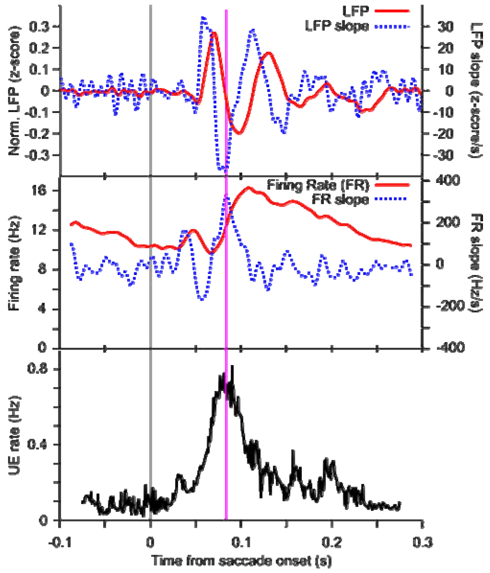

FIG. 1: Top: Average local field potential (LFP) from trials aligned to the onset of saccadic eye movements during free viewing of natural-scene images (red: average LFP signal, blue: its instantaneous slope). As predicted by our conceptual model that interprets the LFP as a modulating firing threshold the steepest negative slope of the LFP coincides with the peak of the occurrence of excess spike synchrony among neurons. Middle: mean firing rate of neurons triggered by saccade onset (red: mean, blue: its instantaneous slope). Bottom: The degree of excess spike synchrony among neurons measured as Unitary Event (UE) rate (Grün et al, 2002a). The additional coincidence of the negative slope of the LFP with the positive peak of the derivative of the firing rate indicates that the saccade-related LFP oscillations modulate the timing of visually evoked spikes of many neurons. As a consequence, spikes of different neurons become synchronized. Figure from Ito et al, 2011.

model that explains the LFP dynamics by the concerted spiking activity in neuronal groups (termed assemblies) that contribute the observed surplus synchrony. In this framework, we could infer that neurons participate in different constellations but contribute only a fraction of their spikes to temporally precise spike configurations. This finding provides direct evidence for the hypothesized relation that precise spike synchrony constitutes a major temporally and spatially organized component of the LFP. Moreover, the results demonstrate how knowledge on the interplay of brain signals at multiple scales can grant access to macroscopic descriptions of the underlying network dynamics.

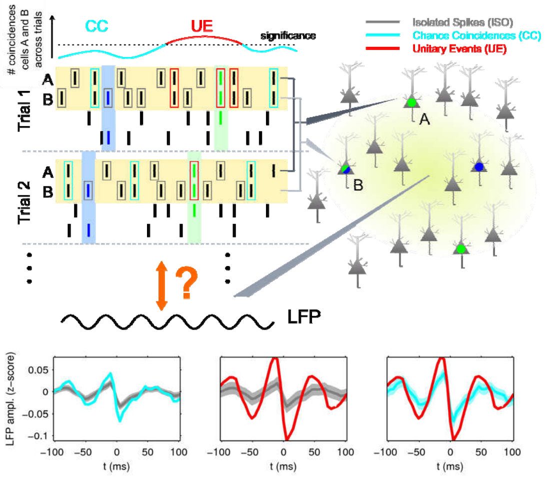

FIG. 2: Analyzing how concerted neural activity is related to the LFP in recordings from motor cortex of the behaving monkey. Top: Schematic representation. Spikes of two neurons (A and B, yellow background) and an LFP are recorded in two trials from three separate electrodes (right) spaced at approximately 400 µm. The spikes of one recorded neuron are classified as chance coincidence (CC, cyan) or Unitary Event (UE, red) if they are precisely (±3 ms) synchronized with a spike of the second neuron recorded in parallel, and otherwise as isolated (ISO, gray). In contrast to CCs, UEs identify coincidences in epochs where the high number of observed coincidences across trials (top curve) significantly exceeds the prediction based on the firing rates. In UE epochs, synchrony between both neurons is commonly explained by their reliable and temporally confined co-activation in a neuronal assembly (e.g., green and blue colored spikes and background). Bottom: Comparison of the average LFP around each class of spikes (aligned at 0 ms) reveals a strong phase relationship between significant coincidences (UE) and the LFP. Figure from Denker et al, 2011.

The local field potential (LFP) reflects activity of many neurons in the vicinity of the recording electrode and is therefore useful for studying local network dynamics. Much of the nature of the LFP is, however, still unknown. There are, for instance, contradicting reports on the spatial extent of the region generating the LFP. In [3] we employed a simplified mathematical and a detailed biophysical model to investigate the size of the region contributing to the LFP (see Fig.3). We find that the size of the generating region depends on the neuron morphology, the synapse distribution, and the correlation in synaptic activity. For uncorrelated activity, the LFP represents cells in a small region (within a radius of a few hundred micrometers). If the LFP contributions from different cells are correlated, the size of the generating region is determined by the spatial extent of the correlated activity.

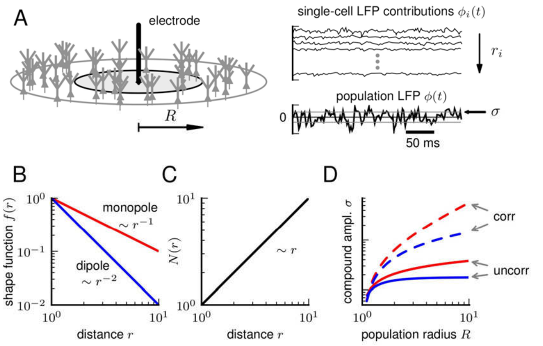

FIG.3: How local is the LFP? (A) Left: Sketch of the model setup. Cells (gray) are homogeneously distributed on a disc of radius R with the tip of the electrode in the center. Right: The superposition of LFP contributions $\varphi_i(t)$ of individual cells at distances r_i results in a population LFP $\varphi(t)$. The dependence of its amplitude $\sigma(R)$ (standard deviation) on the population radius R (see panel D) defines the electrode reach. (B) Dependence of the single-cell LFP amplitude f(r) (shape function) on the cell-electrode distance r for hypothetical current monopole (red) and dipole sources (blue). (C) Number N(r) of cells on a ring of radius r. (D) Dependence of the compound amplitude $\sigma(R)$ on the population radius R for populations of uncorrelated (solid curves) and correlated (dashed curves) monopole (red) and dipole sources (blue). The LFP generated by neurons exhibits dipole character (blue curves). For uncorrelated activity, the LFP amplitude $\sigma(R)$ saturates for increasing R: the LFP reach is finite (solid blue curve in D). Correlated activity, in contrast, leads to a non-saturating LFP amplitude $\sigma(R)$: the LFP reach becomes arbitrarily large (dashed blue curve in D). Figure from Linden et al, 2011.

This work was partially funded by the Research Council of Norway (eVita [eNEURO], NOTUR), EU Grant 15879 (FACETS), EU Grant 269921 (BrainScaleS), BMBF Grant 01GQ0420 to BCCN Freiburg, Next-Generation Supercomputer Project of MEXT, Japan, and the Helmholtz Alliance on Systems Biology

---

[1] Ito J, Maldonado P, Singer W, Grün S (2011) Saccade-related modulations of neuronal excitability support synchrony of visually elicited spikes. Cereb. Cortex 21 (11): 2482-2497. doi: 10.1093/cercor/bhr020.

[2] Denker M, Roux S, Linden H, Diesmann M, Riehle A, Grün S (2011) The local field potential reflects surplus spike synchrony. Cereb. Cortex 21 (12): 2681-2695. doi: 10.1093/cercor/bhr040.

[3] Linden H, Tetzlaff T, Potjans T C, Pettersen K H, Grün S, Diesmann M, Einevoll G (2011) Modeling the Spatial Reach of the LFP. Neuron 72, 859-872 doi: 10.1016/j.neuron.2011.11.006.

Electronic structure of a magnetic oxide directly on silicon

M. Müller[1], C. Caspers[1], A. X. Gray[2], A. M. Kaiser[1,2], A. Gloskowskii[3], C. S. Fadley[2], W. Drube[4], C. M. Schneider[1]

[1] Peter Grünberg Institut (PGI-6), Forschungszentrum Jülich, 52425 Jülich
[2] Department of Physics, University of California Davis, Davis, CA 95616, USA
[3] Institut für Analytische und Anorganische Chemie, Johannes Gutenberg-Universität, 55128 Mainz
[4] DESY Photon Science, Deutsches Elektronen-Synchrotron, 22603 Hamburg

We present an electronic structure study of a magnetic oxide/semiconductor model system, EuO on Silicon, which is dedicated for efficient spin injection and detection in silicon-based spintronics devices. A combined electronic structure analysis of Eu core levels and valence bands using hard x-ray photoemission spec- troscopy was performed to quantify the nearly ideal stoichiometry of EuO "spin filter" tunnel barriers directly on silicon, and the absence of silicon oxide at the EuO/Si interface. These re- sults provide evidence for the successful integra- tion of a magnetic oxide tunnel barrier silicon, paving the way for the future integration of mag- netic oxides into functional spintronics devices.

Accenting semiconductor electronics with spin functionality is a major thrust of current spintron- ics research. At present, considerable efforts are being made to replace conventional ferromagnet/semiconductor (FM/SC) or FM/oxide/SC contacts - which have hitherto been underlying many key experiments - with functional magnetic contact materials that could substantially alter the efficiency of spin injection and detection in semiconductor-based spintronics devices. In particular, magnetic oxides (MO) offer the unique combination of both generating almost fully spin polarized tunnel currents via a true "spin filter" effect and facilitating a conductance matched magnetic tunnel contact to a SC . Establishing MO tunnel contacts as efficient spin injectors and detectors bears large potential for ultimately realizing both high current transfer ratios *and* high magnetic sensitivities at the CMOS level, i. e. directly on Si.

With the goal to integrate ultrathin films of magnetic oxide as efficient spin-selective tunnel barriers directly on silicon, we present a study of the electronic properties of a MO/SC model system, Europium monoxide (EuO) on Si, that are dedicated for the use as spin injector and collector contacts. EuO is predicted to be chemically stable in direct contact with silicon. However, ferromagnetic EuO is very difficult to synthesize due to its large reactivity towards higher oxides, i. e. Eu_2O_3. Furthermore, any excess oxygen may readily oxidize the Si surface, which can lead to a loss of tunneling spin polarization.

We succeeded in preparing high-quality EuO/Si(001) heterostructures with bulk-like magnetic properties.

We used hard x-ray photoelectron spectroscopy (HAXPES) to probe the electronic structure of EuO tunnel barriers and the EuO/Si interface [1, 2]. Due to its large information depth—exceeding 10 nm at photon energies of 10 keV —HAXPES is a perfectly suited technique to probe the chemical quality of buried layers and interfaces (Fig. 1).

By studying photoemission spectroscopy from both core and valence levels, we obtain a comprehen- sive set of information on the electronic structure of EuO/Si(001). Fig. 2 (a)–(f) shows the Eu 4*s* and Eu 4*d* core levels, as well as the Eu 4*f* valence bands for stoichiometric EuO and O-rich Eu_2O_3 on Si [1, 2]. Eu cations in stoichiometric, ferromagnetic EuO are divalent, whereas Eu^{3+} antiferromagnetic contributions are expected in O-rich EuO. A quantitative peak anal- ysis of the divalent and trivalent spectral contributions in the Eu 4*s*, 4*d* and 4*f* spectra is employed to extract the EuO chemical composition. We assign the individual spectral features observed in the Eu core level and valence spectra. Fig. 2 (a) and (b) shows the Eu 4*s* core level spectra for both EuO compounds. The prominent double-peak struc- ture is caused by coupling of the 4*s* core level with the localized Eu 4*f* state, which leads to an exchange splitting $\Delta E = 7.4$ eV of the 4*s* inner shell.

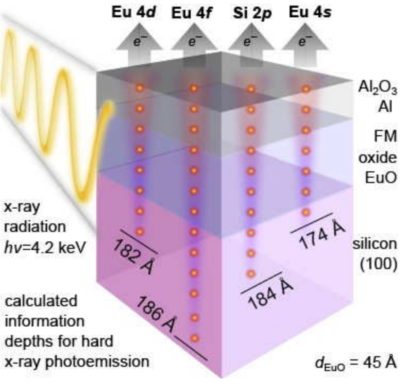

FIG. 1: Schematics of a hard x-ray photoemission spectroscopy (HAXPES) experiment of an Al/EuO/Si heterostructure probing the buried EuO thin film and the EuO/Si interface.

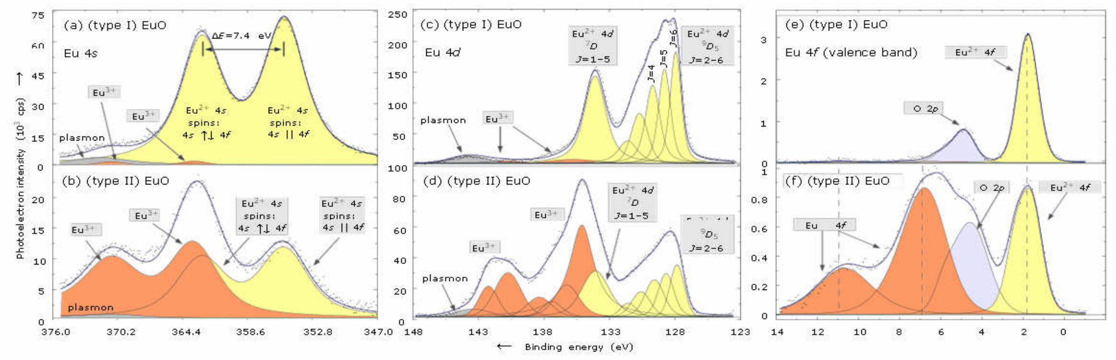

FIG. 2: Hard x-ray photoemission spectra from (a), (b) Eu 4s core levels and (c), (d) Eu 4d core levels, as well as (e), (f) Eu 4f valence bands, recorded at an photon excitation energy of 4.2 keV in normal emission geometry. A quantitative peak analysis yields a relative fraction of Eu^{3+} cations of only (3.1 ± 1.5)% for stoichiometric EuO and of (60.2 ± 4.8)% for O-rich Eu$_2$O$_3$.

For (type I) EuO, the $4s$ double-peak is assigned to divalent Eu^{2+} spectral contributions, whereas an additional, overlapping trivalent Eu^{3+} double-peak feature ap- pears in Fig. 2(b), that is chemically shifted by 8.1 eV towards higher binding energy.

The Eu $4d$ core level spectra are depicted in Fig. 2(c) and (d). They show a complex multiplet structure distributed in a wide energy range due to the strong $4d$–$4f$ exchange interaction and much weaker $4d$ spin-orbit splitting. Therefore, the $4d$ spectra cannot be separated into their $4d_{3/2}$ and $4d_{5/2}$ components. We can attribute the two main spectral contributions of the $4d$ spectra to a $J = L - S$ multiplet splitting caused by $4d$–$4f$ interaction, and assign the peaks to the ^7D and ^9D multiplets, respectively. The fine structure of the ^7D final state is not resolved, whereas the $J = 2$–6 components in the ^9D state is easily identified. Once more, we clearly observe a mainly divalent Eu^{2+} valency in EuO, but significant spectral contributions from Eu^{3+} cations in O-rich EuO.

We move on to the analysis of the Eu $4f$ valence bands in Fig. 2 (e) and (f). The pronounced peak located at 1.8 eV below E_F displays the Eu^{2+} $4f$ final state multiplet. Spectral contributions up to 4.5 eV binding energy are attributed to valence bands of overlapping Eu^{2+} $4f$ and O $2p$ states. The chemically shifted Eu^{3+} $4f$ multiplet structure in O-rich EuO is located between 5 and 13 eV.

We finally performed a quantitative peak analysis by fitting the spectral contributions with convoluted Gaussian-Lorentzian curves. The result of the fitting procedure is shown by the solid lines in Fig. 2(a)–(f), which match the experimental data points very well. From the integrated spectral intensities of the divalent Eu^{2+} and trivalent Eu^{3+} components, we derive a rel- ative fraction of Eu^{3+} cations of only (3.1 ± 1.5)% for stoichiometric EuO and of (60.2 ± 4.8)% for O-rich Eu$_2$O$_3$.

The local chemistry and bonding at the EuO/silicon transport interface was probed via photoemission from the Si 2p core level recorded in normal and 45° off-normal emission geometry at 4.2 keV. In this way, the information depth of the escaping photoelectrons is substantially varied, which allows one to distinguish spectral contributions from bulk and interface-like electronic states of the buried Si substrate. For stoichiometric EuO/Si(100), we confirm the chemical stability of the EuO/Si(001) interface as predicted by thermodynamic calculations, whereas in O-rich EuO/Si(100) features on the high binding energy side of Si^{n+} 2p states indicate the presence of interfacial SiO$_x$.

We presented an electronic structure study of a magnetic oxide/semiconductor model system, EuO on Silicon. We succeeded in stabilizing ultrathin EuO films on Si(001), and confirmed their nearly ideal stoichiometry using core-level and valence band hard x-ray photoemission spectroscopy. Moreover, we identified a chemically stable EuO/Si interface, with no signs of silicon oxide formation. With the aim to establish this novel class of spin injector/collector con- tacts on silicon, high-quality EuO magnetic oxide tun- nel barriers will be integrated into silicon-based trans- port devices in the near future.

---

[1] C. Caspers, M. Müller, A. X. Gray, A. M. Kaiser, A. Gloskovskii, W. Drube, C. S. Fadley, and C. M. Schneider, Electronic structure of EuO spin filter tunnel contacts directly on silicon, Phys. Status Solidi RRL 5, Vol. 12, 441 (2011)

[2] C. Caspers, M. Müller, A. X. Gray, A. M. Kaiser, A. Gloskovskii, W. Drube, C. S. Fadley, and C. M. Schneider, Chemical stability the magnetic oxide EuO directly on silicon observed by high-energy photoemission spectroscopy, Physical Review B 84, 205217 (2011)

Catalytic Growth of N-doped MgO on Mo(001)

M. Grob[1], M. Pratzer[1], M. Ležaić[2], M. Morgenstern[1]

[1] II. Physikalisches Institut B, RWTH Aachen University
[2] Peter Grünberg Institut-1, Forschungszentrum Jülich

A simple pathway to grow thin films of N-doped MgO (MgO:N), which has been found experimentally to be a ferromagnetic d^0 insulator, is presented. It relies on the catalytic properties of a Mo(001) substrate using growth of Mg in a mixed atmosphere of O_2 and N_2. Scanning tunneling spectroscopy reveals that the films are insulating and exhibit an N-induced state slightly below the conduction band minimum.

Recently, it has been found that MgO:N-films grown by molecular beam epitaxy (MBE) exhibit ferromagnetism after being annealed at 1020 K [1]. The optimized N-concentration x was 2.2% exhibiting coercive fields as large as 60 mT at T=10 K and magnetic moments per N-atom of 0.3 μ_B barely reducing up to room temperature. A Curie temperature $T_C \approx 550K$ has been extrapolated and indications that N is incorporated substitutionally on the O-site have been deduced from core level spectroscopy. Moreover, independent studies of N implantation (80 keV) into MgO led to a hysteresis with a coercive field of 30 mT at 300 K [2].

The high T_C proposed originally has been challenged by going beyond the mean-field approximation [3] or by considering correlation effects [4,5]. Partly, even the absence of ferromagnetism was found [4]. This renders the high T_C observed experimentally into obvious disagreement to current theory asking for more detailed studies.

MgO:N films, in addition, exhibit bipolar resistive switching behaviour [6] prior to annealing. Resistance contrasts as large as 4 orders of magnitude, switching currents as low as 100 nA and switching times into both states below 10 ns have been obtained [1]. This makes MgO:N also interesting for nonvolatile memories. However, the incorporation of N into MgO is difficult due to the strongly endothermal incorporation of N atoms with respect to N_2 (energy cost per N atom: 10 eV) [7]. It requires, e.g., atomic beams of N and O [1] or N^+ implantation [2]. Here, we demonstrate a simplified pathway using the catalytic abilities of a Mo(001) substrate. Thus, we establish a model system of MgO:N for surface science. Mo(001) is chosen since thin MgO films of high quality can be grown epitaxially due to the relatively small lattice mismatch of 6% [8]. Moreover, catalytic properties of Mo with respect to N_2 are known, as, e.g., for the nitrogenase within bacteria using molybdenum enzymes as catalyst [9]. Catalytic N_2 dissociation on surfaces has been induced successfully for the electronically similar W(001). We have grown thin films of MgO:N with thicknesses up to ten monolayer (ML) at optimal doping. Scanning tunneling spectroscopy (STS) revealed that the Fermi level is well within the band gap indicating insulating behaviour. An unoccupied state close to the conduction band is found, which is not present in pure MgO films.

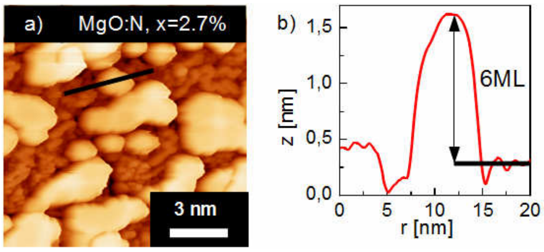

FIG. 1: a) STM image of 7 ML $MgO_{0.973}N_{0.027}$ film on Mo(001) with thicker islands (bright areas) on top of a wetting layer of 1-2 ML;(50x50)nm², U = 3V, I = 0.5nA. b) Line profile along the black line marked in (a) with height of the island above the wetting layer marked.

The experiments are performed in ultra-high vacuum at a base pressure of $p=5\cdot10^{-11}$ mbar. The MgO:N films are prepared by MBE of magnesium at O_2 pressure $p_{O2}=1\cdot10^{-7}$mbar and $p_{N2}=5\cdot10^{-6}$ mbar. The deposition temperature T_D is 300 K, if not given explicitly. After MgO:N deposition, the samples are annealed at 1100 K for 10 min. Figure 1(a) shows a scanning tunneling microscopy (STM) image of 7 ML $MgO_{0.973}N_{0.027}$. It exhibits islands on top of an MgO:N wetting layer. x within the MgO films was determined by Auger electron spectroscopy (AES) at primary electron energy of 1 keV being sensitive to the upper 2 nm (9 to 10 ML) only [11]. Up to x=6% is achieved at T_D=850 K. Next, we prepared MgO:N films with a thickness of up to 100ML at T_D=900 K. The nitrogen amount decreased dramatically with film thickness as shown in figure 2. Assuming homogeneous distribution of N, this implies that the amount of N in both films is roughly the same evidencing that N_2 is dissociated on the Mo(100) surface only. We assume that during MgO growth or annealing, the atomic N from the surface is incorporated into the MgO film. To support this scenario, we fit the data assuming a constant areal concentration n of N atoms by x=n/d, d denotes the number of MgO ML and n represents the concentration of N atoms with respect to the sum of N and O atoms. If we assume that all N atoms are substitutionally incorporated into the first monolayer of MgO:N, the fit curve plotted in figure 2(a) shows excellent agreement with the measured data points using n=21.6%. Assuming interstitial impurities, i.e. dumbbells of NO [7], the equation has to be slightly modified and results in n=18.2%. Nearly the same n is be achieved by another preparation method: We exposed the Mo crystal to N_2 ($p=5\cdot10^{-6}$ mbar) at 300 K for 10 min. Afterwards, we grew MgO without N_2 at T_D=900 K leading to very similar N concentrations as shown in figure 2(a).

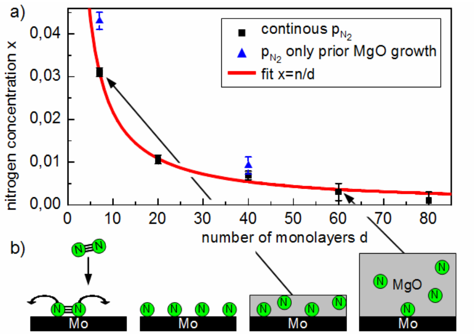

FIG. 2: a) Nitrogen concentration x as a function of monolayers d; different symbols mark different preparation methods; fit curve assumes a constant amount of nitrogen atoms (see text). b) Sketch of N_2 *incorporation: left:* N_2 *dissociation on Mo(001); right: incorporation of N into MgO leaving the amount of N independent of MgO thickness.*

Thus, obviously, the dissociation of N_2 takes place at the Mo(001) only. Finally, a third preparation has been performed: 10ML of pristine MgO were grown first. Subsequently, 10 ML MgO:N are deposited. No nitrogen was found in the sample, i.e. x < 0.2%. Thus, if Mo is covered by MgO, the catalytic effect of the substrate is inhibited.

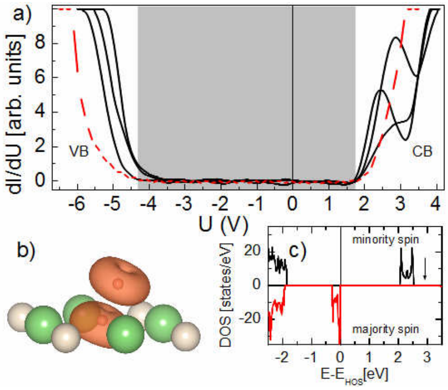

FIG. 3: a) dI/dU(U) spectra measured by STS on a 11 ML high $MgO_{0.96}N_{0.04}$ *island* (U_{stab} = 3V, I_{stab} = 0.5nA, U_{mod} = 40mV) *at several positions (straight lines) and on a 11 ML thick pristine MgO island (dashed line). b) Calculated charge density of the unoccupied N-induced states of a N-N dimer at the surface. Large green and small white spheres show Mg and O. c) Calculated density of states (DOS) for N-N dimer at MgO surface, HOS: highest occupied state; all states between -1.2eV and 3eV are N-induced; CBM is marked by arrow.*

Figure 3 compares STS curves of 11 ML films of $MgO_{0.96}N_{0.04}$ and undoped MgO [10]. Doping by N leads to a shift of the Fermi level E_F towards the valence band by about 1 eV and an additional peak with maximum at 0.3 eV below the conduction band minimum (CBM). The peak energy varies laterally by ±0.3 eV for different positions. Density functional (DFT) calculations of bulk MgO with substitutional N predict occupied p-levels close to the valence band maximum (VBM) and an unoccupied, spin polarized level within the middle of the band gap, if self interaction correction is included [4,5].

This disagrees with our experiment. We performed first-principles DFT calculations including the surface within the spin-polarized generalized gradient approximation [12]. Three different configurations with N atoms in the surface layer have been calculated: (i) one N-atom substituting an oxygen, (ii) one N-atom at the interstitial site and (iii) an N-N dimer with one N atom being substitutional and the other at the nearest interstitial site. In case (ii), the calculation was initiated with an N interstitial, but the system relaxed to a configuration where N and O exchanged their places, i.e. N ended up substitutionally and O interstitially. However, the N derived p-states for case (i) and (ii) are found within 2.2 eV above VBM very similar as for MgO bulk [4,5]. We conclude that a more complex N structure as, e.g., the N-N dimer at the surface shown in Fig. 3(b) and exhibiting unoccupied N-type p-states close to CBM (Fig. 3(c)), is responsible for the observed peak.

In conclusion, we prepared thin films of N-doped MgO with an N-concentration up to 6% by using the catalytic effect of Mo(001) for N_2 dissociation. Compared with pristine MgO, an additional state close to the conduction band minimum has been observed by STS which could not be attributed to simple N impurity configurations.

Discussions with P. Mavropoulos and S. Parkin as well as financial support by SFB 917-A3 and HGF_YIG VH-NG-409 are gratefully acknowledged.

[1] C. H. Yang, Ph. D. thesis, Stanford university, Stanford 2010.

[2] L. Chun-Ming *et al.*, Chin. Phys. B 20, 047505 (2011).

[3] P. Mavropoulos, M. Ležaić, and S. Blügel, Phys. Rev. B 80, 184403 (2009).

[4] A. Droghetti, C.D. Pemmaraju, and S. Sanvito, Phys. Rev. B 78, 140404 (2008); V. Pardo and W. E. Pickett, Phys. Rev. B 78, 134427 (2008).

[5] I. Slipukhina, P. Mavropoulos, S. Blügel, and M. Ležaić, Phys. Rev. Lett. 107, 137203 (2011).

[6] R. Waser, R. Dittmann, G. Staikov, and K. Szot, Adv. Mat. 21, 2632 (2009).

[7] M. Pesci, F. Gallino, C. Di Valentin. and G. Pacchioni, J. Phys. Chem. C 114, 1350 (2010).

[8] S. Benedetti, H. M. Benia, N. Nilius, S. Valeri, and H. J. Freund, Chem. Phys. Lett. 430, 330 (2006).

[9] J. Chatt, J. R. Dilworth, R. L. Richards, and J. R. Sanders, Nature 224, 1201 (1969).

[10] C. Pauly, M. Grob, M. Pezzotta, M. Pratzer, and M. Morgenstern, Phys. Rev. B 81,125446 (2010).

[11] A. Akkerman *et al.*, phys. stat. sol. (b) 198, 769 (1996).

[12] J. P. Perdew, K. Burke, and M. Ernzerhof, Phys. Rev. Lett. 77, 3865 (1996).

Synthesis and Theory of the Metastable Bixbyite-Type V_2O_3

C. Wessel[1], D. Weber[2], M. Lerch[2], R. Dronskowski[1]

[1]Institute of Inorganic Chemistry, RWTH Aachen University
[2]Institut für Chemie, TU Berlin

A metastable bixbyite-type polymorph of vanadium sesquioxide, V_2O_3, is known since 2011. Beyond 550°C the novel material transforms to corundum-type V_2O_3. Density-functional theory calculations including explicit electronic correlation corroborate the metastability of bixbyite-type V_2O_3 and further predict that it is approximately 0.1 eV less stable than the well-known corundum-type phase. Both experiment and theory confirm the metastable character of the novel material.

Living matter (e.g., the human body) mostly consists of compounds which are composed of hydrogen, oxygen and carbon. Remarkably and fortunately enough, living matter does not spontaneously decompose into the simple low-energy compounds water and carbon dioxide because of the existence of an energy barrier which needs to be surpassed for this decomposition. Thus, the living world resides in a metastable state such that this very metastability enables human beings' existence—until their death, the final thermodynamic ground state. Apart from living matter, metastable states also exist in the field of inorganic chemistry. The most popular example is carbon with its two allotropes: the thermodynamically stable graphite and the high-pressure allotrope diamond. The latter only persists as long as the system is in a nonequilibrium state. In general, high-temperature syntheses result in thermodynamically stable products, while metastable compounds are only attained by elaborate syntheses under exceptional conditions. Using such experimental conditions, a huge amount of metastable compounds with fascinating characteristics may be made by the creative chemist. For example, Weber *et al.* very recently synthesized a metastable polymorph of vanadium sesquioxide in the cubic bixbyite structure with the lattice parameter a = 9.3947(2) Å, namely by the reaction of vanadium trifluoride with a water-saturated gaseous mixture of 10 vol % hydrogen in argon [1].

In recent years vanadium oxides have attracted a great deal of attention because of their extraordinary physical and chemical behavior. These materials are used in various technical applications, e.g., as catalysts, cathode materials for high-density lithium batteries and as chemical sensors, to name but a few.

Likewise, a considerable amount of research has been focused on vanadium sesquioxide, V_2O_3, as this material is a prototype for a Mott insulator. At about 170 K the onset of a magnetic ordering takes place which goes along with a structural phase transition and a change of conducting behavior. At low temperature vanadium sesquioxide is an insulator and crystallizes in a monoclinic structure (M1 phase) with an antiferromagnetic spin ordering. Above 170 K, however, a phase transition occurs to the well-known corundum-type structure which exhibits an exceptionally large c/a ratio of 2.823 [2].

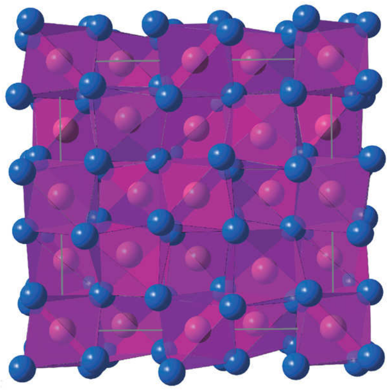

FIG. 1: Crystal structure of bixbyite-type V_2O_3 with V atoms in purple and O atoms in blue. The coordination polyhedra are indicated.

The bixbyite type is a fluorite-derived defective structure. One arrives at this structure by doubling the lattice parameter of the fluorite type in all directions and by removal of one quarter of the anions in an ordered manner. In Figure 1 the bixbyite-type unit cell and the coordination polyhedra of the vanadium atoms are depicted. In this structure the cations occupy the two symmetry-inequivalent Wyckoff positions 8a (0,0,0) and 24d (x,0,1/4), and the anions are located on the general position 48e (x,y,z). Vanadium is coordinated by six oxygen atoms which form an octahedron whereas oxygen is tetrahedrally coordinated by vanadium atoms.

The metastable character of bixbyite-type V_2O_3 was confirmed by *in situ* high-temperature X-ray powder diffraction experiments in an argon atmosphere. At about 823 K the bixbyite type undergoes a phase transition to the corundum polymorph, see Figure 2. Additionally, V_2O_3 with the bixbyite structure is easily oxidized to V_2O_5 at approximately 523 K. Even at ambient temperatures, spontaneous oxidation of the bixbyite-type V_2O_3 to vanadium dioxide occurs after three weeks.

Quantum-chemical calculations employing density-functional theory were carried out with the plane-wave code VASP. In order to approximate the self-interaction correction and the electron–electron Coulomb interaction, the GGA+U method was applied in the rotationally invariant approach according to Liechtenstein with U = 2.8 eV and J = 0.93 eV because these parameters have been successfully used in the literature [3].

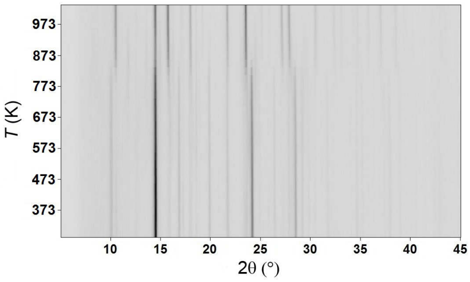

FIG. 2: Temperature-resolved X-ray powder diffraction patterns of the new V_2O_3 *polymorph in argon atmosphere. The bixbyite-type transforms into the corundum-type* V_2O_3 *at about 823 K.*

In the process of the quantum-chemical calculations the lattice parameters and atomic positions were fully optimized. For theoretically accessing finite-temperatures and analyzing the dynamic stability, phonon calculations were performed by employing the FROPHO program. For this purpose a supercell was created and, subsequently, all symmetry-inequivalent atoms were slightly shifted off their equilibrium position. Based on the resulting Hellmann–Feynman forces the force constants were calculated to eventually arrive at the dynamical matrix. Thermodynamic properties at finite temperature are easily accessible by combining the eigenvalues (phonon frequencies) of the matrix with Bose–Einstein statistics [4].

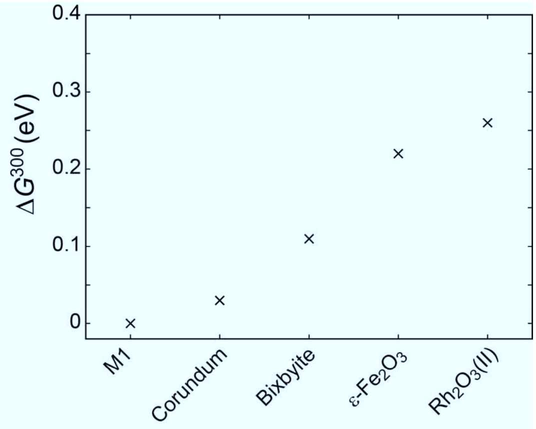

FIG. 3: Density-functional-theory calculated relative Gibbs free energy of the six energetically lowest V_2O_3 *polymorphs.*

The relative Gibbs free energy at 300 K of the six energetically lowest polymorphs is shown in Fig. 3. Corroborating the experiment, the low-temperature monoclinic structure (M1) and the high-temperature corundum type are preferred in terms of energy. The new bixbyite-type polymorph is only about 0.1 eV less stable than the monoclinic structure. This result emphasizes the classification of bixbyite-V_2O_3 as an unstable compound in terms of the thermochemical state function G.

The phonon band structure along special points of the Brillouin zone and the phonon density of states (pDOS) was calculated for vanadium sesquioxide in the bixbyite structure, and it is depicted in Figure 4.

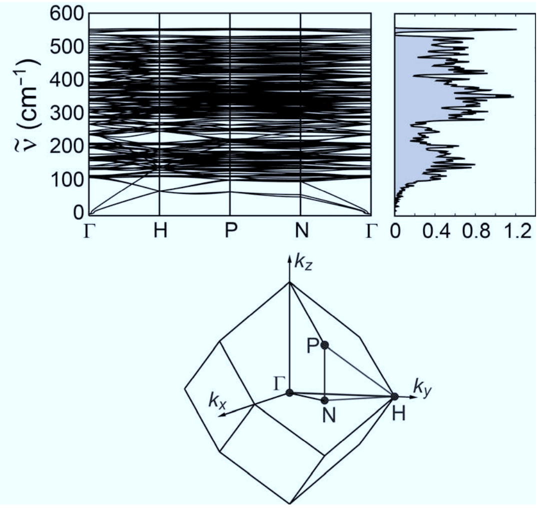

FIG. 4: Phonon band structure (top left), phonon density of states (top right) and Brillouin zone (bottom) [5] for the V_2O_3*-bixbyite structure.*

Because only positive values are present in the diagrams, bixbyite-type V_2O_3 can be classified as a dynamically stable phase. In general imaginary modes in the phonon band structure and pDOS reveal an inherent structural instability. We conclude that the bixbyite-type polymorph does not spontaneously transform into the monoclinic or corundum polymorph, and with that information bixbyite-V_2O_3 can be characterized as being theoretically metastable.

Financial support by the Deutsche Forschungsgemeinschaft through the Priority Programme 1415 (Crystalline Non-Equilibrium Phases) is gratefully acknowledged.

---

[1] D. Weber, A. Stork, S. Nakhal, C. Wessel, C. Reimann, W. Hermes, A. Müller, T. Ressler, R. Pöttgen, T. Bredow, R. Dronskowski, M. Lerch, *Inorg. Chem.* 50, 6762 (2011).

[2] N. F. Mott, *Metal-Insulator Transition*, Taylor and Francis Ltd, London, 1974.

[3] S. Y. Ezhov, V. I. Anisimov, D. I. Khomskii, G. A. Sawatzky, *Phys. Rev. Lett.* 83, 4136 (1999).

[4] R. P. Stoffel, C. Wessel, M.-W. Lumey, R. Dronskowski, *Angew. Chem. Int. Ed.* 49, 5242 (2010).

[5] M. I. Aroyo, J. M. Perez-Mato, C. Capillas, E. Kroumova, S. Ivantchev, G. Madariaga, A. Kirov, H. Wondratschek, *Z. Kristallogr.* 221, 15 (2006); M. I. Aroyo, A. Kirov, C. Capillas, J. M. Perez-Mato, H. Wondratschek, *Acta Crystallogr. A* 62, 115 (2006).

Orbital-order melting in rare-earth manganites: the role of super-exchange

E. Pavarini[1], **A. Flesch**[1], **G. Zhang**[1], **E. Koch**[2]

[1]Institute for Advanced Simulation-3, Forschungszentrum Jülich, 52425 Jülich
[2]German School for Simulation Sciences

We study the mechanism of orbital-order melting observed at temperature T_{OO} in the series of rare-earth manganites. We find that the purely electronic many-body super-exchange mechanism yields a transition temperature T_{KK} that decreases with decreasing rare-earth radius, and increases with pressure, opposite to the experimental T_{OO}. We show that the tetragonal crystal-field splitting reduces T_{KK} further increasing the discrepancies with experiments. This proves that super-exchange effects, although very efficient, in the light of the experimentally observed trends, play a minor role for the melting of orbital ordering in rare-earth manganites.

The role of orbital degrees of freedom in the physics of $LaMnO_3$, and in particular the co-operative Jahn-Teller transition, is debated since long [1,2]. Ab-initio LDA+*U* calculations show that Coulomb repulsion effects are key to understanding the orbitally-ordered antiferro-magnetic ground state. The purely electronic super-exchange mechanism alone [1], however, is not sufficient to explain the presence of co-operative Jahn-Teller distortions in nanoclusters up to T ~ 1150 K (orbitally disordered phase). Still, super-exchange effects are rather large: T_{KK}, the temperature at which super-exchange alone, i.e., in the absence of static Jahn-Teller distortions due to electron-phonon coupling, would drive the transition, is remarkably close to T_{OO}, the temperature at which the co-operative Jahn-Teller distortion disappears in resonant X-ray and neutron scattering. This fact could indicate that super-exchange, although insufficient to explain the persistence of Jahn-Teller distortions in the orbitally disordered phase, plays a major role in the orbital order-to-disorder transition (orbital order melting) observed at T_{OO}. Here we resolve this issue.

Remarkably, orbital-order melting has been observed in the full series of orthorhombic rare-earth (RE) manganites $REMnO_3$. These systems are perovskites (Fig. 1) with electronic configuration Mn $3d^4$ ($t^3_{2g}e^1_g$). In the co-operative Jahn-Teller phase ($T < T_{OO}$), the MnO_6 octahedra are tilted and rotated, and exhibit a sizable Jahn-Teller distortion with long and short MnO bonds antiferro-ordered in the xy plane and ferro-ordered along z. Neutron and X-ray diffraction data show that T_{OO} increases from 750 K to ~ 1500 K with decreasing ionic radius IR (La → Dy); under increasing pressure eventually orbital order melts, while Jahn-Teller distortions still persist in nanoclusters.

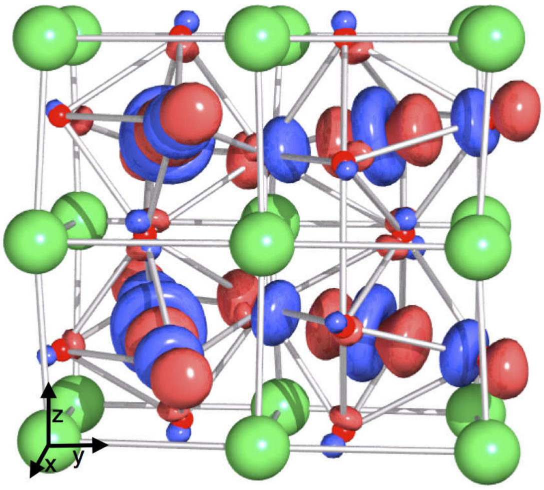

FIG. 1: Orbital-order in $TbMnO_3$, as obtained by LDA+DMFT calculations. The pseudo-cubic axes pointing along Mn-Mn bonds are shown in the left corner.

In this work we [3] clarify the role of the purely electronic super-exchange mechanism in orbital-order melting. To do this, we perform ab-initio calculations based on the local density approximation (LDA) + dynamical mean-field theory (DMFT) method in the paramagnetic phase for fixed atomic position, explicitly setting to zero the static Jahn-Teller crystal-field splitting ε_{JT} , and excluding the effect of phonons. Apart from ε_{JT} , a tetragonal crystal-field splitting, ε_T , is present. We show that, in the absence of such crystal-field splitting, while in $LaMnO_3$ $T_{KK} \sim T_{OO}$, in all other systems T_{KK} is 2-3 times smaller than T_{OO}. Thus, while T_{OO} strongly increases with decreasing ionic radius, T_{KK} slightly decreases. Taking the tetragonal splitting into account, these trends are enhanced even further. This proves that, although very large, in view of the reported experimental trends, super-exchange plays a minor role in the orbital- melting transition.

We solve the DMFT quantum impurity problem using a quantum Monte Carlo (QMC) solver, working with the full self-energy matrix in orbital space and a 4 Mn supercell with the Pbnm space group; this ensures that we properly account for the point symmetries and the essential k-dependence. We construct the LDA Wannier functions via the downfolding procedure based on the Nth-Order Muffin-Tin (NMTO) method. Additionally, we perform calculations based on the Linearized Augmented Plane Wave approach (LAPW) and construct maximally localized Wannier functions following the Marzari-Vanderbilt procedure. The band-structures and parameter trends obtained with the two methods are very similar.

Our results are shown in Fig. 2. While $T_{KK} \sim T_{OO}$ in $LaMnO_3$, in all other systems T_{KK} is a factor 2-3 smaller than the experimental estimate for T_{OO}. Moreover, T_{KK} is maximum in $LaMnO_3$, and roughly decreases with ionic radius from RE=La to Tb, then increases again. T_{KK} also increases under pressure. These trends are opposite to those reported experimentally for the orbital melting temperature. They can be ascribed to the increasing distortions along the $REMnO_3$ series, and the decrease in volume and tilting/rotation with increasing pressure. Finally, for all systems super-exchange favors the occupation of the orbital $\theta\rangle=-\sin\theta\,|x^2-y^2\rangle+\cos\theta|3z^2-r^2\rangle$, with θ = 90°, while experimentally $\theta \sim 108°$ in $LaMnO_3$ increasing with decreasing ionic radius to 114° in $TbMnO_3$. Due to the competition between the tetragonal crystal-field splitting ε_T and super-exchange (which favor the occupation of different orbitals), T_{KK} is reduced even further. In Fig. 3 we show the results for ε_T fixed at ~ 130 meV, sizable but smaller than for any of the considered systems. We find that at the reduced critical temperature, super-exchange rotates the orbital towards 90°. The change in T_{KK} is small for $LaMnO_3$, but T_{KK} is reduced to 400 K for $NdMnO_3$, and even more for $DyMnO_3$ and $TbMnO_3$. Furthermore, in the zero temperature limit, the smaller T_{KK}, the closer is θ to 180°. Thus a fixed $\varepsilon_T \sim$ 130 meV enhances the trend found for $\varepsilon_T = 0$: T_{KK} is larger in $LaMnO_3$, and decreases going to $DyMnO_3$. Still, even for $LaMnO_3$, θ is significantly larger than the experimental 108°. This means that a Jahn-Teller crystal-field splitting ε_{JT} is necessary to explain the experimental θ; Fig. 3 shows that such splitting has to increase for the series RE=La, Nd, Dy, Tb.

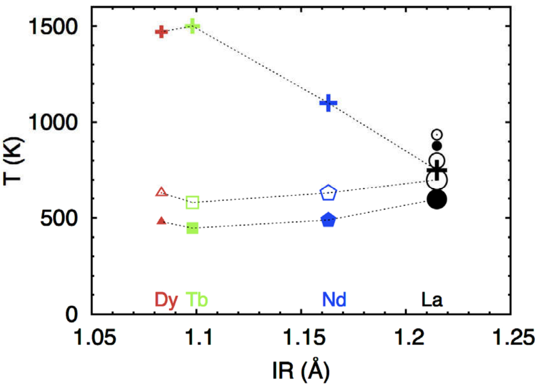

FIG. 2: Orbital-order transition temperature TKK versus RE3+ radius in the REMnO₃ series, with RE=Dy (triangles), Tb (squares), Nd (pentagons), La (circles). Full (empty) symbols: T_{KK} from LDA+DMFT total-energy (order parameter) calculations. Symbols of decreasing size: P=0 GPa, 5.4 GPa and 9.87 GPa. Crosses: Experimental values (ambient pressure).

Taking into account that tetragonal splitting actually increases with decreasing pressure, and substituting La with Nd, Tb, or Dy, this trend is enhanced even more. For ε_T corresponding to the real structures, down to 150 K we find no super-exchange transition for all systems but $LaMnO_3$.

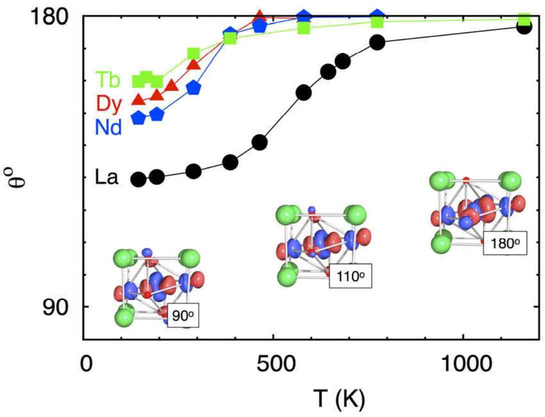

FIG. 3: Rotation of the most occupied state |θ› as a function of temperature in the presence of a 130 meV tetragonal crystal field. The orbitals are shown for TbMnO₃. The most occupied orbital remains well defined in the full temperature range; the orbital polarization is merely reduced by 30% at ~800 K.

In conclusion, for the orbital-melting transition in rare-earth manganites $REMnO_3$, we find that many-body super-exchange yields a transition temperature T_{KK} very close to T_{OO} only in $LaMnO_3$, while in all other systems T_{KK} is less than half T_{OO}. Moreover, we find that a tetragonal splitting ε_T reduces T_{KK} even further; ε_T increases when La is substituted with Nd, Tb or Dy and decreases under pressure, further enhancing the discrepancy with experiments. Finally, super-exchange effects become larger with increasing pressure, while experimentally orbital order eventually melts. Our work thus proves that, in the light of the experimentally observed trends, super-exchange plays a minor role in the orbital-melting transitions of rare-earth manganites.

We acknowledge financial support through the Deutsche Forschungsgemeinschaft through research unit FOR1346.

---

[1] K.I. Kugel and D.I. Khomskii, Zh. Eksp. Teor. Fiz. 64, 1429 (1973) [Sov. Phys. JEPT 37, 725 (1973)].

[2] J.B. Goodenough, Phys. Rev. 100, 564 (1955); J. Kanamori, J. Appl. Phys. Supp. 31, 148 (1960).

[3] A. Flesch, G. Zhang, E. Koch, E. Pavarini, Phys. Rev. B 85, 035124 (2012).

Probing the oxygen vacancy distribution in resistive switching Fe-$SrTiO_3$ MIM-structures by micro-XANES

C. Lenser[1], A. Kuzmin[2], J. Purans[2], A. Kalinko[2], R. Waser [1,3] and R. Dittmann[1]

[1]Peter Grünberg Institut-7, Forschungszentrum Jülich, 52425 Jülich
[2] Institute of Solid State Physics, University of Riga, Latvia
[3] Institut für Werkstoffe der Elektrotechnik, RWTH Aachen University

Resistive switching metal-insulator-metal (MIM)-structures were fabricated from epitaxial Fe-doped $SrTiO_3$ thin films to study the distribution of oxygen vacancies in a switched memristor cell using a micro-focused x-ray beam. In addition to the main filament, we found that the concentration of oxygen vacancies increases homogeneously over the whole electrode area during the electroforming procedure. The XANES observed at the location of the filament exhibits distinct differences to the surrounding area, which are interpreted with full-multiple-scattering XANES calculations to derive from oxygen vacancy clustering in the first coordination shell around Fe.

Binary and ternary metal oxides as emergent materials for non-volatile memory applications are receiving an increasing amount of scientific attention due to the promising scalability, retention and switching characteristics of this material class [1]. The key role of oxygen non-stoichiometry and oxygen-deficient oxide-phases as the underlying mechanism of the resistance change has been recognized for many different oxide systems (e.g. TiO_2, Ta_2O_5, $SrTiO_3$). It is becoming widely accepted that the resistance switching process in $SrTiO_3$ is related to the movement and creation of oxygen vacancies and the associated electron doping. However, direct experimental reports of the redox-reaction induced by an electric field are rare [2].

In this contribution, the distribution of oxygen vacancies in a switched memristor cell fabricated from epitaxial Fe-doped $SrTiO_3$ will be investigated by spatially resolved x-ray absorption near-edge structure (XANES). $SrTi_{0.95}Fe_{0.05}O_3$ was grown epitaxially by pulsed laser deposition (PLD) on a conducting Nb:$SrTiO_3$ substrate. Pt top electrodes were sputter-deposited and structured via optical lithography. XANES measurements at the Fe K-edge with a 7 µm beam spot on the sample were performed at the beamline ID03 (ESRF, France). Figure 1 compares the Fe K-edge XANES of the virgin thin film to that recorded in the anodic and cathodic regions of an electrocolored single crystal [3]. The cathode was found to contain only Fe3+ ions and Fe3+-VO complexes in the ratio ~ 70/30, and notably no Fe4+ [3]. The almost perfect coincidence of the thin film XANES with that of the reduced cathode implies that the virgin thin film is already oxygen deficient after growth, and that the Fe3+/Fe4+ redox pair does not serve as an indicator for local resistance changes. The shoulder at 7122 eV excitation energy that marks Fe3+-VO complexes is indicated by "S" in figure 1.

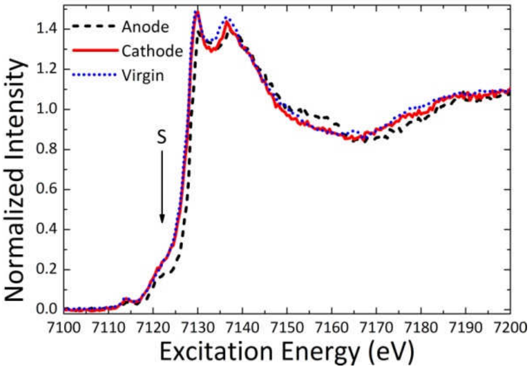

FIG. 1: Fe K-edge XANES recorded on the virgin thin film (dots), the cathode region (solid) and the anode region (dash) of an electrocolored Fe-doped SrTiO3 single crystal. The intensity of the shoulder at 7122 eV excitation energy (marked S by the arrow) is a fingerprint of the presence of an oxygen vacancy in the first coordination shell of Fe3. The chemical state of the virgin film – according to the XANES – is similar to that of the cathode, and the Fe centers in the film are primarily cubic Fe3+ centers, with a significant percentage of axial Fe3+-VO centers.

After an electroforming step with a +7V DC voltage applied to the top electrode, the formed memristor can be switched between different resistance states with a bipolar voltage sweep. The current-voltage hysteresis is shown in figure 2(a), the "Set"-state is reached with a negative voltage sweep polarity. A low voltage readout (figure 2(b)) reveals the "Set"-state to show ohmic behavior, while the "Reset"-state shows distinctly non-linear behavior.

A Fe-K edge fluorescence map recorded at 7122 eV excitation energy to maximize the sensitivity to Fe3+-VO reveals one location on the electrode pad with increased intensity, corresponding to the main filament. Moreover, the Fe3+-VO concentration as measured by the intensity of the shoulder S is increased under the whole electrode area as compared to the virgin film.

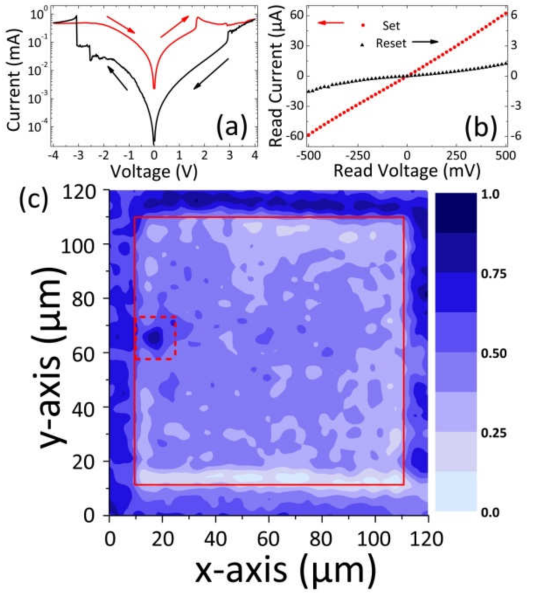

FIG. 2: Figure 2 (a): I(V)-characteristics of the investigated memristor after electroforming. (b): Low voltage, non-destructive read-out sweeps in the low resistance "Set"-state (dots) and the high resistance "Reset"-state (triangles). (c): Fe Kα fluorescence map of the switched memristor, recorded at 7122 eV excitation energy (shoulder S). The intensity variations under the electrode correspond to the oxygen vacancy content, the maximum in the dashed box indicates the presence of the conducting filament. The absolute intensity outside the electrode area (solid lines) is higher since the fluorescence radiation is not attenuated, but cannot be directly compared to the intensity under the electrode.

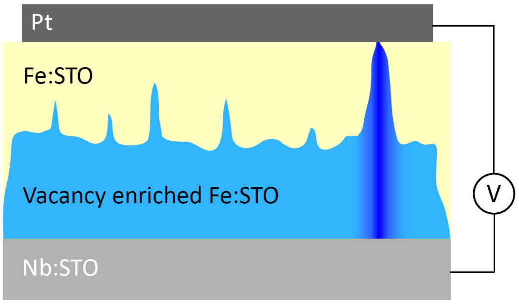

FIG. 3: Schematic model of the oxygen vacancy distribution in the switched memristor.

The important consequence is that before breakdown is achieved during the electroforming, a homogeneous front of vacancy enrichment propagates into the material. Furthermore, the Fe K-edge XANES at the filament location is interpreted via full multiple-scattering calculations and indicates oxygen vacancy clustering in the first shell of Fe [4]. The oxygen vacancy distribution in the formed device is sketched in figure 3.

In summary, we have shown PLD-grown $SrTi_{0.95}Fe_{0.05}O_3$ thin films to contain Fe3+ and a high degree of Fe3+-VO complexes in the as-deposited state. We demonstrate through micro-focused XANES on a resistively switched MIM-structure that electroforming increases the Fe3+-VO complex concentration homogeneously over the whole electrode area until local breakdown is achieved. Full multiple-scattering XANES calculations suggest that the observed XANES in the region of the conducting filament can be interpreted by the association of two oxygen vacancies to the probed Fe in the filament region.

This work was financially supported by the EC FP7 MATERA project FMRSM and the NRW-EU Ziel 2-Programm.

---

[1] R. Waser, R. Dittmann, G. Staikov, and K. Szot, Adv. Mater. 21, 2632 (2009).

[2] M. Janousch, G. I. Meijer, U. Staub, B. Delley, S. F. Karg, and B. P. Andreasson, Adv. Materials 19, 2232 (2007).

[3] C. Lenser, A. Kalinko, A. Kuzmin, D. Berzins, J. Purans, K. Szot, R. Waser, and R. Dittmann, Phys. Chem. Chem. Phys. 13, 20779 (2011).

[4] C. Lenser, Ch. Lenser, A. Kuzmin, J. Purans, A. Kalinko, R. Waser and R. Dittmann, J. Appl. Phys. in press

Strained $SrTiO_3$ films on sapphire

R. Wördenweber[1], T. Grellmann[1], K. Greben[1], J. Schubert[2], R. Kutzner[1], E. Hollmann[1]

[1]Peter Grünberg Institut-8, Forschungszentrum Jülich, 52425 Jülich
[2]Peter Grünberg Institut-9, Forschungszentrum Jülich, 52425 Jülich

Owing to the strong connection between strain and ferroelectricity, large shifts of the Curie temperature and polarization are observed in strained ferroelectric material. In this work, the effects of lattice-mismatch induced stress upon the crystallographic structure, strain, and generation of different types of defects in epitaxial $SrTiO_3$ films on CeO_2 buffered sapphire are examined and discussed in context with the resulting impact of strain on the polarization of the ferroelectric layers. Depending on the thickness of the $SrTiO_3$ layer, characteristic changes in their structural perfection and crystallographic orientation with respect to the substrate system are observed. For thin films, misfit dislocations partially compensate the stress in the $SrTiO_3$ layer, whereas cracks develop in thicker $SrTiO_3$ films. The structural modifications and the formation of defects can be explained in a model based on lattice misfit induced stress and energy considerations. It is demonstrated that intrinsic mismatch and thermal mismatch must be considered to explain strain dependent effects such as induced ferroelectricity and modifications of the permittivity of these complex heteroepitaxial layer systems

Pseudomorph strained-layer epitaxial growth has quickly turned from a mere curiosity into a major technology for advanced semiconductor devices and structures for solid state research. It has been demonstrated that mechanical strain can have dramatic effects on the electromagnetic properties of thin films. The most significant effect has been observed in the incipient ferroelectric oxide $SrTiO_3$ (STO) where a ferroelectric transition can be induced and an enhancement of the transition temperature T_c up to room temperature has been reported [1,2]. For epitaxially grown thin films, the strain is naturally induced by the underlying substrate (clamping effect). The strain is caused by the lattice mismatch and the differences in thermal expansion coefficients between the substrate and the STO film. Therefore the development of strained epitaxial STO films on suitable substrates and the analysis of their ferroelectric and structural properties are of large interest for various applications in the semiconductor technology, ranging from high-frequency devices to specific sensor applications.

Here we report on induced ferroelectricity of STO films grown on different substrates. We will focus on epitaxially grown films on the microwave suitable substrate sapphire. For this system, ferroelectricity is observed up to $T_c \approx 200K$ which cannot be explained by standard structural analysis obtained from room temperature XRD measurements.

A series of STO films is grown on $NdGaO_3$ (110) (NGO), $DyScO_3$ (110) (DSO), and CeO_2 buffered r-cut sapphire (Al_2O_3) via pulsed laser deposition and magnetron sputter technology. Due to the lattice mismatch, STO films on DSO substrates are expected to be exposed to tensile strain, whereas NGO would lead to compressive strain parallel to the film surface (in-plane). As demonstrated in fig. 1b, the STO films on NGO and DSO behave as expected. The in-plane lattice parameter $a_{||}$ is elongated or distorted for STO on DSO or on NGO, respectively, and compensated by the out-off plane parameter $a_\perp$. As a consequence and in agreement with the theory [3], in-plane ferroelectricity is induced in STO on DSO, whereas no ferroelectricity is measured in STO on NGO (see fig. 1a).

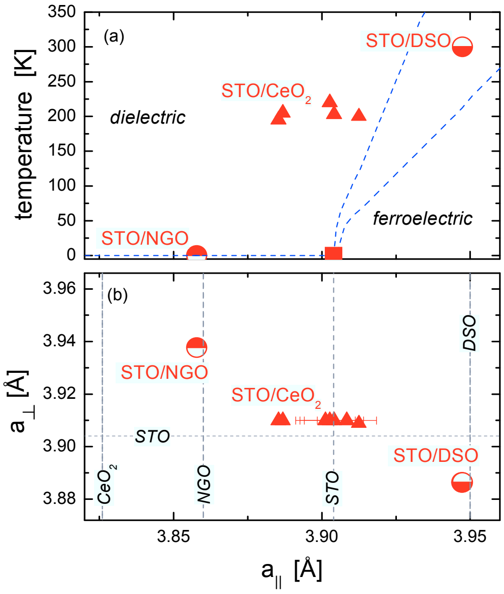

Fig. 1: Ferroelectric transition temperature T_c (a) and out-off-plane lattice parameter (b) for STO on different substrates as function of in-plane lattice parameter. The dashed lines represent the theoretical predictions for the regime of the phase transition from ferroelectric to dielectric behavior according to [3] in (a) and the nominal lattice parameter for the different substrate systems in (b).

The STO films on CeO_2 buffered sapphire behave quite differently. The lattice mismatch between the CeO2 and STO does not seem to affect the in-plane lattice parameter of the STO in the same way observed for the other systems (STO on NGO and DSO). STO films on CeO_2/sapphire seem to be nearly unstrained at room temperature (fig.1b). However, the ferroelectric properties of the films are well affected. In contrast to the theoretical predictions

[3], in-plane ferroelectricity is induced in STO on sapphire, and Tc values up to 200K are observed. In order to understand this unexpected behavior, we analyzed the structural and mechanical properties of STO films on sapphire in more detail.

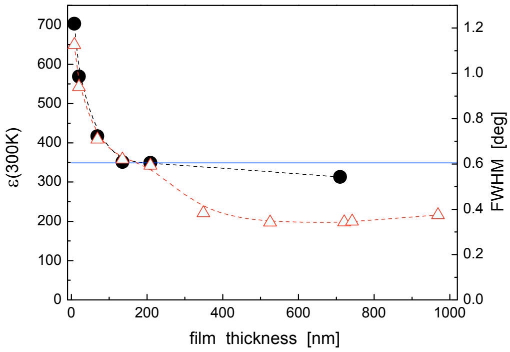

Fig. 2: Thickness dependence of the permittivity (circles) and FWHM of the STO (200) XRD rocking curve (triangles) of the STO layers on CeO_2 buffered sapphire. The solid line indicates values for the room temperature permittivity of a STO single crystal.

A first indication that stress is also imposed on the films on sapphire and results in a modification of structural and dielectric properties is provided by a comparison of XRD and permittivity data for films of different thicknesses (Fig. 2). A clear indication is given by the observation of crack formation in thick STO films on sapphire (fig. 3).

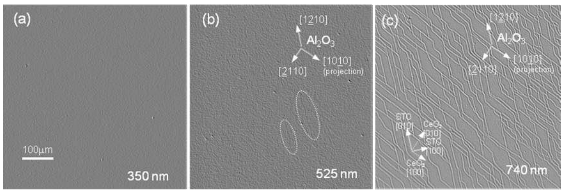

Fig. 3: Microscope images (area: 590µmx587µm) of the surface of STO films of thickness d_{STO}=350nm (a), 525nm (b), and 740nm(c). The crystallographic orientations of the substrate, CeO_2 buffer and STO layer are determined via XRD diffraction experiments; they are identical for all images and indicated. The dashed ellipses in (b) mark hardly visible cracks in the STO film of medium thickness.

All samples with a thin STO layer ($d_{STO} \leq$ 350nm) show a smooth surface and no cracks. In contrast, all thick STO films ($d_{STO} \geq$ 525nm) reveal cracks. As shown in fig. 3b (d_{STO} =525nm), first a few cracks with finite lateral extension (typically < 200µm) are present. All cracks point in the same crystallographic direction, i.e. the [010] direction of STO which is identical to the [1$\underline{2}$10] direction of r-cut sapphire. With increasing thickness, a 'network of cracks' develops (see fig. 3c). The cracks are oriented along two crystallographic directions, i.e. along the [1$\underline{2}$10] and the [10$\underline{1}$0] direction of the r-cut sapphire. Since there is no distinguished crystallographic orientation of the STO and CeO_2 layers equivalent to the [10$\underline{1}$0] direction of the r-cut sapphire, this indicates that the cracks are generated by the difference in the expansion coefficients of sapphire and STO, and that the (in-plane) expansion coefficient of sapphire is slightly anisotropic.

Heteroepitaxial strained-layer growth signifies a major technology for use in advanced semiconductor and correlated devices, as well as for other structures in solid state research. The most fundamental questions in strained-layer growth are, (i) up to what thicknesses are heteroepitaxial layers stable, (ii) which type of misfit defects will develop and (iii) what happens upon modifications to the misfit (for instance due to cooling of the film)? It is generally believed that below a critical thickness the strained state is the thermodynamic equilibrium state, and above a critical thickness a strained layer may be metastable or it may relax [4]. Different critical thicknesses might be associated to different types of misfit defects, e.g., dislocations, misalignments, or even cracks [5]. Stress in heteroepitaxially grown films results from both an *intrinsic* and a *temperature-dependent* component. The main reason for the development of intrinsic stress in heteroepitaxially grown films is given by the nominal lattice mismatch $\varepsilon_o = (a_{film} - a_{substrate})/a_{film}$ at growth conditions [4,5], where a represents the lattice parameter of the film and substrate, respectively. The thermal contribution to the stress arises from the difference in thermal expansion coefficients of the film and the underlying substrate. These two (intrinsic and extrinsic (here temperature-dependent)) contributions generate defects (ranging from misfit dislocations to cracks) in our heteroepitaxial STO films. A detailed description of the model is given in ref. [6].

The importance of *intrinsic* and *thermal induced* stresses for the understanding of structural modifications, the formation of defects, and the resulting ferroelectric properties of heteroepitaxially grown STO films is demonstrated. A model (details in ref [6]) is developed to describe (i) the generation of misfit dislocations during growth and (ii) the crack formation during cooling of the sample. In general, the misfit in lattice constant and thermal expansion can be a very powerful tool to engineer the properties of heteroepitaxial films and, in particular, the ferroelectric properties of STO, suitable for various applications in semiconductor technology ranging from tunable high-frequency devices to microwave sensor concepts.

---

[3] J. H. Haeni et al., Nature 430, 758 (2004).

[2] R. Wördenweber et al., J. Appl. Phys. 102, 044119 (2007).

[3] N. A. Pertsev et al., Phys. Rev. B 61, R825 (2000); 65, 219901(E) (2002).

[4] J. R. Downes et al., Semicond. Sci. Technol. 9, 1265 (1994).

[5] A.G. Zaitsev et al., Appl. Supercond. 1997, Inst. of Phys. Conf. Ser. 158, 25 (1997).

[6] E. Hollmann et al., J. Appl. Phys. 105, 114104 (2009).

Effect of Charge Compensation Mechanisms on the Conductivity at $LaAlO_3$ /$SrTiO_3$ Interfaces

F. Gunkel[1], P. Brinks[2], S. Hoffmann-Eifert[1], R. Dittmann[1], M. Huijben[2], J. E. Kleibeuker[2], G. Koster[2], G. Rijnders[2], and Rainer Waser[1]

[1]Peter Grünberg Institut-7, Forschungszentrum Jülich, 52425 Jülich
[2]MESA+ Institute for Nanotechnology, University of Twente, The Netherlands

The equilibrium high temperature conductance (HTEC) of $LaAlO_3/SrTiO_3$ (LAO/STO)-heterointerfaces was investigated as a function of ambient oxygen partial pressure (pO_2). Metallic conducting interfaces were obtained for LAO grown on STO single crystals as well as on STO-buffered LSAT substrates. For both structures, the high temperature sheet carrier density n_S of the LAO/STO-interface saturates at a value of about $1x10^{14}cm^{-2}$ for reducing conditions, which indicates the presence of interfacial donor states. A significant decrease of n_S is observed at high oxygen partial pressures. According to the defect chemistry model of donor-doped STO, this behavior for oxidizing conditions can be attributed to the formation of cation vacancies as charge compensating defects.

The role of defects is a focus of the ongoing discussion about the electronic properties of the conducting interface between the two insulators $LaAlO_3$ (LAO) and $SrTiO_3$ (STO). Besides the model of charge transfer due to the polar nature of LAO, it is generally accepted that defects in the vicinity of the LAO/STO interface can have a large impact on the electronic properties. At the extreme, the interdiffusion of La-ions on Sr-sites ($\mathrm{La}_{\mathrm{Sr}}^{\bullet}$), and the creation of oxygen vacancies ($\mathrm{V}_{\mathrm{O}}^{\bullet\bullet}$) within the STO lattice, have even been considered as sole origin of the interface conduction.

In this study, the LAO/STO-interface is discussed from a defect chemical point of view [1]. Besides the above described defects, also cation vacancies in the STO lattice, i.e. Sr-vacancies ($\mathrm{V}_{\mathrm{Sr}}''$) and Ti-vacancies ($\mathrm{V}_{\mathrm{Ti}}''''$), were considered in order to draw a complete picture of the LAO/STO-interface (see Fig. 1). The conducting LAO/STO-interfaces are fabricated by pulsed laser deposition (PLD) of LAO on TiO_2-terminated STO single crystal substrates, and by the heteroepitaxial growth of LAO and STO on LSAT ($(La,Sr)(Al,Ta)O_3$) single crystal substrates. Both types of heterostructures show metallic conductance behaviour at low temperatures as revealed by Hall measurements. In contrast to the standard LAO/STO-heterostructure, the electron mobility at the LAO/STO-interface on LSAT exhibits only a weak temperature dependence [2]. This indicates a more defective interface region originating from the STO growth process [3].

The particular defect structure of the LAO/STO-interface was investigated by means of high temperature conductance measurements in equilibrium with the surrounding atmosphere (HTEC). In the studied temperature range (950K-1100K), the decisive defect reactions at the LAO/STO-interface are activated, and hence, strive for a well-defined thermodynamic equilibrium state, which is related to the ambient oxygen pressure (pO_2). The resulting conductance characteristics contain information about the chemical reactions, which take place at the LAO/STO-interface, and the corresponding defect concentrations. Using this method, we could exclude that mobile oxygen vacancies are the sole origin of the electronic charge carriers at the interface [4]. In fact, the temperature- and oxygen partial pressure independent plateau region, which is found for reducing atmospheres, indicates the presence of immobile donor states ($\mathrm{D}^{\bullet}$) close to the interface. In the pO_2-independent plateau region, the sheet electron density n_S approaches a value of $1x10^{14}$ cm^{-2} for both samples (LAO/STO and LAO/STO/LSAT). This value is consistent with the carrier densities obtained from low temperature Hall measurements [2] as well as from spectroscopic investigations [5].

The HTEC measurements on LAO/STO systems

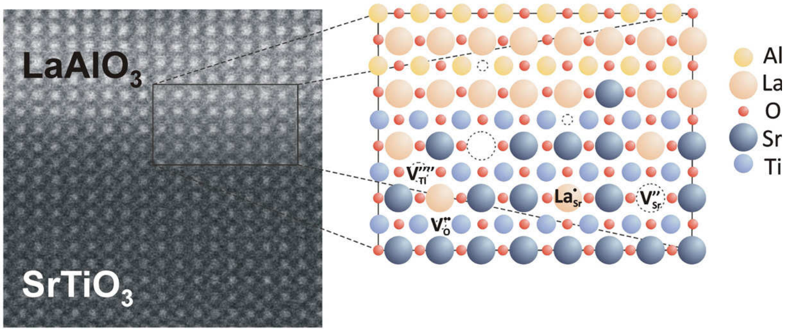

FIG 1: HAADF-image of the LAO/STO-interface (from Ref. [4]) and a schematic illustration of possible defects in the STO lattice close to the interface: Oxygen vacancies ($V_O^{\bullet\bullet}$); interdiffused La-dopants ($La_{Sr}^{\bullet}$); Sr-vacancies (V_{Sr}''); Ti-vacancies (V_{Ti}'''').

grown on LSAT substrates additionally revealed a very interesting feature at oxidizing conditions. The observation of this effect was possible due to the low intrinsic conductance of the LSAT single crystal, while, for the standard LAO/STO-system, the interface behaviour under oxidizing conditions is mainly hidden by the large intrinsic conductance contribution of the $SrTiO_3$ single crystal [4].

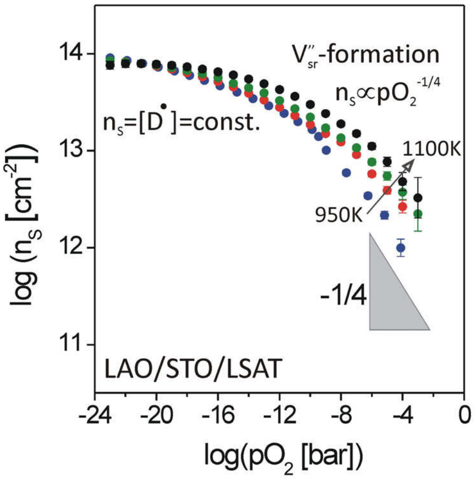

FIG 2: pO_2-dependence of the sheet carrier density, n_S, of the LAO/STO interface on LSAT obtained from HTEC measurements (from Ref. [1]); A pO_2- and temperature independent region is found for reducing conditions indicating the presence of interfacial donor states ($D^\bullet$). For oxidizing atmosphere, n_S decreases proportional to $pO_2^{-1/4}$ which can be attributed to the formation of acceptor-like Sr-vacancies.

Starting from the plateau region at low oxygen partial pressure (see Fig. 2), the interfacial electron density starts to decrease for increasing pO_2. This decrease becomes proportional to $pO_2^{-1/4}$ for higher oxidizing conditions. In this region, n_S is no longer temperature independent. In contrast, n_S is thermally activated exhibiting an activation energy E_A of approximately 1eV. As will be discussed below, this change of behaviour can be seen as an indication for the formation of additional defects in the vicinity of the LAO/STO-interface.

The measured HTEC characteristics of the LAO/STO interfaces resemble in good agreement the HTEC behavior of donor-doped STO [6]. Therefore, the corresponding defect chemistry model was transferred to the LAO/STO heterostructures. In the pO_2-independent region, each donor is compensated by a free electron which contributes to the interface conduction (full electronic compensation). This can be expressed by the charge neutrality condition $n=[D^\bullet]$, whereas the concentration of extrinsic donors $[D^\bullet]$ is considered as a pO_2-independent parameter.

In order to maintain charge neutrality, the observed decrease of n below the donor level $[D^\bullet]$ requires the formation of additional compensating defects which carry a negative net charge. This yields to the conclusion that cation vacancies, either Sr-vacancies (V''_{Sr}) or Ti-vacancies (V''''_{Ti}), have to be considered as acceptor-type electron traps in the vicinity of the LAO/STO-interface [1]. Considering this scenario, the defect chemistry model of STO predicts a decrease of the electron density proportional to $pO_2^{-1/4}$ (in the limiting case of a full ionic compensation of the extrinsic donors). Hence, the observation of this characteristic behaviour can be regarded as an indication of the formation of cation vacancies in the vicinity of the LAO/STO-interface in oxidizing atmosphere.

The in-situ study of the HTEC of LAO/STO-heterostructures emphasizes the importance of crystal disorder for the electronic properties of the LAO/STO-interface. The observed pO_2- and temperature-independence of the sheet electron density for reducing conditions supports the idea of a donor-type conduction mechanism at the LAO/STO-interface such as provided by cation-intermixing. Furthermore, the decrease of n_S in oxidizing conditions indicates a complex charge compensation mechanism in the vicinity of the interface, which involves the formation of cation vacancies at high oxygen partial pressures. This implies that oxygen annealing after the growth of LAO/STO-heterostructures - which is commonly thought to merely remove oxygen vacancies from the STO substrate - can also result in an increased cation vacancy concentration at the interface. These additional defects can reduce the electron density and, moreover, can act as scatter centers at low temperatures.

As pivotal result of this study, it has been shown that in the vicinity of the LAO/STO-interface exchange reactions in the cation sublattice, i.e., formation and annihilation of strontium vacancies take place at typical growth temperatures and have to be considered in the discussion of the LAO/STO interface.

This work was performed during a bilateral collaboration of the PGI-7 and the MESA+Institute of the University of Twente, Enschede.

---

[1] F. Gunkel P. Brinks, S. Hoffmann-Eifert, R. Dittmann, M. Huijben, J. E. Kleibeuker, G. Koster, G. Rijnders, and R. Waser., Appl. Phys. Lett. 100, 052103 (2012).

[2] P. Brinks, W. Siemons, J. E. Kleibeuker, G. Koster, G. Rijnders, M.Huijben, Appl. Phys. Lett. 98, 242904 (2011).

[3] D. J. Keeble, S. Wicklein, R. Dittmann, L. Ravelli, R. A. Mackie, and W. Egger, Phys. Rev. Lett. 105, 226102 (2010).

[4] F. Gunkel, S. Hoffmann-Eifert, R. Dittmann, S. B. Mi, C. L. Jia, P. Meuffels, R. Waser, Appl. Phys. Lett. 97, 012103 (2010).

[5] G. Berner, S. Glawion, J. Walde, F. Pfaff, H. Hollmark, L. C. Duda, S. Paetel, C. Richter, J. Mannhart, M. Sing, and R. Claessen, Phys. Rev. B 82, 241405 (2010).

[6] R. Moos and K. H. Haerdtl, J. Am. Ceram. Soc. 80, 2549 (1997).

Crystal- and Defect-Chemistry of Reduction Resistant Fine Grained Thermistor Ceramics on $BaTiO_3$-Basis

C. Pithan[1], **H. Katsu**[2], **R. Waser**[1,3], **H. Takagi**[2]

[1]Peter Grünberg Institut-7, Forschungszentrum Jülich, 52425 Jülich
[2]Materials Development Department, Murata Manufacturing Corporation Ltd., Yasu, Shiga, Japan
[3]Institut für Werkstoffe der Elektrotechnik, RWTH Aachen

The PTCR-effect in donor-doped $BaTiO_3$-based ceramics with excessive BaO that are sintered under reducing conditions and subsequently re-oxidized relies on the formation of acceptor type Ti-vacancies in the regions around the grain-boundaries. During sintering also vacancies of oxygen are locally created at these internal solid-solid interfaces, but in the course of the post-sintering annealing these vacancies are filled again with oxygen ions captured from the atmosphere. The proposed defect chemical mechanism has been established from thorough electrical characterization including temperature tuning impedance spectroscopy and measurements of DC-conductivity carried out at different temperatures and partial pressures of oxygen. ^{18}O-tracer diffusion experiments in conjunction with SNMS supported the suggested defect chemical scenario and confirmed, that enhanced diffusivity of oxygen along grain boundaries only occurs in BaO-rich ceramics. Stoichiometric compositions of $BaTiO_3$ only revealed bulk diffusion and no grain boundary diffusion.

Bulk polycrystalline thermistor ceramics on $BaTiO_3$-basis with positive temperature coefficient (PTC) posses an increasing current limiting electric insulation resistance when they are heated above the Curie temperature T_C of the ferroelectric compound $BaTiO_3$. This behavior relies on the developement of resistive back-to-back Schottky barriers formed at the grain boundaries, when the ceramics are sintered and cooled usually under oxidizing conditions. The mechanism responsible for the resistivity jump of typically several orders of magnitude is well understood, particularly in terms of point defect chemistry [1, 2]. Here the formation of the insulating grain boundaries depends on the absorption of oxygen combined with the segregation of acceptor-type metal vacancies, enriched at these interfaces.

Only in the rather recent past multilayer PTC thermistors [3-5] consisting of laminated metallic (Ni- or Ti-based alloys) and ceramic layers on the basis of donor-doped $BaTiO_3$ formulations with BaO-excess that are configured in a consecutive but alternating serial order have been developed. These devices have to be sintered under reducing atmosphere at a partial pressure of oxygen $p(O_2)$ below 10^{-7} MPa in order to prevent oxidation of the internal electrodes. They only achieve their distinct PTC-characteristics after a gentle post-sintering re-oxidation process. The exact physico-chemical mechanism for this behavior has practically not been clarified so far and therefore the present study reports on the crystal- and defect-chemistry of La-doped BaO-rich $BaTiO_3$ ceramics.

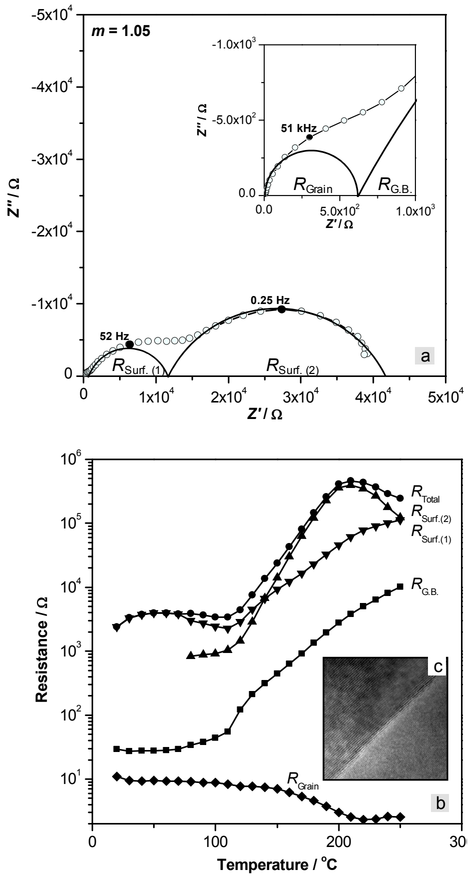

FIG 1: (a) Cole-Cole diagram at 160°C showing the frequency response locus of $(Ba_{1.048}La_{0.002})TiO_{3+\delta}$ with a Ba-excess of 5 at.-%, sintered at 1300 °C at $p(O_2)=10^{-9}$ MPa and re-oxidized in air for 2 hours. The small inset represents the high frequency end of the impedance spectrum. (b) Temperature dependence of the total resistance R_{Total} and different resistive components arising from the response of the grains (R_{Grain}), of the grain boundaries ($R_{G.B.}$) and the ceramics surfaces ($R_{Surf.}$) for this material. (c) High resolution TEM-image of a grain boundary.

The communicated results [6] are based on impedance spectroscopic experiments, high temperature DC-conductivity measurements carried out at partial pressures of oxygen $p(O_2)$ in the range from 10^{-20} MPa up to 0.1 MPa, the determination of ^{18}O-tracer diffusion profiles and the analytical, crystallographic and microstructural characterization using X-ray diffraction and electron microscopy.

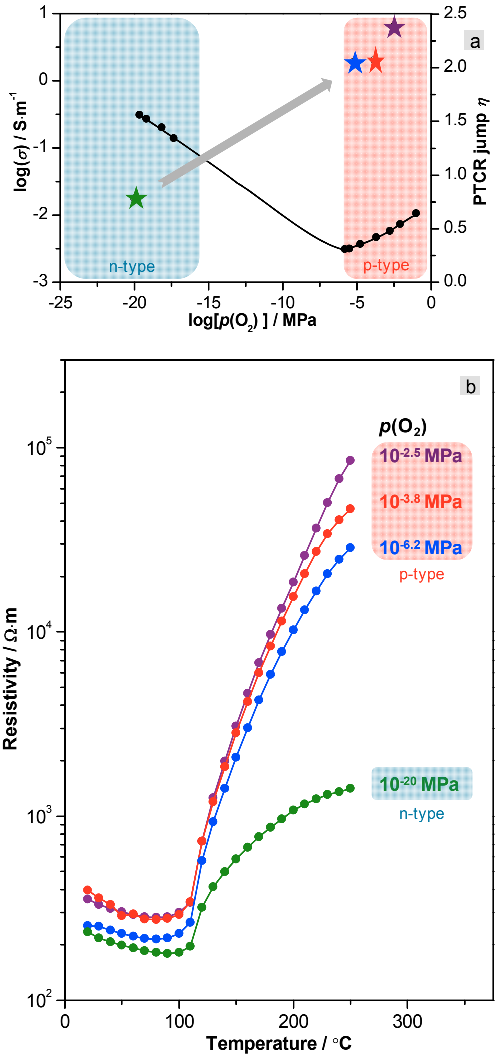

FIG. 2: DC conductivity and the PTC-parameter η (white symbols) quantifying the height of the jump in resistivity upon heating in measured in situ in dependence of p(O₂) at 700°C for the same material described in figure 1. The PTC effect is efficiently enhanced when post sintering annealing is performed in the region of overall p-type semiconduction (dark gray area) above p(O₂)=10⁻⁶ MPa at this temperature. The grain boundaries become insulating, while the grain interior still shows n-type semiconduction. Part (a) reveals a representatively chosen Kröger-Vink diagram and the p(O₂) dependence of h, while part (b) represents the corresponding PTC-characteristics of resistivity upon annealing at different partial pressures of oxygen after sintering under reducing conditions.

Figure 1 shows for an example of a $BaTiO_3$-ceramic with BaO-excess processed in the way described before that the total PTC-response (R_{Total} versus temperature in fig.1b) depends on several contributions. According to this the microstructure consists of semiconducting grains that are separated by more insulating grain boundaries, showing a distinct positive temperature coefficient of resistance. The absolute values of resistance at high temperatures seem however to be governed by external surface layers, that disappear after grinding and reappear after a second re-oxidation treatment. Interestingly the BaO-excess does not result in any wetting of the grain boundaries by a secondary phase or in the formation of extended defects in the lattice (fig.1c). Crystallographic data show that the lattice constants of the $BaTiO_3$ matrix are practically not affected by the BaO-content, suggesting that the bulk solubility is very low. It is assumed that BaO is preferentially enriched in the grain boundary regions. This behavior does not seem to depend on the kind of donor used. SIMS investigations after re-oxidation with the isotope ^{18}O prove that the resistive surface layers are due to enhanced oxygen diffusion along grain boundaries. This is only the case in hyper-stoichiometric compositions with BaO-excess. Ceramics with a Ba:Ti ratio of exactly 1 do not show this behaviour. Thermogravimetric studies revealed that in fact the total O-uptake during reoxidation increases with increasing amount of BaO-excess.

A more detailed study of the defect chemical relations in BaO-rich donor doped $BaTiO_3$ supports the idea that excessive BaO dissolves mainly in the grain boundary region resulting in the local formation of both Ti- and O-vacancies upon sintering in reducing atmosphere. During re-oxidation O-vacancies are filled again preferentially by grain boundary diffusion and the acceptor type Ti-vacancies finally remain to form the insulating barrier layers on the grain boundaries. This interpretation is supported by the results of figure 2. Exactly the same tendencies are observed if instead of La^{3+} that exclusively replaces Ba^{2+} is substituted by Nb^{5+}, acting as a donor on the Ti-site of the perovskite lattice.

In summary the defect chemistry of grain boundaries in BaO-rich and donor doped $BaTiO_3$ ceramics can be defined as follows:

$$m'\mathrm{BaO} + \mathrm{BaTiO_3} \; f \; \mathrm{Ba}_{1+m'}\mathrm{TiO}_{3+m'}$$

$$° \; (1+m')\mathrm{Ba}_{Ba}^{\prime} + \mathrm{Ti}_{Ti}^{\prime} + m'\mathrm{V}_{Ti}^{\prime\prime\prime\prime} + (3+m')\mathrm{O}_{O}^{\prime} + 2m'\mathrm{V}_{O}^{\cdot\cdot}$$

$$\text{and } \mathrm{V}_{O}^{\cdot\cdot} + \frac{1}{2}\mathrm{O}_2^{gas} \; f \; \mathrm{O}_{O}^{\prime} \text{ (after re-oxidation).}$$

---

[1] W. Heywang, Solid State Electron. 3, 51 (1961).

[2] J. Daniels et al., Philips Res. Rep. 31, 544 (1976).

[3] K. Mihara et al., US-Patent 7,075,408 B2 (2006).

[4] H. Niimi et al., Jap. J. Appl. Phys. 46, 675 (2007).

[5] H. Niimi et al., Jap. J. Appl. Phys. 46, 6715 (2007).

[6] H. Katsu, Ph.-D. Thesis, Aachen University (2011).

Unusual Ferroelectric and Piezoelectric Properties of Silicon Doped Hafnium Oxide Thin Films

U. Boettger[1], I. Mueller[1], J. Mueller[2], T. Boescke[3], U. Schroeder[3]

[1] Institut für Werkstoffe der Elektrotechnik, RWTH Aachen University
[2] Fraunhofer Center Nanoelectronic Technologies, Dresden
[3] NaMLab GmbH, Dresden

Stable crystalline phases with ferro-electric and piezoelectric properties can be created in thin hafnium oxide films with suitable dopants and processing. Films with a thickness of 10 nm and few mol% of SiO_2 crystallize in a mixture of mono-clinic and tetragonal phases. The formation of the monoclinic phase is inhibited if crystallization occurs under capping resulting in an non-centro-symmetric orthorhombic phase. This phase clearly shows ferroelectric as well as piezoelectric behavior with a remanent polarization of about 12 µC/cm^2 and a coercive field of 1 MV/cm. Ferroelectric hafnium oxide is ideally suited for ferroelectric field effect transistors and capacitors due to its excellent compatibility to silicon technology.

Ferroelectric materials are promising candidates for low power, high density future nonvolatile memory technologies. However, the integration of conventional ferroelectrics like lead zirconate titanate or strontium bismuth tantalate runs into limitations in standard CMOS technology. The arrangement of ferroelectric thin film capacitors over the bit lines which is usually realized in ferro-electric random access memories (FRAM) need additional buffer layers to avoid the oxidation of the plug during high temperature crystallization step and to protect the ferroelectric layer itself from hydrogen damage during BEOL (back end of line) process. Conformal deposition technologies and etch processes able to cope with the material properties and larger physical thickness of the commonly used metal-ferroelectric-metal stacks are still inadequate and hindering future 3D scaling. Therefore, there is a need for “new” ferroelectric materials meeting the requirements of CMOS technology. It is known that hafnium oxide undergoes the phase transitions “cubic to tetragonal” and “tetragonal to monoclinic” during cooling from high-temperatures above 2803 K down to room temperature [1]. In thin HfO_2 films a mixture of monoclinic and tetragonal phases is observed due to surface energy effects. Suitable amounts of SiO_2 additives between 5-10 mol% as well as the presence of a top electrode during crystallization (mechanical encapsulation, capping) will stabilize the tetragonal phase and reduce the monoclinic phase fraction [2,3]. Here, the influence of capping on Si:HfO_2 films with Si content below 5 mol%, where the stabilization of the tetragonal phase is incomplete, is investigated.

Thin films of Si:HfO_2 in a thickness range 7-10 nm were deposited on titanium nitride electrodes by metal organic atomic layer deposition process based on Tetrakis-(ethylmethylamino)-hafnium and Tetrakis-dimethylamino-silane metalorganic precursors and ozone [4]. Additives between 2 and 6 mol% SiO_2 were defined by varying the precur-sor cycle ratio. The process flows for uncapped (*crystallization before top electrode deposition*) and capped (*crystallization after top electrode deposition*) capacitors are illustrated in Fig. 1.

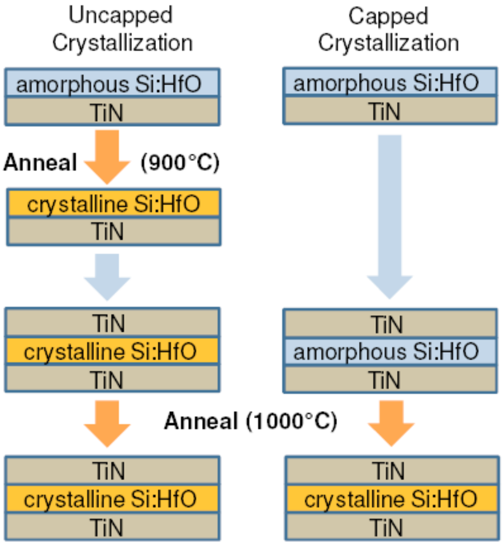

FIG 1: Process flows for the fabrication of Si:HfO_2 based metal-oxide-metal (MIM) capacitors with high-temperature crystallization before and after top electrode deposition. The oxide thickness is approximately 8 nm, while the electrode thickness is 10 nm [4].

A detailed investigation of the electrical properties of capped Si:HfO_2 MIM structures at different compositions were made by monitoring the capacitance-voltage and the polarization-voltage characteristics [4]. It could be clearly shown that for an additive of 3.6 mol% SiO_2 and capped species a hysteretic $P(V)$ behavior is observed (Fig. 2, top left) corresponding with maximal $C(V)$ values around the coercive voltages (not shown). For uncapped capacitors a linear behavior is present. Further evidence for the ferroelectric behavior was obtained by measurement of the piezoelectric displacement using a double beam laser interferometer [5], see Fig. 2 (left below). The mechanical response of the ferroelectric sample shows clear evidence of piezoelectric behavior, which is a prerequisite for ferroelectricity.

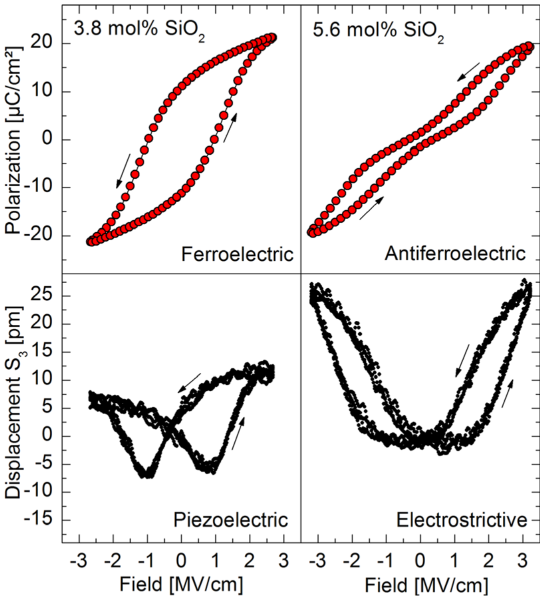

FIG 2: Polarization (top row) and piezoelectric displacement (bottom row) measurement of MIM capacitor samples with ferroelectric (left column) and antiferroelectric (right column) Si:HfO2 insulators [5].

Increasing the amount of SiO_2 additive of thin film capacitors leads to a disappearance of the ferroelectric phase. For 5.6 mol% SiO_2, a narrowed polarization curve and a electrostrictive displacement are observed (Fig. 2, right column) indicating an antiferroelectric or relaxor-like phase [4].

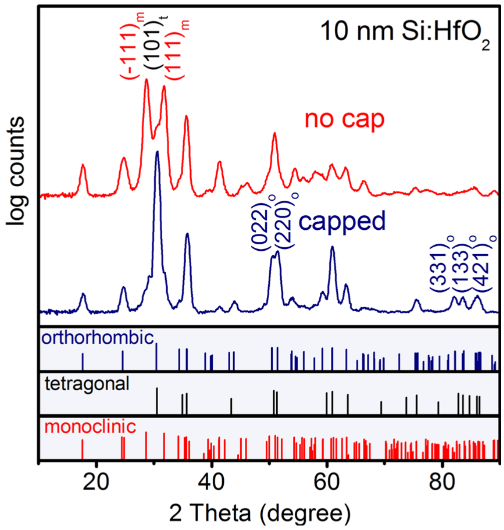

FIG 3: Grazing incidence x-ray diffraction of uncapped and capped HfO_2 samples with SiO_2 additives where ferroelectricity was observed in MIM capacitors [4].

The reported HfO_2 bulk phases which are referred to as the space groups p42/nmc, Fm3m, P21/c, Pbca and Pbcm are centrosymmetric and there-fore not ferroelectric. GI-XRD measurements of samples at a composition which showed ferroelectricity revealed distinct differences between crystallization with and without capping (Fig. 3) [4]. The analysis of the diffractogram suggests that the formed phase fits very well to an orthorhombic structure. The known orthorhombic forms of HfO_2 (Pbca, Pbcm) are centrosymmetric. However, a similar XRD pattern was found for a seldom orthorhombic phase ($Pbc2_1$) in Mg stabilized ZrO_2 [7]. Since the crystal chemistry of ZrO_2 is almost identical to that of HfO_2, the same crystalline phases are expected for both compounds. In contrast to the other two orthorhombic forms of ZrO_2, the $Pbc2_1$ space group is not centrosymmetric and therefore does not exclude ferroelectricity. Curiously, it seems that the dielectric properties of this phase in ZrO_2 have never been investigated.

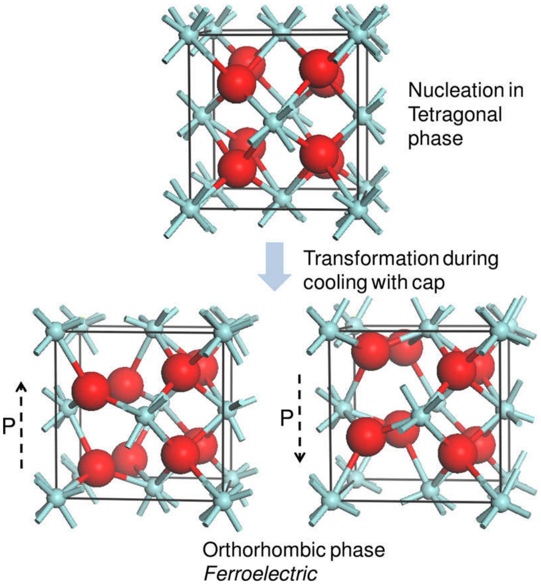

FIG. 4: The formation of the orthorhombic phase proceeds by transformation from the tetragonal phase during cooling with a cap. The bottom row indicates two different polarization states of the ferroelectric phase. Large atoms are oxygen and small atoms are hafnium [4].

In conclusion, this is a report about the evidence for the formation of ferroelectric (and antiferroelectric) crystalline phases in SiO_2 doped HfO_2 thin films which may be a “new” suitable material for ferroelectric-based future nonvolatile memory applications.

[1] J. Wang, H. P. Li, and R. Stevens, J. Mater. Sci. 27, 5397 (1992).

[2] D. Fischer, A. Kersch, Microelectron. Eng. 84, 2039 (2007).

[3] D. H. Triyoso et al., Appl. Phys. Lett. 89, 132903 (2006).

[4] T. Boescke, J. Mueller, D. Braeuhaus, U. Schroeder, and U. Boettger Appl. Phys. Lett. 99, 102903 (2011).

[5] P. Gerber, A. Roelofs, O. Lohse, C. Kugeler, S. Tiedke, U. Boettger, and R. Waser, Rev. Sci. Instrum. 74, 2613 (2003).

[6] T. Boescke; J. Mueller; D. Braeuhaus; U. Schroeder; U. Boettger, IEDM Techn. Dig. (2011) 547-550.

[7] E. H. Kisi and C. J. Howard, Key Eng. Mater. 153, 1 (1998).

Electric dipole rotation in flux-closure domains in ferroelectric $\mathrm{Pb(Zr,Ti)O_3}$

C.L. Jia[1], K. Urban[1], M. Alexe[2], D. Hesse[2], I. Vrejoiu[2]

[1] Peter Grünberg Institut-5: Microstructure Research, Forschungszentrum Jülich and Ernst Ruska Centre for Microscopy and Spectroscopy with Electrons

[2] Max Planck Institute of Microstructure Physics, Weinberg 2, D-06120 Halle

Low-dimensional ferroelectric structures are very promising for next generation ultrahigh density memory devices. Depolarizing fields, created by incompletely compensated charges at the surfaces and interfaces, depress the polarization of such structures. Theory suggests that with uncompensated surface charges local dipoles can organize in flux-closure structures in thin films and vortex structures in nano-size ferroelectrics, reducing depolarizing fields. By aberration-corrected transmission electron microscopy, we obtain experimental evidence for continuous rotation of the dipoles closing the flux of 180° domains in a ferroelectric perovskite thin film.

Ferroelectric thin films have demonstrated great potential for microelectronic applications [1]. In ferroelectric random access memories information is stored and read by switching and detecting the polarization orientation in the ferroelectric material. Microscopically polarization switching is realized through the motion of domain walls driven by an external electric field. Phenomenologically, domain arrangements are characterized by the angle between polarization directions in adjacent domains. In epitaxial thin-film systems, the domain pattern is determined by the growth conditions and by the mechanical interface strain and the electric boundary conditions related to the depolarization field at surfaces or interfaces. Ideally two such boundary conditions can be distinguished depending on whether the surface or interface charges are perfectly screened or unscreened.

Theoretical investigations have shown that in very small ferroelectric structures, of a size of a few nanometers, the local dipoles should organize in vortices rather than in domains with uniform polarization, due to the large depolarization fields [2]. The observations described below, in addition to giving evidence of the existence of flux-closure structures at a 180° domain wall, represent on atomic scale a direct experimental proof of continuous polarization rotation. Using atomic-resolution aberration-corrected transmission electron microscopy domain structures are studied of the epitaxial thin-film system $\mathrm{PbZr_{0.2}Ti_{0.8}O_3}$ (in the following abbreviated by PZT) on $\mathrm{SrTiO_3}$ (STO) [3]. We employ the negative spherical aberration imaging (NCSI) technique, which allows not only to locate all the atomic species but also to measure their positions, unit cell by unit cell, with a precision of a few picometers.

Figure 1 shows an atomic resolution image of an area including the interface between the PZT layer and the STO substrate. In Fig. 1 the structure (one projected unit cell) of PZT is indicated schematically in two regions (positions of Zr/Ti, PbO/SrO, and O atomic columns, seen end-on, are indicated by red, yellow and blue circles, respectively).

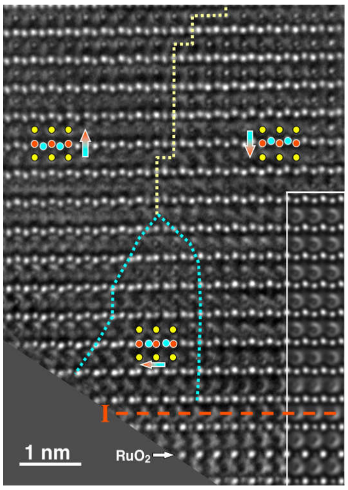

Fig. 1. Atomic-resolution image of a flux closure structure with continuous dipole rotation in PbZr0.2Ti0.8O3 (PZT) close to the interface to the SrTiO3 (STO) substrate. The interface is marked by a horizontal dashed line ("I"), which is determined based on a SrRuO3 marker layer with a nominal thickness of 1.5 unit cells at the STO/PZT interface. The RuO2 marker layer is also indicated. In the image recorded along the crystallographic [$\bar{1}\,\bar{1}\,0$] direction, the atomic structure and the electric dipole direction (arrows) are given. In the image two larger domains with 180 ° orientation can be identified. The domain wall is indicated by a yellow dotted line. In the center of the lower half of the image an approximately triangular area (the domain wall is indicated by a dotted blue line) can be seen, where in the center, the dipole direction makes an angle of 90° with the two large domains. The inset on the right-hand side shows a calculated image demonstrating the excellent match between the atomic model and the specimen structure.

Due to the particular imaging conditions, dynamic electron scattering yields a sharp bright contrast in the approximately 11 nm thick sample for the Zr/Ti and the O atom columns, while the SrO and PbO atomic columns are relatively weak. The film-substrate interface was marked by depositing a nominally 1.5 unit cells thick layer of $\mathrm{SrRuO_3}$ (SRO) on STO prior to the deposition of PZT. The interface, denoted by a horizontal dashed line, is then determined by observing the plane of RuO_2 serving as a marker.

The vertical shift in the Zr/Ti positions with respect to the adjacent O positions indicates that PZT is in a polarized state. On the left-hand side of Fig. 1, this shift is upward, while on the right-hand side, it is downward, resulting in the polarization-vector directions indicated by the arrows. This indicates the existence of two domains in a 180° orientation relation. By mapping the individual atom shifts, the position of the domain wall (dotted line) is localized. The horizontal width of this wall is about one $[\bar{1}\ \bar{1}\ 0]$ projected crystal unit cell, which is in agreement with the results of earlier measurements [4]. At the bottom interface, in between the two 180° domains, *in-plane* displacements of the Zr/Ti positions with respect to the adjacent oxygen positions are observed.

Figure 2 displays an atomic displacement map superimposed on an image obtained by converting the grey-scale contrast of Fig. 1 into a false-colour scale to enhance contrast. The arrows located at the Zr/Ti column positions indicate the modulus and the direction of the "off-centre" displacement with respect to the middle point of the horizontal line connecting the two neighbouring O atom positions (taking the cubic structure with an inscribed oxygen octahedron in the non-polar state as a reference). The scale at the bottom left indicates a displacement of 40 pm. We note that a uniform atomic shift of this magnitude corresponds to an integral polarization of 108 $\mu C/cm^2$ [4].

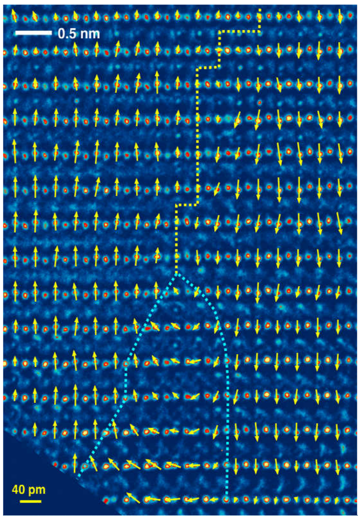

Fig. 2. Map of the atomic displacement vectors. The displacement of the Zr/Ti atoms (arrows) from the center of the projected oxygen octahedra is shown here superposed on the atomic image of Fig. 1. To enhance contrast, the grey scale is converted into a false-colour representation. The length of the arrows represents the modulus of the displacements with respect to the yellow scale bar in the lower left corner. The arrowheads point into the displacement directions. Note the continuous rotation of the dipole directions from "down" (right-hand side) to "up" (left) which closes the electric flux of the two 180° domains.

The displacement map provides direct evidence of a continuous rotation of the dipole direction from downward in the right-hand domain through a 90° orientation to upward in the left-hand domain, forming a particular type of flux-closure structure. The reorientation of the dipoles occurs within a well-defined area of triangular shape with the maximum width at the interface of about 2.5 nm. The displacement vector modulus is small at the top, increasing towards the interface. The transition region from the downward orientation of the electric dipoles to the 90° orientation is about two projected unit cell widths on the right-hand side and up to about twice as wide on the left-hand side. No direct information is available on possible atom shifts along the $[\bar{1}\ \bar{1}\ 0]$ viewing direction. However, the fact that we do not observe any in-plane elongation of the projected atom column contrast can be interpreted as evidence of the dipole rotation occurring exclusively in the image plane.

Our results provide direct experimental evidence for the continuous rotation of the atomic-scale polarization dipoles over a distance directly relevant for the formation of vortex structures as predicted by theory [2]. Our observations agree well with the results of calculations for thin-film epitaxial systems by first-principles techniques where it was found that, as observed in the present work, the lateral extension of the flux-closing area is quite narrow. Furthermore, theory yields a continuous rotation of the polarization direction rather than a closure domain with a 90° polarization orientation and relatively narrow domain boundaries, as known for ferromagnetics.

Our work demonstrates the unique capabilities of unit-cell-by-unit-cell mapping of the dipole vector by means of atomic-resolution transmission electron microscopy. This technique can therefore be employed to study further details of domain structures close to interfaces in ferroelectric heterostructures and of vortex-like structures in ferroelectric materials. Since these structures are sensitive to the balance between competitive interactions, even small changes in the interface properties could have substantial effects on the depolarization field behaviour. In fact, theory predicts quite dramatic effects for thicknesses of the order of a few nanometres in the PZT layer, where the top and bottom layers (metallic or insulating) cannot be treated separately [5]. In addition, unit-cell-thick "dead" layers, e.g. due to local deviations in permittivity caused by non-stoichiometry, are expected to change the flux-closure domain structure. Such investigations are also of potential significance for further progress in technology, in which thinner and thinner and smaller and smaller ferroelectric heterostructure systems are being considered for microelectronic applications.

---

[1] N. Setter, R. Waser, Acta Mater. 48, 151 (2000).

[2] I. Naumov, L. Bellaiche, H. Fu, Nature 432, 737 (2004).

[3] C.L. Jia *et al.*, Science 331, 1420 (2011).

[4] C.L. Jia *et al.*, *Nat. mater.* 7, 57 (2008).

[5] S. Prosandeev, L. Bellaiche, *Phys. Rev.* B 75, 172109 (2007).

Filament Detection in Resistively Switching $SrTiO_3$ in Forming-Free Devices

S. Stille[1], R. Dittmann[2], J. Perlich[3], S.V. Roth[3], R. Waser[2,4], and U. Klemradt[1]

[1]II. Physikalisches Institut B, RWTH Aachen University
[2]Peter Grünberg Institut-7, Forschungszentrum Jülich
[3]HASYLAB at DESY, Hamburg
[4]Institute of Materials in Electrical Engineering 2, RWTH Aachen University

We investigated the influence of Ti top electrodes on the resistive switching properties of $SrTiO_3$ thin film devices. Above a Ti layer thickness of 5 nm, the initial resistance is strongly reduced, giving rise to forming-free devices. Grazing incidence small angle X-ray scattering measurements indicate that the reduction of the $SrTiO_3$ thin film occurs in a filamentary way. We attribute this behavior to the preferential reduction of $SrTiO_3$ thin films along highly defective areas.

The development of the next memory generation for information technology is based largely on the understanding of new materials. One promising approach consists of the use of resistively switching oxides, which change their electrical resistance due to the change of valences in the contained cations [1]. This effect can be observed in many transition metal oxides like titanates [2], manganates [3,4] and zirconates [5]. In $SrTiO_3$ (STO), bipolar resistive switching was first observed around 12 years ago [2]. Since this material is well understood with respect to its structural and electronic properties, it provides a useful model system to obtain further insight into the physical mechanisms of resistive switching due to valence changes. The change in resistance in this kind of materials originates from doping by the introduction of oxygen vacancies. If an electric field is applied to the sample, oxygen vacancies migrate preferentially along extended defects inside the STO film [6]. This results in the formation of filamentary structures of high conductivity, which usually need a first irreversible forming step to develop, typically realized by applying an electric field to the sample [7,8]. To avoid the necessity of this first forming step, forming-free devices are of great interest. Reactive electrode materials [9-11] are suitable for this purpose.

In this work memory cells in metal-insulator-metal (MIM) geometry have been studied by grazing incidence small angle X-ray scattering (GISAXS) experiments at HASYLAB beamlines BW4 and P03. The sample geometry is sketched in Fig. 1a. The substrate is metallically conductive due to Nb doping. The 20 nm thick active layer, consisting of Fe-doped $SrTiO_3$ (Fe:STO), has been deposited by pulsed laser deposition. Ti was used for the top electrodes owing to its small scattering cross section for X-rays. Furthermore, it is reactive and thus gives rise to forming-free memory devices. For electrical characterization, an additional Pt capping layer of 5 nm thickness has subsequently been sputtered on top to prevent the Ti from oxidation by air and thus increase the influence on the Fe:STO layer. The memory cells have been laterally patterned by optical lithography [12].

As can be seen in Fig. 1b, the initial resistance R_i of the memory cells shows a significant dependence on the thickness of the Ti layer. Despite the strong variation of R_i, the initial resistance of the memory cells can clearly be divided in two regions indicated in the graph. Above a layer thickness of 5 nm Ti, R_i drops by several orders of magnitude. Fig. 1c shows representative I-V characteristics for different electrode thicknesses. Whereas Ti layers of up to 3 nm thickness require a first forming cycle (indicated in red), the reduced initial resistance of samples with thicker layers leads to forming-free devices.

Recent progress focuses on the study of structural changes due to the influence of the reactive Ti top electrodes. For this, Ti/20 nm Fe:STO/Nb:STO samples have been prepared with 5 and 15 nm thick Ti layers. The resulting GISAXS pattern of an as-deposited sample is presented in Fig. 2a.

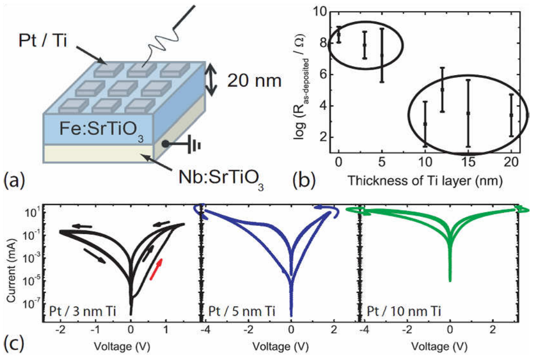

FIG. 1: (a) Sketch of the sample geometry. (b) Initial resistance of Pt/Ti/Fe:STO/Nb:STO MIM structures vs. thickness of Ti layer determined at ± 100 mV. (c) Representative I-V curves of samples with different electrode thicknesses [12].

This pattern could not be observed in reference samples consisting only of 20 nm Fe:STO/Nb:STO. A vertical cut along q_y = 0.2 nm-1 is presented in Fig. 2b. The Yoneda peak at $q_z \approx 0.75$ nm^{-1} is followed by an oscillating intensity, indicated by the arrows. From its periodicity of Δq_z = (0.29 ± 0.03) nm-1, the height of the scatterers can be calculated to be (21.7 ± 2.2) nm. This holds for both (5 and 15 nm) Ti electrodes, and the observed structure is therefore related to the 20 nm thick Fe:STO film.

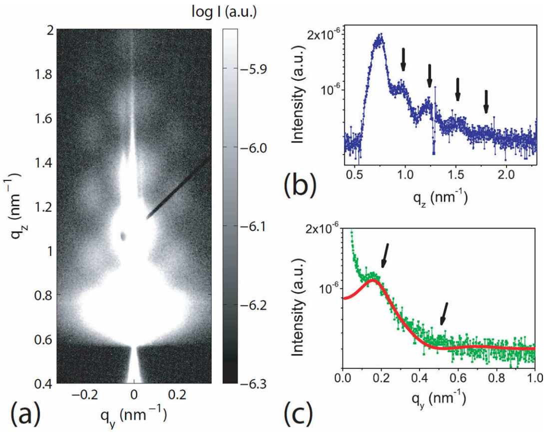

FIG. 2: (a) GISAXS pattern for sample 5 nm Ti/20 nm Fe:STO/Nb:STO. A laterally formed structure can be seen. (b) Vertical cut along q_y *= 0.2 nm*$^{-1}$*. (c) Lateral cut along* q_z *= 0.95 nm*$^{-1}$*. Red line: Simulated GISAXS intensity. [12]*

A lateral cut along q_z = 0.95 nm^{-1} (Fig. 2c) yields a correlation maximum for the observed pattern at q_y = 0.152 nm^{-1}. Simulations with the software FitGISAXS [13] (red line in Fig. 2c) have been performed to obtain more quantitative information on the scatterers, which were modeled in a first approximation as cylinders with a different electron density compared to the surrounding STO film. The simulation of the off-plane (q_y) intensity was performed in a way that the correlation maximum (left arrow in Fig. 2c) was reproduced, as well as the right slope. The cylindrical form factor then led to a minimum (right arrow), which is compatible with the experimental data, yielding a mean cylinder diameter of D ≈ 15 nm. The correlation peak gives a mean distance between the scatterers of D′ = 30 nm. In conclusion, it has been shown that GISAXS, aided by computer simulations, is a powerful technique to elucidate the structural changes in $SrTiO_3$ thin films and thus provides insight into physical properties of as-deposited, forming-free MIM devices. We obtained experimental evidence that the deposition of reactive Ti electrodes on top of Fe:STO thin films leads to a laterally formed structure inside the Fe:STO film, which can be related to the presence of well-conducting, filamentary structures.

[1] R. Waser, R. Dittmann, G. Staikov, and K. Szot, Adv. Mater. 21, 2635 (2009).

[2] Y. Watanabe, J. Bednorz, A. Bietsch, C. Gerber et al., Appl. Phys. Lett. 78, 3738 (2001).

[3] H. Oshima, K. Miyano, Y. Konishi, M. Kawasaki, and Y. Tokura, Appl. Phys. Lett. 75, 1473 (1999).

[4] A. Asamitsu, Y. Tomioka, H. Kuwahara, and Y. Tokura, Nature 388, 50 (1997).

[5] A. Beck, J. Bednorz, C. Gerber, C. Rossel, and D. Widmer, Appl. Phys. Lett. 77, 139 (2000).

[6] K. Szot, W. Speier, G. Bihlmayer, and R. Waser, Nature Mater. 5, 312 (2006).

[7] T. Menke, R. Dittmann, P. Meuffels, K. Szot, and R. Waser, J. Appl. Phys. 106, 114507 (2009).

[8] R. Muenstermann, T. Menke, R. Dittmann, S. Mi, C.-L. Jia et al., J. Appl. Phys. 108, 124504 (2010).

[9] Y.S. Chen, H.Y. Lee, P.S. Chen, T.Y. Wu et al., IEEE Electron Device Lett. 31, 1473 (2010).

[10] C. Hermes, R. Bruchhaus, and R. Waser, IEEE Electron Device Lett. 32, 1588 (2011).

[11] W. Wang, S. Fujita, and S. Wong, IEEE Electron Device Lett. 30, 763 (2009).

[12] S. Stille, Ch. Lenser, R. Dittmann, A. Koehl, I. Krug, R. Muenstermann, J. Perlich, C.M. Schneider, U. Klemradt, and R. Waser, submitted (2012).

[13] D. Babonneau, J. Appl. Crystallogr. 43, 929 (2010).

Origin of the Nonlinear Switching Kinetics and Scaling Studies of Valence Change Memory Cells

S.Menzel[2], M. Waters[1], A. Marchewka[2], U. Böttger[2], R. Dittmann[1], R. Waser[1,2]

[1]Peter Grünberg Institut-7, Forschungszentrum Jülich
[2]Institut für Werkstoffe der Elektrotechnik 2 – RWTH Aachen University

Experimental pulse length-pulse voltage studies of $SrTiO_3$ memristive cells which reveal nonlinearities in the switching kinetics of more than nine orders of magnitude were performed. The experimental results are interpreted using an electro-thermal 2D finite element model. The nonlinearity arises from a temperature increase in a few nanometer thick disc-shaped region at the Ti electrode and a corresponding exponential increase in oxygen vacancy mobility. Our model fully reproduces the experimental data and it provides essential design rules for optimizing the cell concept of valence change memories. The model is generic in nature: it is applicable to all those oxides which become *n*-conducting upon chemical reduction and which show significant ion conductivity at elevated temperatures.

Valence change memory (VCM) cells are a promising candidate for next generation non-volatile, high speed and highly scalable memory cells [1,2]. Particularly, a huge nonlinearity in the switching kinetics is needed to meet the demands posed by the voltage-time dilemma [2]. It is widely accepted that the drift of oxygen vacancies on the nanoscale and a subsequent electrochemical redox process are responsible for the VCM effect. Hereby, the movement of oxygen vacancies due to ion hopping is the limiting factor in the switching process. The mobility of ions can be either field accelerated or temperature activated. But, a detailed investigation of the dominating process has not been shown yet. Herein, we report on experimental switching kinetics studies on $SrTiO_3$ based VCM cells. The experimental results are interpreted using an electro-thermal 2D finite element model which allows for discriminating between the field and temperature contribution to the ion mobility enhancement. This electro-thermal model is subsequently employed to investigate the scaling potential of VCM cells.

The $SrTiO_3$ thin films with 1 at% Fe-doping of 50 nm thickness were grown by pulsed laser deposition (PLD) on (100)-oriented 1 at% Nb-doped $SrTiO_3$ (Nb:STO) single crystals serving both as substrate and bottom electrode. Subsequently, circular top electrodes of 50 µm diameter were prepared by magnetron sputtering of Pt (50 nm)-covered Ti (50 nm) through a shadow mask. By a wet-etching step using buffered HF solution a part of the bottom electrode was exposed. Al wire bonding of the bottom electrode was used to achieve an ohmic contact. An initial quasistatic *I-V* sweep was used to electroform the VCM cell.

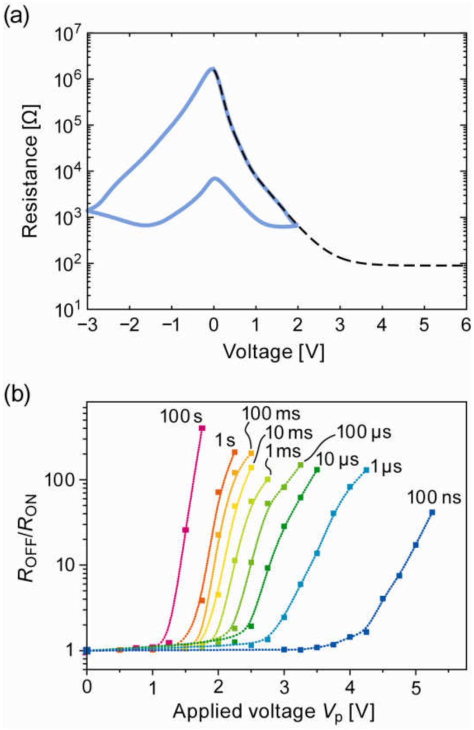

FIG 1: (a) R-V characteristic of a measured cell (blue curve) and in the simulation (black dashed curve). (b) SET switching dynamics of the corresponding sample for different pulse amplitudes and pulse widths, shown as the R_{OFF}/R_{ON} ratio as a function of the applied voltage amplitude of the pulse and the pulse duration..(Redrawn from [3]).

The fabricated VCM cells were electrically characterized by performing quasistatic *I-V* sweeps as well as by defined voltage pulses. Thereby, the voltage was always applied to the top electrode. The measured quasistatic *R-V* characteristic is shown in Figure 1a. Apparently, the low resistive state (ON state) and the high resistive state (OFF state) exhibit a nonlinear voltage dependence. A quasistatic resistance ratio $R_{OFF}/R_{ON} > 100$ is observed for moderate SET and RESET voltages of 2 V and −3 V, respectively. Pulse measurements with a pulse duration Δt_p ranging from 100 ns to 100 s and a pulse amplitude V_p ranging from 0.5-5 V were performed. Before and after a SET voltage pulse, the cell resistance was measured quasistatically to determine the resistance change. The cell was subsequently RESET to its initial OFF state using a quasistatic *I*-*V* sweep. Figure 1b depicts the resulting resistance change. A highly nonlinear switching kinetics is visible. Changing V_p by a factor of 5 leads to a change of 9 orders of magnitude in the Δt_p required to SET the cell.

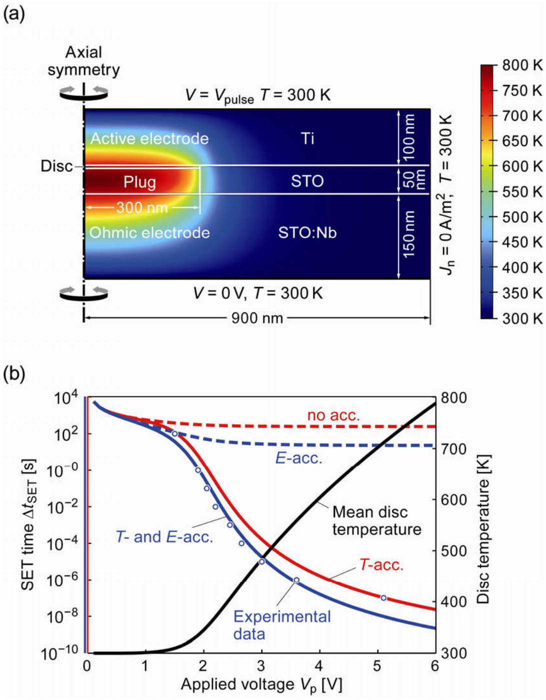

FIG. 2: (a) Cross section of the simulated cell. The temperature distribution for Vp = 5 V is shown in color. (b) Calculated SET time depending on the applied voltage for the four different cases in red and blue. The black line corresponds to the mean disc temperature used for the calculations. The experimental data are extracted from Figure 1(b) for a resistance ratio $R_{OFF}/R_{ON} = 30$ and shown as open circles.(Redrawn from [3]).

To interpret the experimental data we consider a 2D axisymmetric finite element simulation model of the VCM cell (see Figure 2(a)). The simulated cell comprises an *n*-conducting cylindrical region ("plug") grown during electroforming in the $SrTiO_3$ film and a disc shaped region at the top electrode interface ("disc"). The conductivity in the disc region is fitted so that the experimental *R*-*V* characteristic is obtained (cf. Figure 1a). The movement of oxygen vacancies through this interfacial disc region triggers the switching event. The SET time can thus be estimated from the disc thickness and the drift velocity of oxygen vacancies as $\Delta t_{\mathrm{SET}} = l_{\mathrm{disc}}/v_{\mathrm{drift}}$. The drift velocity is calculated according to the Mott-Gurney law of ion hopping as

$$v_{\mathrm{drift}} \propto \left(T/K\right)^{-1} \exp\left(\Delta W_{\mathrm{A}}/kT\right)\cdot E_0 \sinh\left(E_{\mathrm{disc}}/E_0\right).$$

Here, the activation energy $\Delta W_A = 1.01$ eV, the characteristic field $E_0 = 1$ MV/cm, and $E_{\mathrm{disc}} = V_{\mathrm{disc}}/l_{\mathrm{disc}}$. Hence, the SET time depends on the volt drop across the disc V_{disc} and the mean disc temperature *T*. These quantities are extracted from numerical FEM simulations of the field and temperature distribution with the VCM cell. For this, the heat equation is solved for along with the continuity equation [3].

Figure 2a shows the simulated temperature distribution for an applied voltage $V_p = 5$ V. Apparently, the highest temperature emerges in the disc region. The resulting SET times (*T*- and *E*-acc.) are depicted in Figure 2b along with the mean disc temperature and the experimental data. Here, it is discriminated between the contributions of the field acceleration (*E*-acc.), the temperature acceleration (*T*-acc.). For comparison the non accelerated case for a purely linear drift (no-acc.) is shown. A best fit to the experimental temperature is obtained for a combination of field and temperature acceleration. Evidently, the latter is the dominating factor in interpreting the origin of the nonlinear switching kinetics. It has been shown that for all reasonable alternative scenarios, either the fitting procedure fails dramatically or unphysical parameter values have to be used [3].

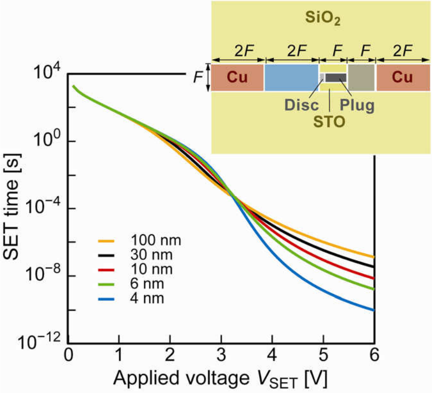

FIG. 3 Calculated SET time depending on the applied voltage for temperature and field accelerated switching. The cell geometry is shown in the inset. The feature size F has been used as a parameter for the set of calculations. The disc thickness is 3 nm in all simulations and the diameter of the filament is 0.4 F.

To project the scaling potential of VCM cells the electro-thermal simulation model is applied to a nanosized axisymmetric VCM cell with an active electrode and an ohmic electrode as well as Cu interconnects and an adjacent SiO_2 layer (see inset in Figure 3), while the dimensions scale with *F*. Figure 3 shows the calculated SET times depending on the applied voltage. Apparently, the switching speed for $V_{\mathrm{SET}} > 3.5$ V increases for smaller feature sizes *F*. This demonstrates that nanosized VCM cells are feasible.

---

[1] R. Waser, R. Dittmann, G. Staikov, K. Szot, Adv. Mater. 21, 2632 (2009).

[2] A. Sawa, Mater. Today, 11, 28 (2008).

[3] S. Menzel, M. Waters, A. Marchewka, U. Böttger, R. Dittmann, R. Waser, Adv. Funct. Mater., 21, 4487, (2011).

.

Controlled quantized conductance in AgI based resistive switches highlights opportunity for atomic-scale memory

S. Tappertzhofen[1], **I. Valov**[2], **R. Waser**[1,2]

[1] IWE II: Institut für Werkstoffe der Elektrotechnik II, RWTH Aachen University
[2] PGI 7: Peter Grünberg Institut 7, Forschungszentrum Jülich

Resistive switches are considered to be a potential candidate to overcome the obstacles of current memory devices as they offer the prospect of ultimately high scalability. On the way towards future information technology we report on silver iodide (AgI) based resistive switches where we observed controllable quantize conductance of a nanosized metallic filament within a solid electrolyte, raising the prospect of an atomic-scale memory.

As the conventional charge based non-volatile Flash memory is expected to approach its downscaling limit within the next years, researchers are prospecting alternative concepts to overcome the obstacles of current information technology. Recently, high attention has been paid to the resistive switching random access memories (ReRAM) based on nano-ionic redox phenomena as potential candidates [1]. Within the context of ReRAMs electrochemical metallization cells (ECM) represent emerging memory devices due to their fast operation, prospect of scalability, low energy consumption, ease of fabrication and potential multibit storage.

The ECM cell arrangement as depicted in figure 1 consists of a nanoscale electrolyte material sandwiched between an electrochemically inert counter electrode (e.g. platinum) and a working electrode (e.g. silver). The resistance of the cell can be reversibly modulated between a high resistive state (HRS) and a low resistive state (LRS), depending on the voltage polarity of an applied voltage pulse. Hereby, the resistance transition is attributed to the electrochemical formation and rupture of a nanoscale metallic filament [2]. The HRS and LRS can be assigned to binary OFF and ON states. Quantized conductance values for the cell resistance have been observed only in "atomic switch" type memory with a vacuum gap between the electrolyte and the counter electrode [3]. However, for purely solid state electrolyte based ECM cells being highly attractive for practical use a similar behavior has not been reported yet.

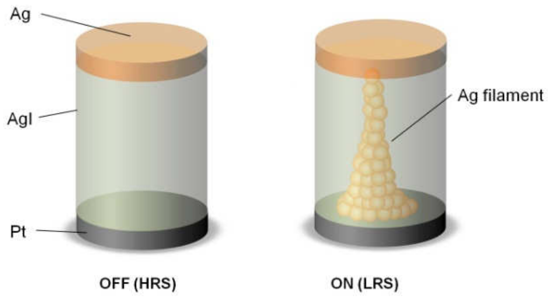

Fig. 1: Schematic of a AgI based resistive switch in OFF state (HRS) and ON state (LRS). Formation and rupture of a metallic filament is believed to be responsible for resistance transition.

In this contribution we fabricated Pt/AgI/Ag micro crossbars with AgI electrolyte of thickness of 30 nm using conventional physical vapor deposition such as thermal evaporation and sputtering. Special attention has been paid to the pattern transfer since AgI is very sensitive towards chemicals (e.g. basic resist developer) and UV light which is needed for lithography. We employed an alternative pattern transfer process avoiding the impact of basic chemical and UV light demonstrating the prospect of downscaling to lateral dimensions of 100 nm and below.

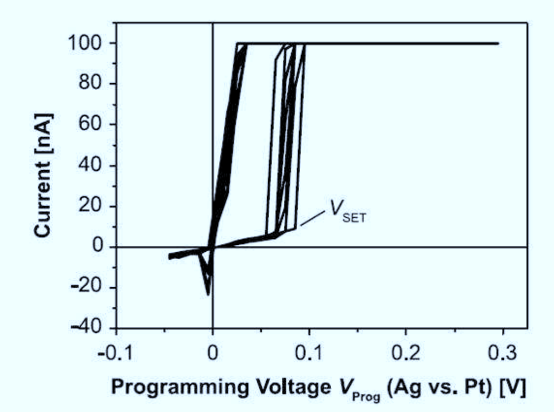

Fig. 2: Resistive switching of AgI based micro crossbars. [4].

AgI micro-crossbars show reliable resistive switching characteristics (figure 2) and multibit storage can be achieved by varying the current compliance needed to prevent damage of the cell in the LRS during voltage sweeping [4].

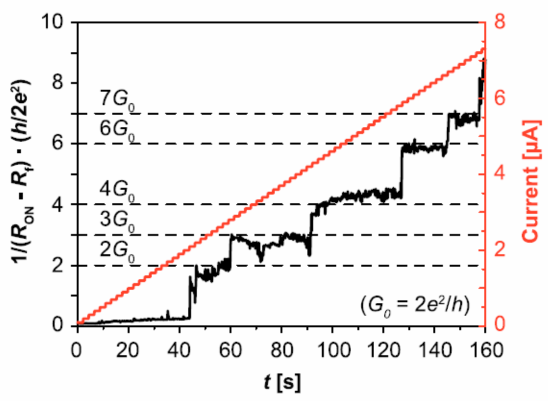

Fig. 3: Quantized conductance values during current sweeping show that multiple of the single atomic point contact conductivity are dominating the cell resistance RON. For simplification, the filament resistance Rf is subtracted [4].

Similar switching characteristics have been lately reported for other material systems such as SiO2 [2]. We now successfully observed quantized resistances in LRS within a current window by current sweeping as shown in figure 3 [4].

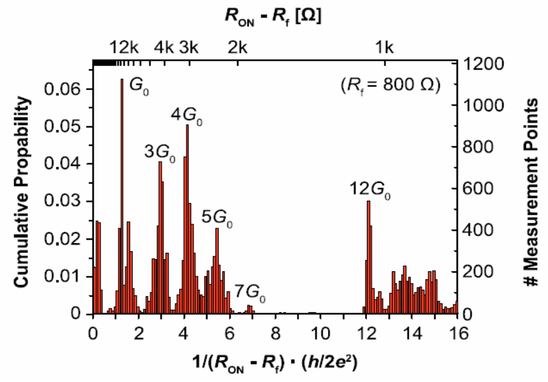

Fig. 4: Cumulative statistics of controllable quantized conductance of AgI based memory cells [4].

These resistances imply the existence of quantized conductance higher than G0 = 78 µS which can be identified as multiple of the single atomic point contact conductivity. The switching behavior clearly indicates that the actual cell resistance is dominated by some few or just a single atom which highlights the potential of an ultimate atomic scale memory. By adjusting the current during current sweeping we were able to control the quantized cell conductance and thus the number of filament atoms being responsible for the cell resistance. This is further supported by a cumulative statistics depicted in figure 4.

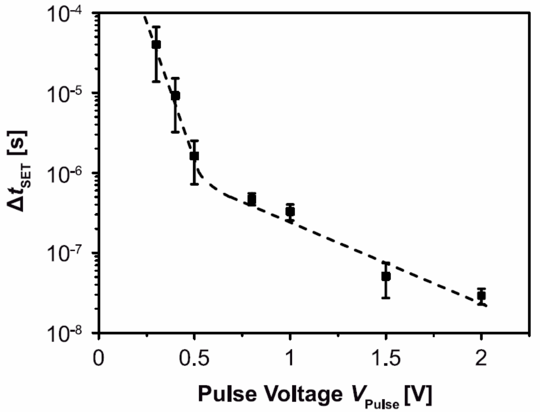

Fig. 5: Non linear switching kinetics of Pt/AgI/Ag cells [4].

Beside quantized conductance the switching kinetics has been analyzed in respect to short pulse lengths in the nanosecond range as well. Resistive switching within at least 10 ns has been observed. Figure 5 depicts the strong non linearity of the switching kinetics which is advantageous for memory applications [5].

In summary, we successfully observed a controllable quantized conductance of resistive switching AgI micro crossbars giving the prospect of an ultimate scalability of these memory devices.

---

[1] R. Waser et. al. Nat. Mater. 6, 833-840 (2007)

[2] I. Valov et. al. Nanotechnology 22 (2011)

[3] K. Terabe et. al. Nature 433, 47-50 (2005)

[4] S. Tappertzhofen et. al. Nanotechnology 23 (2012)

[5] S. Tappertzhofen et. al. Nanotechnology 22 (2011)

Reconstruction of the Projected Crystal Potential Using HRTEM – Prospects for Materials Science Investigations

M. Lentzen[1], **J. Barthel**[1]

[1] Ernst Ruska Centre for Microscopy and Spectroscopy with Electrons and
Peter Grünberg Institute: Microstructure Research (PGI-5), Forschungszentrum Jülich

The projected electrostatic crystal potential is reconstructed from an exit wave function, which has been reconstructed before from a through-focus series of atomic-resolution images recorded with a high-resolution transmission electron microscope (HRTEM). The potential reconstruction includes the self-consistent fit of object thickness, residual lens defocus, phenomenological absorption, and object tilt. The prospects of potential reconstruction are explored by investigating the microsctructure of a BSCF crystal, which exhibits a polytype structure with closely spaced twin boundaries and a high concentration of oxygen vacancies.

In modern high-resolution electron microscopy various reconstruction methods have proven to be invaluable tools for materials science investigations. They comprise wave function reconstruction methods, which aim to eliminate unwanted imaging artifacts as non-linear contrast modulation and contrast delocalisation owing to the presence of lens aberrations. One of these methods, used also in this work, is the widely known focus-variation method [1, 2].

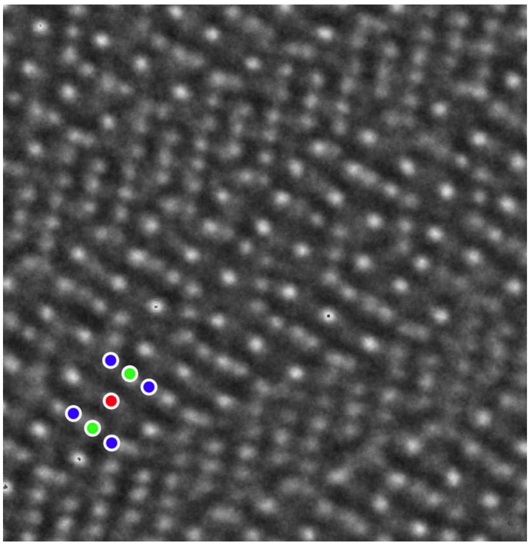

FIG. 1: High-resolution image of BSCF at bright-atom pass-band conditions, red: Ba/Sr, green: Co/Fe, blue: O. Frame size is 3.4 nm × 3.4 nm.

In the past two decades various forms of potential reconstruction methods have been proposed, which aim to eliminate the problems occuring in the structural interpretation of reconstructed exit wave functions, imposed by the effects of dynamical electron diffraction. These effects give rise to a non-linear relation of scattering power and modulation of the wave function [3], and the local modulation can be further obscured by the presence of crystal tilt.

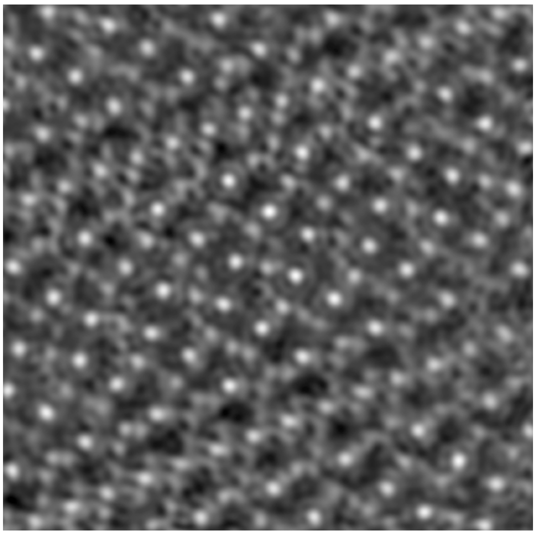

FIG. 2: Phase of reconstructed exit wave function of BSCF. Frame size is 3.4 nm × 3.4 nm.

Materials science investigations using potential reconstruction methods in combination with wave function reconstruction methods require knowledge beyond the idealised conditions for the reconstruction algorithms: in particular object thickness, crystal tilt, residual wave aberrations, and phenomenological absorption are often unknown in experiments. Extensive simulation studies using the channelling model of dynamical electron diffraction [3] and a rapid and stable potential reconstruction algorithm had revealed that the projected crystal potential can be determined for thick objects [4]. A breakthrough for the application in materials science investigations had been achieved by showing that object thickness, residual defocus, and phenomenological absorption can be fitted self-consistently together with the projected potential [5].

The last corner stone, preventing application of the potential reconstruction so far, has been added recently, namely the successful self-consistent fit of crystal tilt [6]. The prospects of potential reconstruction for materials science were explored by investigating the the microstructure of a $Ba_{0.5}Sr_{0.5}Co0.8Fe_{0.2}O_3$ (BSCF) crystal, whose perovskite unit cells can form a variety of polytype structures through rearrangement of oxygen octahedra. A through-focus series of 20 images was recorded from a thin specimen of BSCF with an aberration-corrected TITAN 80-300 operated at 300 kV.

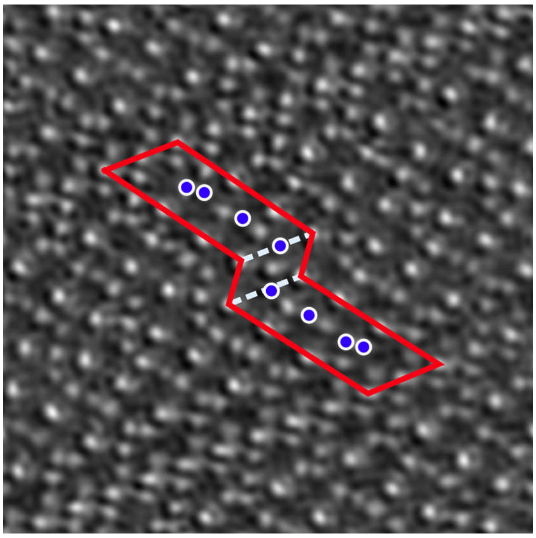

FIG. 3: Reconstructed projected potential of BSCF, frame 3.4 nm by 3.4 nm, red: projected unit cell, blue: oxygen columns used for histogram analysis, dashed: Σ3 twin boundaries.

Next an exit wave function was reconstructed from the series using the TrueImage package (FEI, Eindhoven), which was then subjected to numerical correction eliminating residual aberrations up to the instrumental information limit of 0.08 nm. Finally the projected crystal potential was reconstructed from the corrected exit wave function using the methods described in [5, 6], and the following parameters were determined through self-consistent fit: 8.4 nm object thickness, 1.6 nm residual defocus, and 7.0 nm^{-1} crystal tilt. The final mismatch of model and experimental exit wave function was S = 4.5%, which is a reasonably small value in view of nearly the same amount of mismatch between model and experimental images during the exit wave reconstruction.

The advantage of potential reconstruction over high-resolution imaging alone can be judged by comparing the structural information accessible through the image intensity (Fig. 1), through the phase of the reconstructed exit wave function (Fig. 2), or through the reconstructed projected potential map (Fig. 3). Although the image was recorded with a pass-band up to the information limit very fine details cannot be seen owing to delocalisation. Investigation of the exit wave reveals such details; they are, however, slightly delocalised and corrupted by the presence of crystal tilt. In the potential map the effects of tilt are strongly reduced, and the non-linear distortion of the atomic contrast modulation owing to dynamical diffraction is eliminated.

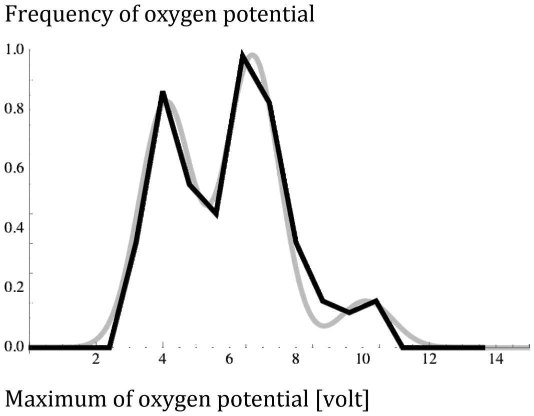

FIG. 4: Histogram analysis of oxygen columns, black: frequency of oxygen potential maxima, grey: fit of the distribution with three gaussians.

Numerical evaluation of the projected potential map allows a quantitative investigation of the projected crystal structure of the BSCF crystal, containing closely-spaced Σ3 twin boundaries, in particular the disorder on the oxygen sublattice. Column-by-column measurement of the maxima of the projected oxygen potential reveals through a histogram of the potential maxima single oxygen atom precision of 2.6 volt per atom (Fig. 4). The three maxima of the potential distribution indicate the presence of a high concentration of oxygen vacancies.

One of us, J. B., gratefully acknowledges funding from the German Federal Ministry of Economics and Technology within the COORETEC initiative.

---

[1] W. Coene, G. Janssen, M. Op de Beeck, D. Van Dyck, Phys. Rev. Lett. 20, 3743 (1992).

[2] A Thust, W. M. J. Coene, M. Op De Beeck, D. Van Dyck, Ultramicroscopy 64, 211 (1996).

[3] K. Kambe, G. Lehmpfuhl, F. Fujimoto, Z. Naturforsch. A 29, 1034 (1974).

[4] M. Lentzen, K. Urban, Acta Cryst. A 56, 235 (2000).

[5] M. Lentzen, Ultramicroscopy 110, 517 (2010).

[6] M. Lentzen, Proceedings MC2011 Kiel, IM2 P133 (2011).

Elastic Energy of Metadislocations in Complex Metallic Alloys

M. Feuerbacher and M. Heggen

Ernst Ruska-Centrum und Peter Grünberg Institut (PGI-5)

A parameterized expression for the Burgers vectors of metadislocations is derived. We calculate the elastic line energy of metadislocations and demonstrate that the experimentally observed occurrence of Fibonacci relations between the members of a metadislocation series is due to energy minimization.

Complex metallic alloys (CMAs) are intermetallic compounds with a complex structure and a unit cell typically containing some hundred to some thousand atoms. As a result of the large lattice parameters, in these materials conventional dislocation-based mechanisms are prone to failure. The elastic line energy of a perfect dislocation would articulately exceed physically reasonable values. Metadislocations, first observed in the CMA ε-Al-Pd-Mn [1], are line defects mediating plastic deformation in a variety of CMAs. They have small Burgers vectors, hence low elastic line energies, and are accommodated in the lattice via the formation of a slab of phase that is different but closely related to the host. Fig. 1a and 1b depict metadislocations in the orthorhombic phases ε_6 and ε_{28} of the system Al-Pd-Mn, respectively. To date, metadislocations were further observed in monoclinic Al-Pd-Fe phases (Fig. 1c), in orthorhombic $Al_{13}Co_4$, and in orthorhombic Taylor phases (Fig. 1d).

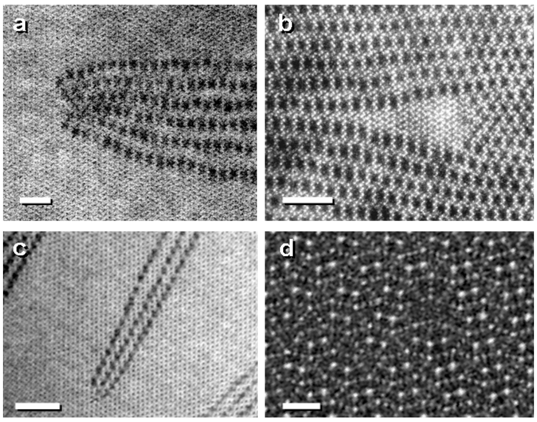

FIG. 1: Metadislocations with six associated phason halfplanes in ε_6-Al-Pd-Mn (a) and in ε_{28}-Al-Pd-Mn (b). Metadislocations in ξ-Al-Pd-Fe (c) and in T-Al-Mn-Pd (d). Scale bar 10 nm for (a – c) and 1 nm for (d).

In a given CMA structure series of metadislocations with different Burgers vector lengths exist. Within a metadislocation series, the Burgers vectors of the individual members are related by factors of τ, where is the golden mean. The latter comes into play due to the icosahedral local order occurring in CMA structures. Metadislocations with different Burgers vector length are associated with different quantities of related phase. It is experimentally found that the quantity of associated related phase within a metadislocation series follows a Fibonacci sequence. From a purely geometric point of view, however, it is not clear why the characteristic parameters of metadislocations are restricted to Fibonacci related numbers since other metadislocations, can be constructed equally well. In this paper, we calculate energy diagrams which show that the experimentally observed metadislocations are those of lowest elastic energy [2].

Fig. 2 depicts the tiling of a metadislocation in the ε_6-phase. The metadislocation core is represented by the dark-grey tile, the ideal ε_6-phase by flattened hexagons in alternating orientations, and the slab of related phase is realized by six phason halfplanes, represented by banana-shaped nonagons and regular pentagons (light grey). Superposed to the tiling is a Burgers circuit around the dislocation core starting at the solid point at the upper left and following the edges of the tiling in the direction of the arrows. The circuit yields a Burgers vector $\vec{b}_\varepsilon = -c/\tau^4[0\quad 0\quad 1]$, which, for ε_6-Al-Pd-Mn corresponds to a Burgers vector length of 1.83 Å.

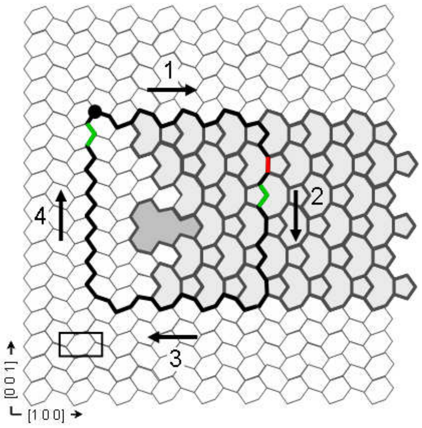

FIG. 2: Burgers circuit around a metadislocation in the ε_6-structure.

In order to obtain an expression valid also for the other metadislocations in the series the expression is parameterized using parameters p and h chosen as follows: p corresponds to the number of phason halfplanes the metadislocation is associated to and h corresponds to the number of hexagon planes on the left-hand side of the dislocation core. This yields the expression

$$b_{\varepsilon} = c\left(\frac{\tau^{2}}{2}p - h\right). \qquad (1)$$

The parameterization implies the construction of a metadislocation according to a generalized Volterra process: a metadislocation is constructed by removing h hexagon halfplanes from an ideal ε-phase lattice, and filling the gap with p phason halfplanes. Since the thickness ratio of the hexagon and phason planes corresponds to an irrational number, the hexagon halfplanes can only be partially compensated or overcompensated. The resulting gap or overlap corresponds to the Burgers vector of the dislocation.

The elastic strain energy per unit length of dislocation can be approximated as $E_{el} \approx \mu b^{2}$, where μ is the shear modulus of the material. Inserting eq. (1) yields a parametrized expression for the elastic energy of a metadislocation, which can be represented in the form of an energy map in terms of the parameters p and h.

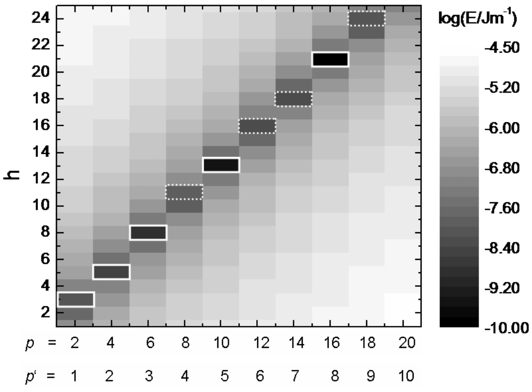

FIG. 3: Elastic energy of metadislocations in ε- and ξ-phases. Experimentally observed metadislocations in ε-Al-Pd-Mn are marked by boxes with solid white outline, further hypothetical metadislocations are marked by boxes with dashed outline. The upper abscissa (p) holds for orthorhombic ε-phases, the lower abscissa (p') for monoclinic ε-phases and ξ-phases.

Figure 3 shows the elastic energy for a wide range of (p,h) doublets, where $p/2$ and h are natural numbers. Each box represents the logarithm of the elastic energy of the corresponding metadislocation. The darkest grey represents the lowest energy values. We find a valley of low energies along a line, which is approximately diagonal in Fig. 3. The range of plotted (p,h) doublets contains five experimentally observed metadislocations, which correspond to particularly low energy values and are indicated by solid white boxes. There are further, hypothetical, metadislocations, which also possess relatively low energy, but which are not observed experimentally, for example those with 8, 12, or 14 associated phason halfplanes. These are indicated by boxes with dashed outline.

Following this approach, metadislocations with the highest number of associated phason halfplanes seem the most favorable. However there are additional factors which have not been accounted for, the most evident of which is the energy cost resulting from the inclusion of the associated phason halfplanes. Taking this into account by an additive linear term in the expression for the elastic energy, we find that metadislocations with six phason planes have the lowest energy. This is in agreement with the experimental observation frequency.

Following a similar approach, we can treat metadislocations in ξ-phases and monoclinic ε-phases (c.f. Fig. 1c). We find the expression

$$b_{\xi} = c'\left(\tau^{2} p' - h'\right). \qquad (2)$$

which has a very similar form as eq. (1). Substituting *p/2* by *p'*, *h* by *h'*, and *c* by *c'*, Fig. 3 holds for metadislocations in the ξ-structure as well using the lower abscissa.

The energy diagram shown in Fig. 4 holds for metadislocations in Taylor-phases [3] (c.f. Fig. 1d), where s corresponds to the number of stacking faults the metadislocation is associated to and m corresponds to the number of c-lattice constants antagonizing the [0 0 1] shift introduced by the s associated stacking faults. We can accordingly understand the construction of the metadislocation such that the [0 0 1] shift introduced by s associated stacking faults is partially compensated or overcompensated by m “inserted” (1 0 0) hexagon planes, and the difference corresponds to the Burgers vector of the dislocation. The same diagram also holds for metadislocations in orthorhombic $Al_{13}Co_{4}$, taking into account the parameter s' on the lower abscissa.

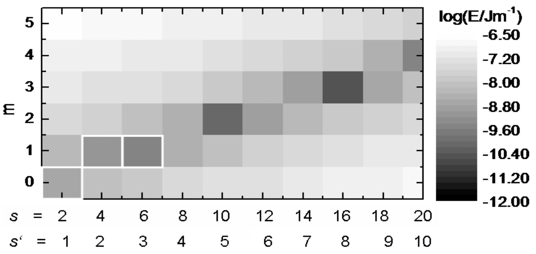

FIG. 4: Elastic energy of metadislocations in T-phases and in $Al_{13}Co_{4}$. Experimentally observed metadislocations in T-Al-Mn-Pd phase are marked by boxes. The upper abscissa (s) holds for T-phases, the lower abscissa (s') for $Al_{13}Co_{4}$.

In conclusion we find that metadislocation formation is not generally restricted to Fibonacci related construction parameters. Metadislocations with other, non-Fibonacci related construction parameters are generally possible, but do not form since they have higher elastic line energy.

[1] H. Klein, M. Feuerbacher, P .Schall P, K. Urban, Phys. Rev. Lett. 82, 3468, 1999.

[2] M. Feuerbacher and M. Heggen, Acta Mat. 60, 1703, 2012.

[3] M. Heggen, L. Houben, M. Feuerbacher, Nature Mat. 9, 332, 2010.

Low Field Magnetic Resonance Imaging with tuned high-Tc SQUID

Chao Liu[1,3], Yi Zhang[1,3], Longqing Qiu[2,3], Hui Dong[2,3], Hans-Joachim Krause[1,3], Xiaoming Xie[2,3], Andreas Offenhäusser[1,3]

[1] Institute of Complex Systems-8 and Peter Grünberg Institut-8: Bioelectronics, Forschungszentrum Jülich
[2] State Key Laboratory of Functional Materials for Informatics, Shanghai Institute of Microsystem and Information Technology (SIMIT), Chinese Academy of Sciences (CAS), Shanghai 200050, China
[3] Joint Research Laboratory on Superconductivity and Bioelectronics, Collaboration between CAS-Shanghai and FZJ

In order to improve low-field (LF) Magnetic Resonance Imaging (MRI) measurements with a tuned high-T_c radio-frequency (rf) Superconducting Quantum Interference Device (SQUID) as a signal detector, we use a permanent magnet pair for sample pre-polarization. MRI images are acquired by using filtered back projection reconstruction. The projections are obtained by recording free induction decay (FID) or spin echo (SE) signals with the gradient field applied at different angles. For every projection, the sample is first pre-polarized in the gap of the PM pair and then mechanically transported to the measuring position underneath the tuned SQUID. Taking 12 projections, two-dimensional LF-MRI images of two water phantoms are obtained without averaging, exhibiting a spatial resolution of about 0.2 mm.

Recently, LF-MRI using a SQUID as a signal detector was demonstrated [1] at low measurement field B_m in the µT range. The magnetization M of the sample is proportional to the pre-polarization field B_p while B_m determines the Larmor frequency f_L. The precession signals scale only with B_p when a SQUID is employed as detector because of its frequency-independent sensitivity. However, the technical relevance of MRI at low field is usually limited by the relatively low signal-to-noise ratio.

It is very difficult to generate a polarization field B_p larger than 50 mT using copper-wire-wound coils at room temperature [2] because of the dissipated heat due to the large coil current, the difficulty to switch off B_p quickly because of the large coil inductance, and flux trapping in the SQUID.

In order to overcome this, we use sample pre-polarization by a permanent magnet (PM). Two NdFeB disk magnets are integrated with a soft iron yoke, generating a B_p field of about 1 T. A tuned high-T_c (HTS) rf SQUID is used as signal detector. The MRI images are acquired by using filtered back projection reconstruction. Each measurement is performed by first pre-polarizing the sample in the gap of the PM pair and then mechanically transporting it to the measuring position. Because of the strong polarizing field and the high sensitivity of the tuned SQUID, the FID and SE signals can be recorded without averaging.

Our LF-MRI measurement setup schematically shown in Fig. 1 is designed for small-size samples. It consists of four parts: a coil system, a tuned HTS rf SQUID, a PM pair with yoke, and a mechanical transport system.

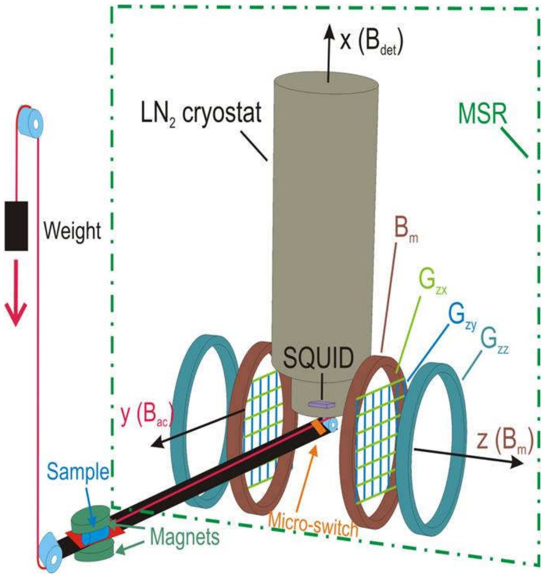

FIG. 1: Schematic of the LF-MRI setup.

The 2-D MRI coil system includes a Helmholtz coil pair for the generation of the measurement field B_m, three coil pairs generating the gradient field components G_{zx}, G_{zy}, and G_{zz}, and an excitation field B_ac coil pair to generate the π/2 or π pulse.

A Helmholtz coil pair of 22 cm diameter provides a B_m of 212 µT along the z-direction. An excitation field B_ac in the y-direction is produced by a coil pair (not shown in Fig. 1). The gradient field $G_{zz} = \mathrm{d}B_z/\mathrm{d}z$ is generated by a Maxwell coil, whereas the other two gradient fields, $G_{zx} = \mathrm{d}B_z/\mathrm{d}x$ and $G_{zy} = \mathrm{d}B_z/\mathrm{d}y$ are produced by planar multi-loop gradient coils. When the filtered back projection reconstruction is utilized to create 2-D MRI images, the direction of the gradient field in the y-z plane can be rotated stepwise by adjusting the strength of G_{zz} and G_{zy}.

The tuned HTS rf SQUID combines an rf SQUID magnetometer and a LC resonant circuit, which is inductively coupled to the SQUID [3]. The tuned rf SQUID not only improves the sensitivity to 6 ~ 7 fT/Hz at $f_L \approx 9$ kHz but also provides the large detection area of the L coil which is 40 mm in diameter [3].

Once the sample arrives at the measuring position, a micro-switch produces a TTL pulse to start the measurement sequence shown in Fig. 2. First, a π/2 pulse of B_{ac} is applied to tilt the sample magnetization M perpendicular to B_m. A Q-switch circuit damps the ringing in the LC circuit induced by the ac pulse [4] before the FID signal is recorded. Subsequently, a π pulse of B_{ac} is applied to obtain a SE signal. After the recordings, the sample is transported back to the gap of the PM pair for pre-polarization and the gradient field is rotated to acquire the next projection.

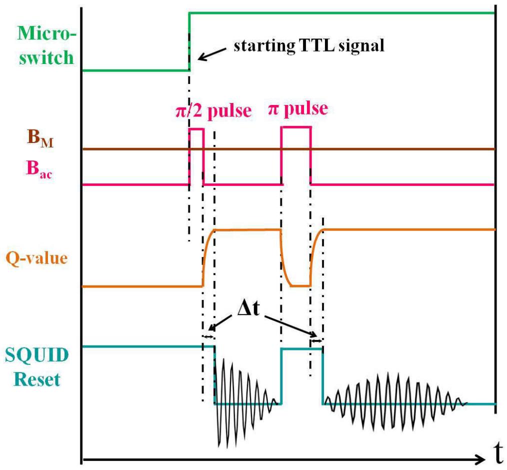

FIG. 2: Pulse sequence used in the measurements.

The filtered back projection reconstruction was utilized for 2-D MRI measurements [5]. In the y-z plane, each projection corresponded to a gradient field $G_{z(y\text{-}z)}$ of about 20 Hz/cm, with its direction rotated step by step to cover 180°. For all projections, both FID and SE signals were recorded without averaging.

We performed LF-MRI measurements with water phantoms [6]. Image quality generally increases with increasing number of projections. To illustrate this effect, images were reconstructed from 6 and from 12 projections, as shown in Fig. 3 (a). Here, sample #1 with five isolated cylinder-shaped bores filled with tap water (1 × 0.2 ml with diameter of 6 mm in the center and 4 × 0.35 ml with diameter of 8 mm around it) was utilized. The MRI image reconstructed from 6 projections was distorted because of the low number of projections. When the number of projections was increased to 12, the image quality was clearly improved.

Usually, the echo signal is utilized to reconstruct the image. Here we make a comparison between the images of sample #2 reconstructed from FID and Echo signals. The sample #2 is a plexiglass slab with two cylinder-shaped bores, 7.5 mm in diameter, filled with tap water (0.35 ml each), and separated by a distance of 13 mm. The photo of the sample #2 and its reconstructed 2-D MRI images with 12 projections are shown in Fig. 3 (b). Geometrical shapes of the images reconstructed from both FID and SE signals are in good agreement with the dimensions of the sample.

The spatial resolution Δx of MRI in one dimension can be expressed as $\Delta x = 2\pi\delta l / \gamma G$, where δl is the linewidth of the NMR spectrum, γ the gyromagnetic ratio of proton ($\gamma/2\pi$ = 42.58 MHz/T), and G the applied gradient field strength (47 μT/m). For the measured 0.4 Hz linewidth of sample #2, a spatial resolution of about 0.2 mm was reached.

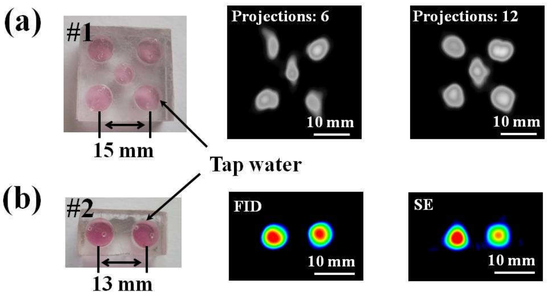

FIG. 3: Sample photos and their 2-D LF-MRI images. The tap water in the sample photos was pink-colored and the sample substrates were made from plexiglass. (a) Photo of sample #1 and its 2-D MRI images reconstructed from FID signals for different numbers of projections. (b) Photo of sample #2 and its 2-D MRI images reconstructed from FID and SE signals.

The quality of the images demonstrates that it is feasible to image small-sized samples with 1 T pre-polarization, sample movement and a tuned SQUID detector [6]. The performance was significantly improved over pre-polarization by a copper coil. MRI images were reconstructed from 12 projections without averaging. In our present scheme, a relatively long relaxation time T_2 of the sample on the order of seconds is required. In the future, not only the homogeneity of B_m should be improved to reduce the distortions of the reconstructed MRI image, but also the sample transport time should be shortened to lower the requirement on the sample's T_2.

---

[4] R. McDermott et al., Proc. Natl. Acad. Sci. 101, 7857 (2004)

[2] V.S. Zotev et al., IEEE Trans. Appl. Supercond. 17, 839 (2007)

[3] L.Q. Qiu, Y. Zhang, H.-J. Krause, A.I. Braginski, A. Usoskin, Rev. Sci. Instrum. 78, 054701 (2007)

[4] H. Dong, Y. Zhang, H.-J. Krause, X. Xie, A.I. Braginski, A. Offenhäusser, SUST 22, 125022 (2009)

[5] H. Dong, Y. Zhang, H.-J. Krause, X. Xie, A. Offenhäusser, IEEE TAS 21 (2011) 509 (2011).

[6] C. Liu, Y. Zhang, L.Q. Qiu, H. Dong, H.-J. Krause, X. Xie, A. Offenhäusser, submitted to SUST (2012).

Piezoelectricity in Non-Polar Block Copolymers

C. W. Pester[1], M. Ruppel[2], H. G. Schoberth[1], K. Schmidt[3], C. Liedel[1], P. van Rijn[1], K. A. Schindler[1], S. Hiltl[1], T. Czubak[1], J. Mays[4], V. S. Urban[5], and A. Böker[1]

[1] Lehrstuhl für Makromolekulare Materialien und Oberflächen, DWI an der RWTH Aachen
[2] Chemical Sciences Division, Oak Ridge National Laboratory, Oak Ridge, TN 37831, USA.
[3] Materials Research Laboratory, University of California Santa Barbara, Santa Barbara, CA 93106, USA.
[4] Center for Nanophase Materials Sciences, Oak Ridge National Laboratory, Oak Ridge, TN 37831, USA.
[5] Neutron Scattering Science Division, Oak Ridge National Laboratory, Oak Ridge, TN 37831, USA.

We elaborate on the discovery of piezoelectric properties in non-polar block copolymers by means of in-situ synchrotron small-angle X-ray scattering [1]. The piezoelectric suscep-tibility of poly(styrene-b-isoprene) (SI) block copolymer lamellae is up to an order of magnitude higher when compared to classic piezoelectric materials. The electroactive response increases with temperature and is found to be strongest in the disordered phase, which can be interpreted by anisotropic behavior of polymer coil conformations.

While most polymers are typical dielectrics, which may exhibit paraelectric properties such as electrostriction [2], the block copolymers we used unveiled an initially unexpected response to applied electric fields [3]. This work presents the first study of converse piezoelectric properties in non-crystalline polymer systems, consisting of non-polar monomers, and evaluates its evolution with temperature to yield detailed information on electric field–polymer interaction on a molecular level. The observed properties should hold generally and suggest that block copolymers may provide a valuable new route to piezoelectric materials.

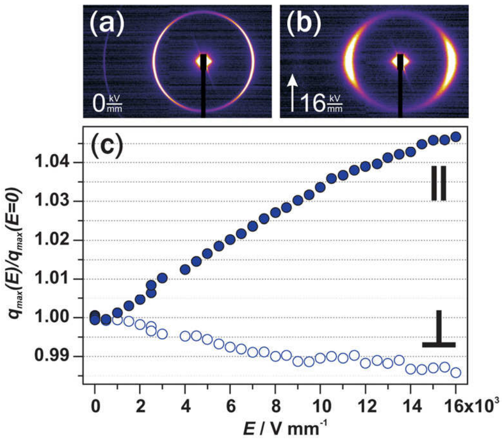

FIG. 1: 2D-scattering patterns for a 33.5 wt% solution of SI in toluene at room temperature in the absence (a) and presence of an electric field of 16 kVmm−1 (b). Filled and empty symbols represent $q_{max}(E)/q_{max}(E=0)$ data for parallel and perpendicular lamellae, respectively. Error bars are smaller than symbols and were omitted. An arrow indicates the direction of the electric field vector. Evolution of normalized qmax with electric field E (c).

Figure 1a,b depicts representative X-ray scattering patterns of a lyotropic block copolymer solution, exhibiting a lamellar morphology, in the presence of an external electric field. Modest field intensities readily align lamellae predominantly parallel to the applied field [4,5]. Higher intensities change the periodicity of parallel-oriented lamellae: their distance decreases normal to an increasing electric field [3]. This is evident from Figure 1b, which depicts the anisotropic scattering of the lamellar lyotropic phase. The analysis of scattered intensities parallel and normal to the electric field direction (Figure 1c) reveals that lamellae oriented parallel to the applied field are primarily affected in the phase separated state, while the periodicity of lamellae oriented perpendicular to field direction is barely altered. Both linearity and direction of the electroactive response indicate a converse piezoelectric behavior in contrast to bare electrostriction and/or Maxwell stress due to electrostatic forces typical for paraelectric materials.

To quantify the temperature-dependent electro-active response of block copolymers, the piezo-electric susceptibility κ(T), is determined from the initial slope of a linear fit to $q_{max}(E,T)$ data according to Equation 1 (Figure 1).

$$\kappa(T) = -\frac{d\lambda}{dE} = -\frac{1}{dE}\left[\frac{q_{\max}(E=0,T)}{q_{\max}(E,T)} - 1\right] \qquad (1)$$

Further, the *piezoelectric asymmetry* Γ(T), quantifying differences in electroactive behavior in dependence of initial structural orientation towards the field vector, is defined as

$$\Gamma(T) = \frac{|\kappa_{\perp}(T)|}{|\kappa_{\parallel}(T)|} \qquad (2)$$

Considering the evolution of the piezoelectric susceptibility with temperature (Fig. 2), three regions may be distinguished: i) For temperatures below the order-disorder transition temperature T_{ODT} barely any piezoelectric effect may be attested for perpendicular oriented lamellae, i.e., $\kappa_{\perp}(T<T_{ODT}) \approx 0$ pmV^{-1} and hence Γ(T) ≈ 0. Contrary, parallel-oriented lamellae exhibit a positive piezoelectric susceptibility $\kappa_{||}(T<T_{ODT})$ with magnitudes ranging from 2000–5000 pmV^{-1} ; that is, the lamellar spacing decreases in the presence of an external electric

field. ii) In close proximity to the order-disorder transition, $\kappa_{||}(T)$ increases significantly with temperature. Remarkably, $\kappa_{\perp}$ becomes negative, indicating an increasing periodicity of lamellae oriented normal to the applied field. Moreover, $|\kappa_{\perp}(T)|$ converges to about the same magnitude as observed for parallel oriented lamellae and $\Gamma(T)$ increases accordingly. iii) In the disordered phase, piezoelectric susceptibilities for both orientations are con-siderably higher in comparison to the ordered phase and converge to comparable magnitudes for higher polymer concentrations. Consequently, $\Gamma(T) \rightarrow 1$ above ODT, which indicates block copolymer chains that are increasingly more sensitive to an applied field irrespective of field orientation.

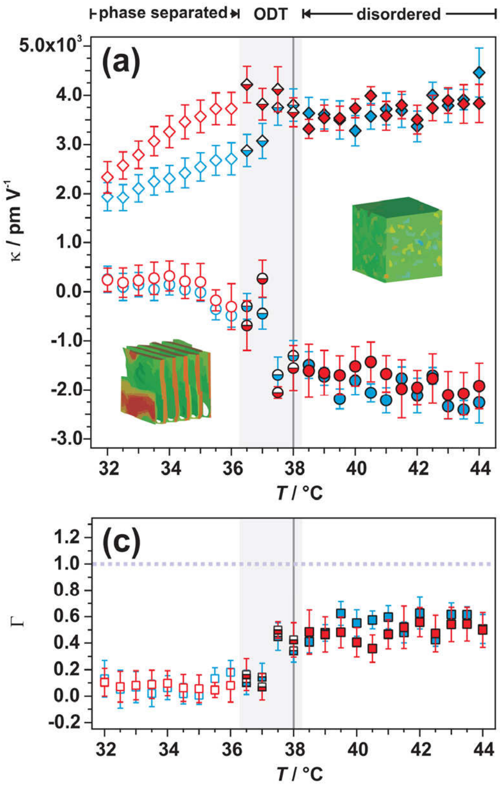

FIG. 2: Evolution of the piezoelectric susceptibility with temperature for block copolymer lamellae oriented perpendicular ($\kappa_{\perp}(T)$, circles) and parallel to an applied field ($\kappa_{||}(T)$, rhombi) for a 30.5 wt.% solution of SI in toluene (a). The insets in (a) represent simulation data of the lamellar and disordered phase. Piezoelectric asymmetry $\kappa(T)$ for both concentrations according to Eq. 2 (b). Heating and cooling cycles are color coded in red and blue, respectively. Empty symbols represent the lamellar phase, half-filled symbols illustrate the ODT region (also indicated by gray background shading), and filled symbols highlight data obtained in the disordered phase. The dark gray line indicates T_{ODT} for respective block copolymer solutions in the absence of an electric field and the dashed line indicates the ideal case of a symmetric electroactive response irrespective of electric field orientation.

In contrast to classical piezoelectric materials, which lose their electroactive response when the molecular structure becomes isotropic above a certain temperature, for the block copolymer system discussed herein the piezoelectric susceptibility remains high in the vicinity of T_{ODT}. In fact, the highest converse piezoelectric susceptibilities are observed above ODT, where system anisotropy diminishes.

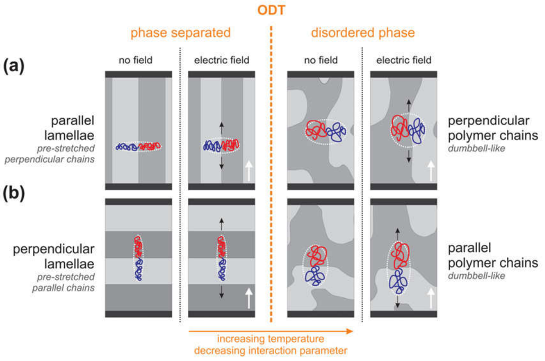

FIG. 3: Schematic representations of the effect of an external electric field on the polymer chain conformation below and above ODT for orientations parallel (a) and normal (b) to field direction. Black horizontal bars indicate the electrodes. Black arrows indicate the chain distortion by Kuhn segment reorientation in the presence of an applied field. The bold white arrows indicate the direction of the electric field vector.

On a molecular level, for temperatures in the vicinity of ODT, nanostructures begin to disintegrate to form a disordered phase consisting of dumbbell-like polymer chains [6,7], and the enthalpic penalty for unlike monomer–monomer contacts diminishes. The more Gaussian-like chain conformation of unlike blocks is anticipated to facilitate chain distortion by an applied field without bias with respect to chain orientation (Fig. 3). Indeed, the magnitudes of the piezoelectric susceptibilities adapt comparable values and $\Gamma(T)$ sharply increases with temperature.

---

[1] C.W. Pester, M. Ruppel, H.G. Schoberth, K. Schmidt, C. Liedel, P. van Rijn, K.A. Schindler, S. Hiltl, T. Czubak, J. Mays, V.S. Urban, A. Böker, Adv. Mater 23, 4047 (2011)

[2] T. Furukawa, N. Seo, Jpn. J. Appl. Phys. 29, 675 (1990).

[3] K. Schmidt, H. G. Schoberth, M. Ruppel, H. Zettl, H. Hänsel, T. M. Weiss, V. Urban, G. Krausch, A. Böker, Nature Mater. 7, 142 (2008).

[4] T. L. Morkved, M. Lu, A. M. Urbas, E. E. Ehrichs, H. M. Jaeger, P. Mansky, T. P. Russell, Science 273, 931 (1996).

[5] V. Olszowka, M. Hund, V. Kuntermann, S. Scherdel, L. Tsarkova, A. Böker, ACS Nano 3, 1091 (2009).

[6] K. Almdal, J. H. Rosedale, F. S. Bates, G. D. Wignall, G. H. Fredrickson, Phys. Rev. Lett. 65, 1112 (1990).

[7] E. Helfand, Z. R. Wasserman, Macromolecules 9, 879 (1976).

Gateable micro channel plate detector for extreme ultraviolet radiation with high temporal resolution

R. Freiberger[1], J. Hauck[1], D. Lvovsky[2], R. Adam[2], S. Danylyuk[1], L. Juschkin[1]

[1]RWTH Aachen University, Chair for the Technology of Optical Systems
[2]Peter Grünberg Institut-6, Forschungszentrum Jülich

Research in ultrafast nanoscale phenomena requires high spatial and temporal resolution detectors. Optical imaging microscopes achieve high time resolution but low spatial resolution and scanning microscopes vice versa. Extreme ultraviolet imaging microscopy closes this gap but demands a suited two dimensional detector with high sensitivity and fast gating ability.

In this work a new BURLE's 2-micron pore microchannel plate photoelectron multiplier together with a phosphor screen is used as a detector and further optimized with respect to its time resolution. The operation voltage of the electron-multiplier is pulsed for 1.25 ns. Only during that time the detector is highly sensitive to extreme ultraviolet light. A custom built impedance transformer delivers high currents into the plates' capacitance. This leads to a short charging time and ensures a narrow temporal sensitivity window.

The following attributes of the detector system are analyzed:

- **Temporal behavior is measured by femtosecond illumination with high harmonics generation radiation at different relative delays. The sensitivity curve has a width of 2 ns. Electronic timing jitter is below 150 ps.**
- **Spatial resolution is determined by mapping the shadow of a sharp edge on the detector. The smearing gives information about the modulation transfer function. The resolution limit according to the Rayleigh criterion is at 12 lp/mm or a minimum resolvable pitch of 80 µm.**

In summary the detector provides a spatial resolution down to 80 nm and a time resolution shorter than 2 ns using a discharge produced plasma EUV source and a zone plate based microscope with a magnification of ~1000x. This is a highly interesting combination and will help to investigate a variety of short time processes in nanoscience [1].

The micro channel plate (MCP) detectors demonstrate high sensitivity to the extreme ultraviolet (EUV) radiation (spectral range of about 1 – 50 nm wavelength). Incident EUV photons produce free photoelectrons at the front face of the array of photoelectron multipliers. A caesiumiodide coating extends the sensitivity into the long wavelength range to 200 nm (6.2 eV). The avalanche breakdown in the channels multiplies the primary electrons by a factor up to 350.000. The MCP voltage is pulsed to achieve time resolved imaging. A Marx-generator with pulse forming and impedance matching electronics delivers a 1.25 ns HV-pulse to charge the plates' capacitance. Additionally, a constant offset-voltage enables adjustment of the gain. At the backside of the MCP the escaping electron cloud is proximity focused on a phosphor screen and converted to green light. A fiber optic guides the light from the vacuum to the atmospheric side.

Technical Information: The micro channels form a hexagonal mesh with 2.8 μm spacing and 2 μm channel diameter at an aspect ratio of the channel length to its diameter L/D=60. MCP and phosphor screen are mounted on a CF-63 vacuum flange with high voltage feedthroughs for easy handling. The MCP is circular with a sensitive area of 18 mm diameter.

Together with the mounting ring the capacitance sums up to 300±50 pF. Since charging time is in the range of $\tau = RC$, low loading impedance (R⍰ 50 Ω) is important. A custom built 25:1 impedance transformer based on the Guanella design [2] translates the 50 Ω impedance of the HV-pulser to 2 Ω.

The pulse enters the five transmission lines Z_T=10 Ω in series. Each transmission line carries a voltage of U·⍰ at a current of I. At the output the pulses are added in parallel to a current of 5·I and a voltage of U·⍰. The output impedance is 10 Ω / 5 = 2Ω. The coupling capacitor C_C = 6 nF transmits the short pulse but isolates the transformer from the offset voltage U_0. The transformer has been constructed to be plugged onto the MCP contacts inside the vacuum chamber, thus minimizing parasitic inductance and resistance.

Temporal Response: The detectors temporal behavior has been investigated by observing the detector-signal after short excitation by a EUV light pulse with known pulse energy and varying delays between detector triggering and EUV flash. The short EUV light pulses are generated in a HHG process in a commercial KM-Labs XUUS beam line at the PGI-6, Forschungszentrum Jülich. A 35 fs, 3 mJ, 800 nm laser pulse is weakly focused into a glass cavity filled with low pressure (50 mbar) Argon gas. The strong electric field intensity allows high frequency up conversion. At the output an aluminum filter blocks the infrared laser light but transmits EUV radiation with wavelengths below 80 nm. The light is focused by a toroid mirror and spectrally dispersed by a reflective grating until it excites photoelectrons on the MCP detector.

For synchronization the exact time base of the fs-oscillator is used. The pulses come at a constant frequency of 2 kHz. The delay generator counts 500 µs to the next pulse with <40 ps jitter and activates the MCP and CCD at the proper moments. The CCD captures a picture of the phosphor screen during 2 s. As the HV-pulser runs at a repetition-rate of 10 Hz, 20 EUV pulses are intensified by the high gain of the HV-pulse while 3980 pulses are amplified by the offset-voltage of 650 V. Pulse to pulse intensity jitter of the HHG process is measured to be ~10%. Thus the uncertainty due to beam instability lies below 3%. The synchronization error has been checked with a high bandwidth oscilloscope to be under 1 ns. The jitter is calculated to be below 150 ps, which is not resolvable with the available oscilloscope of 2 GS/s bandwidth. The CCD images are spatially integrated over the area of the luminous spot. The results are plotted over the relative delay. Figure 1 shows the data which follows a Gaussian curve with offset. The width of the sensitivity window is 2 ns (FWHM).

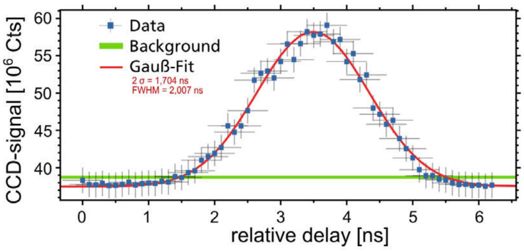

FIG. 1: Time scan through the sensitivity window. The detector is triggered at varying relative delays to the EUV light. The sensitivity rises by a factor of 107 (peak) during 2 ns (FWHM). The background is produced by an offset-voltage of 650V which amplifies 199 pulses with a low gain in contrast to the single pulse that is amplified by the high voltage pulse.

Spatial resolution: Spatial resolution has been measured by a knife-edge test using several variations of discharge based EUV sources, EUV filters and distances (at two different experimental setups) in order to investigate the influence of two errors: finite emitter size and diffraction effects. The first effect is determined by geometrical optics. Edge spreading caused by the source size is calculated to be below 750 nm which is irrelevant for the measurement because it is less than the MCP's channel width. Diffraction influence can be minimized by limiting the illumination spectrum to a short wavelength range. Al and Nb filters are inserted into the beam pass that cut the spectrum above 80 nm and 18 nm. From a scalar diffraction simulation the edge transition is expected to have a diffraction limited width of 10 µm for 18 nm light.

For comparison, the edge spread function of a mounting pad has been additionally investigated. That is an area on the MCP where channels are still filled with glass to provide mechanical stability while adjoining channels are empty and can amplify photoelectrons. This region produces an inherently sharp cutoff at the back of the MCP.

The resulting MTF is shown in Figure 2. It quickly drops to 9% contrast (corresponding to Rayleigh criterion) for approx. 12 lp/mm. Spatial resolution reduction is most likely caused by the electron diffusion after the MCP. The electrons leave the channel with some transversal momentum. During acceleration to the phosphor screen the electron cloud spreads wider. There are basically two ways to compensate this effect: reduction of the flight time to the phosphor screen or of the transversal momentum. The first can be achieved by decreasing spacing between MCP and phosphor (currently 1 mm) and rising the phosphor bias voltage (currently 4 kV with possible maximum of 5 kV). Latter can be done by coating the channel ends with gold to reduce the electric field at the output. In this case the electrons will not be pulled to the channel walls anymore and will escape at smaller divergence angles. This comes at the cost of less gain since a part of the channel length is used for guiding instead of amplification.

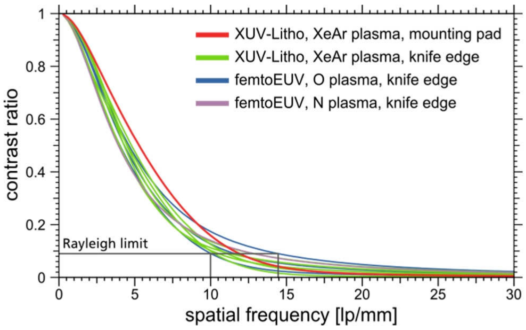

FIG. 2: Fourier transform of the normalized line spread function (LSF), derived from ESF, delivers the modulation transfer function (MTF).

In summary, temporal behavior and spatial resolution of a BURLE's 2-micron pore MCP detector have been investigated. The pulsing circuit is optimized by a custom built 25:1 transformer. As a result the gain rises by a factor of 107 in a time-window of 2 ns (FWHM). Trigger delay of 80 ns is determined for timing electronics and HV-pulse generator to activate the detector. Spatial resolution is determined to be at 12 line pairs per mm for the Rayleigh criterion, which is below manufacturer's specifications and will need to be compensated by a higher magnification of the EUV microscope.

---

[1] R. Freiberger, J. Hauck, M. Reininghaus, D. Wortmann, L. Juschkin, Proc. SPIE 8076, 80760K (2011).

[2] J. Sevick, *Transmission Line Transformers*, Noble Publishing (2001).

Publications

Aabdin, Z.; Winkler, M.; Bessas, D.; König, J.; Peranio, N.; Eibl, O.; Hermann, R.; Böttner, H.
Sb2Te3 and Bi2Te3 Thin Films Grown by Molecular Beam Epitaxy at Room Temperature
Material Research Society Symp. Proc. 1329, I04-04 (2011)

Abouzar, M.H.; Moritz, W.; Schöning, M.J.; Poghossian, A.
Capacitance-voltage and impedance-spectroscopy characteristics of nanoplate EISOI capacitors
Physica Status Solidi A, 208 (2011) 6, 1327 - 1332

Abouzar, M.H.; Poghossian, A.; Pedraza, A.M.; Gandhi, D.; Ingebrandt, S.; Moritz, W.; Schöning, M.J.
An array of field-effect nanoplate SOI capacitors for (bio-)chemical sensing
Biosensors & Bioelectronics, 26 (2011) 6, 3023 - 3028

Adam, R.; Grychtol, P.; Cramm, S.; Schneider, C.M.
Time-resolved measurements of Ni(80)Fe(20)/MgO/Co trilayers in the extreme ultraviolet range
Journal of Electron Spectroscopy and Related Phenomena, 184 (2011) 3/6, 291 - 295

Addou, R.; Shukla, A.K.; Deniozou, Th.; Heggen, M.; Feuerbacher, M.; Groening, O.; Fournee, V.; Dubois, J.M.; Ledieu, J.
Lead adsorption on the Al13Co4(100) surface: heterogeneous nucleation and pseudomorphic growth
New Journal of Physics, 13 (2011) 103011

Ahl, J.-P.; Behmenburg, H.; Giesen, C.; Regolin, I.; Prost, W.; Tegude, F. J.; Radnoczi, G. Z.; Pécz, B.; Kalisch, H.; Jansen, R. H.; Heuken, M.
Gold catalyst initiated growth of GaN nanowires by MOCVD
Physica Status Solidi (c) 8, 2315-2317 (2011)

Akola, J.; Larrucea, J.; Jones, R.O.
Polymorphism in phase-change materials: melt-quenched and as-deposited amorphous structures in Ge2 Sb2 Te5 from density functional calculations
Physical Review B, 83 (2011) 9, 094113

Alshakran, M.; Beltramo, G.; Giesen, M.; Ibach, H.
Electrical and structural properties of stepped, partially reconstructed Au(11n) surfaces in HClO4 and H2SO4 electrolytes
Surface Science, 605 (2011) 1/2, 232 - 239

Al-Zubi, A.; Bihlmayer, G.; Blügel, S.
Magnetism of 3d transition-metal monolayers on Rh(100)
Physical Review B, 83 (2011) 2, 024407

Al-Zubi, A.; Bihlmayer, G.; Blügel, S.
Modeling magnetism of hexagonal Fe monolayers on 4d substrates
Physica Status Solidi B, 248 (2011) 10, 2242 - 2247

Amekura, H.; Ishikawa, N.; Okubo, N.; Ridgway, M.C.; Giulian, R.; Mitsuishi, K.; Nakayama, Y.; Buchal, Ch.; Mantl, S.; Kishimoto, N.
Zn nanoparticles irradiated with swift heavy ions at low fluences: Optically-detected shape elongation induced by nonoverlapping ion tracks
Physical Review B, 83 (2011) 20, 205401

Anbarasu, M.; Wuttig, M.
Understanding the structure and properties of phase change materials for data storage applications
Journal of the Indian Institute of Science, 91, 259 (2011)

Andergassen, S.; Costi, T. A.; Zlatic, V.
Mechanism for large thermoelectric power in molecular quantum dots described by the negative-U Anderson model
Physical Review B, 84, 241107(R) (2011)

Andergassen, S.; Pletyukhov, M.; Schuricht, D.; Schoeller, H.; Borda, L.
A renormalization-group analysis of the interacting resonant level model at finite bias: Generic analytic study of static properties and quench dynamics
Physical Review B, 83, 205103 (2011)

Antonova, E.; Näther, C.; Kögerler, P.; Bensch, W.
Organic Functionalization of Polyoxovanadates: Sb–N Bonds and Charge Control
Angewandte Chemie Int. Ed. 50, 764 (2011).

Arida, H.A.; Al-haddad, A.S.; Schöning, M.J.
New solid-state organic membrane based lead-selective micro-electrode
International Journal of Electrochemical Science, 6 (2011) 9, 3858 - 3867

Armbrüster, M.; Wowsnick, G.; Friedrich, M.; Heggen, M.; Cardoso, R.
Synthesis and Catalytic Properties of Nanoparticulate Intermetallic Ga-Pd Compounds
Journal of the American Chemical Society, 133 (2011) 23, 9112 - 9118,

Arndt, J.; Stockert, O.; Schmalzl, K.; Faulhaber, E.; Jeevan, H. S.; Geibel, C.; Schmidt, W.; Loewenhaupt, M.; Steglich, F.
Spin fluctuations in normal state CeCu2Si2 on approaching the quantum critical point
Physical Review Letters, 106 (2011) 246401

Atakaramians, S.; Shahraam, A.V.; Nagel, M.; Rasmussen, H.K.; Bang, O.; Monro, T.M.; Abbott, D.
Direct probing of evanescent field for characterization of porous terahertz fibers
Applied Physics Letters 98 (2011) 12

Atodiresei, N.; Caciuc, V.; Lazic, P.; Blügel, S.
Engineering the magnetic properties of hybrid organic-ferromagnetic interfaces by molecular chemical functionalization
Physical Review B, 84 (2011) 17, 172402

Austgen, M.; Köhl, D.; Zalden, P.; Kubart, T.; Nyberg, T.; Pflug, A.; Siemers, M.; Berg, S.; Wuttig, M.
Sputter yield amplification by Tungsten doping of Al2O3 employing reactive serial co-sputtering: process characteristics and resulting film properties
Journal of Physics D: Appl. Phys. 44, 345501 (2011)

Avila-Brande, D.; Boese, M.; Houben, L.; Schubert, J.; Luysberg, M.
Strain-Induce Shift of the Crystal-Field Splitting of SrTiO(3) Embedded in Scandate Multilayers
ACS Applied Materials & Interfaces, 3 (2011) 5, 1545 – 1551

Baca, S.G.; Botezat, O.; Filippova, I.; Speldrich, M.; Jeanneau, E.; Kögerler, P.
A Heptanuclear Iron(III) Oxo-Carboxylate Cluster
Zeitschrift für Anorganische und Allgemeine Chemie, 637 (2011) 7/8, 821 - 823

Baca, S.G.; Breukers, S.; Ellern, A.; Kögerler, P.
An octanuclear iron(III) isobutyrate wheel
Acta Crystallographica C 67, 371 (2011)

Baca, S.G.; Speldrich, M.; Ellern, A.; Kögerler P.
{Fe6O2}-Based Assembly of a Tetradecanuclear Iron Nanocluster
Materials Science Forum, 4 (2011) 1, 300 - 310

Bäcker, M.; Delle, L.; Poghossian, A.; Biselli, M.; Zang, W.; Wagner, P.; Schöning, M.J.
Electrochemical sensor array for bioprocess monitoring
Electrochimica Acta, 56 (2011) 26, 9673 – 9678

Bäcker, M.; Pouyeshman, S.; Schnitzler, T.; Poghossian, A.; Wagner, P.; Biselli, M.; Schöning, M.J.
A silicon-based multi-sensor chip for monitoring of fermentation processes
Physica Status Solidi A, 208 (2011) 6, 1364 - 1369

Balanetskyy, S.; Meisterernst, G.; Feuerbacher, M.
The Al-rich region of the Al-Mn-Ni alloy system. Part I: Ternary phases at 750-950 degrees C
Journal of Alloys and Compounds, 509 (2011) 9, 3787 - 3794

Balanetskyy, S.; Meisterernst, G.; Grushko, B.; Feuerbacher, M.
The Al-rich region of the Al-Mn-Ni alloy system. Part II: Phases equilibria at 620 - 1000°C
Journal of Alloys and Compounds, 509 (2011) 9, 3795 - 3805

Barannik, A.A.; Cherpark, N.T.; Ni, N.; Tanatar, M.A.; Vitusevich, S.A.; Skesanov, V.N.; Canfield, P.C.; Prozorov, R.; Glamazdin, V.V.; Torokhtii, K.I.
Millimeter-wave study of London penetration depth temperature dependence in Ba(Fe(0.926)Co(0.074))(2)As(2) single crystal
Low Temperature Physics, 37 (2011) 8, 725 – 728

Bar Sadan, M.; Maoz, B.M; Tirosh, E.; Markovich, G.
Defect-induced magnetism in chemically synthesized nanoscale sheets of MgO
Physical Review B, 83 (2011) 16, 161201

Bar Sadan, M.; Maoz, B.M.; Tirosh, E.; Popov, I.; Rosenberg, Y.; Markovich, G.
Highly defective MgO nanosheets from colloidal self-assembly
Journal of Materials Chemistry, 21 (2011) 26, 9532 - 9537

Bauer, D.; Mavropoulos, P.; Lounis, S.; Blügel, S.
Thermally activated magnetization reversal in monatomic magnetic chains on surfaces studied by classical atomistic spin-dynamics simulations
Journal of Physics: Condensed Matter, 23 (2011) 39, 394204

Baumgärtel, M.; Hell, M.; Das, S.; Wegewijs, M.R.
Transport and accumulation of spin anisotropy
Physical Review Letters, 107 (2011) 8, 087202

Becker, S.; Karrasch, C.; Mashoff, T.; Pratzer, M.; Liebmann, M.; Meden, V.; Morgenstern, M.
Probing electron-electron interactions in quantum Hall systems by scanning tunnelling spectroscopy
Physical Review Letters, 106, 156805 (2011)

Behmenburg, H.; Giesen, C.; Srnanek, R.; Kovac, J.; Kalisch, H.; Heuken, M.; Jansen, R. H.
Investigation of AlN buffer layers on 6H-SiC for AlInN HEMTs grown by MOVPE
Journal of Crystal Growth, 316, 42-45, (2011)

Beigmohamadi, M.; Mchedlidze, T.; Berghoff, B.; Sohal, R.; Suckow, S.; Arguirov, T.; Wilck, N.; Mayer, J.; Spangenberg, B.; Kittler, M.
Structural characterization of crystallized Si thin film material by HRTEM and Raman spectroscopy
Physica Status Solidi A, 208 (2011) 3, 588 - 591

Belle, C. J.; Bonamin, A.; Simon, U.; Santoyo-Salazar, J.; Pauly, M.; Bégin-Colin, S.; Pourroy, G.
Size Dependent Gas Sensing Properties of Spinel Iron Oxide Nanoparticles
Sensors and Actuators B Chem. 160, 942-950 (2011)

Bentmann, H.; Kuzumaki, T.; Bihlmayer, G.; Blügel, S.; Chulkov, E. V.; Reinert, F.; Sakamoto, K.
Spin orientation and sign of the Rashba splitting in Bi/Cu(111)
Physical Review B, 84 (2011) 11, 115426

Bergqvist, L.; Sato, K.; Katayama-Yoshida, H.; Dederichs, P.H.
Computational materials design for high-T(c) (Ga,Mn)As with Li codoping
Physical Review B, 83 (2011) 16, 165201

Bert, J.A.; Koshnick, N.C.; Bluhm, H.; Moler, K.A.
Fluxoid fluctuations in mesoscopic superconducting rings
Physical Review B 84, 134523 (2011).

Betzinger, M.; Friedrich, C.; Blügel, S.; Görling, A.
Local exact exchange potentials within the all-electron FLAPW method and a comparison with pseudopotential results
Physical Review B, 83 (2011) 4, 045105

Biercuk, M.J.; Bluhm, H.
Phenomenological study of decoherence in solid-state spin quibts due to nuclear spin diffusion
Physical Review B 83, 235316 (2011)

Birkel, C. S.; Claudio, T.; Panthöfer, M.; Birkel, A.; Koll, D.; Kieslich, G.; Schmidt, J.; Hermann, R.; Tremel, W.
Properties of spark plasma sintered nanostructured Zn1 xSb
Physica Status Solidi A, 208 (2011) 8, 1913 - 1919

Birkel, C. S.; Kieslich, G.; Bessas, D.; Claudio, T.; Branscheid, R.; Kolb, U.; Panthöfer, M.; Hermann, R.; Tremel, W.
Wet chemical synthesis and a combined x-ray and Mössbauer study of the formation of FeSb2 nanoparticles
Inorganic Chemistry, 50 (2011) 22, 11807 - 11812

Bischoff, D.; Güttinger, J.; Dröscher, S.; Ihn, T.; Ensslin, K.; Stampfer, C.
Raman spectroscopy on etched graphene nanoribbons
Journal of Applied Physics, 109 073710 (2011)

Blömers, Ch.; Lepsa, M.I.; Luysberg, M.; Grützmacher, D.; Lüth, H.; Schäpers, Th.
Electronic phase coherence in InAs nanowires
Nano Letters, 11 (2011) 9, 3550 – 3556

Bluhm, H.
Harnessing nonlinearity for linear measurements
Physics 4, 29 (2011)

Bluhm, H.; Foletti, S.; Halperin, B.I.; Yacoby, A., Neder, I.; Rudner, M.S.
Semi-classical model for the dephasing of a two-electron spin qubit coupled to a coherently evolving nuclear spin bath
Physical Review B 84, 035441 (2011).

Bocquet, F.C.; Giovanelli, L.; Amsalem, P.; Petaccia, L.; Topwal, D.; Gorovikov, S.; Abel, M.; Koch, N.; Porte, L.; Goldoni, A.; Themlin, J.-M.
Final-state diffraction effects in angle-resolved photoemission at an organic-metal interface
Physical Review B, 84 (2011), 241407

Bocquet, F.C.; Ksari, Y.; Giovanelli, L.; Porte, L.; Themlin, J.-M.
High-temperature desorption of C60 covalently bound to 6H-SiC(0001)-(3x3)
Physical Review B, 84 (2011) 7, 075333

Bohrn, U.; Stütz, E.; Fleischer, M.; Schöning, M.J.; Wagner, P.
Eukaryotic cell lines as a sensitive layer for rapid monitoring of carbon monoxide
Physica Status Solidi A, 208 (2011) 6, 1345 - 1350

Boschker, H.; Huijben, M.; Vailionis, A.; Verbeek, J.; Bals, S.; van Tendeloo, G.; Luysberg, M.; Houwman, G.; Koster, G.; Blank, D.H.A.; Rijnders, G.
Optimized fabrication of high quality La0:67Sr0:33MnO3 thin films considering all essential characteristics
Journal of Physics D - Applied Physics, 44 (2011) 20, 205001

Braune, C.; Borgelt, C.; and Grün, S. (2011)
Finding Ensembles of Neurons in Spike Trains by Non-linear Mapping and Statistical Testing Proc. 10th Int. Symposium on Intelligent Data Analysis (IDA 2011, Porto, Portugal)
Springer-Verlag, Berlin, Germany 2011

Bravyi, S.; DiVincenzo, D.P.; Loss, D.
Schrieffer-Wolff transformation for quantum many-body systems
Annals of Physics, 326 (2011) 10, 2793 - 2826

Bringer, A.; Schäpers, Th.
Spin precession and modulation in ballistic cylindrical nanowires due to the Rashba effect
Physical Review B, 83 (2011) 11, 115305

Bruchhaus, R.; Münstermann, R.; Menke, T.; Hermes, C.; Lentz, F.; Weng, R.; Dittmann, R.; Waser, R.
Bipolar resistive switching in oxides: mechanisms and scaling
Current Applied Physics, 11 (2011) 2, E75 - E78

Brüderle, D.; Petrovici, M.; Vogginger, B.; Ehrlich, M.; Pfeil, T.; Millner, S.; Grübl, A.; Wendt, K.; Müller, E.; Schwartz, M.O.; de Oliveira, D.; Jeltsch, S.; Fieres, J.; Schilling, M.; Müller, P.; Breitwieser, O.; Petkov, V.; Muller, L.; Davison, A.; Krishnamurthy, P.; Kremkow, J.; Lundqvist, M.; Muller, E.; Partzsch, J.; Scholze, S.; Zühl, L.; Mayr, C.; Destexhe, A.; Diesmann, M.; Potjans, T.; Lansner, A.; Schüffny, R.; Schemmel, J.; Meier, K. A
Comprehensive workflow for general-purpose neural modeling with highly configurable neuromorphic hardware systems
Biol Cybern 104 (2011) 4-5, 263-296

Brüggemann, D.; Wolfrum, B.; Maybeck, V.; Mourzina, Y.; Jansen, M.; Offenhäusser, A.
Nanostructured gold microelectrodes for extracellular recording from electrogenic cells
Nanotechnology, 22 (2011) 26, 265104

Brumme, T.; Neucheva, O.A.; Toher, C.; Gutiérrez, R.; Weiss, C.; Temirov, R.; Greuling, A.; Kaczmarski, M.; Rohlfing, M.; Tautz, F.S.; Cuniberti, G.
Dynamical bistability of single-molecule junctions: A combined experimental and theoretical study of PTCDA on AG(111)
Physical Review B, 84 (2011), 115449

Buchkremer, A.; Linn, M. J.; Reismann, M.; Eckert, T.; Witten, K. G.; Richtering, W.; von Plessen, G.; Simon, U.
Stepwise thermal and photothermal dissociation of a hierarchical superaggregte of DNA-functionalized gold nanoparticles
Small 7, 1397-1402 (2011)

Burghaus, J.; Sougrati, M. T.; Möchel, A.; Houben, A.; Hermann, R.; Dronskowski, R.
Local ordering and magnetism in Ga0.9Fe3.1N
Journal of Solid State Chemistry, 184 (2011) 9, 2315 – 2321

Busse, C.; Lazic, P.; Djemour, R.; Coraux, J.; Gerber, T.; Atodiresei, N.; Caciuc, V.; Brako, R.; N'Diaye, A.T.; Blügel, S.; Zegenhagen, J.; Michely, T.
Graphene on Ir(111): Physisorption with Chemical Modulation
Physical Review Letters, 107 (2011) 3, 036101

Caciuc, V.; Lennartz, M .C.; Atodiresei, N.; Karthäuser, S.; Blügel, S.
Fine tuning of the electronic structure of n-conjugated molecules for molecular electronics
Nanotechnology, 22 (2011) 14, 145701

Calvo, H.L.; Pastawski, H.M.; Roche, S.; Foa Torres, L.E.F.
Tuning laser-induced band gaps in graphene
Applied Physics Letters 98, 232103 (2011)

Caravati, S.; Colleoni, D.; Mazzarello, R.; Kühne, T. D.; Krack, M.; Bernasconi, M.; Parrinello, M.
First Principles Study of Nitrogen Doping in Cubic and Amorphous Ge2Sb2Te5
Journal of Physics: Condensed Matter 23, 265801 (2011)

Carbone, C.; Gardonio, S.; Moras, P.; Lounis, S.; Heide, M.; Bihlmayer, G.; Atodiresei, N.; Dederichs, P. H.; Blügel, S.; Vlaic, S.; Lehnert, A.; Ouazi, S.; Rusponi, S.; Brune, H.; Honolka, J.; Enders, A.; Kern, K.; Stepanow, S.; Krull, C.; Balashov, T.; Mugarza, A.; Gambardella, P.
Self-Assembled Nanometer-Scale Magnetic Networks on Surfaces: Fundamental Interactions and Functional Properties
Advanced Functional Materials, 21 (2011) 7, 1212 - 1228

Caspers, C.; Müller, M.; Gray, A. X.; Kaiser, A. M.; Gloskovskii, A.; Drube, W.; Fadley, C. S.; Schneider, C. M.
Chemical stability the magnetic oxide EuO directly on silicon observed by hard x-ray photoemission spectroscopy
Physical Review B, 84 (2011) 20, 205217

Caspers, C.; Müller, M.; Gray, A. X.; Kaiser, A. M.; Gloskovskii, A.; Drube, W.; Fadley, C. S.; Schneider, C. M.
Electronic structure of EuO spin filter tunnel contacts directly on silicon
Physica Status Solidi-Rapid Research Letters, 5 (2011) 12, 441 - 443

Chang, L. J.; Schweika, W.; Kao, Y.-J.; Chou, Y. Z.; Perßon, J.; Brückel, T.; Yang, H. C.; Chen, Y. Y.; Gardner, J. S.
Magnetic correlations in HoxTb2-xTi2O7
Physical Review B, 83 (2011) 14, 144413

Chang, L. J.; Su, Y.; Kao, Y.-J.; Chou, Y. Z.; Kakurai, K.; Mittal, R.; Schneider, H.; Brückel, T.; Balakrishnan, G.; Lees, M. R.
The temperature evolution of the magnetic correlations in pure and diluted spin ice Ho2-xYxTi2O7
Physica B: Condensed Matter, 406 (2011) 12, 2393 – 2396

Chen, T.; Carius, R.; Dasgupta, A.; Houben, L.; Huang, Y.; Luysberg, M.; Yang, D.; Finger, F.
Microcrystalline Silicon Carbide Window Layers in Silicon Thin Film Solar Cells
Solar Energy Materials and Solar Cells, 98 (2011), 380 - 378

Cherpak, N.T.; Barannik, A.A.; Bunyaev, S.A.; Prokopenko, Yu.V.; Torokhtii, K.I.; Vitusevich, S.A.
Millimeter-Wave Surface Impedance Characterization of HTS Films and Single Crystals Using Quasi-Optical Sapphire Resonators
IEEE Transactions on Applied Superconductivity, 21 (2011) 3, 591 – 594

Chilian, B.; Khajetoorians, A.A.; Lounis, S.; Costa, A.T.; Mills, D.L.; Wiebe, J.; Wiesendanger, R.
Anomalously large g factor of single atoms adsorbed on a metal substrate
Physical Review B, 84 (2011) 21, 212401

Chmielak, B.; Waldow, M.; Matheisen, Chr.; Ripperda, Chr.; Bolten, J.; Wahlbrink, Th.; Nagel, M.; Merget, F.; Kurz, H.
Pockels effect based fully integrated, strained silicon electro-optic modulator
Optics Express. 19 (2011) 18

Cottin, M. C.; Bobisch, C. A.; Schaffert, J.; Jnawali, G.; Sonntag, A.; Bihlmayer, G.; Möller, R.
Anisotropic scattering of surface state electrons at a point defect on Bi(111)
Applied Physics Letters, 98 (2011) 2, 022108

Dadda, J.; Müller, E.; Perlt, S.; Höche, T.; Bauer Pereira, P.; Hermann, R.
Microstructures and Nanostructures in long-term Annealed AgPb18SbTe20 (LAST-18) Compounds and their Influence on the Thermoelectric Properties
Journal of Materials Research, 26 (2011) 15, 1800 - 1812

Danilchenko, B.A.; Tripachko, N.A.; Lev, S.; Petrychuk, M.V.; Sydoruk, V.A.; Sundquist, B; Vitusevich, S.A.
1/f noise and mechanisms of the conductivity in carbon nanotube bundles
Carbon, 49 (2011) 15, 5201 - 5206

Debus, Ch.; Spickermann, G.; Nagel, M.; Bolívar, P.H.
All-Electronic Terahertz Spectrometer for Biosensing
Microwave and Optical Technology Letters 53 (2011) 12

Denker, M.; Roux, S.; Lindén, H.; Diesmann, M.; Riehle, A.; Grün, S.
The Local Field Potential Reflects Surplus Spike Synchrony
Cerebral Cortex 21 (2011) 12, 2681 – 2695

Desmarais, J.; Ihlefeld, J.F.; Heeg, T.; Schubert, J.; Schlom, D.G.; Huey, B.D.
Mapping and statistics of ferroelectric domain boundary angles and types
Applied Physics Letters, 99 (2011) 16, 162902

Diakhate, M. S.; Hermann, R.; Möchel, A.; Sergueev, I.; Sondergaard, M.; Christensen, M.; Verstraete, M. J.
Thermodynamic, thermoelectric and magnetic properties of FeSb2: A combined first-principles and experimental study
Physical Review B, 84 (2011) 12, 125210

Dippel, A.-C.; Schneller, T.; Dornseiffer, J.; Waser, R.
PbTiO3 nanoparticle precursors for chemical solution deposited electroceramic thin films
Journal of Sol-Gel Science and Technology, 57 (2011) 1, 36 - 42

Disch, S.; Wetterskog, E.; Hermann, R.P.; Salazar-Alvarez, G.; Busch, P.; Brückel, T.; Bergström, L.; Kamali, S.
Shape induced symmetry in self-assembled mesocrystals of iron oxide nanocubes
Nano Letters, 11 (2011) 4, 1651 - 1656

Divin, Y.; Lyatti, M.; Poppe, U.; Urban, K.; Pavlovskiy, V.
Josephson Spectroscopy for Identification of Liquids
IEEE Transactions on Applied Superconductivity, 21 (2011) 3, 311 - 314

DiVincenzo, D.P.
Toward Control of Large-Scale Quantum Computing
Science, 334 (2011) 6052, 50 - 51

Döring, S.; Schönbohm, F.; Berges, U.; Schreiber, R.; Bürgler, D.E.; Schneider, C.M.; Gorgoi, M.; Schäfers, F.; Papp, C.; Balke, B.; Fadley, C.S.; Westphal, C.
Hard x-ray photoemission using standing-wave excitation applied to the MgO/Fe interface
Physical Review B, 83 (2011), 165444

Dong, H.; Zhang, Y.; Krause, H.-J.; Xie, X.; Offenhäusser, A.
Low field MRI detection with tuned HTS SQUID magnetometer
IEEE Transactions on Applied Superconductivity, 21 (2011) 3, 509 – 513

Dunin-Borkowski, R.E.; Kadkhodazadeh, S.; Semenova, E.S.; Yvind, K.
Investigating the chemical and morphological evolution of GaAs capped InAs/InP quantum dots emitting at 1.5 mu m using aberration-corrected scanning transmission electron microscopy
Journal of Crystal Growth, 329 (2011) 1, 57 - 61

Durgun Özben, E.; Lopes, J.M.J.; Nichau, A.; Lupták, R.; Lenk, S.; Besmehn, A.; Bourdelle, K.K.; Zhao, Q.T.; Schubert, J.; Mantl, S.
Rare-earth oxide/TiN gate stacks on high mobility strained silicon on insulator for fully depleted metal-oxide-semiconductor field-effect transistors
Journal of Vacuum Science and Technology B, B29 (2011) 1, 01A903

Durgun Özben, E.; Lopes, J.M.J.; Nichau, A.; Lupták, R.; Lenk, S.; Besmehn, A.; Bourdelle, K.K.; Zhao, Q.T.; Schubert, J.; Mantl, S.
Rare-Earth Scandate/TiN Gate Stacks in SOI MOSFETs Fabricated with a Full Replacement Gate Process
IEEE Transactions on Electron Devices, 58 (2011) 3, 617 - 622

Durgun Özben, E.; Lopes, J.M.J.; Nichau, A.; Schnee, M.; Lenk, S.; Besmehn, A.; Bourdelle, K.K.; Zhao, Q.T.; Schubert, J.; Mantl, S.
Integration of LaLuO3 (k 30) as High-k Dielectric on Strained and Unstrained SOI MOSFETs with Replacement Gate Process
IEEE Electron Device Letters, 32 (2011) 1, 15 – 17

Durgun Özben, E.; Schnee, M.; Nichau, A.; Mussmann, V.; Lupták, R.; Lopes, J.M.J.; Lenk, S.; Bourdelle, K.K.; Zhao, Q.T.; Schubert, J.; Mantl, S.
LaScO3 as higher-k dielectric for p-MOSFETs
Microelectronic Engineering, 88 (2011) 7, 1323 - 1325

Ebert, Ph.; Schaafhausen, S.; Lenz, A.; Sabitova, A.; Ivanova, L.; Dähne, U.; Hong, Y.L.; Gwo, S.; Eisele, H.
Direct measurement of the band gap and Fermi level position at InN(1120)
Applied Physics Letters, 98 (2011) 6, 062103

Eickelkamp, M.; Weingarten, M.; Rahimzadeh Khoshroo, L., Ketteniss, N.; Behmenburg, H.; Heuken, M.; Donoval, D.; Chvála, A.; Kordoš, P.; Kalisch, H.; Vescan, A.
Electrical Properties of Thermally Oxidized AlInN/AlN/GaN-based Metal Oxide Semiconductor Hetero Field Effect Transistors (MOSHFET)
Journal of Applied Physics, 110, 084501 (2011)

Eickelkamp, M.; Weingarten, M.; Rahimzadeh Khoshroo, L.; Behmenburg, H.; Heuken, M.; Kalisch, H.; Jansen, R. H.; Vescan, A.
On the Thermal Oxidation of AlInN/AlN/GaN Heterostructures
Physica Status Solidi C 8, No. 7–8, 2213–2215 (2011)

Eremeev, S.V.; Bihlmayer, G.; Vergniory, M.; Koroteev, Yu. M.; Menshikova, T.V.; Henk, J.; Ernst, A.; Chulkov, E.V.
Ab initio electronic structure of thallium-based topological insulators
Physical Review B, 83 (2011) 20, 205129

Fahle, D.; Behmenburg, H.; Mauder, C.; Kalisch, H.; Jansen, R. H.; Kitahata, H.; Brien, D.; Strauch, G.; Schmitz, D.; Heuken, M.; Vescan A.
Growth of GaN in a Planetary MOCVD Hotwall System
Physica Status Solidi C 8, No. 7–8, 2041–2043 (2011)

Fang, X.; Kögerler, P.; Furukawa, Y.; Speldrich, M.; Luban, M.
Molecular Growth of a Core–Shell Polyoxometalate
Angewandt Chemie Int. Ed. 50, 5212 (2011).

Feuerbacher, M.; Ali, K.; Reissner, M.; Steiner, W.
Mossbauer investigations of crystalline and quasicrystalline Al(3)(Mn, Fe) compounds
Journal of Physics: Condensed Matter, 23 (2011) 47, 475501

Feuerbacher, M.; Jaglicic, Z.; Vrtnik, S.; Dolinsek, J.
Magnetic properties of FeAl(2) and Fe(2)Al(5)
Physical Review B, 83 (2011) 22, 224427

Flöhr, F.; Liebmann, M.; Sladej, K.; Günel, Y.; Haas, F.; Hardtdegen, H.; Schäpers, T.; Grützmacher, D.; Morgenstern, M.
Manipulating epitaxial InAs nanowires with micrometer precision
Review of Scientific Instruments, 82, 113705 (2011)

Foa Torres, L.E.F.; Calvo, H.L.; Rocha, C.G.; Cuniberti, G.
Enhancing single-parameter quantum charge pumping in carbon-based devices
Applied Physics Letters 99, 092102 (2011)

Fournier, N.; Wagner, C.; Weiss, C.; Temirov, R.; Tautz, F.S.
Force-controlled lifting of molecular wires
Physical Review B, 84 (2011) 3, 035435

Freiberger, R.; Hauck, J.; Reininghaus, M.; Wortmann, D.; Juschkin, L.
Time resolved EUV pump-probe microscopy of fs-laser induced nanostructure formation
Proc. SPIE 8076, 80760K (2011)

Fricke, R.; Zentis, P. D.; Rajappa, L. T.; Hofmann, B.; Banzet, M.; Offenhäusser, A.; Meffert, S. H.
Axon guidance of rat cortical neurons by microcontact printed gradients
Biomaterials, 32 (2011) 8, 2070 - 2076

Friedrich, C.; Müller, M.C.T.D.; Blügel, S.
Band convergence and linearization error correction of all-electron GW calculations: The extreme case of zinc oxide vol 83, 081101, 2011. Correction
Physical Review B, 84 (2011) 3, 039906

Friedrich, C.; Müller, M.C.T.D.; Blügel, S.
Band convergence and linearization error correction of all-electron GW calculations: The extreme case of zinc oxide
Physical Review B, B83 (2011) 8, 081101

Frielinghaus, R.; Goß, K.; Trellenkamp, S.; Houben, L.; Schneider, C. M.; Meyer, C.
Comprehensive characterization of an individual carbon nanotube transport device
Physica Status Solidi B, 248 (2011) 11, 2660 - 2663

Fringes, S.; Volk, C.; Norda, C.; Terres, B.; Dauber, J.; Engels, S.; Trellenkamp, S.; Stampfer, C.
Charge detection in a bilayer graphene quantum dot
Physica Status Solidi B, 248 (2011) 11, 2684 - 2687

Fujii, H.; Sato, K.; Bergqvist, L.; Dederichs, P.H.; Katayama-Yoshida, H.
Interstitial Donor Codoping Method in (Ga,Mn)As to Increase Solubility of Mn and Curie Temperature
Applied Physics Express, 4 (2011) 4, 043003

Galanakis, I.; Sasioglu, E.
High Tc half-metallic fully-compensated ferrimagnetic Heusler compounds
Applied Physics Letters, 99 (2011) 5, 052509

Galanakis, I.; Sasioglu, E.
Stability of ferromagnetism against doping in half-metallic alloys
Journal of Applied Physics, 109 (2011) 11, 113912

Galanakis, I.; Sasioglu, E.
Structural-induced antiferromagnetism in Mn-based full Heusler alloys: The case of Ni(2)MnAl
Applied Physics Letters, 98 (2011) 10, 102514

Galanakis, I.; Sasioglu, E.
Variation of the magnetic properties of Ni2MnGa Heusler alloy upon tetragonalization: a first-principles study
Journal of Physics D - Applied Physics, 44 (2011) 23, 235001

Garcia-Sanchez, F.; Kakay, A.; Hertel, R.; Asselin, P.
Depinning of transverse domain walls from notches in magnetostatically coupled nanostrips
Applied Physics Express, 4 (2011), 033001

Gasparyan, F. V.; Poghossian, A.; Vitusevich, S. A.; Petrychuk, M. V.; Sydoruk, V. A.; Siqueira, J. R. Jr.; Oliveira, O. N. Jr.; Offenhäusser, A.; Schöning, M. J.
Low-Frequency Noise in Field-Effect Devices Functionalized With Dendrimer/Carbon-Nanotube Multilayers
IEEE Sensors Journal, 11 (2011) 1, 142 - 149

Gasparyan, F.V.; Vitusevich, S.A.; Offenhäusser, A.; Schöning, M.J.
Modified charge fluctuation noise model for electrolyte-insulator-semiconductor devices
Modern Physics Letters B, 25 (2011) 11, 831 - 840

Gerharz, J.; Padmaraju, K.; Moers, J.; Grützmacher, D.
Etching titanium nitride gate stacked on high-k dielectric
Microelectronic Engineering, 88 (2011) 8, 2541 - 2543

Ghosh, A. K.; Hollmann, E.; Wördenweber, R.
Study of Matching Fields in Kagome Patterned YBCO Thin Films
IEEE Transactions on Applied Superconductivity, 21 (2011) 3, 3196 – 3199

Gilles, S.; Kaulen, C.; Pabst, M.; Simon, U.; Offenhäusser, A.; Mayer, D.
Patterned self-assembly of gold nanoparticles on chemical templates fabricated by soft UV nanoimprint lithography
Nanotechnology, 22 (2011) 29, 295301 – 295308

Glavic, A.; Voigt, J.; Perßon, J.; Su, Y.; Schubert, J.; de Groot, J.; Zande, W.; Brückel, T.
High quality TbMnO3 films deposited on YAlO3
Journal of Alloys and Compounds, 509 (2011) 16, 5061 - 5063

Goß, K.; Peica, N.; Thomsen, C.; Maultzsch, J.; Schneider, C.M.; Meyer, C.
Index assignment of a carbon nanotube rope using tip-enhanced Raman spectroscopy
Physica Status Solidi B, 248 (2011) , 2577 - 2580

Goß, K.; Smerat, S.; Leijnse, M.; Wegewijs, M.R.; Schneider, C.M.; Meyer, C.
Spin-dependent electronic hybridization in a rope of carbon nanotubes
Physical Review B, 83 (2011) , 201403(R)

Grap, S.; Andergassen, S.; Paaske, J.; Meden, V.
Spin-orbit interaction and asymmetry effects on Kondo ridges at finite magnetic field
Physical Review B 83, 115115 (2011)

Gray, A. X.; Papp, C.; Ueda, S.; Balke, B.; Yamashita, Y.; Plucinski, L.; Minar, J.; Braun, J.; Ylvisaker, E. R.; Schneider, C. M.; Pickett, W. E.; Ebert, H.; Kobayashi, K.; Fadley, C. S.
Probing bulk electronic structure with hard X-ray angle-resolved photoemission
Nature Materials, 10 (2011) 10, 759 - 764

Greuling, A.; Rohlfing, M.; Temirov, R.; Tautz, F.S.; Anders, F.B.
Ab initio study of a mechanically gated molecule: From weak to strong correlation
Physical Review B, 84 (2011) 12, 125413

Grushko, B.; Kapush, D.
X-ray powder diffraction data for the Al-Ni-Pt x-phase, Al73Ni7.2Pt19.8
Powder Diffraction, 26 (2011) 3, 283 - 229

Grushko, B.; Kapush, D.; Konoval, V.
A study of the Al-Ni-Pt alloy system. Phase equilibria at 1100 and 1300°C
Powder Metallurgy and Metal Ceramics, 50 (2011) 7-8, 462 - 470

Grushko, B.; Kapush, D.; Velikanova, T.Ya.; Samuha, S.; Meshi, L.
An investigation of the Al-Rh-Ru phase diagram above 50at.%
Journal of Alloys and Compounds, 509 (2011) 31, 8018 - 8021

Grushko, B.; Mi, S.B.
A study of the Al-rich region of the Al-Cu-Mo alloy system
Journal of Alloys and Compounds, 509 (2011) 4, L30 - L33

Grushko, B.; Mi, S.B.
X-ray powder diffraction data for Al-Cu-W phases
Powder Diffraction, 26 (2011) 70 - 73

Güttinger, J.; Seif, J.; Stampfer, C.; Capelli, A.; Ensslin, K.; Ihn, T.
Time-resolved charge detection in graphene quantum dots,
Physical Review B 83 165445 (2011).

Güttinger, J.; Stampfer, C.; Frey, T.; Ihn, T.; Ensslin, K.
Transport through a strongly coupled graphene quantum dot in perpendicular magnetic field
Nanoscale Research Letters 6 253 (2011).

Gun, J.; Gutkin, V.; Lev, O.; Boyen, H.-G.; Saitner, M.; Wagner, P.; D'Olieslaeger, M.; Abouzar, M. H.; Poghossian, A.; Schöning, M. J.
Tracing gold nanoparticle charge by electrolyte-insulator-semiconductor devices
Journal of Physical Chemistry C, 115 (2011) 11, 4439 - 4445

Gundareva, I.I.; Volkov, O.Y.; Lyatti, M.; Divin, Y.; Gubankov, V.N.; Pavlovskiy, V.V.
Evolution of electrical and electrodynamic properties of YBa2Cu3O7-x bicrystal Josephson junctions with oxygen loading
IEEE Transactions on Applied Superconductivity, 21 (2011) 3, 147 - 150

Guo, X.
Can we achieve significantly higher ionic conductivity in nanostructured zirconia?
Scripta Materialia, 65 (2011) 2, 96 – 101

Haack, G.; Moskalets, M.; Splettstoesser, J.; Büttiker, M.
Coherence of single-electron sources from Mach-Zehnder interferometry
Physical Review B 84, 081303(R) (2011)

Hahn, H.; Lükens, G.; Ketteniss, N.; Kalisch, H.; Vescan, A.
Recessed-Gate Enhancement-Mode AlGaN/GaN Heterostructure Field-Effect Transistors on Si with Record DC Performance
Applied Physics Express 4 (2011) 11, 114102

Hanuschkin, A.; Diesmann, M.; Morrison, A.
A reafferent and feed-forward model of song syntax generation in the Bengalese finch
Journal of Computational Neuroscience, 31 (2011) 3, 509 – 532

Hanuschkin, A.; Morrison, A.; Diesmann, M.
Compositionality of arm movements can be realized by propagating synchrony.
Journal of Computational Neuroscience, 30 (2011) 3, 675-697

Hauck, J.; Freiberger, R.; Juschkin, L.
Performance benchmark of a gateable microchannel plate detector for extreme ultraviolet radiation with high temporal resolution
Proc. SPIE 8076, 80760R (2011)

Heggen, M.; Houben, L.; Feuerbacher, M.
Metadislocations in the complex metallic alloys T-Al-Mn-(Pd,Fe)
Acta Materialia, 59 (2011) 11, 4458 - 4466

Heide, M.; Bihlmayer, G.; Blügel, S.
Non-planar Dzyaloshinskii spirals and magnetic domain walls in non-centrosymmetric systems with orthorhombic anisotropy
Journal of Nanoscience and Nanotechnology, 11 (2011) 4, 3005 - 3015

Heinze, S.; von Bergmann, K.; Menzel, M.; Brede, J.; Kubetzka, A.; Wiesendanger, R.; Bihlmayer, G.; Blügel, S.
Spontaneous atomic-scale magnetic skyrmion lattice in two dimensions
Nature Physics, 7 (2011) 713 - 718

Helbling, T.; Roman, C.; Durrer, L.; Stampfer, C.; Hierold, C.
Gauge Factor Tuning, Long-Term Stability, and Miniaturization of Nanoelectromechanical Carbon-Nanotube Sensors
IEEE Transactions on Electron Devices 99 1-8 (2011)

Helias, M.; Deger, M.; Rotter, S.; Diesmann, M.
Finite post synaptic potentials cause a fast neuronal response
Frontiers in Neuroscience, 5 (2011) 19, 1 – 16

Herbert, S.; Hochschulz, F.; Maryasov, A.; Juschkin, L.; Danylyuk, S.
Challenges of high-speed EUV mask blank inspection
Proc. of the 35th Workshop on Compound Semiconductor Devices and Integrated Circuits, WOCSDICE 2011, ed. by V. Raineri and F. Roccaforte, 183-184 (2011)

Hermann, R.
Emerging Leaders Generation of the Mössbauer
Mössbauer Effect Reference and Data Journal 34(2), 42 - 44 (2011)

Hermann, R.
Neutrons for global energy solutions, A foresight study
Neutron News 22, 3, 4 - 5 (2011)

Hermes, C.; Bruchhaus, R.; Waser, R.
Forming-free TiO2-based resistive switching devices on CMOS-compatible W-plugs
IEEE Electron Device Letters, 32 (2011) 11, 1588 - 1590

Hermes, C.; Wimmer, M.; Menzel, S.; Fleck, K.; Gruns, G.; Salinga, M.; Böttger, U.; Bruchhaus, R.; Schmitz-Kempen, T.; Wuttig, M.; Waser, R.
Analysis of transient currents during ultrafast switching of TiO2 nanocrossbar devices
IEEE Electron Device Letters, 32 (2011) 8, 1116 - 1118

Herrero-Martin, J.; Mazzoli, C.; Scagnoli, V.; Paolasini, L.; Walker, H.; Xiao, Y.; Brückel, T.; Mittal, R.; Kumar, N.; Dhar, S.K.; Thamizhavel, A.; Su, Y.
EuFe2As2: Magnetic Structure and Local Charge Distribution Anisotropies as Seen by Resonant X-ray Scattering
Journal of Superconductivity and Novel Magnetism 24, 1-2, 705 - 709 (2011)

Hess, L. H.; Jansen, M.; Maybeck, V.; Hauf, M. V.; Seifert, M.; Stutzmann, M.; Sharp, I. D.; Offenhäuser, A.; Garrido, J. A.
Graphene Transistor Arrays for Recording Action Potentials from Electrogenic Cells
Advanced Materials, 23 (2011) 43, 5045 – 5049

Hiltscher, B.; Governale, M.; Splettstoesser, J.; König, J.
Adiabatic pumping in a double-dot Cooper-pair beam splitter
Physical Review B 84, 155403 (2011)

Hirahara, T.; Bihlmayer, G.; Sakamoto, Y.; Yamada, M.; Miyazaki, H.; Kimura, S-i.; Blügel, S.; Hasegawa, S.
Interfacing 2D and 3D topological insulators: Bi(111) bilayer on Bi2Te3
Physical Review Letters, 107 (2011) 16, 166801

Hirn, S.; Semmler-Behnke, M.; Schleh, C.; Wenk, A.; Lipka, J.; Schäffler, M.; Takenaka, S.; Möller, W.; Schmid, G.; Simon, U.; Kreyling, W. G.
Particle size-dependent and surface charge-dependent biodistribution of gold nanoparticles after intravenous administration
European Journal of Pharmaceutics and Biopharmaceutics 7 (3), 407-416 (2011)

Hofmann, B.; Kätelhön, E.; Schottdorf, M.; Offenhäusser, A.; Wolfrum, B.
Nanocavity electrode array for recording from electrogenic cells
Lab on a Chip, 11 (2011), 1054-1058

Hong, H.-B.; Krause, H.-J.; Song, K.-B.; Choi, C.-J.; Chung, M.-A.; Son, S.-w.; Offenhäusser, A.
Detection of two different influenza A viruses using a nitrocellulose membrane and a magnetic biosensor
Journal of Immunological Methods, 365 (2011) 1/2, 95 - 100

Houben, L.; Weidenbach, M.; Bar-Sadan, M.; Enyashin, A.N.; Yadgarov, L.; Popov, I.; Tenne, R.; Seifert, G.
New Route for Stabilization of 1T-WS(2) and MoS(2) Phases
Journal of Physical Chemistry, 115 (2011) 50, 24586 - 24591

Hrauda, N.; Zhang, J.; Wintersberger, E.; Etzelstorfer, T.; Mandl, B.; Stangl, J.; Carbone, D.; Holý, V.; Jovanovic, V.; Biasotto, C.; Nanver, L.K.; Moers, J.; Grützmacher, D.; Bauer, G.
X-ray Nanodiffraction on a Single SiGe Quantum Dot inside a Functioning Field-Effect Transistor
Nano Letters, 11 (2011) 7, 2875 – 2880

Hüske, M.; Wolfrum, B.
Fabrication of a nanoporous dual-electrode system for electrochemical redox cycling
Physica Status Solidi A, 208 (2011) 6, 1265 – 1269

Ibach, H.; Rajeswari, J.; Schneider, C.M.
An electron energy loss spectrometer designed for studies of electronic energy losses and spin waves in the large momentum regime
Review of Scientific Instruments, 82 (2011) 12, 123904

Ibach, H.; Rajeswari, J.; Schneider, C.M.
An electron energy loss spectrometer designed for studies of electronic energy losses and spin waves in the large momentum regime
Review of Scientific Instruments, 82 (2011) 12, 123904

Ielmini, D.; Bruchhaus, R.; Waser, R.
Thermochemical resistive switching: materials, mechanisms, and scaling projections
Phase Transitions, 84 (2011) 7, 570 - 602

Ito, J.; Maldonado, P.; Singer, W.; Grün, S.
Saccade-Related Modulations of Neuronal Excitability Support Synchrony of Visually Elicited Spikes
Cerebral Cortex, 21 (2011) 11, 2482 – 2497

Jazbec, S.; Jaglicic, Z.; Vrtnik, S.; Wencka, M.; Feuerbacher, M.; Heggen, M.; Roitsch, S.; Dolinsek, J.
Geometric origin of magnetic frustration in the μ-Al4Mn giant-unit-cell complex intermetallic
Journal of Physics: Condensed Matter, 23 (2011) 4, 045702

Jia, C.L.; Urban, K.W.; Alexe, M.; Hesse, D.; Vrejoiu, I.
Direct Observation of Continuous Electric Dipole Rotation in Flux-Closure Domains in Ferroelectric Pb(Zr,Ti)O(3)
Science, 331 (2011) 6023, 1420 – 1423

Juergens, S.; Splettstoesser, J.; Moskalets, M.
Single-particle interference versus two-particle collisions
EPL (Europhysics Letters) 96 (2011) 3, 37011

Jung, P.; Klein, H.; Henry, J.; Chen, J.
Effect of implanted deuterium on tensile properties of helium-doped RAFM EUROFER97
Journal of Nuclear Materials, 417 (2011) 1/3, 1013 - 1017

Juschkin, L.; Maryasov, A.; Herbert, S.; Aretz, A.; Bergmann, K.; Lebert, R.
EUV dark-field microscopy for defect inspection
The 10th International Conference on X-ray Microscopy, AIP Conf. Proc. 1365, 265-268 (2011)

Kadlec, C.; Goian, V.; Rushchanskii, K.Z.; Kuzel, P.; Lezaic, M.; Kohn, K.; Pisarev, R.V.; Kamba, S.
Terahertz and infrared spectroscopic evidence of phonon-paramagnon coupling in hexagonal piezomagnetic YMnO3
Physical Review B, 84 (2011) 17, 174120

Kaiser, A.M.; Gray, X.; Conti, G.; Son, J.; Greer, A.; Perona, A.; Rattanachata, A.; Saw, A. J.; Bostwick, A.; Yang, S.; Yang, S.H.; Gullikson, E.M.; Kortright, J.; Stemmer, B.S.; Fadley, C.S.
Suppression of Near-Fermi Level Electronic States at the Interface in a LaNiO3/SrTiO3 Superlattice
Physical Review Letters, 107 (2011) 11, 116402

Kaiser, A.M.; Schoppner, C.; Romer, F.M.; Hassel, C.; Wiemann, C.; Cramm, S.; Nickel, F.; Grychtol, P.; Tieg, C.; Lindner, J.; Schneider, C.M.
Nano and picosecond magnetization dynamics of weakly coupled CoFe/Cr/NiFe trilayers studied by a multitechnique approach
Physical Review B, 84 (2011) 13, 134406

Kaiser, A.M.; Wiemann, C.; Cramm, S.; Schneider, C.M.
Spatially resolved observation of uniform precession modes in spin-valve systems
Journal of Applied Physics, 109 (2011) 7, 07D305

Kajewski, D.; Wrzalik, R.; Wojtyniak, M.; Pilch, M.; Szade, J.; Szot, K.; Lenser, Ch.; Dittmann, R.; Waser, R.
Local conductivity of epitaxial Fe-doped SrTiO3 thin films
Phase Transitions, 84 (2011) 5/6, 483 - 488

Kakudate, T.; Tsukamoto, S.; Nakaya, M.; Nakayama, T.
Initial stage of adsorption of octithiophene molecules on Cu(111)
Surface Science, 605 (2011) 11/12, 1021 - 1026

Kallis, K.T.; Keller, L.O.; Küchenmeister, C.; Horstmann, J.T.; Knoch, J.; Fiedler, H.
Nanofin based filaments for sensor applications
Microelectronic Engineering, 88 (2011) 8, 2290-2293

Kampeis, P.; Lieblang, M.; Krause, H.-J.
Application of Magnetic Filters in Bioprocess Engineering Part 3-New Measuring Method for Quantification of Magnetic Beads in Flowing Suspensions
Chemie Ingenieur Technik, 83 (2011) 6, 851 - 857

Karrasch, C.; Andergassen, S.; Meden, V.
Supercurrent through a serial quantum dot close to singlet-triplet degeneracy
Physical Review B, 84, 134512 (2011)

Karthäuser, S.
Control Molecule-based Transport for Future Molecular Devices
Journal of Physics: Condensed Matter, 23 (2011) 1, 013001

Kaye, M. D.; Schmalzl, K.; Conti Nibali, V.; Tarek, M.; Rheinstädter, M. C.
Ethanol enhances collective dynamics of lipid membranes
Physical Review E, 83 (2011) 5, 050907

Khajetoorians, A.A.; Lounis, S.; Chilian, B.; Costa, A.T.; Zhou, L.; Mills, D.L.; Wiebe, J.; Wiesendanger, R.
Itinerant Nature of Atom-Magnetization Excitation by Tunneling Electrons
Physical Review Letters, 106 (2011) 3, 037205

Khoruzha, V.G.; Kornienko, K.E.; Pavlyuchkov, D.V.; Grushko, B.; Velikanova, T.Ya.
The Al-Cr-Fe phase diagram. I Phase equilibria at subsolidus temperatures over composition range 58-100 At.% Al alloys
Powder Metallurgy and Metal Ceramics, 50 (2011) 1-2, 83 - 97

Khoruzha, V.G.; Kornienko, K.E.; Pavlyuchkov, D.V.; Grushko, B.; Velikanova, T.Ya.
The Al-Cr-Fe phase diagram. II. Liquidus surface and phase equilibria for crystallization of 58-100 at.% Al alloys
Powder Metallurgy and Metal Ceramics, 50 (2011) 3/4, 217 - 229

Kim, S.K.; Hoffmann-Eifert, S.; Reiner, M.; Waser, R.
Relation between enhancement in growth and thickness-dependent crystallization in ALD TiO2 thin films
Journal of the Electrochemical Society, 158 (2011) 1, D6 - D9

Kirchner, P.; Li, B.; Spelthahn, H.; Henkel, H.; Schneider, A.; Friedrich, P.; Kolstad, J.; Keusgen, M.; Schöning, M.J.
Thin-film calorimetric H(2)O(2) gas sensor for the validation of germicidal effectivity in aseptic filling processes
Sensors and Actuators B, 154 (2011) 2, 257 – 263

Kirchner, P.; Oberländer, J.; Friedrich, P.; Berger, J.; Suso, H.-P.; Kupyna, A.; Keusgen, M.; Schöning, M.J.
Optimisation and fabrication of a calorimetric gas sensor built up of a polyimide substrate for H2O2 monitoring
Physica Status Solidi A, 208 (2011) 6, 1235 - 1240

Kisner, A.; Heggen, M.; Fernández, E.; Lenk, S.; Mayer, D.; Simon, U.; Offenhäusser, A.; Mourzina, Y.
The Role of Oxidative Etching in the Synthesis of Ultrathin Single-Crystalline Au Nanowires
Chemistry-a European Journal, 17 (2011) 34, 9503 - 9507

Klatt, G.; Gebs, R.; Schaefer, H.; Nagel, M.; Janke, Chr.; Bartels, A.; Dekorsy, Th.
High-Resolution Terahertz Spectrometer
IEEE Journal Of Selected Topics In Quantum Electronics17 (2011) 1

Knoch, J.; Appenzeller, J.
Electronic transport in carbon nanotube field-effect transistors, in Molecular and Nanotubes, Ed. Oliver Hayden and Kornelius Nielsch
Springer Verlag 2011.

Koehl, D.; Luysberg, M.; Wuttig, M.
Highly textured zinc oxide films by room temperature ion beam assisted deposition
Physica Status Solidi - Rapid Research Letters, 3 (2009)//8, 236 - 238

Kohara, S.; Akola, J.; Morita, H.; Suzuya, K.; Weber, J.K.R.; Wilding, M.C.; Benmore, C.J.
Relationship between topological order and glass forming ability in densely packed enstatite and forsterite composition glasses
Proceedings of the National Academy of Sciences of the United States of America, 108 (2011) 36, 14780 - 14785

Kovacs, A.; Sadowski, J.; Siusys, A.; Kasama, T.; Dunin-Borkowski, R.E.; Wojciechowski, T.; Reszka, A.; Kowalski, B.
GaAs-MnAs nanowires
Physica Status Solidi B, 248 (2011) 7, 1576 - 1580

Kowalzik, P.; Atodiresei, N.; Gingras, M.; Caciuc, V.; Blügel, S.; Waser, R.; Karthäuser, S.
Single Electron Tunneling through a Tailored Arylthio-coronene
Journal of Physical Chemistry C, 115 (2011) 18, 9204 – 9209

Kretinin, A.V.; Shtrikman, H.; Goldhaber-Gordon, D.; Hanl, M.; Weichselbaum, A.; von Delft, J.; Costi, T.; Mahalu, D.
Spin-1/2 Kondo effect in an InAs nanowire quantum dot: Unitary limit, conductance scaling, and Zeeman splitting
Physical Review B, 84 (2011) 245316,

Kröger, I.; Stadtmüller, B.; Kleimann, C.; Rajput, P.; Kumpf, C.
Normal incidence x-ray standing wave study of copper-phthalocyanine submonolayers on Cu(111) and Au(111)
Physical Review B, 83 (2011) 19, 195414

Kröger, I.; Stadtmüller, B.; Wagner, C.; Weiss, C.; Temirov, R.; Tautz, F.S.; Kumpf, C.
Modelling intermolecular interactions of physisorbed organic molecules using pair potential calculations
Journal of Chemical Physics, 135 (2011) , 234703

Krumrain, J.; Mussler, G.; Borisova, S.; Stoica, T.; Plucinski, L.; Schneider, C. M.; Gruetzmacher, D.
MBE growth optimization of topological insulator Bi2Te3 films
Journal of Crystal Growth, 324 (2011), 115 - 118

Kügeler, C.; Zhang, J.; Hoffmann-Eifert, S.; Kim, S.K.; Waser, R.
Nanostructured resistive memory cells based on 8-nm-thin TiO2 films deposited by atomic layer deposition
Journal of Vacuum Science and Technology A, 29 (2011) 1, 01AD01

Kunkel, S.; Diesmann, M.; Morrison, A.
Limits to the development of feed-forward structures in large recurrent neuronal networks
Front. Comput. Neurosci. 4 (2011), 160. doi: 10.3389/fncom.2010.00160

Lappe, S.C.L.L.; Church, N.S.; Kasama, T.; Fanta, A.B.D.; Bromiley, G.; Dunin-Borkowski, R.E.; Feinberg, J.M.; Russell, S.; Harrison, R.J.
Mineral magnetism of dusty olivine: A credible recorder of pre-accretionary remanence
Geochemistry Geophysics Geosystems, 12 (2011)

Laref, A.; Sasioglu, E.; Galanakis, I.
Exchange interactions, spin waves, and Curie temperature in zincblende half-metallic sp-electron ferromagnets: the case of CaZ (Z = N, P, As, Sb)
Journal of Physics: Condensed Matter, 23 (2011) 29, 296001

Lebert, R.; Farahzadi, A.; Diete, W.; Schäfer, D.; Phiesel, C.; Wilhein, T.; Herbert, S.; Maryasov, A.; Juschkin, L.; Esser, D.; Hoefer, M.; Hoffmann, D.
Actinic EUV-mask metrology: tools, concepts, components
Proc. SPIE 7985, 79850B (2011)

Lecourt, F.; Ketteniss, N.; Behmenburg, H.; Defrance, N.; Hoel, V.; Eickelkamp, M.; Vescan, A.; Giesen, C.; Heuken, M.; De Jaeger, J.-C.
InAlN/GaN HEMTs on Sapphire Substrate with 2.9 W/mm Output Power Density at 18 GHz
Electron Device Letters 32, Vol. 07, 1340 (2011)

Lecourt, F.; Ketteniss, N.; Behmenburg, H.; Defrance, N.; Hoel, V.; Eickelkamp, M.; Vescan, A.; Giesen, C.; Heuken, M.; De Jaeger, J.-C.
RF performance of InAlN/AlN/GaN HEMTs on sapphire substrate
Electronics Letters 47 , 212 (2011)

Lee, D.-K.; Fischer, C.C.; Valov, I.; Reinacher, J.; Stork, A.; Lerch, M.; Janek, J.
An EMF cell with a nitrogen solid electrolyte - on the transference of nitrogen ions in yttria-stabilized zirconia
Physical Chemistry Chemical Physics, 13 (2011) 3, 1239 - 1242

Lehmann, J.; Shevchenko, N.; Mücklich, A.; Borany, J.V.; Skorupa, W.; Schubert, J.; Lopes, J.M.J.; Mantl, S.
Millisecond flash-lamp annealing of LaLuO3
Microelectronic Engineering, 88 (2011) 7, 1346 - 1348

Lencer, D.; Salinga, M.; Wuttig, M.
Design Rules for Phase-Change Materials in Data Storage Applications
Advanced Materials 23, 2030 (2011)

Lennartz, M. C.; Atodiresei, N.; Caciuc, V.; Karthäuser, S.
Identifying Molecular Orbital Energies by Distance-Dependent Transition Voltage Spectroscopy
Journal of Physical Chemistry C, 115 (2011) 30, 15025 - 15030

Lennartz, M.C.; Baumert, M.; Karthäuser, S.; Albrecht, M.; Waser, R.
Dihydroxy (4-thiomorpholinomethyl) benzoic acids - From molecular asymmetry to diode characteristics
Langmuir, 27 (2011) 10312

Lenser, C.; Kalinko, A.; Kuzmin, A.; Berzins, D.; Purans, J.; Szot, K.; Waser, R.; Dittmann, R.
Spectroscopic study of the electric field induced valence change of Fe-defect centers in SrTiO(3)
Physical Chemistry Chemical Physics, 13 (2011) 46, 20779 - 20786

Lezaic, M.; Spaldin, N.A.
High-temperature multiferroicity and strong magnetocrystalline anisotropy in 3d-5d double perovskites
Physical Review B, 83 (2011) 2, 024410

Lezaic, M.; Mavropoulos, Ph.; Blügel, S.
Complex magnetic behavior and high spin polarization in Fe3-xMnxSi alloys
Physical Review B, 83 (2011) 9, 094434

Li, H.; Yan, J.-Q.; Kim, J. W.; McCallum, R. W.; Lograsso, T. A.; Vaknin, D.
Anisotropic magnetoelastic coupling in single-crystalline CeFeAsO as seen via high-resolution x-ray diffraction
Physical Review B, 84 (2011) 22, 220501

Liebsch, A.
Correlated Dirac fermions on the honeycomb lattice studied within cluster dynamical mean field theory
Physical Review B, 83 (2011) 3, 035113

Liebsch, A.
High-energy pseudogap induced by Hund coupling in a degenerate Hubbard model
Physical Review B, 84 (2011) 18, 180505

Linden, H.; Tetzlaff, T.; Potjans, T.C.; Pettersen, K.H.; Grün, S.; Diesmann, M.; Einevoll, G.T.
Modeling the Spatial Reach of the LFP
Neuron, 72 (2011) 5, 859 – 872

Lindla, F.; Boesing, M.; van Gemmern, P.; Bertram, D.; Keiper, D.; Heuken, M.; Kalisch, H.; Jansen, R. H.
Employing exciton transfer molecules to increase the lifetime of phosphorescent red organic light emitting diodes
Appl. Phys. Lett. 98, 173304 (2011)

Lindla, F.; Boesing, M.; Zimmermann, C.; van Gemmern, P.; Bertram, D.; Keiper, D.; Heuken, M.; Kalisch, H.; Jansen, R. H.
Hybrid white organic light-emitting diode with a mixed-host interlayer processed by organic vapor phase deposition
J. of Photon. for Energy 1, 011013 (2011)

Liu, B.; Jin, Q.; Zhang, Y.; Mayer, D.; Krause, H.-J.; Zhao, J.; Offenhäusser, A.
A simple poly(dimethylsiloxane) electrophoresis microchip integrated with a contactless conductivity detector
Microchimica Acta, 172 (2011) 1/2, 193 - 198

Liu, B.; Zhang, Y.; Mayer, D.; Krause, H.-J.; Jin, Q.; Zhao, J.; Offenhäusser, A.
A simplified poly(dimethylsiloxane) capillary electrophoresis microchip integrated with a low-noise contactless conductivity detector
Electrophoresis, 32 (2011) 6/7, 699 - 704

Logsdail, A.J.; Akola, J.
Interaction of Au(16) Nanocluster with Defects in Supporting Graphite: A Density-Functional Study
Journal of Physical Chemistry C, 115 (2011) 31, 15240 - 15250

Lopes, J.M.J.; Durgun Özben, E.; Schnee, M.; Luptak, R.; Nichau, A.; Tiedemann, A.; Yu, W.; Zhao, Q.T.; Besmehn, A.; Breuer, U.; Luysberg, M.; Lenk, St.; Schubert, J.; Mantl, S.
Electrical and structural properties of ternary rare-earth oxides on Si and higher mobility substrates and their integration as high-k gate dielectrics in MOSFET devices
ECS Transactions, 35 (2011) 4, 461 - 479

Loth, S.; Morgenstern, M.; Wulfhekel, W.
Jenseits des Gleichgewichts: Rastertunnelmikroskopie mit Zeitauflösung.
Physik in unserer Zeit 42, 168 (2011)

Lounis, S.; Zahn, P.; Weismann, A.; Wenderoth, M.; Ulbrich, R. G.; Mertig, I.; Dederichs, P. H.; Blügel, S.
Theory of real space imaging of Fermi surface parts
Physical Review B, 83 (2011) 3, 35427

Lounis, S.; Costa, A.T.; Muniz, R.B.; Mills, D.L.
Theory of local dynamical magnetic susceptibilities from the Korringa-Kohn-Rostoker Green function method
Physical Review B, 83 (2011) 3, 035109

Luckas, J.; Kremers, S.; Krebs, D.; Salinga, M.; Wuttig, M.; Longeaud, C.
The influence of a tremperature dependent bandgap on the energy scale of modulated photocurrent experiments
Journal of Applied Physics, 110, 013719 (2011)

Lupták, R.; Lopes, J.M.J.; Lenk, St.; Holländer, B.; Durgun Özben, E.; Tiedemann, A.T.; Schnee, M.; Schubert, J.; Habicht, S.; Feste, S.; Mantl, S.; Breuer, U.; Besmehn, A.; Baumann, P.K.; Heuken, M.
Atomic layer deposition of HfO2 and Al2O3 layers on 300 mm Si wafers for gate stack technology
Journal of Vacuum Science and Technology B, B29 (2011) 1, 01A301

Luysberg, M.; Boschker, H.; Huijben, M.; Vailionis, A.; Verbeeck, J.; van Aert, S.; Bals, S.; van Tendeloo, G.; Houwman, E.P.; Koster, G.; Blank, D.H.A.; Rijnders, G.
Optimized fabrication of high-quality La(0.67)Sr(0.33)MnO(3) thin films considering all essential characteristics
Journal of Physics D - Applied Physics, 44 (2011) 20, 205001

Mairoser, T.; Schmehl, A.; Melville, A.; Heeg, T.; Zander, W.; Schubert, J.; Shai, D.; Monkman, E.J.; Shen, K.M.; Regier, T.Z.; Schlom, D.G.; Mannhart, J.
Influence of the substrate temperature on the Curie temperature and charge carrier density of epitaxial Gd-doped EuO films
Applied Physics Letters, 98 (2011) 10, 102110

Malaestean, I.L.; Speldrich, M.; Ellern, A.; Baca, S.G.; Kögerler, P.
Heterometal Expansion of Oxozirconium Carboxylate Clusters
Dalton Trans. 40, 331 (2011).

Malvestuto, M.; Carleschi, E.; Fittipaldi, R.; Gorelov, E.; Pavarini, E.; Cuoco, M.; Maeno, Y.; Parmigiani, F.; Vecchione, A.
Electronic structure trends in the Sr(n+1)Ru(n)O(3n+1) family (n=1,2,3)
Physical Review B, 83 (2011) 16, 165121

Manheller, M.; Karthäuser, S.; Blech, K.; Simon, U.; Waser, R.
Electrical Characterization of single Biphenyl-propanethiol capped 4nm Au Nanoparticles
IEEE-NANO, 919-923 (2010), DOI: 10.1109/NANO.2010.5697841

Mani Krishna, K.V.; Arya, A.; Heggen, M.; Dey, G.K.; Feuerbacher, M.; Banerjee, S.
Novel defects in Al-Pd-Fe complex metallic alloys: A micromechanical modelling approach
Intermetallics, 19 (2011) 99 - 104

Maryasov, A.; Herbert, S.; Juschkin, L.; Lebert, R.; Bergmann, K.
EUV actinic mask blank defect inspection: results and status of concept realization
Proc. SPIE 7985, 79850C (2011)

Matsunaga, T.; Yamada, N.; Kojima, R.; Shamoto, S.; Sato, M.; Tanida, H.; Uruga, T.; Kohara, S.; Takata, M.; Zalden, P.; Bruns, G.; Sergueev, I.; Wille, H.C.; Hermann, R.; Wuttig, M.
Phase-Change Materials: Vibrational Softening upon Crystallization and Its Impact on Thermal Properties
Advanced Functional Materials, 21 (2011) 12, 2232 – 2239

Matsunaga, T.; Akola, J.; Kohara, S.; Honma, T.; Kobayashi, K.; Ikenaga, E.; Jones, R. O.; Yamada, N.; Takata, M.; Kojima, R.
From local structure to nanosecond recrystallization dynamics in AgInSbTe phase-change materials
Nature Materials, 10 (2011) 129 - 134

Mauder, C.; Lutsenko, E.V.; Rzheutski, M.V.; Reuters, B.; Zubialevich, V.Z.; Pavlovskii, V.N.; Yablonskii, G.P.; Heuken, M.; Kalisch, H.; Vescan, A.
Irregular spectral position of E || c component of polarized photoluminescence from m-plane InGaN/GaN multiple quantum wells grown on LiAlO2
Applied Physics Letters 99, 232114 (2011)

Mauder, C.; Tuna, Ö.; Gutrath, B.; Behmenburg, H.; Rzheutskii, M.V.; Lutsenko, E.V.; Yablonskii, G.P.; Noyong, M.; Simon, U.; Heuken, M.; Kalisch, H.; Vescan, A.
Highly n-type doped InGaN Films for efficient direct Solar Hydrogen Generation
Physica Status Solidi (c),8 (2011), 7-8, Doi: 10.1002/pssc.201100400

Mauder, C.; Reuters, B.; Behmenburg, H.; De Souza, R.A.; Woitok, J.F.; Chou, M.M.C.; Heuken, M.; Kalisch, H.; Jansen, R.H.
Mechanisms of Impurity Incorporation during MOVPE Growth of m-plane GaN Layers on LiAlO2
Physica Status Solidi (c) 8, 2050-2052 (2011)

Mauder, C.; Reuters, B.; Wang, K.R.; Fahle, D.; Trampert, A.; Rzheutski, M.V.i; Lutsenko, E.V.; Yablonskii, G.P.; Woitok, J.F.; Chou, M.,M.C.; Heuken, M.; Kalisch, H.; Jansen, R.H.
Effect of indium incorporation on optical and structural properties of m-plane InGaN/GaN MQW on LiAlO2 substrates
Journal of Crystal Growth 315, 246-249 (2011)

Mauder, C.; Booker, I.D.; Fahle, D.; Boukiour, H.; Behmenburg, H.; Rahimzadeh Khoshroo, L.; Woitok, J.F.; Vescan, A.; Heuken, M.; Kalisch, H.; Jansen, R. H.
On the anisotropic wafer curvature of GaN-based heterostructures on Si(110) substrates grown by MOVPE
Journal of Crystal Growth 315, 220-223 (2011)

Mchedlidze, T.; Beigmohamadi, M.; Berghoff, B.; Sohal, R.; Suckow, S.; Arguirov, T.; Wilck, N.; Mayer, J.; Spangenberg, B.; Kittler, M.
Structural characterization of crystallized Si thin film material by HRTEM and Raman spectroscopy
Physica Status Solidi: pss / A 208 (2011) 3

Meier, F; Lounis, S.; Wiebe, J.; Zhou, L.; Heers, S.; Mavropoulos, Ph.; Dederichs, P.H.; Blügel, S.; Wiesendanger, R.
Spin polarization of platinum (111) induced by the proximity to cobalt nanostripes
Physical Review B, 83 (2011) 7, 075407

Menzel, S.; Water, M.; Marchewka, A.; Böttger, U.; Dittmann, R.; Waser, R.
Origin of the ultra-nonlinear switching kinetics in oxide-based resistive switches
Advanced Functional Materials, 21 (2011) 23, 4487 - 4492

Meshi, L.; Samuha, S.; Kapush, D.; Pavlyuchkov, D.; Grushko, B.
New complex intermetallic in the Al-Rh-Ru alloy system
Journal of Alloys and Compounds, 509 (2011) 23, 6551 - 6555

Mesic, B.; Schroeder, H.
Integration of perovskite oxide dielectrics into complementary metal-oxide-semiconductor capacitor structures using amorphous TaSiN as oxygen diffusion barrier
Journal of Applied Physics, 110 (2011) 6, 064117

Meuffels, P.; Schroeder, H.
Comment on "Exponential ionic drift: fast switching and low volatility of thin-film memristors"
by D.B. Strukov and R.S. Williams in Appl. Phys. A (2009) 94:515-519

Meyer, C.; Morgan, C.; Schneider, C.M.
Spin transport in ferromagnetically contacted Carbon Nanotubes
Physica Status Solidi B, 248 (2011) 11, 2680 - 2683

Mi, S.B.
Structural properties of epitaxial SrCuO(2) thin films on SrTiO(3) (001) substrates
Thin Solid Films, 519 (2011) 7, 2071 - 2074

Miasojedovas, S.; Mauder, C.; Krotkus, S.; Kadys, A.; Malinauskas, T.; Jarašiūnas, K.; Heuken, M.; Kalisch, H.; Vescan, A.
High-excitation luminescence properties of m-plane GaN grown on LiAlO2 substrates
Journal of Crystal Growth 329, 33-38 (2011)

Mikulics, M.; Fox, A.; Marso, M.; Grützmacher, D.; Donoval, D.; Kordos, P.
Electrical and structural characterization of AlGaN/GaN fiel-effect transistors with recessed gate
Vacuum, (2011), 1 - 3

Mikulics, M.; Kordos, P.; Gregusová, D.; Adam, R.; Kocan, M.; Wu, S.; Zhang, J.; Sobolewski, R.; Grützmacher, D.; Marso, M.
Monolithic Integration of Ultrafast Photodetector and MESFET in the GaN Material System
IEEE Photonics Technology Letters, 23 (2011) 17, 1189 - 1191

Minamisawa, R.A.; Schmidt, M.; Özben, E.D.; Lopes, J.M.J.; Hartmann, J.M.; Bourdelle, K.K.; Schubert, J.; Zhao, Q.T.; Buca, D.; Mantl, S.
High mobility strained Si(0.5)Ge(0.5)/SSOI short channel field effect transistors with TiN/GdScO(3) gate stack
Microelectronic Engineering, 88 (2011) 9, 2955 - 2958

Miras H.N., Stone D., Long D.-L., McInnes E.J.L., Kögerler P., Cronin L.
Exploring the Structure and Properties of Transition Metal Templated {VM17(VO4)2}
Inorganic Chemistry 50, 8384 (2011)

Mishra, S.K.; Mittal, R.; Chaplot, S. L.; Ovsyannikov, S.V.; Trots, D.M.; Dubrovinsky, L.; Su, Y.; Brückel, T.; Matsuishi, S.; Hosono, H.; Garbarino, G.
Pressure dependence of the low-temperature crystal structure and phase transition behavior of CaFeAsF and SrFeAsF: A synchrotron x-ray diffraction study
Physical Review B, 84 (2011) 22, 224513

Mitrovic, I.Z.; Simutis, G.; Davey, W.M.; Sedghi, N.; Hall, S.; Dhanak, V.R.; Alexandrou, I.; Wang, Q.; Lopes, J.M.J.; Schubert, J.
Study of interfaces and band offsets in TiN/amorphous LaLuO3 gate stacks
Microelectronic Engineering, 88 (2011) 7, 1495 - 1498

Mittal R., Zbiri M., Rols S., Su Y., Xiao Y., Chaplot S.L., Schober H., Johnson M., Chatterji T., Matsuishi S., Hosono H., Brückel T.
Phonon Dynamics in Parent and Superconducting FeAs Compounds
Chinese Journal of Physics 49, 1, 403 - 413 (2011)

Mittal, R.; Mishra, S. K.; Chaplot, S. L.; Ovsyannikov, S. V.; Greenberg, E.; Trots, D. M.; Dubrovinsky, L.; Su, Y.; Brückel, T.; Matsuishi, S.; Hosono, H.; Garbarino, G.
Ambient- and low-temperature synchrotron x-ray diffraction study of BaFe2As2 and CaFe2As2 at high pressures up to 56 GPa
Physical Review B, 83 (2011) 5, 054503

Miyamoto, K.; Wagner, T.; Mimura, S.; Kanoh, S.; Yoshinobu, T.; Schöning, M.J.
Constant-phase-mode operation of the light-addressable potentiometric sensor
Sensors and Actuators B, 154 (2011) 2, 119 - 123

Miyamoto, K.; Wagner, T.; Yoshinobu, T.; Kanoh, S.; Schöning, M.J.
Phase-mode LAPS and its application to chemical imaging
Sensors and Actuators B, 154 (2011) 1, 28 - 32

Miyamoto, K.; Wagner, T.; Yoshinobu, T.; Kanoh, S.; Schöning, M.J.
Phase-mode operation of FDM-LAPS
Sensor Letters, 9 (2011) 2, 691 - 694

Miyamoto, K.; Yoshida, M.; Sakai, T.; Matsuzaka, A.; Wagner, T.; Kanoh, S.; Yoshinobu, T.; Schöning, M.J.
Differential setup of light-addressable potentiometric sensor with an enzyme reactor in a flow channel
Japanese Journal of Applied Physics, 50 (2011) 4, 04DL08-1

Möchel, A.; Sergueev, I.; Nguyen, N.; Long, G. J.; Grandjean, F.; Johnson, D.C.; Hermann, R.
Lattice dynamics in the FeSb3 skutterudite
Physical Review B, 84 (2011) 6, 064302: 1 - 9

Möchel, A.; Sergueev, I.; Wille, H.-C.; Juranyi, F.; Schober, H.; Schweika, W.; Brown, S.R.; Kauzlarich, S.M.; Hermann, R.
Lattice dynamics in the thermoelectric Zintl compound Yb14MnSb11
Physical Review B, 84 (2011) 18, 184303

Möchel, A.; Sergueev, I.; Wille, H.-C.; Voigt, J.; Prager, M.; Stone, M. B.; Sales, B. C.; Guguchia, Z.; Shengelaya, A.; Keppens, V.; Hermann, R.
Lattice dynamics and anomalous softening in the YbFe4Sb12 skutterudite
Physical Review B, 84 (2011) 18, 184306

Molitor, F.; Güttinger, J.; Stampfer, C.; Dröscher, S.; Jacobsen, A.; Ihn, T.; Ensslin, K.
Electronic properties of graphene nanostructures
Journal of Physics: Condensed Matter 23 243201 (2011)

Morawski, I.; Blicharski, J.; Voigtländer, B.
Voltage preamplifier for extensional quarz sensors used in scanning force microscopy
Review of Scientific Instruments, 82 (2011) 6, 063701

Morgenstern, M.
Scanning Tunneling Spectroscopy in CFN Lectures of Functional
Nanostructures Volume 2, ed. by M. Vojta, C. Röthig, and G. Schön, Springer, Berlin 2011.

Morgenstern, M.
Scanning tunneling microscopy and spectroscopy of graphene on insulating substrates
(chosen for Best of Pss 2011)
Physica Status Solidi (Feature article) 248, 2423 (2011)

Müller, M.; Schneider, C.M.; Luysberg, M.
Observation of Spin Filtering in Magnetic Insulator Contacts to Silicon
Applied Physics Letters, 98 (2011), 142503

Müller, M.; Luysberg, M.; Schneider, C.M.
Magnetic properties of EuS spin filter tunnel contacts to silicon
Journal of Applied Physics, 109 (2011) 7, 07C710

Müller, M.; Schreiber, R.; Schneider, C.M.
Controlling magnetic properties of EuS-based spin valve structures on Si(001)
IEEE Transactions on Magnetics, 47 (2011) 6, 1635 - 1638

Nagel, M.; Michalski, A.; Botzem, T.; Kurz, H.
Near-field investigation of THz surface-wave emission from optically excited graphite flakes
Optics Express, 19 (2011) 5

Nagel, M.; Michalski, A.; Kurz, H.
Contact-free fault location and imaging with on-chip terahertz time-domain reflectometry
Optics Express. 19 (2011) 13

Nair, H. S.; Kumar, C.M.N.; Bhat, H. L.; Elizabeth, S.; Brückel, T.
Effect of substitution of Y on the structural, magnetic, and thermal properties of hexagonal DyMnO3 single crystals
Physical Review B, 83 (2011) 10, 104424

Nandi, S.; Su, Y.; Xiao, Y.; Price, S.; Wang, X.F.; Chen, X.H.; Herrero-Martín, J.; Mazzoli, C.; Walker, H.C.; Paolasini, L.; Francoual, S.; Shukla, D.K.; Strempfer, J.; Chatterji, T.; Kumer, C.M.N.; Mittal, R.; Ronnow, H.M.; Rüegg, Ch.; McMorrow, D.F.; Brückel, T.
Strong coupling of Sm and Fe magnetism in SmFeAsO as revealed by magnetic x-ray scattering
Physical Review B, 84 (2011) 5, 054419

Nanver, L.K.; Jovanovic, V.; Biasotto, C.; Moers, J.; Grützmacher, D.; Zhang, J.J.; Hrauda, N.; Stoffel, M.; Pezzoli, F.; Schmidt, O.G.; Miglio, L.; Kosina, H.; Marzegalli, A.; Vastola, G.; Mussler, G.; Stangl, J.; Bauer, G.; van der Cingel, J.; Bonera, E.
Integration of MOSFETs with SiGe dots as stressor material
Solid-State Electronics, 60 (2011) 1, 75 - 83

Nelles, J.; Rodríguez-Castellón, E.; Simon, U.
Electrical Properties of Thin Layers consisting of Surface Functionalized Silicon Nanoparticles
Mater. Res. Soc. Symp. Proc., Vol. 1359, (2011), Doi: 10.1557/opl.2011.769

Nepijko, S.A.; Krasyuk, A.; Oelsner, A.; Schneider, C.M.; Schonhense, G.
Quantitative measurements of magnetic stray field dynamics of Permalloy particles in a photoemission electron microscopy
Journal of Microscopy, 242 (2011) 2, 216 -220

Netzel, C.; Mauder, C.; Wernicke, T.; Reuters, B.; Kalisch, H.; Heuken, M.; Vescan, A.; Weyers, M.; Kneissl, M.
Strong charge carrier localization interacting with extensive nonradiative recombination in heteroepitaxially grown m-plane GaInN quantum wells
Semiconductor Science and Technology 26, 105017 (2011)

Ney, A.; Kovàcs, A.; Ney, V.; Ye, S.; Ollefs, K.; Kammermeier, T.; Wilhelm, F.; Rogalev, A.; Dunin-Borkowski, R.E.
Structural,chemical and magnetic properties of secondary phases in Co-doped ZnO
New Journal of Physics, 13 (2011) 103001,

Niederdraenk, F.; Seufert, K.; Stahl, A.; Bhalerao-Panajkar, R.S.; Marathe, S.; Kulkarni, S.K.; Neder, R.B.; Kumpf, C.
Ensemble modeling of very small ZnO nanoparticles
Physical Chemistry Chemical Physics, 13 (2011) 2, 498 – 505

Novotny, T.; Haupt, F.; Belzig, W.
Nonequilibrium phonon backaction on the current noise in atomic-sized junctions
Physical Review B 84, 113107 (2011)

Okawa, Y.; Mandal, S.K.; Hu, C.; Tateyama, Y.; Goedecker, S.; Tsukamoto, S.; Hasegawa, T.; Gimzewski, J.K.; Aono, M.
Chemical Wiring and Soldering toward All-Molecule Electronic Circuitry
Journal of the American Chemical Society, 133 (2011) 21, 8227 - 8233

Ono, T.; Tsukamoto, S.
First-principles study on atomic configuration of electron-beam irradiated C60 film
Physical Review B, 84 (2011) 16, 165410

Ono, T.; Tsukamoto, S.; Egami, Y.; Fujimoto, Y.
Real-space calculations for electron transport properties of nanostructures
Journal of Physics: Condensed Matter, 23 (2011) 39, 394203

Panaitov, G.; Thiery, S.; Hofmann, B.; Offenhäusser, A.
Fabrication of gold micro-spine structures for improvement of cell/device adhesion
Microelectronic Engineering, 88 (2011) 8, 1840 - 1844

Panek, J.J.; Mazzarello, R.; Novic, M.; Jezierska-Mazzarello, A.
Impact of Mercury(II) on the Proteinase K Catalytic Center: Investigations via Classical and Born-Oppeinheimer Molecular Dynamics
Molecular Diversity 15, 215 (2011)

Papp, C.; Plucinski, L.; Minar, J.; Braun, J.; Ebert, H.; Schneider, C.M.; Fadley, C.S.
Band mapping in x-ray photoelectron spectroscopy: An experimental
and theoretical study of W(110) with 1.25 keV excitation
Physical Review B, 84 (2011) 4, 045433

Pavarini, E.
Lattice distortions in KCuF3: a paradigm shift?
Annalen der Physik, 523 (2011) 10, 865 - 866

Pavunny, S.P.; Thomas, R.; Kalkur, T.S.; Schubert, J.; Fachini, E.; Katiyar, R.S.
Fabrication and electrical characterization of high-k LaGdO3 thin films and field effect transistors
ECS Transactions, 35 (2011) 2, 297 - 304

Pavunny, S.P.; Thomas, R.; Murari, N.M.; Schubert, J.; Mussmann, V.; Luptak, R.; Kalkur, T.S.; Katiyar, R.S.
Structural and Electrical Properties of Lanthanum Gadolinium Oxide: Ceramic and Thin Films for High-k Application
Integrated Ferroelectrics, 125 (2011) 1, 44 - 52

Pester, C.W.; Ruppel, M.; Schoberth, H.G.; Schmidt, K.; Liedel, V; van Rijn, P.; Schindler, K.A.; Hiltl, S. Czubak, T.; Mays, J.; Urban, V.S.; Böker, A.
Piezoelectric Properties of Non-Polar Block Copolymers
Advanced Materials, 2011, 23, 4047.

Pletyukhov, M.; Schuricht, D.
Non-equilibrium transport through quantum dots with Dzyaloshinsky--Moriya--Kondo interaction
Physical Review B, 84, 041309 (2011)

Plucinski, L.; Mussler, G.; Krumrain, J.; Herdt, A.; Suga, S.; Gruetzmacher, D.; Schneider, C.M.
Robust surface electronic properties of topological insulators: Bi2Te3 films grown by molecular beam epitaxy
Applied Physics Letters, 98 (2011) 22, 222503

Poghossian, A.; Malzahn, K.; Abouzar, M.H.; Mehndiratta, P.; Katz, E.; Schöning, M.J.
Integration of biomolecular logic gates with field-effect transducers
Electrochimica Acta, 56 (2011) 26, 9661 - 9665

Poghossian, A.; Wagner, H.; Schöning, M.J.
Functional testing and characterisation of (bio-)chemical sensors on wafer level
Sensors and Actuators B, 154 (2011) 2, 169 - 173

Popova, D.; Bringer, A.; Blügel, S.
Theory of the inverse Faraday effect in view of ultrafast magnetization experiments
Physical Review B, 84 (2011) 21, 214421

Potjans, W; Diesmann, M.; Morrison, A.
An Imperfect Dopaminergic Error Signal Can Drive Temporal-Difference Learning. PLoS
Computational Biology, 7 (2011) 5, e1001133

Puschnig, P.; Reinisch, E.-M.; Ules, T.; Koller, G.; Soubatch, S.; Ostler, M.; Romaner, L.; Tautz, F.S.; Ambrosch-Draxl, C.; Ramsey, M.G.
Orbital tomography: Deconvoluting photoemission spectra of organic molecules
Physical Review B, 84 (2011), 235427

Raissi, M.; Regula, G.; Hadj Belgacem, C.; Rochdi, N.; Bozzo-Escoubas, S.; Coudreau, C.; Holländer, B.; Fnaiech, M.; D'Avitaya, F.A.; Lazzari, J.-L.
Different architectures of relaxed Si1-xGe/Si preudo-substrates grown by low-pressure chemical vapor deposition: Structural and morphological characteristics
Journal of Crystal Growth, 328 (2011) 1, 18-24

Raji A. T., Mazzarello R., Scandolo S., Nsengiyumva S., Härting M., Britton D. T.
Intrinsic Defects and Krypton Impurity Atoms in HCP Titanium: a First-Principles Study
Physical Review B, 83, 054120 (2011)

Raji A. T., Mazzarello R., Scandolo S., Nsengiyumva S., Härting M., Britton D. T.
Defects in Ion-implanted HCP-Titanium: A First-Principles Study of Electronic Structures
Solid State Communications 151, 1889 (2011)

Rauter, P.; Mussler, G.; Grützmacher, D.; Fromherz, T.
Tensile strained SiGe quantum well infrared photodetectors based on a light-hole ground state
Applied Physics Letters, 98 (2011) 21, 211106

Redhammer, G. J.; Senyshyn, A.; Tippelt, G.; Roth, G.
Magnetic spin structure of pyroxene-type MnGeO3
Journal of Physics-Condensed Matter 23 (25) Article Number: 254202 (2011).

Redhammer, G. J.; Senyshyn, A.; Meven, M.; Roth, G.; Prinz, S.; Pachler, A.; Tippelt, G.; Pietzonka, C.; Treutmann, W.; Hoelzel, M.; Pedersen, B.; Amthauer, G.
Nuclear and incommensurate magnetic structure of NaFeGe2O6 between 5 K and 298 K and new data on multiferroic NaFeSi2O6
Physics and Chemistry of Minerals, 38 (2) 139-157 (2011).

Ritchie, C.; Speldrich; M.; Gable, R.W.; Sorace, L.; Kögerler, P.; Boskovic ,C.
Utilizing the Adaptive Polyoxometalate [As2W19O67(H2O)]14– To Support a PolynuclearLanthanoid-Based Single-Molecule Magnet
Inorganic Chemistry 50, 7004 (2011).

Romanyuk, K.; Cherepanov, V.; Voigtländer, B.
Symmetry and shape of reconstructed two-dimensional islands
Physical Review B, 83 (2011), 205413

Rosezin, R.; Linn, E.; Kügeler, C.; Bruchhaus, R.; Waser, R.
Crossbar logic using bipolar and complementary resistive switches
IEEE Electron Device Letters, 32 (2011) 6, 710 - 712

Rosezin, R.; Meier, M.; Breuer, U.; Kügeler, C.; Waser, R.
Electroforming and Resistance Switching Characteristics of Silver-Doped MSQ With Inert Electrodes
IEEE Transactions on Applied Superconductivity, 10 (2011) 2, 338 – 343

Rosezin, R.; Linn, E.; Nielen, L.; Bruchhaus, R.; Waser, R.
Integrated complementary resistive switches for passive high-density nanocrossbar arrays
IEEE Electron Device Letters, 32 (2011) 2, 191 - 193

Sadowski, J.; Domagala, J.; Mathieu, R.; Kovàcs, A; Kasama, T.; Dunin-Borkowski, R.E.; Dietl, T.
Formation process and superparamagnetic propeties of (Mn,Ga)As nanocrystals in GaAs fabricated by annealing of (Ga,Mn)As layers with low Mn content
Physical Review B, 84 (2011) 24, 245306

Sakalauskas, E.; Reuters, B.; Rahimzadeh Khoshroo, L.; Kalisch, H.; Heuken, M.; Vescan, A.; Röppischer, M.; Cobet, C.; Gobsch, G.; Goldhahn, R.
Dielectric function and optical properties of quaternary AlInGaN alloys
Journal of Applied Physics 110, 013102 (2011)

Sakalauskas, E.; Behmenburg, H.; Schley, P.; Gobsch, G.; Giesen, C.; Kalisch, H.; Jansen, R.H.; Heuken, M.; Goldhahn, R.
Dielectric function of Al-rich AlInN in the range 1–18 eV
Physica Status Solidi A 208, No. 7, 1517–1519 (2011)

Sakuma, R.; Friedrich, C.; Miyake, T.; Blügel, S.; Aryasetiawan, F.
GW calculations including spin-orbit coupling: Application to Hg chalcogenides
Physical Review B, 84 (2011) 8, 085144

Salinga, M.; Wuttig, M.
Phase-Change Memoires on a Diet
Science 332, 543 (2011)

Samain, L.; Silversmit, G.; Sanyova, J.; Vekemans, B.; Salomon, H.; Gilbert, B.; Grandjean, F.; Long, G. L.; Hermann, R. P.; Vincze, L.; Strivay, D.
Fading of modern Prussian blue pigments in linseed oil medium
Journal of Analytical Atomic Spectrometry, 26 (2011) 5, 930 - 941

Sandratskii, L.M.; Mavropoulos, Ph.
Magnetic excitations and femtomagnetism of FeRh: A first-principles study
Physical Review B, 83 (2011) 17, 174408

Sanetra, N.; Feig, V.; Wolfrum, B.; Offenhäusser, A.; Mayer, D.
Low impedance surface coatings via nanopillars and conductive polymers
Physica Status Solidi A, 208 (2011), 1284 - 1289

Sarreshtedari, F.; Hosseini, M.; Razmkhah, S.; Mehrany, K.; Kokabi, H.; Schubert, J.; Banzet, M.; Krause, H.J.; Fardmanesh, M.
Analytical Model for the Extraction of Flaw-Induced Current Interactions for SQUID NDE
IEEE Transactions on Applied Superconductivity, 21 (2011) 1, 3442 - 3446

Sasioglu, E.; Friedrich, C.; Blügel, S.
Effective Coulomb interaction in transition metals from constrained random-phase approximation
Physical Review B, 83 (2011) 12, 121101(R),

Schlipf, M.; Betzinger, M.; Friedrich, C.; Lezaic, M.; Blügel, S.
HSE hybrid functional within the FLAPW method and its application to GdN
Physical Review B, 84 (2011) 12, 125142

Schneller, T.; Halder, S.; Waser, R.; Pithan, C.; Dornseiffer, J.; Shiratori, Y.; Houben, L.; Vyshnavi, N.; Majumber, S.B.
Nanocomposite thin films for miniaturized multi-ayer ceramic capacitors prepared from barium titanate nanoparticle based hybrid solutions
Journal of Materials Chemistry, 21 (2011) 22, 7953-7965

Schnez, S.; Güttinger, J.; Stampfer, C.; Ensslin, K.; Ihn, T.
The relevance of electrostatics for scanning-gate microscopy
New Journal of Physics 13 053013 (2011).

Schroeder, H.; Pandian, R.; Miao, J.
Resistive switching and changes in microstructure
Physica Status Solidi A, 208 (2011) 2, 300 - 316

Schubert, F.; Mokrousov, Y.; Ferriani, P.; Heinze, S.
Noncollinear magnetism in freestanding and supported monatomic Mn chains
Physical Review B, 83 (2011) 16, 165442

Schuricht, D.
Local density of states of a quarter-filled one-dimensional Mott insulator with a boundary
Physical Review B, 84, 045122 (2011)

Schuricht, D.; Essler, F.H.L.; Jaefari, A.; Fradkin, E.
Boundary effects on the local density of states of one-dimensional Mott insulators and charge density wave states
Physical Review B, 83, 035111 (2011)

Sedghi, N.; Mitrovic, I.Z.; Lopes, J.M.J.; Schubert, J.; Hall, S.
Investigation of Electron and Hole Charge Trapping in LaLuO3 Stack MOS Capacitor Using the Three-Pulse CV Technique
ECS Transactions, 35 (2011) 4, 531 - 543

Seemann, K.; Freimuth, F.; Zhang, H.; Blügel, S.; Mokrousov, Y.; Bürgler, D.E.; Scheider, C.M.
Origin of the Planar Hall Effect in Nanocrystalline Co60Fe20B20
Physical Review Letters, 107 (2011) 8, 086603

Sergueev, I.; Wille, H.-C.; Hermann, R.; Bessas, D.; Shvydko, Y.V.; Zajac, M.; Rüffer, R.
Milli-electronvolt monochromatization of hard X-rays with a sapphire backscattering monochromator
Journal of Synchrotron Radiation, 18 (2011) 5, 802 - 810

Siegrist, T.; Jost, P.; Volker, H.; Woda, M.; Merkelbach, P.; Schlockermann, C.; Wuttig, M.
Disorder-induced localization in crystalline phase-change materials
Nature Materials 10, 202 (2011)

Silkin, I.V.; Koroteev, Yu.M.; Eremeev, S.V.; Bihlmayer, G.; Chulkov, E.V.
Three- and Two-Dimensional Topogical Insulators in Pb2Sb2Te5, Pb2Bi2Te5, and Pb2Bi2Se5 Layered Compounds
JETP Letters, 94 (2011) 3, 217 - 221

Simons, T.; Simon, U.
Zeolithe H-ZSM-5: A Microporous Proton Conductor for the in situ monitoring of DeNOx-SCR
Mater. Res. Soc. Symp. Proc. Vol. 1330, (2011), DOI: 10.1557/opl.2011.1337

Singh, R.; Scholz, R.; Christiansen, S.; Mantl, S.; Reiche, M.
Investigation of a hydrogen implantation-induced blistering phenomenon in Si0.70Ge0.30
Semiconductor Science and Technology, 26 (2011) 12, 125001

Skoromets, V.; Kadlec, F.; Nemec, H.; Rychetsky, I.; Panaitov, G.; Müller, V.; Fattakhova-Rohlfing, D.; Moch, P.; Ku¸el, P.
Tuning of dielectric properties of SrTiO3 in the terahertz range
Physical Review B, 84 (2011) 17, 174121

Slawinski, M.; Bertram, D.; Heuken, M.; Kalisch, H.; Vescan, A.
Electrothermal characterization of organic light-emitting diodes employing finite-element simulation
Organic Electronics 12 (2011) 1399–1405

Slipukhina, I.; Mavropoulos, P.; Blügel, S.; Lezaic, M.
Ferromagnetic Spin Coupling of 2p Impurities in Band Insulators Stabilized by an Intersite Coulomb Interaction: Nitrogen-Doped MgO
Physical Review Letters, 107 (2011) 13, 137203

Slomski, B.; Landolt, G.; Meier, F.; Patthey, L.; Bihlmayer, G.; Osterwalder, J.; Dil, J.H.
Manipulating the Rashba-type spin splitting and spin texture of Pb quantum well states
Physical Review B, 84 (2011) 19, 193406

Sluka, V.; Kakay, A.; Deac, A.M.; Burgler, D.E.; Hertel, R.; Schneider, C.M.
Spin-Transfer Torque Induced Vortex Dynamics in Fe/Ag/Fe Nanopillars
Journal of Physics D - Applied Physics, 44 (2011) 38, 384002

Smith, J.T.; Sandow, C.; Das, S.; Minamisawa, R.A.; Mantl, S.; Appenzeller, J.
Silicon Nanowire Tunneling Field-Effect Transistor Arrays: Improving Subthreshold Performance Using Excimer Laser Annealing
IEEE Transactions on Electron Devices, 58 (2011) 7, 1822 - 1829

Sofer, Z.; Sedmidubsky, D.; Moram, M.; Macková, A.; Marysko, M.; Hejtmánek, J.; Buchal, C.; Hardtdegen, H.; Václavu, M.; Perina, V.; Groetzschel, R.; Mikulics, M.
Magnetism in GaN layers implanted by La, Gd, Dy and Lu
Thin Solid Films, 519 (2011) 18, 6120 - 6125

Song, F.; Müller, F.; Behr, R.; Fang, L.; Klushin, A.M.
Self-Emission From Arrays of Overdamped Josephson Junctions
IEEE Transactions on Applied Superconductivity, 21 (2011) 3, 315 - 318

Song, F.; Müller, F.; Scheller, T.; Semenov, A.; He, M.; Fang, L.; Hübers, H.-W.; Klushin, A.M.
Compact tunable sub-terahertz oscillators based on Josephson junctions
Applied Physics Letters, 98 (2011), 142506

Soni, R.; Meuffels, P.; Staikov, G.; Weng, R.; Kügeler, C.; Petraru, A.; Hambe, M.; Waser, R.; Kohlstedt, H.
On the stochastic nature of resistive switching in Cu doped Ge0.3Se0.7 based memory devices
Journal of Applied Physics, 110 (2011), 054509

Sosso, G.C.; Caravati, S.; Mazzarello, R.; Bernasconi, M.
Raman Spectra of Cubic and Amorphous Ge2Sb2Te5 from First Principles
Physical Review B, 83, 134201 (2011)

Soubatch, S.; Kröger, I.; Kumpf, C.; Tautz, F.S.
Structure and growth of tetracene on Ag(111)
Physical Review B, 84 (2011) 19, 195440

Speldrich, M.; Schilder, H.; Lueken, H.; Kögerler, P.
A Computational Framework for Magnetic Polyoxometalates and Molecular Spin Structures: CONDON 2.0
Israel Journal of Chemistry, 51 (2011) 2, 215.

Stadtmüller, B.; Kröger, I.; Reinert, F.; Kumpf, C.
Submonolayer growth of CuPc on noble metal surfaces
Physical Review B, 83 (2011) 8, 085416

Stampfer, C.; Fringes, S.; Güttinger, J.; Molitor, F.; Volk, C.; Terrés, B.; Dauber, J.; Engels, S.; Schnez, S.; Jacobsen, A.; Dröscher, S.; Ihn, T.; Ensslin, K.
Transport in Graphene Nanostructures
Frontiers of Physics 6 271-293 (2011)

Steffens, P.; Friedt, O.; Sidis, Y.; Link, P.; Kulda, J.; Schmalzl, K.; Nakatsuji, S.; Braden, M.
Magnetic excitations in the metallic single-layer ruthenates Ca2-xSrxRuO4 studied by inelastic neutron scattering
Physical Review B, 83 (2011) 5, 054429

Steinmann, W.; Walter, S.; Seide, G.; Gries, T.; Roth, G.; Schubnell, M.
Structure, Properties, and Phase Transitions of Melt-Spun Poly(vinylidene fluoride) Fibers
Journal of Applied Polymer Science 120 (1) 21-35 (2011).

Stemme, F.; Geßwein, H.; Drahus, M.D.; Holländer, B.; Azucena, C.; Binder, J.R.; Eichel, R.-A.; Haußelt, J.; Bruns, M.
Characterization of non-stoichiometric co-sputtered Ba0.6Sr0.4(- Ti1-xFex)1+xO3- thin films for tunable passive microwave applications
Analytical and Bioanalytical Chemistry, (2011), online first

Stepina, P.; Koptev, E.S.; Dvurechenskii, A.V.; Nikiforov, A.I.; Gerharz, J.; Moers, J.; Grützmacher, D.
Giant mesoscopic photoconductance fluctuations in Ge/Si quantum dot system
Applied Physics Letters, 98 (2011) 14, 142101

Stockert, O.; Arndt, J.; Faulhaber, E.; Geibel, C.; Jeevan, H. S.; Kirchner, S.; Loewenhaupt, M.; Schmalzl, K.; Schmidt, W.; Si, Q.; Steglich, F.
Magnetically driven superconductivity in CeCu2Si2
Nature Physics, 7 (2011) 2, 119 - 124

Strozecka, A.; Muthukumar, K.; Larsson, J.A.; Dybek, A.; Dennis, T.J.S.; Myslivecek, J.; Voigtländer, B.
Electron-induced excitation of vibrations of Ce atoms inside a C-80 cage
Physical Review B, 83 (2011) 16, 165414

Szade, J.; Szot, K.; Kulpa, M.; Kubacki, J.; Lenser, Ch.; Dittmann, R.; Waser, R.
Electronic structure of epitaxial Fe-doped SrTiO3 thin films
Phase Transitions, 84 (2011) 5/6, 489 - 500

Szafranek, B.; Schall, D.; Otto, M.; Neumaier, D.; Kurz, H.
High On/Off Ratios in Bilayer Graphene Field Effect Transistors Realized by Surface Dopants
Nano Letters11 (2011) 7

Szot, K.; Rogala, M.; Speier, W.; Klusek, Z.; Besmehn, A.; Waser, R.
TiO2-a prototypical memristive material
Nanotechnology, 22 (2011) 25, 1 - 21

Tappertzhofen, S.; Linn, E.; Nielen, L.; Rosezin, R.; Lentz, F.; Bruchhaus, R.; Valov, I.; Böttger, U.; Waser, R.
Capacity based nondestructive readout for complementary resistive switches
Nanotechnology, 22 (2011) 39, 395203

Tappertzhofen, S.; Linn, E.; Nielen, L.; Rosezin, R.; Lentz, F.; Bruchhaus, R.; Valov, I.; Böttger, U.; Waser, R.
Redox Processes in Silicon Dioxide Thin Films using Copper Microelectrodes
Applied Physics Letters, 99 (2011) 20, 203103

Terrés, B.; Dauber, J.; Volk, C.; Trellenkamp, S.; Wichmann, U.; Stampfer, C.
Disorder induced Coulomb gaps in graphene constrictions with different aspect ratios
Applied Physics Letters 98 032109 (2011).

Terrés, B.; Borgwardt, N.; Dauber, J.; Volk, C.; Engels, S.; Fringes, S.; Weber, P.; Trellenkamp, S.; Wichmann, U.; Stampfer, C.
Transport in kinked bi-layer graphene interconnects
Proceedings of the 6th IEEE International Conference on Nano/Micro Engineered and Molecular Systems, Kaohsiung, Taiwan, February 20-23, 1037-1040, (2011).

Tillmann, K.; Garbrecht, M.; Spiecker, E.; Jäger, W
Quantitative atom column position analysis at the incommensurate interfaces of a (PbS)(1.14)NbS(2) misfit layered compound with aberration-corrected HRTEM
Ultramicroscopy, 111 (2011) 3, 245 - 250

Toher, C.; Temirov, R.; Greuling, A.; Pump, F.; Kaczmarski, M.; Cuniberti, G.; Rohlfing, M.; Tautz, F.S.
Electrical transport through a mechanically gated molecular wire
Physical Review B, 83 (2011) 15, 155402

Tomforde, J.; Bensch, W.; Kienle, L.; Duppel, V.; Merkelbach, P.; Wuttig, M.
Thin Films of GeSbTe-Based Phase Change Materials: Microstructure and in Situ Transformation
Chemistry of Materials 23, 3871 (2011)

Tòth, A.; Törcsik, A.; Tombàcz, E.; Olàh, E.; Heggen, M.; Li, C.L.; Klummpp, E.; Geissler, E.; Làszlò, K.
Interaction of phenol and dopamine with commercial MWCNTs
Journal of Colloid and Interface Science, 364 (2011) 469 - 475

Tsukamoto, S.; Egami, Y.; Hirose, K.; Blügel, S.
Stabilized scattering wave-function calculations using the Lippmann-Schwinger equation for long conductor systems
Physical Review B, 84 (2011) 11, 115443

Tsunashima, R.; Long, D.-L.; Endo, T.; Noro, S.; Akutagawa, T.; Nakamura, T.; Quesada Cabrera, R.; McMillan, P.F.; Kögerler, P.; Cronin, L.
Exploring the thermochromism of sulfite-embedded polyoxometalate capsules
Physical Chemistry Chemical Physics, 13, 7295 (2011).

Tsuruoka, T.; Terabe, K.; Hasegawa, T.; Valov, I.; Waser, R.; Aono, M.
Effects of Moisture on the Switching Characteristics of Oxide-Based, Gapless-Type Atomic Switches
Advanced Functional Materials, DOI: 10.1002/adfm.201101846, Article first published online: 14 OCT 2011

Tuna, Ö.; Behmenburg, H.; Giesen, C.; Kalisch, H.; Jansen, R.H.; Yablonskii, G.P.; Heuken, M.
Dependence of InN properties on MOCVD growth parameters
Phys. Status. Solidi C 8, No. 7-8, 2044-2046 (2011)

Valldor, M.; Hermann, R.; Wuttke, J.; Zamponi, M.; Schweika, W.
Spin correlation in the extended kagome system YbaCo3FeO7
Physical Review B, 84 (2011) 22, 224426

Volk, C.; Fringes, S.; Terrés, B.; Dauber, J.; Engels, S.; Trellenkamp, S.; Stampfer, C.
Electronic excited states in bilayer graphene double quantum dots
Nano Letters, 11 (9) 3581–3586 (2011). (or: arXiv:1105.1912).

Volkov, O.Y.; Divin, Y.; Gubankov, V.N.; Gundareva, I.; Pavlovskiy, V.V.
Terahertz characterization of external resonant systems by high-Tc Josephson Junctions
IEEE Transactions on Applied Superconductivity, 21 (2011) 3, 306 – 310

Valov, I.; Luerssen, B.; Mutoro, E.; Gregoratti, L.; deSouza, R.A.; Bredow, T.; Günther, S.; Barinov, A.; Dudin, P.; Martin, M.; Janek, J.
Electrochemical activation of molecular nitrogen at the Ir/YSZ interface
Physical Chemistry Chemical Physics, 13 (2011) 8, 3394 – 3410

Valov, I.; Waser, R.; Jameson, J.R.; Kozicki, M.N.
Electrochemical metallization memories-fundamentals, applications, prospects
Nanotechnology, 22 (2011) 25, 254003

Wada, M.; Murakami, S.; Freimuth, F.; Bihlmayer, G.
Localized edge states in two-dimensional topological insulators: Ultrathin Bi films
Physical Review B, 83 (2011) 12, 121310(R)

Wagatsuma, N.; Potjans, T.; Diesmann, M.; Fukai, T.
Layer-dependent attentional processing by top-down signals in a visual cortical microcircuit model
Frontiers in Computational Neuroscience, 5 (2011) 31

Wagner, T.; Werner, C.F.; Miyamoto, K.; Schöning, M.J.; Yoshinobu, T.
A high-density multi-point LAPS set-up using VCSEL array and FPGA control
Sensors and Actuators B, 154 (2011) 2, 124 - 128

Walter, S.; Steinmann, W.; Schuette, J.; Seide, G.; Gries, T.; Roth, G.; Wierach, P.; Sinapius, M.
Characterisation of piezoelectric PVDF monofilaments
Materials Technology 26 (3) 140-145 (2011).

Wang, Y.; Chi, J.; Banerjee, K.; Grützmacher, D.; Schäpers, Th.; Lu, J.G.
Field effect transistor based on single crystalline InSb nanowire
Journal of Materials Chemistry, 21 (2011) 8, 2459 - 2462

Wang, Y.; Wang, H.; Zhang, G.; Dong, H.; Xie, X.; Jiang, M.; Zhang, Y.; Krause, H.-J.; Offenhäusser, A.; Mück, M.
Voltage Biased SQUID Bootstrap Circuit: Circuit Model and Numerical Simulation
IEEE Transactions on Applied Superconductivity, 21 (2011) 3, 354 - 357

Wang, W.; Dong, H.; Pacheco, V.; Willbold, D.; Zhang, Y.; Offenhäusser, A.; Hartmann, R.; Weirich, T.; Ma, P.; Krause, H. J.; Gu, Z.
Relaxation behavior study of ultra-small superparamagnetic iron oxide nanoparticles at ultra-low and ultra-high magnetic fields
Journal of Physical Chemistry B, 115 (2011) 49, 14789 - 14793

Wang, Z.; Fan, B.; Zhao, X.J.; Yue, H.W.; He, M.; Ji, L.; Yan, S.L.; Fang, L.; Klushin, A. M.
Characteristics of Off-Chip Millimeter-Wave Radiation from Serial Josephson Junction Arrays
Chinese Physics Letters, 28 (2011) 6, 067401

Weber, D.; Mourzina, Y.; Brüggemann, D.; Offenhäusser, A.
Large-Scale Patterning of Gold Nanopillars in a Porous Anodic Alumina Template by Replicating Gold Structures on a Titanium Barrier
Journal of Nanoscience and Nanotechnology, 11 (2011) 2, 1293 - 1296

Wegewijs, M.R.; Romeike, C.; Schoeller, H.; Hofstetter, W.
Corrigendum: Magneto-transport through single-molecule magnets: Kondo-peaks, zero-bias dips, molecular symmetry and berry's phase
New Journal of Physics, 13 (2011), 079501

Wegewijs, M.R.; Romeike, C.; Schoeller, H.; Hofstetter, W.
Erratum: Kondo-transport spectroscopy of single molecule magnets
Physical Review Letters, 106 (2011) 1, 019902

Wehling, T. O.; Sasioglu, E.; Friedrich, C.; Lichtenstein, A. I.; Katsnelson, M. I.; Blügel, S.
Strength of Effective Coulomb Interactions in Graphene and Graphite
Physical Review Letters, 106 (2011) 23, 236805

Weidenbach, M.; Bar-Sadan, M.; Houben, L.; Albu-Yaron, A.; Levy, M.; Tenne, R.; Popovitz-Biro, R.; Enyashin, A.N.; Seifert, G.; Feuermann, D.; Katz, E.A.; Gordon, J.M.
MoS(2) Hybrid Nanostructures: From Octahedral to Quasi-Spherical Shells within Individual Nanoparticles
Angewandte Chemie-International Edition, 50 (2011) 8, 1810 - 1814

Weidlich, P.H.; Dunin-Borkowski, R.; Ebert, Ph.
Quantitative determination of local potential values in inhomogeneously doped semiconductors by scanning tunneling microscopy
Physical Review B, 84 (2011) 8, 085210

Weidner, T.; Baio, J.E.; Mundstock, A.; Große, C.; Karthäuser, S.; Bruhn, C.; Siemeling, U.
NHC-based self-asssembled monolayers on solid gold substrates
Australian Journal of Chemistry, 64 (2011) 8, 1177

Weischenberg, J.; Freimuth, F.; Sinova, J.; Blügel, S.; Mokrousov, Y.
Ab Initio Theory of the Scattering-Independent Anomalous Hall Effect
Physical Review Letters, 107 (2011) 10, 106601

Wencka, M.; Jazbec, S.; Jagli, Z.; Vrtnik, M.; Feuerbacher, M.; Heggen, M.; Roitsch, S.; Dolinsek, J.
Electrical resistivity of the u-Al4Mn giant-unit-cell complex metallic alloy
Philosophical Magazine, 91 (2011) 19/21, 2756 - 2764

Werner, C.F.; Krumbe, C.; Schumacher, K.; Groebel, S.; Spelthahn, H.; Stellberg, M.; Wagner, T.; Yoshinobu, T.; Selmer, T.; Keusgen, M.; Baumann, M.E.M.; Schöning, M.J.
Determination of the extracellular acidification of Escherrichia Coli by a light-addressable potentiometric sensor
Physica Status Solidi A, 208 (2011) 6, 1340 – 1344

Werner, C.F.; Schusser, S.; Spelthahn, H.; Wagner, T.; Yoshinobu, T.; Schöning, M.J.
Field-programmable gate array based controller for multi spot light-addressable potentiometric sensors with integrated signal correction mode
Electrochimica Acta, 56 (2011) 26, 9656 - 9660

Witten, K. G.; Rech, C.; Eckert, T.; Charrak, S.; Richtering, W.; Elling, L.; Simon, U.
Glyco-DNA Gold Nanoparticles: Lectin-Mediated Assembly and Dual Stimuli Response
Small 7, 1954-1960 (2011)

Wortmann, D.; Blügel, S.
Influence of the electronic structure on tunneling through ferroelectric insulators: Application to BaTiO3 and PbTiO33
Physical Review B, 83 (2011) 15, 155114

Xiang, D.; Pyatkov, F.; Schröper, F.; Offenhäusser, A.; Zhang, Y.; Mayer, D.
Molecular Junctions Bridged by Metal Ion Complexes
Chemistry-a European Journal, 17 (2011) 47, 13166 – 13169

Xiang, D.; Zhang, Y.; Pyatkov, F.; Offenhäusser, A.; Mayer, D.
Gap size dependent transition from direct tunneling to field emission in single molecule junctions
Chemical Communications, 47 (2011), 4760 - 4762

Xiao, Y.; Su, Y.; Kumar, C. M. N.; Ritter, C.; Mittal, R.; Price, S.; Perßon, J.; Brückel, T.
Physical properties, crystal and magnetic structure of layered Fe(1.11)Te(1-) (x) Se (x) superconductors
European Physical Journal B, 82 (2011) 2, 113-121

Yan, M.; Andreas, C.; Kakay, A.; Garcia-Sanchez, F.; Hertel, R.
Fast domain wall dynamics in magnetic nanotubes: Suppression of Walker breakdown and Cherenkov-like spin wave emission
Applied Physics Letters, 99 (2011) 12, 122505

Yang, S.H.; Balke, B.; Papp, Ch.; Doering, S.; Berges, U.; Plucinski, L.; Westphal, C.; Schneider, C.M.; Parkin, S.S.P.; Fadley, C.S.
Determination of layer-resolved composition, magnetization, and electronic structure of an Fe/MgO tunnel junction by standing-wave core and valence photoemission
Physical Review B, 84 (2011) 18,184410

Yang, S.; Huang, S.; Chen, H.; Schnee, M.; Zhao, Q.T.; Schubert, J.; Chen, K.J.
Characterization of high- LaLuO3 thin film grown on AlGaN/GaN heterostructure by molecular beam deposition
Applied Physics Letters, 99 (2011) 18,182103

Yao, H.; Duan, J.; Mo, D.; Günel, H.Y.; Chen, Y.; Liu, J.; Schäpers, Th.
Optical and electrical properties of gold nanowires synthesized by electrochemical deposition
Journal of Applied Physics, 110 (2011) 9, 094301

Yao, H.; Mo, D.; Duan, J.; Chen, Y.; Liu, J.; Sun, Y.; Hou, M.; Schäpers, Th.
Investigation of the surface properties of gold nanowire arrays
Applied Surface Science, 258 (2011) 1, 147 -1 50

Yoon, S.; Dornseiffer, J.; Xing, Y.; Grüner, D.; Shen, Z.; Iwaya, S.; Pithan, C.; Waser, R.
Spark plasma sintering of nanocrystalline BaTiO3-powders: Consolidation behavior and dielectric characteristics
Journal of the European Ceramic Society, 31 (2011) 9, 1723 - 1731

Yoon, S.; Dornseiffer, J.; Xiong, Y.; Grüner, D.; Shen, Z.; Iwaya, S.; Pithan, C.; Waser, R.
Synthesis, spark plasma sintering and electrical conduction mechanism in BaTi3-Cu composites
Journal of the European Ceramic Society, 31 (2011) 5, 773 - 782

Yu, W.; Zhang, B.; Zhao, Q.T.; Hartmann, J.M.; Buca, D.; Nichau, A.; Lupták, R.; Lopes, J.M.; Lenk, S.; Luysberg, M.; Bourdelle, K.K.; Wang, X.; Mantl, S.
High mobility compressive strained Si0.5Ge0.5 quantum well p-MOSFETs with higher-k/metal-gate
Solid-State Electronics, 62 (2011) 1, 185 - 188

Yukhymchuk, V.O.; Kiselov, V.S.; Belyaev, A.E.; Valakh, M.Ya.; Chrusanova, M.V.; Danailov, M.; Vitusevich, S.A.
Raman Spectroscopy of bio-SiC ceramics
Physica Status Solidi A, 208 (2011) 4, 808 – 813

Zaikina, O.V.; Khorujaya, V.G.; Pavlyuchkov, D.; Grushko, B.; Velikanova, T.Ya.
Investigation of the Al-Ti-Pt alloy system at 1100°C
Journal of Alloys and Compounds, 509 (2011) 28, 7565 - 7571

Zaikina, O.V.; Khorujaya, V.G.; Pavlyuchkov, D.; Grushko, B.; Velikanova, T.Ya.
Phase equilibria in Al-Ti-Pd at 930 and 1100°C
Journal of Alloys and Compounds, 509 (2011) 43 - 51

Zalden, P.; Bichara, C.; van Eijk, J.; Hermann, R.; Sergueev, I.; Bruns, G.; Buller, S.; Bensch, W.; Matsunaga, T.; Yamada, N.; Wuttig, M.
Thermal and elastic properties of Ge-Sb-Te based phase-change materials
Mater. Res. Soc. Symp. Proc. 1338, R06-03 (2011)

Zevenbergen, M.A.G.; Singh, P.S.; Goluch, E.D.; Wolfrum, B.L.; Lemay, S.G.
Stochastic Sensing of Single Molecules in a Nanofluidic Electrochemical Device
Nano Letters, 11 (2011) 7, 2881 - 2886

Zhang, B.; Yu, W.; Zhao, Q.T.; Buca, D.; Holländer, B.; Hartmann, J.M.; Zhang, M.; Wang, X.; Mantl, S.
Improved NiSi0.8Ge0.2/Si0.8Ge0.2 Contacs by C+ Pre-Implantation
Electrochemical and Solid State Letters, 14 (2011) 7, H261-H263

Zhang, B.; Yu, W.; Zhao, Q.T.; Mussler, G.; Jin, L.; Buca, D.; Holländer, B.; Hartmann, J.M.; Zhang, M.; Wang, X.; Mantl, S.
Epitaxial growth of Ni(Al)Si0.7Ge0.3 on Si0.7Ge0.3/Si(100) by Al interlayer mediated epitaxy
Applied Physics Letters, 98 (2011) 25, 252101

Zhang, G.; Zhang, Y.; Dong, H.; Krause, H.-J.; Xie, X.; Braginski, A.I.; Offenhäusser, A.; Jiang, M.
An approach to optimization of the superconducting quantum interference bootstrap circuit
Superconductor Science and Technology, 24 (2011) 6, 065023

Zhang, H.; Freimuth, F.; Blügel, S.; and Mokrousov, Y.
Role of Spin-Flip Transitions in the Anomalous Hall Effect of FePt Alloy
Physical Review Letters, 106 (2011) 11, 117202

Zhang, H.; Blügel, S.; Mokrousov, Y.
Anisotropic intrinsic anomalous Hall effect in ordered 3dPt alloys
Physical Review B, 84 (2011) 2, 024401

Zhang, Y.; Zhang, G.; Wang, H.; Wang, Y.; Dong, H.; Xie, X.; Mück, M.; Krause, H.-J.; Braginski, A.I.; Offenhäusser, A.; Jiang, M.
Comparison of noise performance of the dc SQUID bootstrap circuit with that of the standard flux modulation dc SQUID readout scheme
IEEE Transactions on Applied Superconductivity, 21 (2011) 3, 501 - 504

Zhao, Q.T.; Hartmann, J.M.; Mantl, S.
An Improved Si tunnel Field Effect Transistor with a Buried Strained Si1-xGex Source
IEEE Electron Device Letters, 32 (2011) 11, 1480 - 1482

Zheng, Y.; Ellern, A.; Kögerler, P.
A Spin-Frustrated Cobalt(II) Carbonate Pyrochlore Network
Acta Crystallographica - C 67, 56 (2011)

Zhukov, A.A.; Volk, Ch.; Winden, A.; Hardtdegen, H.; Schäpers, Th.
Low-temperature conductance of the weak junction in InAs nanowire in the field of AFM scanning gate
JETP Letters, 93 (2011) 1, 10 - 14

Ziegler, D.; Gava, P.; Güttinger, J.; Molitor, F.; Wirtz, L.; Lazzeri, M.; Saitta, A.M.; Stemmer, A.; Mauri, F.; Stampfer, C.
Variations in the work function of doped single- and few-layer graphene assessed by Kelvin probe force microscopy and density functional theory
Physical Review B, 83 235434 (2011)

Zimmer, C.M.; Schubert, J.; Hamann, S.; Kunze, U.; Doll, T.
Nanoscale photoelectron ionisation detector based of lanthanum hexaboride
Physica Status Solidi A, 208 (2011) 6, 1241 - 1245

Cover pictures refer to the following selected research reports (from left to right)

Engels et al., Transport in Coupled Graphene-Nanotube Quantum Devices, p. 41
Schaal et al., Electrically Conducting Gold Nanopatterns on Structured SAMs by Chemical e-Beam Lithography, p. 103
Korte et al., Selective Adsorption of C_{60} on Ge/Si Nanostructures, p. 39
Jia et al., Electric Dipole Rotation in Flux-closure Domains in Ferroelectric $Pb(Zr,Ti)O_3$, p. 129

JARA | FIT

JARA-FIT

Jülich Aachen Research Alliance
for Fundamentals of
Future Information Technology

Office:

Forschungszentrum Jülich GmbH
52425 Jülich
Germany

Phone: ++49-2461-613107
Email: w.speier@fz-juelich.de

AN INITIATIVE OF

RWTH AACHEN UNIVERSITY

JÜLICH
FORSCHUNGSZENTRUM